

1983

Electrical breakdown and ignition of an electrostatic particulate suspension

Tae-U Yu

Iowa State University

Follow this and additional works at: <https://lib.dr.iastate.edu/rtd>

 Part of the [Mechanical Engineering Commons](#)

Recommended Citation

Yu, Tae-U, "Electrical breakdown and ignition of an electrostatic particulate suspension " (1983). *Retrospective Theses and Dissertations*. 7661.

<https://lib.dr.iastate.edu/rtd/7661>

This Dissertation is brought to you for free and open access by the Iowa State University Capstones, Theses and Dissertations at Iowa State University Digital Repository. It has been accepted for inclusion in Retrospective Theses and Dissertations by an authorized administrator of Iowa State University Digital Repository. For more information, please contact digirep@iastate.edu.

INFORMATION TO USERS

This reproduction was made from a copy of a document sent to us for microfilming. While the most advanced technology has been used to photograph and reproduce this document, the quality of the reproduction is heavily dependent upon the quality of the material submitted.

The following explanation of techniques is provided to help clarify markings or notations which may appear on this reproduction.

1. The sign or "target" for pages apparently lacking from the document photographed is "Missing Page(s)". If it was possible to obtain the missing page(s) or section, they are spliced into the film along with adjacent pages. This may have necessitated cutting through an image and duplicating adjacent pages to assure complete continuity.
2. When an image on the film is obliterated with a round black mark, it is an indication of either blurred copy because of movement during exposure, duplicate copy, or copyrighted materials that should not have been filmed. For blurred pages, a good image of the page can be found in the adjacent frame. If copyrighted materials were deleted, a target note will appear listing the pages in the adjacent frame.
3. When a map, drawing or chart, etc., is part of the material being photographed, a definite method of "sectioning" the material has been followed. It is customary to begin filming at the upper left hand corner of a large sheet and to continue from left to right in equal sections with small overlaps. If necessary, sectioning is continued again—beginning below the first row and continuing on until complete.
4. For illustrations that cannot be satisfactorily reproduced by xerographic means, photographic prints can be purchased at additional cost and inserted into your xerographic copy. These prints are available upon request from the Dissertations Customer Services Department.
5. Some pages in any document may have indistinct print. In all cases the best available copy has been filmed.

**University
Microfilms
International**

300 N. Zeeb Road
Ann Arbor, MI 48106

8316171

Yu, Tae-U

**ELECTRICAL BREAKDOWN AND IGNITION OF AN ELECTROSTATIC
PARTICULATE SUSPENSION**

Iowa State University

PH.D. 1983

**University
Microfilms
International** 300 N. Zeeb Road, Ann Arbor, MI 48106

PLEASE NOTE:

In all cases this material has been filmed in the best possible way from the available copy.
Problems encountered with this document have been identified here with a check mark .

1. Glossy photographs or pages _____
2. Colored illustrations, paper or print _____
3. Photographs with dark background
4. Illustrations are poor copy _____
5. Pages with black marks, not original copy _____
6. Print shows through as there is text on both sides of page _____
7. Indistinct, broken or small print on several pages
8. Print exceeds margin requirements _____
9. Tightly bound copy with print lost in spine _____
10. Computer printout pages with indistinct print _____
11. Page(s) _____ lacking when material received, and not available from school or author.
12. Page(s) _____ seem to be missing in numbering only as text follows.
13. Two pages numbered _____. Text follows.
14. Curling and wrinkled pages _____
15. Other _____

University
Microfilms
International

Electrical breakdown and ignition of an
electrostatic particulate suspension

by

Tae-U Yu

A Dissertation Submitted to the
Graduate Faculty in Partial Fulfillment of the
Requirements for the Degree of
DOCTOR OF PHILOSOPHY

Major: Mechanical Engineering

Approved:

Signature was redacted for privacy.

In Charge of Major Work

Signature was redacted for privacy.

For the Major Department

Signature was redacted for privacy.

For the Graduate College

Iowa State University
Ames, Iowa

1983

TABLE OF CONTENTS

	Page
NOMENCLATURE	xi
I. INTRODUCTION	1
A. Present Study	1
B. Relevance of Study	1
C. Literature Review	4
1. Electrical breakdown	4
a. Breakdown criterion in gases	4
b. Breakdown time lags	10
c. Effect of particles	14
2. Temporal development of a spark breakdown	18
a. Charge transfer	18
b. Energy transfer	22
3. Flammability and ignition limit	27
a. Flammability limit and flame quenching	27
b. Spark ignition	32
c. Effect of uniform inert particles	38
D. Objectives of Investigation	39
II. EXPERIMENTAL DESIGN AND CALIBRATION	42
A. Experimental Design	42
1. Electrostatic suspension	42
2. Moving needle electrode	45
3. Overall experimental setup	51
B. Experimental Instruments	53
C. Calibration	55
1. Particle number density	55
2. Moving needle velocity and position	57

	Page
III. ELECTRICAL BREAKDOWN OF UNIFORM PARTICULATE CLOUDS	68
A. Experimental Procedure	68
B. Results and Discussion	70
1. Breakdown voltage and needle position	70
a. Effect of polarity	70
b. Effect of needle velocity	75
c. Effect of uniform particulate clouds	76
2. Correlation	82
3. Probability	108
C. Conclusion	117
IV. TEMPORAL DEVELOPMENT OF A SPARK BREAKDOWN IN UNIFORM PARTICULATE CLOUDS	120
A. Experimental Technique	120
B. Results and Discussion	126
1. Spark discharge and energy	126
2. Effects of uniform particulate clouds	133
C. Conclusion	141
V. SPARK IGNITION OF UNIFORM PARTICLE-GAS MIXTURES	142
A. Experimental Technique	142
1. Experimental setup	142
2. Flowmeter calibration	143
3. Experimental procedure	147
B. Results and Discussion	150
1. Ignition of combustible gases	150
2. Effect of a moving needle	154
3. Effect of uniform particulate suspensions	156
4. Correlation	163
C. Conclusion	178

	Page
VI. CONCLUSIONS AND RECOMMENDATIONS	182
VII. BIBLIOGRAPHY	187
VIII. ACKNOWLEDGMENTS	198
IX. APPENDIX A: ELECTROSTATIC SUSPENSION	200
X. APPENDIX B: PARTICLE SIZE AND SHAPE DISTRIBUTION	203
XI. APPENDIX C: FLOWMETER	206
XII. APPENDIX D: ERROR ANALYSIS	210

LIST OF TABLES

	Page
Table 2.1. Particle sieve size ranges and averages	56
Table 3.1. Variables influencing spark breakdown in particulate suspensions	86
Table 3.2. Correlation constants	93
Table 10.1. Statistical particle size and shape data obtained by a Lemont Scientific Image Analyzer	204

LIST OF FIGURES

	Page
Figure 2.1. Schematics for uniform electrostatic particulate suspensions	44
Figure 2.2. Layout of experimental setup	46
Figure 2.3. Photograph of experimental setup	47
Figure 2.4. Moving needle electrode shape and dimensions	49
Figure 2.5. Main electrodes	50
Figure 2.6a. Current vs. particle number density at fixed electric field strength, $D = 96 \mu\text{m}$	58
Figure 2.6b. Current vs. particle number density at fixed electric field strength, $D = 96 \mu\text{m}$	59
Figure 2.6c. Current vs. particle number density at fixed electric field strength, $D = 68 \mu\text{m}$	60
Figure 2.6d. Current vs. particle number density at fixed electric field strength, $D = 48 \mu\text{m}$	61
Figure 2.6e. Current vs. particle number density at fixed electric field strength, $D = 34 \mu\text{m}$	62
Figure 2.7. On-off circuit, two-step signals and sketch of electrode gap showing various relevant distances	63
Figure 2.8a. Needle position vs. time, $y \geq 0$	65
Figure 2.8b. Needle position vs. time, $y \leq 0$	66
Figure 3.1. Photograph of a spark triggered by a positive moving needle in a uniform particulate cloud	71
Figure 3.2. Breakdown voltage vs. average non-dimensional needle penetration distance, effect of needle polarity	72

	Page
Figure 3.3. Breakdown voltage vs. average non-dimensional needle penetration distance, effect of needle velocity	77
Figure 3.4a. Particle number density vs. average non-dimensional needle penetration distance at breakdown, L=1.02 cm, and V=10.0, 19.0 KV	79
Figure 3.4b. Particle number density vs. average non-dimensional needle penetration distance at breakdown, L=1.02 cm, and V=16.0 KV	80
Figure 3.4c. Particle number density vs. average non-dimensional needle penetration distance at breakdown, L=1.02 cm, and V=13.0 KV	81
Figure 3.5a. Particle number density vs. average non-dimensional needle penetration distance at breakdown, L=2.00 cm, and V=20.0, 31.3 KV	83
Figure 3.5b. Particle number density vs. average non-dimensional needle penetration distance at breakdown, L=2.00 cm, and V=13.0, 25.5 KV	84
Figure 3.6. Particle number density vs. average non-dimensional needle penetration distance at breakdown, L=0.75 cm, and V=9.5, 11.5, 14.0 KV	85
Figure 3.7. Average particle diameter vs. particle number density at breakdown, $(1-x) > (1-x)_c$	88
Figure 3.8. Particle mean free path parameter vs. average nondimensional needle penetration distance at breakdown, L=1.02 cm	89
Figure 3.9. Particle mean free path parameter vs. average nondimensional needle penetration distance at breakdown, L=2.00 cm	90
Figure 3.10. Particle mean free path parameter vs. average nondimensional needle penetration distance at breakdown, L=0.75 cm	91

	Page
Figure 3.11. Breakdown voltage vs. average non-dimensional needle penetration distance $((1-x)_o$ and $(1-x)_c$)	92
Figure 3.12. Particle mean free path parameter vs. normalized breakdown voltage with needle position	96
Figure 3.13. Particle collision parameter at breakdown needle position vs. normalized breakdown voltage with needle position	98
Figure 3.14. Particle collision probability vs. normalized breakdown voltage with needle position	103
Figure 3.15a. Cumulative positional breakdown distribution, $L=1.02$ cm when $N=0$	109
Figure 3.15b. Cumulative positional breakdown distribution, $L=0.75, 1.02, 2.00$ cm when $N=0$	110
Figure 3.16a. Cumulative positional breakdown distribution $L=1.02$ cm when $ND^2 > (ND^2)_*$	112
Figure 3.16b. Cumulative positional breakdown distribution, $L=1.02$ cm when $ND^2 > (ND^2)_*$	113
Figure 3.17a. Cumulative positional breakdown distribution, $L=1.02$ cm when $ND^2 < (ND^2)_*$	114
Figure 3.17b. Cumulative positional breakdown distribution, $L=1.02$ cm when $ND^2 < (ND^2)_*$	115
Figure 3.17c. Cumulative positional breakdown distribution, $L=1.02$ cm when $ND^2 < (ND^2)_*$	116
Figure 4.1. External circuit for spark current measurement	121
Figure 4.2. Equivalent circuit	121
Figure 4.3. Temporal development of spark breakdown	125
Figure 4.4. Temporal development of spark breakdown associated with a particulate cloud and a positive moving needle	129

	Page
Figure 4.5. Ratio of spark charge to stored charge, without particles	131
Figure 4.6. Ratio of spark energy to stored energy, without particles	134
Figure 4.7. Ratio of spark charge to stored charge, with particles	135
Figure 4.8. Ratio of spark energy to stored energy, with particles	137
Figure 4.9. Time interval between two pulses, with particles	139
Figure 4.10. Peak current magnitude of the first pulse vs. time interval between two pulses, with particles	140
Figure 5.1. Layout for combustible gas mixing	144
Figure 5.2a. Flowmeter calibration, Gilmont B-5284	145
Figure 5.2b. Flowmeter calibration, Gilmont A-2855	146
Figure 5.3. Spark ignition energy vs. fuel-air ratio, without particles	152
Figure 5.4. Spark ignition energy vs. needle-to-plane gas distance, moving needle effect	155
Figure 5.5. Photograph of the spark ignition of a uniform inert particle-gas mixture	157
Figure 5.6a. Spark ignition energy vs. particle number density, $D = 96 \mu\text{m}$	159
Figure 5.6b. Spark ignition energy vs. particle number density, $D = 96 \mu\text{m}$	160
Figure 5.6c. Spark ignition energy vs. particle number density, $D = 96 \mu\text{m}$	161
Figure 5.7. Limiting particle number density for ignition vs. fuel-air ratio	162
Figure 5.8a. Spark ignition energy vs. particle number density, $D = 68 \mu\text{m}$	164

	Page
Figure 5.8b. Spark ignition energy vs. particle number density, $D = 68 \mu\text{m}$	165
Figure 5.9a. Spark ignition energy vs. particle number density, $D = 48 \mu\text{m}$	166
Figure 5.9b. Spark ignition energy vs. particle number density, $D = 48 \mu\text{m}$	167
Figure 5.10. Spark ignition energy vs. particle number density, $D = 34 \mu\text{m}$	168
Figure 5.11. Limiting particle number density for ignition vs. average particle diameter	169
Figure 5.12a. Spark ignition energy vs. particle surface area per mixture volume, $f = 0.038$	171
Figure 5.12b. Spark ignition energy vs. particle surface area per mixture volume, $f = 0.042$	172
Figure 5.12c. Spark ignition energy vs. particle surface area per mixture volume, $f = 0.050$	173
Figure 5.12d. Surface ignition energy vs. particle surface area per mixture volume, $f = 0.062$	174
Figure 5.13. Logarithm of nondimensional spark ignition energy vs. particle surface area per mixture volume	177
Figure 5.14. Nondimensional spark ignition energy vs. particle surface area per mixture volume	179
Figure 5.15. Particle surface area per mixture volume vs. fuel-air ratio	180
Figure 10.1. Histogram of 88-104 μm particles	205
Figure 10.2. Width-length ratio of 88-104 μm particles	205
Figure 12.1. Comparison of experimental breakdown voltage data with Equation 3.10b	226

NOMENCLATURE

a	Constant of Equation 1.2 [$\text{cm}^{-1} \text{ torr}^{-1}$]
A	Function given by Equation 3.2 [$\#/\text{cm}$]
A_i	Nondimensional constant of Equation 1.25
A_s	Surface area of ignition kernel [cm^2]
A_w	Flowmeter geometric dimension [$\text{cm} \frac{\text{sec}}{\text{min}}$]
b	Constant of Equation 1.2 [$\text{V}/\text{cm-torr}$]
B	Function given by Equation 3.3 or 3.4 [$(\text{KV})^{1.121}$]
B_i	Nondimensional constant of Equation 1.25
C_p	Heat capacity of unburned gas at constant pressure [J/gk]
C	Capacitance [F], function given by Equation 3.9, or coefficients of Equation 3.10
C_d	Flowmeter discharge coefficient
C_g	Spark gap capacitor [F]
d	Particle container inside diameter [cm]
d_g	Optimum gap width [cm]
d_q	Quenching distance [cm]
d_s	Cylindrical spark channel diameter [cm]
d_{sq}	Spark quenching distance [cm]
D	Average particle diameter [cm or μm]
D_v	Average particle diameter weighted by volume [cm or μm]
e	Coefficient of restitution of a particle collision against a wall (electrode)
E	Stored capacitor energy [J]

E_f	Electric field strength [V/cm]
E_i	Ignition energy [J]
E_r	Space charge electric field strength [V/cm]
E_s	Spark energy [J]
f	Fuel-air ratio
f_M	Mole fraction of fuel in unburned gas
F	Nondimensional empirical constant of Equation 1.22
g	Gravitational acceleration [cm/sec ²]
G	Constant of Equation 1.19 or 1.20 [$\frac{\Omega}{\text{cm}}(\text{A}^2 \text{sec})^{0.6}$ or $\frac{\Omega}{\text{cm}}(\text{A}^2 \text{sec})^{0.5}$]
G_q	Nondimensional constant of Equation 1.22
h	Distance from AF2 shown in Figure 2.7 [cm]
H	Constant of Equation 5.2 [cm ⁻¹]
i	Current [A]
i_o	Current emitted at cathode [A]
i_g	Spark gap conduction current [A]
i_{C_g}	Spark gap displacement current [A]
I	Intensity of external radiation [$\frac{\mu\text{A}}{\text{cm}^2}$]
J	Current flux [A/cm ²]
k	Nondimensional constant of Equation 1.11
K	Thermal conductivity of unburned gas [$\frac{\text{J}}{\text{cm K sec}}$]
K_s	Spring constant [g/sec ²]
L	Parallel electrode separation distance [cm]
L_g	Spark gap length [cm]

L_i	Inductance of external circuit [H]
L_p	Average effective collision distance in Equation 3.8 [cm]
L_s	Particle characteristic distance in Equation 3.7 [cm]
L_x	Breakdown needle position shown in Figure 2.7 [cm]
m	Mass of a particle [g]
m_n	Effective needle mass [g]
M	Number of time lags exceeded a certain time
M_w	Molecular weight of gas
n_c	Critical number of electron accumulation for streamer discharge
N	Particle number density [cm^{-3}]
N_a	Avogadro's number
P	Pressure [torr or atm]
Pe	Peclet number (Equation 1.21)
q	Flow rate [cm^3/min or ml/min]
Q	Capacitor charge [C]
Q_e	Charge of an electron [C]
Q_p	Charge of a particle [C]
Q_s	Spark charge [C]
\dot{Q}_A	Air flow rate [mL/min]
\dot{Q}_F	Fuel (propane) flow rate [mL/min]
r_s	Radius of ion sphere [cm]
R	Resistor [Ω]
\bar{R}	Universal gas constant [$\text{atm cm}^3/(\text{mole K})$]
R_g	Spark gap resistance [Ω]

R_m	Equivalent resistor given by Equation 4.2 [Ω]
S	Average particle separation distance [cm]
S_a	Adiabatic laminar burning velocity [cm/sec]
S_t	Stokes number given by Equation 11.4
t	Time [sec]
t_s	Time interval from foil 2 to spark shown in Figure 2.7 [sec]
t_f	Time interval from foil 2 to spring shown in Figure 2.7 [sec]
T	Period [sec]
T_a	Adiabatic flame temperature [K]
T_u	Unburned gas temperature [K]
U'	Turbulence intensity [cm/sec]
U	Uncertainty
v_p	Particle velocity [cm/sec]
v_n	Needle velocity [cm/sec]
V	Applied voltage or breakdown voltage [V or KV]
V_g	Spark gap voltage [V]
V_s	Static breakdown voltage [V]
W	Total particle mass in closed system [g]
W_f	Flowmeter float weight [g cm/sec ²]
x	Arithmetic average of nondimensional breakdown needle position
x_c	Critical nondimensional breakdown needle position
x_i	Nondimensional breakdown needle position shown in Figure 2.7

x_p	Particle position above electrode [cm]
y	Reference needle position shown in Figure 2.7 [cm]
Y	Any parameter in Equation 12.1
z	Distance from cathode [cm]
Z	Any quantity in Equation 12.1

GREEK

α	First Townsend coefficient [cm^{-1}]
β	Second Townsend coefficient [cm^{-1}]
δ	Effective width of laminar flame front [cm]
ϵ	Permittivity of gas [$\frac{\text{F}}{\text{cm}}$ or $\frac{\text{C}}{\text{cm V}}$]
ϵ_p	Permittivity of particle [$\frac{\text{F}}{\text{cm}}$ or $\frac{\text{C}}{\text{cm V}}$]
γ	Overall second Townsend coefficient [cm^{-1}]
η	Coefficient of electron attachment [cm^{-1}]
λ	Mean free path of particle clouds [cm]
μ	Gas viscosity [g/cm sec]
ρ	Unburned gas density [g/cm^3]
ρ_f	Flowmeter float density [g/cm^3]
ρ_p	Particle density [g/cm^3]
σ	Standard deviation or particle electrical conductivity [$\Omega^{-1} \text{cm}^{-1}$]
τ	Average statistical time lag [sec]
ω	Natural angular velocity of spring [rad/sec]
ω_r	Reaction rate in flame zone [$\frac{\text{g}}{\text{cm}^3 \text{sec}}$]

SUBSCRIPTS

- o Reference, air, total, initial or particle free condition
- 1 Condition 1
- 2 Condition 2
- 3 Condition 3
- 4 Condition 4
- 5 Condition 5
- 6 Condition 6
- c Critical condition
- st Stoichiometric condition
- t Final condition
- * Transitional condition

I. INTRODUCTION

A. Present Study

The present study is concerned with quantifying the macroscopic electrical breakdown and ignition characteristics of a particulate cloud-gas phase mixture at atmospheric pressure which is confined between parallel plate electrodes. A unique spark breakdown facility has been perfected which is capable of generating clouds of uniform density and which uses a high speed electrode to initiate breakdown. Three fundamental subjects have been identified for detailed study. These are: 1) the electrical breakdown criteria of inert particle-inert gas mixtures (using air), 2) the energy-time relationship in the spark gap during the breakdown, and 3) the ignition criteria of inert particle-combustible gas mixtures. These studies were undertaken in order of increasing complexity. They relate problems in particle technology that are both of current scientific interest and relevant to explosion hazard in industry.

B. Relevance of Study

The influence of particulate matter leading to electrical breakdown or electrical discharge followed by explosion is well-known. For example, the presence of particles in an electrically insulated system, whether they

move freely or remain on the electrodes, can deteriorate electrical performance by lowering the breakdown strength. This problem has been frequently encountered in high-voltage equipment such as gas-insulated circuit breakers, transmission lines, underground cables, current transformers, voltage transformers, high-voltage generators, etc. Other examples are lightning-like discharges from dust clouds, lightning from charged ice particles in clouds, flashovers in a moving fluid containing charged particles, and spark discharges in electrostatic precipitators or painting systems.

Recently, spark breakdown phenomena in particulate clouds was discussed by Colver [1]. The characteristics of the electrical breakdown associated with particles appear to depend on their shape, size, material and number density. Also, the well-known parameters associated with the gas breakdown itself, which include electrode geometry, electrode material and surface condition, electric field distribution, waveform and polarity of the applied voltage, temperature, pressure, and gas mixture, may influence the aforementioned characteristics.

If the electrical discharge associated with or initiated by the particles in a combustible gas is sufficiently intense, ignition and explosion may result. Alternatively, when the dispersed particles are chemically inert, they may exhibit

an inhibiting effect on the ignition and flame propagation processes. From a practical point of view, these inert particles can be used for extinguishing fire (Tryon and McKinnon [2]) or preventing ignition.

Many particles handled in industry are themselves combustible so that they can burn in an oxidizing atmosphere. Some examples of combustible dusts include coal, grain, flour, sugar, starch, plastics, metals, pharmaceuticals, wood dust, textile fluff, and dust from many processes where solid surface are polished, cleaned, stripped or cut. Palmer [3], Bartknecht [4] and Gagan [5] reviewed various types of incidents of dust explosions.

The general characteristics of multiphase ignition and combustion are similar to those of the pure gas phase and may be described by the ignition limit (ignition energy), ignition delay time, rate of heat release and pressure rise, etc. The important factors which affect these characteristics are the temperature, pressure, humidity, turbulence, type and mode of ignition source, and the type and composition of uniform particle-gas mixture.

This study is related to the following questions: 1) how does the particulate cloud influence the electrical spark itself? 2) how does the source ignite the multiphase mixture? and 3) what mechanisms are involved in multiphase flame propagation?

C. Literature Review

1. Electrical breakdown

a. Breakdown criterion in gases Prior to 1900, it was well-known that the current in a plane parallel gap in an ionized gas varied as the electric field strength increased with gas pressure. Real progress toward an understanding of spark breakdown phenomena began with the theory promulgated by Townsend in the early 1900s [6, 7, 8]. More recently, the nature of electrical breakdown and its theoretical basis were qualified in greater detail by Loeb and Meek [9], Loeb [10, 11], Cobine [12], Nasser [13], Raether [14] and Haydon [15].

When a voltage is first applied, the current to the anode increases slowly as the electrons move through the gas with an average velocity determined by their mobility for a given field strength. Random current pulses of less than 10^{-16} A are the first measurable currents. This current also can result from the irradiation of the cathode in the plane gap in air at atmospheric pressure with a suitable source such as photoradiation. Under a constant radiation level, the current increases with voltage until it reaches the saturation level ($\sim 10^{-13}$ A), where all electrons emitted from the cathode and/or produced in the gas are collected at the anode. This current magnitude depends on

the magnitude of radiation incident on the cathode. If it is assumed that no electrons are produced by the effect of the field, there should be no further increase in the current with voltage. This is true for a considerable range of voltage increase, but beyond a certain voltage, the current starts increasing exponentially. This current is termed nonself-sustaining, since the current becomes zero when the radiation source is cut off. A further increase of the voltage leads to an over-exponential increase in the current. This abrupt transition is known as "breakdown." Such a process is self-sustaining because the current becomes independent of the external ionizing source. The nature of the sustained discharge depends on the constants of the external circuit, the gas pressure, the gap length and shape, and the type of the applied voltage (AC, DC, etc.). Different discharge modes like a spark, arc or glow are possible. For example, at atmospheric pressure if the discharge produces a short-lived plasma channel, it is referred to as a spark, whereas, at low pressure, a glow discharge may be observed.

Townsend conducted extensive investigations on the voltage-current relationship which could lead to breakdown. He observed experimentally that as the plate separation distance L increased for a given value of the field strength E_f and pressure P , the current i appeared to increase exponentially with L . This led him to the equation

$$i = i_0 e^{\alpha L} \quad (1.1)$$

where α is called as the first Townsend coefficient and i_0 is the current emitted at the cathode. This relationship can be deduced on a theoretical basis, which means that one electron produces $e^{\alpha L}$ new electrons in traversing the distance L . This is often spoken of as an electron avalanche. The first Townsend coefficient α was found later semiempirically and theoretically to be [13]

$$\alpha = a p \exp\left[-\frac{bP}{E_f}\right] \quad (1.2)$$

where a and b are constants and p is the gas pressure.

Equation 1.1 was later revised [13] to include secondary electron emission effects (γ) at the cathode and electron attachment (η) in the gas giving

$$i = i_0 \frac{\frac{\alpha}{\alpha-\eta} \exp[(\alpha-\eta)L] - \frac{\eta}{\alpha-\eta}}{1 - \frac{\alpha\gamma}{\alpha-\eta} \{\exp[(\alpha-\eta)L] - 1\}} \quad (1.3)$$

Under the general term "Townsend mechanism," the electrical breakdown can be explained that every avalanche between the electrodes produces one or more successor avalanches until the channel conductivity has reached a value high enough to make the self-sustained current theoretically infinite, although in practice it is limited by the external

circuit. Setting the denominator in Equation 1.3 equal to zero gives the Townsend breakdown criterion as

$$\frac{\alpha\gamma}{\alpha-\eta} \exp[(\alpha-\eta)L] - 1 = 1 \quad (1.4)$$

For $\eta=0$, Equation 1.2 and 1.4 combine to give the gap breakdown voltage as a function of PL, the gas pressure-gap length product, according to

$$V = \frac{bPL}{\ln\left[\frac{aPL}{\ln\left(1+\frac{1}{\gamma}\right)}\right]} \approx \frac{bPL}{\ln\left[\frac{aPL}{\ln\left(\frac{1}{\gamma}\right)}\right]} \quad (1.5)$$

It is assumed that γ is independent of E_f/P and that the electric field is uniform ($E_f = V/L$). This relationship is well-known as Paschen's law, $V = f(PL)$, which was discovered by him experimentally in 1889. There are many conditions under which this law does not hold, for example, at extremely high and low PL, and in many conditions where γ depends on E_f/P and when the field is not uniform.

Nasser [13] pointed out that the Townsend mechanism was incompatible with or unable to explain several experimental observations such as: 1) the measured formative time lag was of the order of 10^{-8} sec which was much shorter than that predicted by the Townsend mechanism with any secondary action, 2) the effect of the space charge left over from earlier electron avalanche generations was not

considered in the mechanism, 3) a difficulty exists in the interpretation of the mechanism in the case of a nonuniform electric field, and 4) at high value of PL the formation of a different process becomes responsible for the breakdown.

Raether's cloud chamber studies in the 1930s [14] revealed that besides the occurrence of avalanches, another distinct form of ionization also develops, known as a "streamer" because of its filamentary nature. If the breakdown occurs by a transition from a streamer to a spark, the mechanism involved is sometimes referred to as the streamer-breakdown mechanism. When avalanches reach an amplification of more than some 10^8 electrons near the anode, the field between the avalanche and anode becomes enhanced and accelerates the breakdown process. As electrons enter the anode, leaving an ion sphere behind, a new ionizing process shoots out of this sphere and avalanches in the form of a narrow filament or streamer toward the cathode. The speed of propagation of this streamer was measured to be $1 \sim 2 \times 10^6$ m/sec, one order of magnitude larger than the drift velocity of an electron which is of the order 10^5 m/sec. Based on the assumption that the transition to streamer formation occurs when the space charge field E_r becomes of the same order as the applied uniform electric field E_f , the breakdown criterion is [15]

$$E_r = \frac{Q_e n_c}{4\pi\epsilon_0 r_s^2} \approx E_f \quad (1.6)$$

where r_s is a radius of the ion sphere, Q_e is the electronic charge, ϵ_0 is the permittivity of air, and n_c is the critical charge accumulation number being

$$n_c (=e^{\alpha L}) \approx 10^8$$

The Raether's breakdown criterion is then for air

$$\frac{\alpha}{P} PL = f\left(\frac{V}{PL}\right) \cdot PL = 17.7 + \ln L \quad (1.7)$$

or simply

$$\exp[\alpha L] \approx 10^8 \quad \text{or} \quad \alpha L = 18.5 \quad (1.8)$$

For electronegative gases, the streamer criterion becomes

$$\exp[(\alpha - \eta)L] \approx 10^8 \quad (1.9)$$

Loeb [16], Nasser [13] and Gallo [17] reviewed electrical breakdown in a nonuniform field. The development of a discharge in a nonuniform gap, where the field strength and ionization coefficients are functions of the position in space, differs from that of the uniform field gap in that: 1) in different places of the gap different mechanisms may be at work and 2) the space charge accumulation may seriously attenuate the progress of a discharge resulting in a partial breakdown at the lower voltage than the spark breakdown voltage. The criterion for the Townsend mechanism

of spark breakdown was extended to a nonuniform field for an electronegative gas by Pedersen [18] and Karlsson and Pedersen [19] showing

$$\gamma \int_0^L \exp\left\{\int_0^L (\alpha - \eta) dz\right\} \alpha dz = 1 \quad (1.10)$$

Assuming also that streamers are formed if the rate of photon production attains a certain value, Pedersen obtained the streamer breakdown condition given by

$$\int_0^L (\alpha - \eta) dz = k \quad (1.11)$$

where k is constant depending on the type of gases and nonuniformity. For example, if a uniform field is assumed, k should be about 18.5.

The various factors affecting electrical breakdown in compressed gases were reviewed by Cookson [20, 21] and in vacuum by Farrall [22].

b. Breakdown time lags A finite time will elapse between the application of a breakdown potential and the establishment of a self-sustaining discharge. This time is commonly divided into two parts, a statistical time lag and a formative time lag. The statistical time lag is the time delay until an initiating electron appears in the gap after the application of an electric field. The formative time lag is the actual time between the release of

the initiating electron and the build-up to a spark discharge. Loeb [10] reviewed the first studies of time lags by Zuber [23] and Lane [24]. Their investigations dealt largely with the so-called statistical time lag down to about 10^{-3} seconds. Zuber showed that when the number of lags M out of M_0 which exceeded t seconds were plotted against t , the relation became

$$M = M_0 e^{-t/\tau} \quad (1.12)$$

where τ was the average time lag equivalent to the time lag at $M/M_0 = e^{-1}$. Lane pointed out that $1/\tau$ represents a simultaneous chance that an electron is liberated by the ionizing agent and the electron will start the discharge.

Tilles [25] used a resistance-coupled amplifier and a ballistic galvanometer to measure the time lags in the gap of the copper spheres of 0.952 cm radius and 0.0683 cm separation distance where voltage was suddenly applied from 96 percent of a static sparking voltage V_s to a constant value exceeding V_s in the presence of ultraviolet light from a quartz mercury arc. His results showed the same relationship as described by Equation 1.12 when the intensity of light I resulted in a current of less than 0.4 micro-amperes per square centimeter of clean nickel plate placed in a vacuum. With small overvoltages $(V-V_s)/V_s$ from 1 to 6

percent and a light intensity of less than 0.5, he showed that the average time lag τ could be expressed as

$$\tau = 0.0037 \exp\left[-39.0\left(\frac{V-V_s}{V_s}\right)\right] \cdot I^{-0.76} \quad (1.13)$$

which was in the statistical time lag domain. When the starting voltage was zero, the constant in Equation 1.13 was found to be 0.0078 instead of 0.0037.

White [26] used a flash of ultraviolet radiation coming from a spark in an auxiliary gap to set off a spark under the application of a constant overvoltage and also an electro-optical shutter to observe the time lag between the illumination of a two-sphere gap and the first appearance of light emission as a function of gap length, intensity of illumination, and overvoltage. In air, the time lag was about 10^{-7} seconds for overvoltages of a few percent and increased very rapidly with decreasing overvoltage. Increasing the overvoltage to above 30 or 40 percent reduced the time lag to a more or less constant value of 2 or 3×10^{-8} seconds. The position of the mid-gap streamer was observed to depend on both the overvoltage and the intensity of illumination.

Wilson [27] applied an overvoltage at a definite time to a two-sphere gap already illuminated by a constant source of ultraviolet light, and then measured the time lags using the method of White. His results showed that the distribution

of the breakdown fraction M/M_0 which exceeded a time lag t seconds plotted against the time lag t seemed to be an integral curve similar to that of the Gaussian distribution curve and was a function of overvoltage and illumination intensity. It was also found that the time lag approached 10^{-9} seconds apparently without a lower limit when a sufficiently high overvoltage was used. In order to explain the short time lag, he suggested that the formative time lag was the time for an electron to traverse a short distance in the spark gap so as to produce, by ionizing collisions, sufficient secondary photoelectric mechanisms of electron production in the gas, since neither positive ions nor electrons could possibly have crossed the gap in the intervals observed.

Nasser [13] suggested that the formative time should depend on the mechanism of breakdown that develops under the specific conditions of the gas. If the Townsend mechanism is active, a series of avalanche generation finally leads to breakdown. When streamer breakdown develops, the formative time lag is given primarily by the time required for space-charge formation and the subsequent fast streamer development in a very short time depending on the amount of overvoltage.

c. Effect of particles It is well-known that particles in a gap usually reduce the breakdown voltage, whether they are fixed or free. However, if they are moving freely, the motion is an important factor influencing the initiation of breakdown. The dynamic mechanisms of charging and recharging of a spherical particle were well-established experimentally and theoretically by Colver [28].

Berger [29] reported that based on the minimum breakdown voltage corresponding to one breakdown within 10 minutes the DC breakdown voltage of a steel sphere of 0.2 ~ 1.5 mm radius moving in a uniform field gap of 2 cm width was lower than that of a fixed sphere, but that there was no effect due to polarity. A similar result was observed in a non-uniform field where, in addition, the breakdown voltage depended on the DC polarity, being lowest for a negative innermost electrode in a coaxial system.

A comprehensive study on particle initiated breakdown was reported by Wootton et al. [30]. They noted that breakdown associated with a particle occurred when the particle was near but not touching the electrode. A 60 Hz field breakdown was initiated when the inner conductor was in its positive half cycle. The critical distance between the particle and the electrode decreased from about 2 mm to very small

values as the SF₆ gas pressure was varied from 0 to 100 psig. They reported that the gap between the particle and the electrode (the short gap) could break down without causing overall breakdown in the long gap, and that this short gap breakdown could occur in glow, large-pulse or arc modes depending on the length of the short gap, gas pressure and voltage. The end of the particle facing the long gap emitted appreciable corona currents while the short gap conducted in its various modes so as to supply these currents. AC breakdown was statistically related to the simultaneous occurrence of adequate voltage, correct polarity, particle field alignment, critical particle-to-electrode spacing (for the gas pressure), and an initiatory electron. With multiple particles, the decrease in AC breakdown voltage was thought due to this statistical effect rather than any path resistance effect.

Using coaxial electrodes, Cookson et al. [31] and Cooke et al. [32] observed the so-called fireflies, from a hovering wire particles near any negative electrode (inner or outer), accompanied by intense corona and visible light. The negative inner electrode DC breakdown voltage was substantially lower than the particle-free breakdown level. With a positive inner electrode, the breakdown voltage could vary by a factor of three because of inhibited particle motion.

With spherical particles, fireflies were not observed while the breakdown voltage was lowered. Reversing the polarity had little effect on the breakdown voltage for moving spherical particles.

Anis and Srivastava [33, 34, 35, 36] established breakdown voltage profiles which described the instantaneous breakdown voltage as a function of the particle position. They assumed that at a certain minimum voltage, breakdown may be initiated by a free particle (wire or sphere) when the charged particle is approaching very near to but not in contact with an opposite electrode, thus forming a conducting link between the two. This is immediately followed by the breakdown between the tip of the conducting link and the other electrode. The effect of particle size appeared to be significant on both the critical breakdown voltage and the critical distance. For instance, as the diameter of a spherical particle increased, the critical distance increased, but the breakdown voltage dropped and then tended to level off.

A theoretical attempt was made by Mara and Akazaki [37] to find the field strength near a small conducting sphere floating in a parallel plane gap along with the force acting on the sphere at an arbitrary position in the gap. The particle radius at the critical condition where the

effect of the particle on the breakdown voltage was eliminated was calculated to be the order of 0.1 mm in air. The breakdown voltage was also predicted as a function of the size of a particle and the pressure based on Equation 1.11 with $k=15$ using the maximum field strength near the sphere.

Schulz [38] observed that the AC breakdown voltage of a 50 cm separation gap, consisting of two cylindrical rods, was linearly increased from 292 kv at zero dust particle concentration to 304 kv at 120×10^8 dust particles in one cubic meter. The AC frequency, dust material, and particle diameter were not given. However, with larger particles he added that the mean value of the breakdown voltage could be reduced by about 20% with a homogeneous or a weakly inhomogeneous electric field.

Laghari and Qureshi [39] reviewed the electrical performance of gases under particle contamination. They pointed out that conducting particles can reduce the dielectric strength of gases, while insulating particles are found to have little effect.

Mulcahy [40] compared the DC breakdown voltages of conducting and insulating particles or fibers. When the insulating fibers were blown into a 5 cm gap of 25 cm diameter spherical electrodes, the breakdown voltage was reduced by no more than 3% and by less than 2% when the gap

width was increased to 10 cm. But when conducting particles were blown into a 8 cm gap, the breakdown voltage was reduced by as much as 35%. The reduction in the breakdown voltage by placing individual fibers of known length (both cotton and wood) directly on the ground electrode was, in general, proportional to both the length and the number of fibers. Dry fibers had less effect on the breakdown voltage than slightly damp ones. The fibers used were from 1 to 10 mm in length.

The subject of spark breakdown in particulate clouds has recently been reviewed by Colver [1]. He calculates that the effect of particle precharge has a negligible effect as additional stored charge or energy in the spark.

2. Temporal development of a spark breakdown

a. Charge transfer The temporal growth of current from the Townsend and Streamer stages of spark breakdown were reviewed and predicted theoretically by Raether [14]. Nasser [13] also discussed the difference of the early phase current development between the two mechanisms where current magnitude ranges from μA to mA .

Recently, the complete evolution of breakdown discharge was studied by Marode [41], electrically and optically, using positive point-to-plane electrodes with about a 15 mm gap width in air at atmospheric pressure. The sequence, a

corona discharge to transient arc, led to an entire collapse of the gap potential.

Similar discharge currents were measured by Barreto [42] and Barreto et al. [43, 44], using a gap of $2 \sim 8$ mm width which was illuminated by an external light source. In the first current pulse, they observed a small rise and decay of current which, when integrated in time, yielded around 10^8 elementary charges corresponding to the size of a critical avalanche. After the first minimum, the current increased slowly for about 3 nsec. This time interval was identified with the time it took the streamer to cross a section of the gap at a velocity of 0.7×10^8 cm/sec. The subsequent rapid increase in current and the following damped oscillations were identified with the propagation of a nonlinear fluid discontinuity traveling along the streamer channel. The current trace associated with the whole streamer then decayed to a comparatively negligible current in a time of the order of 100 nsec. This negligible current level was maintained for relatively long times of the order of microseconds. Finally, a current pulse, called a transient arc by Marode, led into the spark itself with final currents of the order of 10 A. In uniform short spark gaps they reasoned that the distance required to produce a critical avalanche becomes longer than the gap so

that no streamer discharge is possible, consistent with what they observed. They were also able to distinguish two basically different forms of the main spark in the form of diffusive discharges and bright discharges, whether the field was uniform or not. The oscilloscope trace of a diffuse discharge was always a smooth sinelike-shaped curve with only a half period which varied between $10 \sim 50$ nsec depending on the capacity and history of the electrode used. The discharge always exhibited a bright cathode spot at the apex of a luminous conical shape. The current of the bright discharge was always made of two consecutive large humps, or, of complete nonsymmetric oscillations with two or three periods. The bright discharges exhibited both bright cathode and anode spots and were louder, brighter, and completed within a time shorter than that for the diffuse discharge.

Parnell [45] and Cobine [12] discussed the influence of the external circuit on the subsequent development of the spark or arc current after initial electrical breakdown. When the initial ionization bridges the gap electrically, the discharge entirely interacts with the external circuit so that the circuit largely controls the magnitude, subsequent development and life of the spark current. Stray capacitance and inductance in the leads and external resistance

constitute an RLC circuit which can lead to oscillations.

Rose and Pride [46] investigated the effect of values of series RLC circuit components on the characteristics of a capacitance spark discharge between two aluminum hemispheres of 10 mm diameter. The spark discharge without series resistance was of a damped oscillatory nature, although the inductance distributed in the circuit was very small in the order of 10^{-7} H which was the same order as Barreto's circuit. The damped oscillatory discharge could be changed by the addition of a large resistor to an aperiodic discharge. This kind of oscillatory current of a capacitor spark discharge was also measured by Lee et al. [47] using a current transformer instead of a series resistor.

Kono et al. [48] observed damped oscillations in the frequency range of 10 ~ 100 KHz, using the conventional ignition coil to generate a high voltage on its secondary coil when the primary coil was suddenly switched to the main pre-charged capacitor. They observed the transition from glow to arc and vice versa when oscillatory voltage and current traces died out. The gap voltage changed discontinuously to a lower voltage whenever the current increased beyond about 0.1 A.

Maly and Vogel [49] showed that if the power source or

the pre-charged capacitor could supply current sufficient to maintain a spark discharge after breakdown (over $1 \sim 10$ nsec), the discharge could ultimately lead to an arc or glow discharge in times in the range of 10^{-8} to 10^{-6} sec and 10^{-5} to 10^{-2} sec, respectively. The voltage and current of the discharges were lowered from the order of 10 kv and 100 A to 100 V and less than 1 A.

A rectangular pulse of an arc discharge in the range of $10 \sim 100$ V and $1 \sim 20$ A was produced by Ballal and Lefebvre [50] with a specially designed external circuit. The duration of discharge could be controlled from 1 to 105 μ sec. Other circuits were also introduced by Eckhoff [51, 52] and Kono et al. [53] which generated long time pulses up to the range of msec.

b. Energy transfer The amount of electrical energy released by a spark is a very important quantity, since it determines the behavior and thermodynamic properties of gases of the spark channel. Generally, the total energy released from the spark gap in the time interval from 0 to t seconds is defined by

$$E_s = \int_0^t i V_g dt \quad (1.14)$$

where i is the spark current and V_g is the spark gap voltage. If the energy is assumed to be delivered only from the

pre-charged capacitor directly to the spark gap without voltage drop through series inductance or resistance, since

$$i = -C \frac{dv_g}{dt} \quad (1.15)$$

for constant C, the spark energy becomes

$$E_s = \frac{1}{2}C[V_{g_o}^2 - V_{g_t}^2] \quad (1.16)$$

and if no charge remains on the capacitor,

$$E_s = \frac{1}{2}CV_{g_o}^2 \quad (1.17)$$

From Ohm's law, $V_g = iR_g$, Equation 1.14 also becomes

$$E_s = \int_0^t i^2 R_g dt \quad (1.18)$$

Lewis and von Elbe [54] and Calcote et al. [55] used the stored energy of Equation 1.17 at the sparking voltage V_{g_o} for the total released spark energy in their ignition studies. Calcote et al. found that only less than 1% of the stored energy was left on their condenser after discharge.

Moorhouse et al. [56] used a variable parallel plate capacitor device. They observed that the spark current was equivalent to a damped oscillation wave of 9 MHz with about 1.2 μ sec duration and that the final voltage of the

condenser was smaller than 5% of the original value.

Kono et al. [57] also found that the residual energy in the capacitor was negligibly small as compared with the stored energy. Thus, they assumed that the energy released in the spark gap was equal to the stored energy minus the lost energy which corresponded to the Joule heating in series resistance. The lost energy calculated from the current trace was increased as the inductance and resistance increased.

However, Kono et al. [48] graphically integrated the product of voltage and current from traces of the spark discharge generated with the ignition coils to obtain the spark energy based on Equation 1.17. The spark energy was much less than the stored energy of the main capacitance.

Ballal and Lefebvre [50] and Eckhoff [51, 52] could easily determine the spark energy from their voltage and current traces, since they obtained the nearly rectangular or smooth pulses in the range of microseconds to milliseconds instead of the damped oscillation traces. Eckhoff related the net spark energy to the initial capacitor energy in which the capacitor energy of a primary coil circuit was not included. As the initial energy was decreasing, the energy supplied by the triggering circuit (primary coil) became significant so that in the range of lower energies,

smaller than 10 mJ, the released spark energy was larger than the stored energy of the main capacitance. When the actual spark energy became greater than 20 mJ, the ratio of the measured energy to the stored energy decreased from unity.

When Rose and Pride [46] plotted on semi-logarithmic scales the amplitudes of successive positive and negative peaks against the times taken from the spark discharge trace of damped oscillations, they formed a linear relationship over a considerable time range up to 80×10^{-8} sec. They assumed that the gap resistance remained sensibly constant in time and calculated the constant resistance based on the response characteristic of an RLC series circuit. For the aperiodic signals recorded with a large circuit resistance, they assumed that following breakdown the gap voltage fell to a very small value due to the establishment of an arc-like discharge so that the energy released in the spark gap became very small because the gap resistance was then only a small fraction of the total resistance. The gap resistance was assumed to be primarily determined by the initial current rise following the breakdown, and tended to be constant for a short period until the arc conditions were established, and then varied according to the arc current. With the gap resistance they calculated the spark energy based on Equation

1.18 and showed that the percentage of energy released in a spark gap decreased with the increase of capacitance and resistance. For example, only 10% of the stored energy was released in the spark when the circuit had 1000 pF and 10Ω .

Lee et al. [47], Knystautas and Lee [58], and Lee and Matsui [59] also assumed a constant gap resistance, smaller than 0.1Ω , and calculated the spark energy of a damped oscillatory current.

Rompe and Weizel [60] derived the temporal variation of gap resistance from the energy equations of a spark channel under the assumptions that: 1) the movement of fluid and the heat and radiation from the channel are negligible, 2) the conductivity of the channel is proportional to its internal energy, and 3) the current is homogeneously distributed over the channel cross-section. The spark resistance derived was

$$R_g = \frac{GL_g}{\left[\int_0^t i^2 dt\right]^{0.5}} \quad (1.19)$$

where L_g is the spark channel length and G is constant.

The equation was modified by Vlastós [61] to

$$R_g = \frac{GL_g}{\left[\int_0^t i^2 dt\right]^{0.6}} \quad (1.20)$$

Hill [62] also calculated the temporal variation of the spark current of the 40 nsec pulse recorded by Barreto et al. [44] in a uniform electric field. The gap resistance was dropped from $10^4 \Omega$ at 1 nsec to 500Ω at 40 nsec. More than 55% of the stored energy was dissipated in 10 nsec after the initiation of a spark.

The damped oscillatory current trace in the frequency range of $100 \sim 10$ MHz was analyzed by Andreev and Vanyukov [63] to estimate the unsteady spark resistance based on the law of energy conservation for a discharge circuit. The gap resistance was varied from a nearly infinitely large value at the beginning of the discharge to a value smaller than 1 ohm in one half-cycle of the first oscillation. The released energy in the first half-cycle of the oscillation was more than 60% of the available energy but showed dependence on the RLC values. They also compared their results with Equation 1.19 given by Rompe and Weizel. It was shown that the resistance of the spark channel could be satisfactorily described by Equation 1.19 only for the discharge of a small inductance.

3. Flammability and ignition limit

a. Flammability limit and flame quenching It is well-known that every combustible gas mixture has its own flammability limit regarded as those limiting fuel-oxidant

mixtures within which a flame will propagate through the mixture. Jones [64] said that the limits are affected by the direction of flame propagation, the design, diameter, and length of the test apparatus, the temperature and pressure of the mixture, the percentage and pressure of water vapor, and indirectly by the source of ignition. For instance, the flammability ranges widen as the tube diameter is made larger, but the change above 5 cm diameter is very small rarely exceeding a few tenths of one percent. Mullins and Penner [65] also discussed various phenomena related to the flammability limit.

The concept of quenching distance is also well-established. Potter [66] noted that the curves of quenching distance versus fuel concentration are paraboloids with a minimum near stoichiometric conditions, while the burning velocity varies with fuel concentration in an inverse way displaying a maximum near stoichiometric conditions. He added that the product of the burning velocity and quenching distance for similar fuel-oxidant system is surprisingly near to being constant. However, the inverse proportionality of the burning velocity and the quenching distance has been estimated and predicted in terms of the heat transfer Peclet number which is the product of an adiabatic laminar flame velocity S_a and a quenching distance d_q divided by the thermal

diffusivity $K/\rho C_p$ of an unburned mixture, i.e.,

$$Pe = \frac{\rho C_p d_q S_a}{K} \quad (1.21)$$

The experimental values of the quenching Peclet number were reported by Putman and Jensen [67] to be about 46 and by Cullen [68] to be from 35 to 50 based on tube diameter.

The first solution for the energy balance equation in a flame considering heat losses was made by Daniell [69] neglecting diffusion heat loss. He demonstrated that a maximum heat loss existed beyond which there were no solutions to the equation, and also showed that the cooling effect of tube walls increased as the tube diameter decreased so that there would exist a minimum tube diameter for flame propagation, i.e., a quenching diameter.

Lewis and von Elbe [54] considered a two-dimensional flame propagating through a tube, and solved the differential equation of energy conservation not including diffusion so as to find the temperature distribution in the combustion wave taking into account heat loss to the tube wall and also the effect of the loss on the burning velocity. The quenching Peclet number based on the critical tube diameter was found to be about 60.

A somewhat more satisfactory analytical procedure for demonstrating the existence of flammability limits and quenching distance was worked out by Spalding [70] on the

basis of straightforward solutions to the relevant one-dimensional conservation equations including enthalpy transport by diffusion into which a suitable heat loss term was incorporated. He explained the flammability limits as mixtures having imaginary burning velocities when the reaction rate is too low compared with the heat loss rate. The predicted Peclet number was about 60.5.

Mayer [71] analyzed an integrated energy equation for the flame front and combined empirical results to give Peclet numbers of 30 to 50 for convective heat loss to a cylinder wall. His theory expressed the variation of the quenching Peclet number with activation energy and adiabatic flame temperature.

Both conduction and radiation heat losses were included in the theory formulated by Berlad and Yang [72] showing the existence of flame extinction limits. Gerstein and Stine [73] integrated numerically one dimensional laminar flame equations with single-step Arrhenius kinetics including conduction and radiation heat loss to the surroundings, and examined the composition flammability limit. Their results showed that in the region where radiation heat loss exceeded conduction heat loss, the composition lean limit decreased very slowly as tube diameter increased, indicating that the apparatus size was no longer important.

Friedman [74] postulated that a flame was quenched when the rate of heat loss to the wall equaled the rate of heat generation by the flame. He was able to show the quenching Peclet number as a function of the adiabatic flame temperature, ignition temperature and cold gas temperature.

Simon et al. [75] proposed the diffusional theory of flame quenching. They assumed that the number of reaction events initiated by the active particles while diffusing to the wall must be sufficiently large so as to maintain the flame. The quenching distances for various surface geometries were predicted by Berlad and Potter [76] assuming that the average number of effective collisions of active particles with gas molecules at which a flame is quenched is independent of tube geometry.

Potter and Berlad [77] argued that the use of the diffusional theory is limited to stoichiometric or lean mixtures because of the difficulties in choosing the reaction kinetics. For hydrocarbon-rich mixtures, they obtained the quenching distance given by

$$d_q^2 = \frac{FG_q Kf_M N_a}{C_p \omega_r} \quad (1.22)$$

The constant G_q depends on the geometry of the quenching surface (12 for slots and 32 for cylinders) and the empirical constant F is equal to about 0.78, whereas f_u is the mole

fraction of an unburned fuel, N_a is the Avagadro's number, and ω_r is the reaction rate.

Potter [66] pointed out that theories based exclusively on the transport of either heat or mass are in general incomplete, since both transport processes must occur in the quenching of most flames. The heat loss by thermal conduction is the major factor in causing flame quenching except for certain exceptional conditions where diffusion may become effective in transferring enthalpy to the wall.

Recently, Aly and Hermance [78] solved numerically the two-dimensional partial differential equations modeling a laminar flame system, freely propagating between cool parallel plates, with single-step Arrhenius kinetics and without radiation loss. Their conclusions were that the quenching Peclet number increased with decreasing fuel concentration in lean mixtures, and remained constant as the Lewis number became smaller than one. The quenching distance decreased with the Lewis number.

b. Spark ignition The characteristics of spark ignition of combustible gas mixtures are expected to be determined by the spark energy, fuel-oxidant-inert gas composition, ambient temperature, pressure, humidity, turbulence, mode of spark (duration time and power density), and electrode geometry and separation distance. Mullins and

Penner [65] reviewed these parameters in detail.

Lewis and von Elbe [54] and Calcote et al. [55] said that the spark ignition energy attains a minimum at a certain critical gap distance, i.e., that a spark quenching distance exists. The minimum ignition energy and the spark quenching distance were observed to have their smallest values for slightly richer than stoichiometric mixtures. Lewis and von Elbe concluded from their experimental results that the minimum ignition energies were approximately proportional to the square of the spark quenching distance, independent of the fuel-oxygen-nitrogen ratio and the pressure. The minimum ignition energy was then predicted to be

$$E_i = \pi d_{sq}^2 \frac{K}{S_a} (T_a - T_u) \quad (1.23)$$

based on the spherical propagation of ignition source and the concept of the minimum excess thermal enthalpy per unit area $K(T_a - T_u)/S_a$ for ignition. The calculated results of the minimum ignition energy from Equation 1.23 were in good agreement with the experimental results.

An empirically based formula for the excess ignition enthalpy was derived by Rosen [79]. Mullins and Penner [65] derived a similar form to that of Lewis and von Elbe neglecting diffusion heat transfer according to

$$E_i = A_s K \left(\frac{T_a - T_u}{\delta} \right) \frac{\delta}{S_a} \quad (1.24)$$

where A_s is the effective area of the ignition kernel and δ is the effective width of the laminar flame front.

Ballal and Lefebvre [80] carried out spark ignition studies to examine the influence of various flow parameters, notably pressure, velocity and turbulence on the spark quenching distance. The quenching distance increased with an increase in turbulence intensity, a decrease in pressure, and with increasing laminar flame speed. The quenching distance was sensibly independent of flow velocity and turbulence scale. The quenching Peclet number was found to vary also with fuel molecular weight. For methane and propane fuel/oxygen/inert gas (Ar, He, CO₂ or N₂) mixtures, the experimentally determined values of the quenching Peclet number were respectively 26, 38, 61 or 48 for laminar flowing gases.

At low turbulence, the spark quenching distance was given by Ballal and Lefebvre [81] as

$$d_{sq} = \frac{A_i K}{\delta C_p [S_a - B_i U']} \quad (1.25)$$

where U' is the turbulence intensity in an rms value of fluctuating velocity and A_i and B_i are empirical constants. From a comparison of the theoretically calculated quenching distance and experimentally measured minimum spark ignition energy, they defined the minimum ignition energy as the

energy required to heat a spherical volume of gas of diameter equal to the spark quenching distance for the mixture up to the adiabatic flame temperature. That is,

$$E_i = \rho C_p (T_a - T_u) \frac{1}{6} \pi d_{sq}^3 \quad (1.26)$$

They pointed out that the quenching distance was not the optimum gap width d_g which corresponded to the minimum ignition energy. The criterion for ignition is that a cylindrical kernel of diameter d_s must have a volume equal to that of a sphere of diameter d_{sq} , i.e.,

$$\frac{1}{4} \pi d_s^2 d_g = \frac{1}{6} d_{sq}^3$$

Assuming $d_s \sim d_{sq}$, they observed empirically that

$$d_g \approx 5 d_{sq} \quad (1.27)$$

Ballal and Lefebvre [82] rederived Equation 1.25 based on a characteristic time criterion for successful ignition such that the time required for the fuel to burn must be equal to or less than the time required for the cold mixture to quench the spark kernel by thermal conduction and turbulent diffusion.

Maly and Vogel [49] reported from interferometric measurements on spark discharge that both ignition and subsequent flame propagation were strongly influenced by the discharge mode (such as the arc, glow and breakdown). Based

on these experimental results, Maly [83] developed a spark ignition model assuming that the energy actually used in the ignition process is only the fraction transferred to the narrow interface layer at the surface of the spark channel which has a thickness of the order of flame front.

The effects of spark duration on the ignition energy were investigated by Kono et al. [53]. The optimum spark duration varied from about 50 to 300 μsec for DC (glow) or AC (1 MHz damped oscillation) discharges. Ballal and Lefebvre [50] found the optimum spark duration of about 60 μsec .

Microsecond exposure Schlieren pictures of developing ignition kernels and flames were reported by Litchfield [84] for the electrostatic spark ignition of 8.5 percent methane-air mixtures at 0.1 atmospheric pressure. The original spark kernels started 3 μsec after the initiation of the spark between two flange electrodes when a shock wave appeared and propagated at an effectively constant velocity over most of the affected region. The kernel radius was represented as a linear function of the logarithm of the time until a visible flame of 1 cm kernel diameter was observed at about 1 μsec after the spark. He also noted that the time interval could be 100 μsec at atmospheric pressure. Moorhouse et al. [56] observed a similar spark kernel development during the ignition of a stoichiometric mixture of

n-pentane with air at 0.75 atm. A flame appeared about 100 μ sec after a spark with a 2 mm kernel diameter.

Hill [85] simulated the temporal development of gas density, pressure, and temperature of the hot gas channel of the spark observed by Barreto et al. [44] without including chemical reactions. Adelman [86] developed a new theory of the channel expansion to fit the Litchfield results. Recently, a numerical investigation was made by Akindele et al. [87] for the spread of hot gas kernels under turbulent and laminar conditions.

Yang [88] formulated general theories to predict the minimum ignition energy of a system for different configurations of the ignition source. Dixon-Lewis and Shepherd [89] and Overley et al. [90] solved the unsteady flame equations numerically considering ignition processes by localized sources.

Barreto et al. [44] pointed out that the minimum electron charge density, about 10^{17} cm^{-3} , at which electrons in a spark discharge hold a total kinetic energy comparable to the thermal energy of neutral gas molecules, is required for channel thermalization of the spark with the observed discharge time of 40 nsec. They also observed that a spark with minimum ignition requirements released the minimum charge density in a uniform field gap of 2 mm width (the quenching distance) with a spark channel of 30 μ m radius.

c. Effect of uniform inert particles Burgoyne

and Thomas [91] showed that the lower limits of hydrogen in air and of ethylene in air were decreased from 4.0 to 3.5 and 3.4 to 2.7% by volume, respectively, when very fine solid particles of iron oxide were added into the fuel-air mixture. The particles were of the order of 300-500 Å and the weight percentage added was about 10^{-2} . Apparently, these fine particles were burning.

The effect of larger inert particles of $10 \sim 50 \mu\text{m}$ radius was studied by Dewitte et al. [92]. These uniformly dispersed alumina or cupric oxide particles in the constant flow of combustible gas mixtures showed significant inhibition effects on the flame. The flame quenching was explained by the drop of the mean kinetic temperature to its limiting value below which no flame could be self-sustaining. Theoretical prediction on the mean limiting temperature based on the kinetic theory of gases agreed well with that calculated from the critical dust concentration which was extrapolated from experimental results. McCamy et al. [93] noted that the effectiveness of fire extinguishment depends on fineness and dispersibility of dry powders and that inert dry particles are less effective than chemical powders.

An asymptotic analysis of the limit of large activation

energy was presented by Joulin [94] and Mitani [95] to investigate the thermal inhibition effect on premixed flames by chemically inert dust. The velocity of the nonadiabatic flame could be determined using two nondimensional parameters related to the heat capacity and size of particles.

D. Objectives of Investigation

From the literature review, it is apparent that a great deal of progress has been made in understanding the various spark breakdown phenomena such as, critical voltage, time lags, temporal development, and energy distribution associated with both pure and combustible gases in the absence of particulate clouds. In contrast, with particles, very little information is available from experimental or theoretical studies which addresses the various roles played by uniform inert particulate clouds either on critical voltage, probability, mode or energy of spark breakdown, or on the limiting energy for ignition of a combustible gas.

Several of these variables have been considered in the present study. Specifically, a uniform suspension of particles has been experimentally investigated for the purpose of obtaining quantitative correlations in air relating the critical breakdown voltage, breakdown needle electrode position, and parallel electrode separation distance in terms of the particle number density and particle

diameter. Correlations were also sought for the effect of inert particulate clouds on the spark ignition energy of combustible gases at atmospheric pressure. Other objectives were identified during the course of this work and subsequently, were developed into the additional studies, these were: the effect of single free particles on spark breakdown; the effect of particulate clouds on breakdown probability; the effect of needle motion and needle polarity on spark breakdown and ignition of a combustible gas; and the measurement of the temporal development of current and energy during spark breakdown. To these ends, a final objective of this study was to design, construct, and evaluate the performance characteristics of a newly conceived spark breakdown system which was capable of generating uniform particulate clouds in the form of an electrically levitated suspension between parallel electrodes. Controlled triggering of the breakdown could be accomplished with a high speed injected needle electrode.

During this study, several interesting phenomena related to the electrical breakdown, spark ignition, and combustion of multiphase mixtures were encountered. The various mechanisms and equations given in the review for spark breakdown in pure gases and for ignition of combustible gases alone proved helpful in interpreting these particle

related phenomena. Recommendations for future investigations were made at the end of this study.

II. EXPERIMENTAL DESIGN AND CALIBRATION

An important consideration in the present study was the production of a particulate cloud of near uniform number density for use in investigating electrical discharge phenomena. Various pneumatic methods have been used to achieve particle dispersion for spark testing. For example, see Hartman et al. [96], Ishihama and Enomoto [97], and Ballal [98]. But such methods can produce dispersion of particles exhibiting locally nonuniform and unsteady behavior which can often lead to difficulties in controlling and measuring the particle number density. However, the electrostatic method of generating a particulate suspension, which was developed by Cotroneo and Colver [99], Colver and Howell [100], and Colver [101], has been shown to generate very uniform and steady particulate clouds for which the particle number density could be measured accurately and also be simply controlled in time. A means of initiating and localizing a spark was perfected using a fast moving needle electrode which penetrated the suspension system.

A. Experimental Design

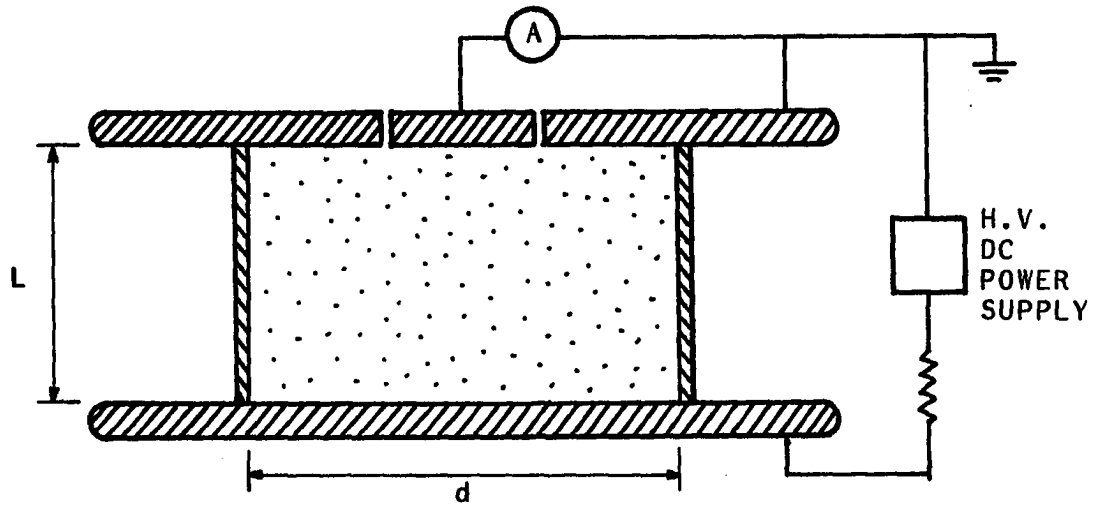
1. Electrostatic suspension

In the same manner as a particle oscillates between two parallel charged electrodes, multiple particles may also be suspended. Basic equations describing the electrostatic

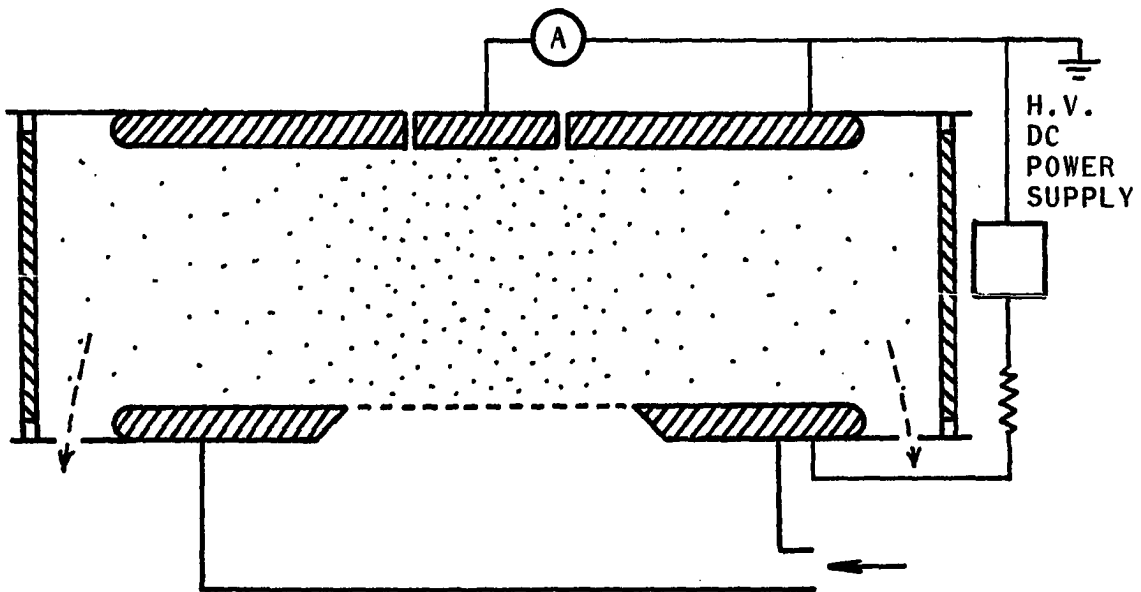
suspension and simple calculations are given in Appendix A. These calculations show that a single spherical copper particle of 96 μm diameter moves at an average speed of 1.554 m/sec and possesses a charge of $3.817 \times 10^{-13} \text{C}$ if it is exposed to a field of 10 kv/cm electric field strength.

However, if the parallel electrode gap is not a closed system, suspended particulate clouds will eventually diffuse out because of particle-particle and particle-electrode collisions. In order to maintain a uniform suspension, two systems were proposed; 1) a closed system using an insulating cylinder between the parallel electrodes, thus confining the particles, and 2) an open system where make-up particles are fed continuously into the suspension. The two systems are sketched in Figure 2.1.

The particle number density could be easily controlled by changing the total quantity of particles in the case of the closed system or by changing the feed rate of particles in the case of the open system. The number density was subsequently calculated based on the total weight of the particles in the closed system or by a current (charge transfer rate) flux measurement for the open system. In the open system, it was expected and observed that the particles suspended above the feed screen of the lower electrode formed a uniform cloud.



(a) Closed system



(b) Open system

Figure 2.1. Schematics for uniform electrostatic particulate suspensions

2. Moving needle electrode

Although the moving needle electrode eliminated the use of high voltage pulses or external radiation sources as a means of triggering the spark, it had to move sufficiently fast so as not to disturb the particle motion during its penetration into the suspension. Since the average particle velocity was expected to be about 1 m/sec, the needle should be designed to move faster than 10 m/sec.

An electromagnet taken from a commercial solenoid valve was first tested but failed to accelerate the needle to a sufficient speed. A compressed air shooting system was then developed and proved successful in driving the needle to the necessary speed, depending on the initial pressure of the compressed air. The schematic layout of the pneumatic system is shown in Figure 2.2. The photograph of the experimental setup, Figure 2.3, also includes this pneumatic system.

A stiff spring was placed at the end of the pneumatic gun so as to eject the needle from the parallel electrode system following a spark. This ejection was necessary since any long time presence of the needle might disturb the particulate suspensions by causing a nonuniform electric field. The brass tube part of the pneumatic gun was 1 cm in inside diameter and 80 cm in length. Parts of the spring

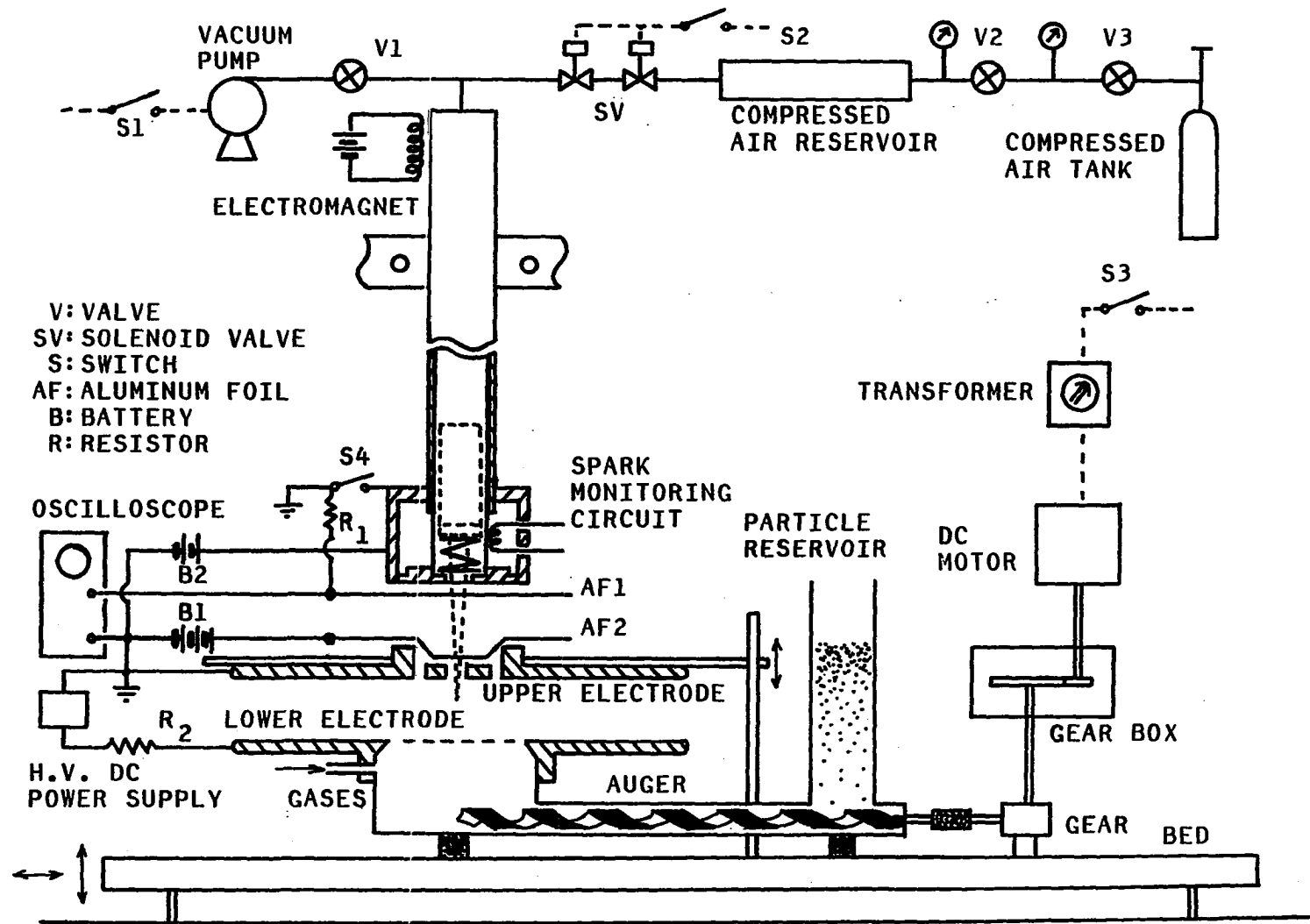


Figure 2.2. Layout of experimental setup

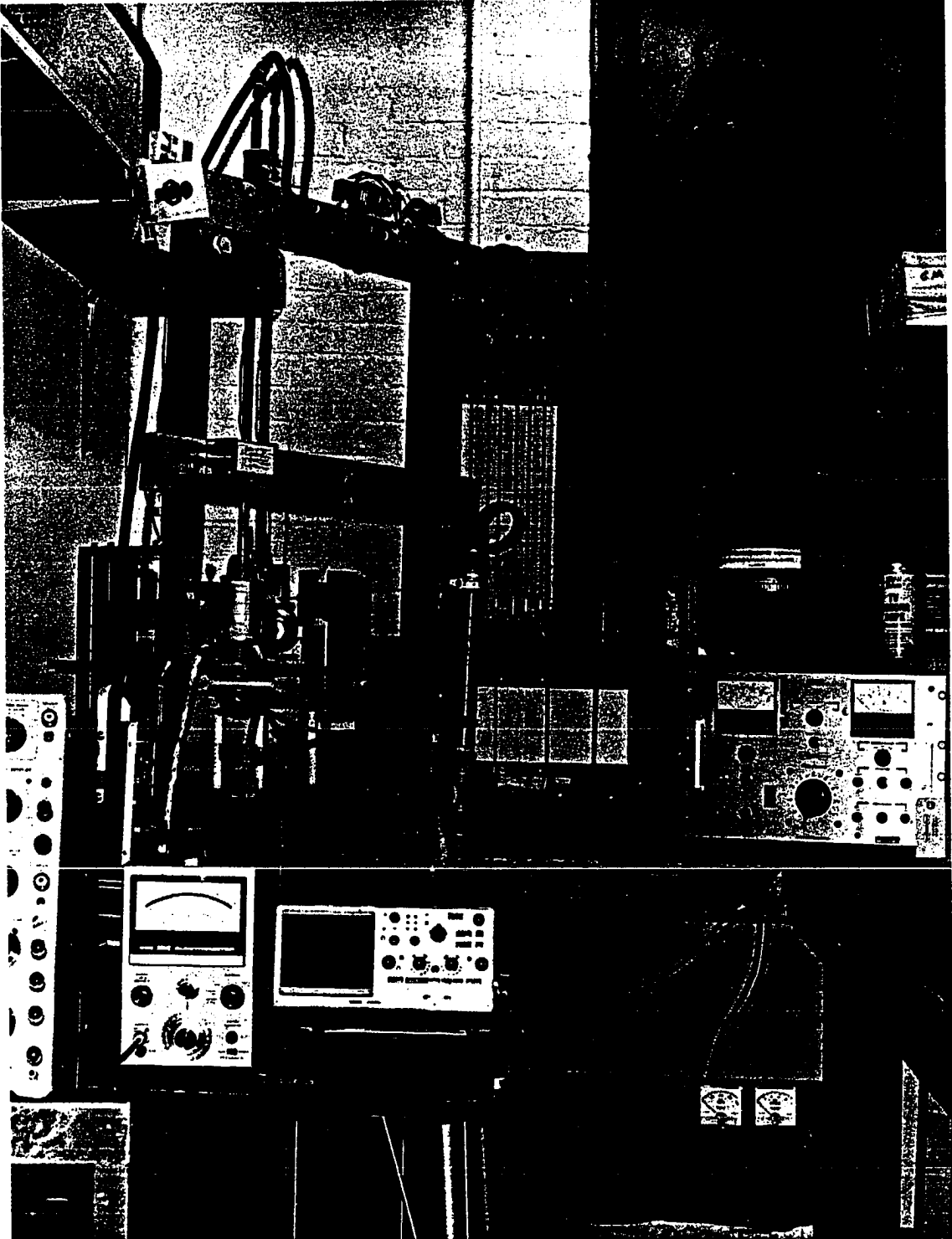


Figure 2.3. Photograph of experimental setup

mounting were constructed of steel and aluminum.

It was found that the long needle electrode was often broken as a result of the decelerating and retracting action of the spring, causing a high stress around the neck portion of the needle. For example, since the spring constant was about 1.5×10^8 g/sec², when the needle of 10g total mass and 5g long nose mass moved at 10 m/sec and was decelerated by the spring, the maximum deceleration force acting on the neck could be calculated to be approximately $5 \text{ (g)} \times 10 \text{ (m/sec)} \times [1.5 \times 10^8 \text{ g/sec}^2 / 10 \text{ (g)}]^{1/2} \approx 194$ Newton, neglecting the spring mass. In order to withstand this force, various needles were designed and failure tested until a final profile was selected. This needle was rounded near the neck and slowly tapered to the tip. Figure 2.4 shows the dimensions and shape of the needle. The long nose and stopper were made from a single piece of steel.

The position and velocity of the moving needle were necessary measurements because of their importance in understanding electrical breakdown and spark ignition triggered by the moving needle. Experimental conditions required that event times to ± 0.01 msec be measured as determined by the needle velocity (10 m/sec) and the penetration distance of the needle into the suspension (~ 1 mm).

To monitor the needle position with time, an LVDT

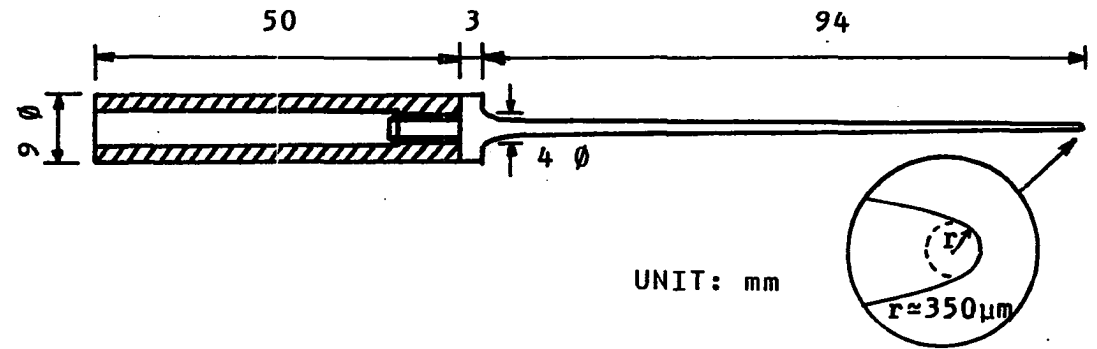
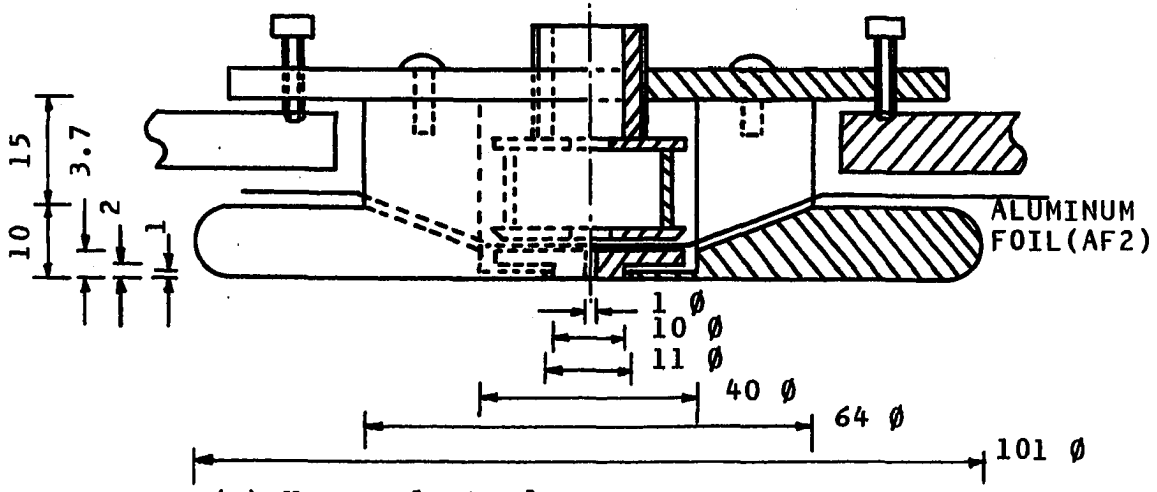
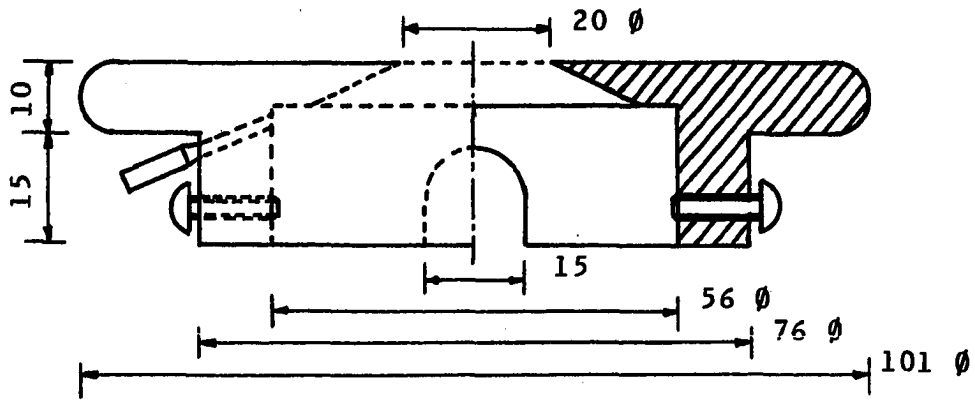


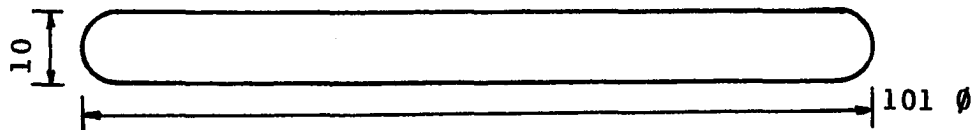
Figure 2.4. Moving needle electrode shape and dimensions



(a) Upper electrode



(b) Lower electrode



(c) Flat electrode

UNIT: mm

Figure 2.5. Main electrodes

(Linear Variable Differential Transformer) was built inside the spring mounting cylinder and tested. However, it was found that the transformer system did not possess the required sensitivity. At the necessary carrier frequency, which had to be greater than 100 KHz ($= 1/0.01$ msec), the LVDT did not respond reliably to the needle motion. The resonance frequency of the LVDT circuit, which was the order of MHz, was tested as a carrier signal but failed to give a linear response. As a result of these problems, the LVDT was replaced by a simpler circuit comprised of two batteries and two spaced aluminum foils. The needle velocity was then accurately determined by switching signals produced as the needle penetrated each aluminum foil and touched the spring (see Figure 2.2).

3. Overall experimental setup

The upper and lower electrodes are sketched in Figures 2.5a and 2.5b. These were specially designed to achieve several purposes: 1) to produce steady state clouds as particles were fed continuously through the inlet hole of the lower electrode, 2) to provide for measurement of the current flux via a known area in the inner part of the upper electrode (this area was made smaller than the screen area of the lower electrode), and 3) to determine the moving needle position accurately by placing an aluminum foil as

close as possible to the surface of the upper electrode. The inner electrode diameter was 1 cm, while the screen diameter was 2 cm. The main electrodes were 10 cm diameter brass disks with rounded edges. The flat removable electrode design (Figure 2.5c) allowed for the glass insulating cylinders to be inserted easily, forming the closed system.

Figures 2.2 and 2.3 show the overall experimental set-up schematically and photographically. The continuous feeding of particles was accomplished by using an auger, particle reservoir and DC motor system. The feed rate was adjusted by controlling the motor speed which was regulated by the output voltage from a transformer. Since the lower electrode and particle reservoir were connected to the DC high voltage power supply, they were insulated with teflon bars from the grounded bed. Similarly, the auger was connected to the gear through a rubber insulating tube. Charge leakage was measured and found to be negligible.

The pneumatic gun could be adjusted relative to the top of the main electrode. Two solenoid valves were used to close completely the compressed air line to assure against leakage which, prior to release, might overcome the electromagnet force which held the needle at the top of the gun. The two solenoid valves were activated simultaneously by a single switch (S2 in Figure 2.2). Following a run, the

needle could be brought back to the top of the gun by opening the valve V1 to which a vacuum pump was connected.

The overall electrode and feeding system could be adjusted vertically and horizontally in order to align the needle and the needle entrance hole (1 mm diameter in the upper electrode) and to adjust the needle penetration depth into the parallel electrode system. In addition, the upper electrode could be moved independently relative to the lower electrode. The upper electrode could also precisely be leveled in parallel with the lower electrode using three screws. All experiments were performed in an environmental room where the temperature and relative humidity could be controlled between 23~26°C and 20~40%, respectively (40% relative humidity is the upper limit to prevent excessive corona, 25°C and 1 atm are the standard condition).

B. Experimental Instruments

The high voltage side of a high voltage DC power supply (Hipotronics Model 850B) was connected to the lower electrode through a large series resistor of the order of 100 MΩ. Three DC voltage ranges were available, 0-10/25/50 kv, with a maximum allowable current of 5 mA at less than 2% rms ripple. The high voltage was measured with the electrostatic voltmeter Model ESH manufactured by Electrical Instrument Service. This voltmeter has a minimum error of less than 1%. Multirange 0-5/15/30/50 kv measurements could be obtained.

Small currents on the order of 10^{-8} A (which was the same order of the particle charge transferred through the inner electrode of 1 cm in diameter) were measured by a Keithley Instruments Model 602 electrometer. The electrometer range is from 10^{-11} A to 0.3 A with less than +2% error of full scale and from 10^{-14} A to 10^{-11} A with better than +4% accuracy.

Two oscilloscopes were used. The first oscilloscope was a Tektronix Model 434 storage scope which has a 14 nsec rise time. This oscilloscope was used for the measurements of the needle position and velocity. The second was a Tektronix Model 475 high speed oscilloscope used to record the current during a spark discharge. The fastest rise time is 1.8 nsec which is sufficient to resolve most of ionization processes of sparks. The input independence is 1 M Ω shunted with 20 pF. The fastest sweep speed is 1 nsec/div. Both oscilloscopes have amplitude scales from 5V to 1 mV per division and were calibrated before measurement.

A Torsion Balance Model EA-1AP with +0.0001g accuracy and an Ainsworth electronic balance Model N-1V with + 0.00001g accuracy were used to weigh the particles.

The total capacitance of the parallel plate electrodes plus leads and external capacitor was measured with an Electro-Measurements Model 250-DA impedance bridge. The

smallest measurable capacitance magnitude with this device is ± 0.1 pF.

C. Calibration

1. Particle number density

If the total mass W of spherical particles, each of diameter D , is suspended uniformly in a container of volume $\pi(d/2)^2 L$, the particle number density N can be calculated by

$$N = \frac{W}{\frac{4}{3} \pi \left(\frac{D}{2}\right)^3 \rho_p \pi \left(\frac{d}{2}\right)^2 L} \quad (2.1)$$

Two Pyrex glass tube containers were used for calibration. The first was 1.10 cm in height and 2.63 cm in inside diameter and the second was 1.00 cm in height and 6.50 cm in inside diameter. The present experiment dealt only with copper particles assumed to have a density ρ_p of 8.954 g/cm³. The copper particles were sieved mechanically and/or acoustically. Arithmetic averages of the copper particles based on sieve sizes are given in Table 2.1. These arithmetic averages were used for the particle diameter D in Equation 2.1.

The copper particles were observed to be reasonably spherical in shape. However, the actual particle size distribution and shape were checked and are discussed in

Appendix B. Possible errors in the calculated particle number density as a result of the actual size and shape distributions are analyzed in Appendix D.

Table 2.1. Particle sieve size ranges and averages

Mechanical sieve		Sonic sieve	
Size range (μm)	Average D (μm)	Size range (μm)	Average D (μm)
295-417	356	30-38	34
125-147	136		
88-104	96		
63-74	68		
44-53	48		
38-44	40		

A closed suspension test was made by putting particles in the Pyrex glass container situated on the flat electrode. The flat electrode was then placed on the lower electrode carefully, moving the upper electrode down to close the container. High voltage was then applied. The particle number density was calculated directly using the weight of the particles in the container. The current through the upper-inner electrode was measured by the electrometer against the calculated particle number density, and the results were used as a calibration for the open suspension system. The

results for 96, 68, 48 and 34 μm particles are shown in Figures 2.6a-e. During calibration the applied voltage was always lower than the minimum breakdown voltage to protect the electrometer from a high current surge. Figure 2.6a shows different types of suspension behavior as the particle number density approaches $7.5 \times 10^3 \text{ \#/cm}^3$. The details of this region were investigated by Bierkamp and Colver [102]. The dip in the curve was observed as particles began to clear from the lower electrode. The present study utilized only the uniform suspension.

2. Moving needle velocity and position

Figures 2.2 and 2.7 show the on-off circuit used for measurements of the position and velocity of the needle during its motion. An aluminum foil strip 1 (AF1) was fixed on the bottom of the pneumatic gun where the surface was insulated electrically. The foil strip 2 (AF2) was placed on the top of (but insulated from) the upper-inner electrode and pressed from above with a Plexiglas disk shown in Figure 2.5a, so as to flatten the foil.

The moving needle functions as two switches, making contacts as it penetrates each strip and touches the spring, thus closing the circuit in Figure 2.7. During the needle penetration from AF1 to AF2, the voltage B_1 across the resistor (R_1) triggers the storage scope and makes a step

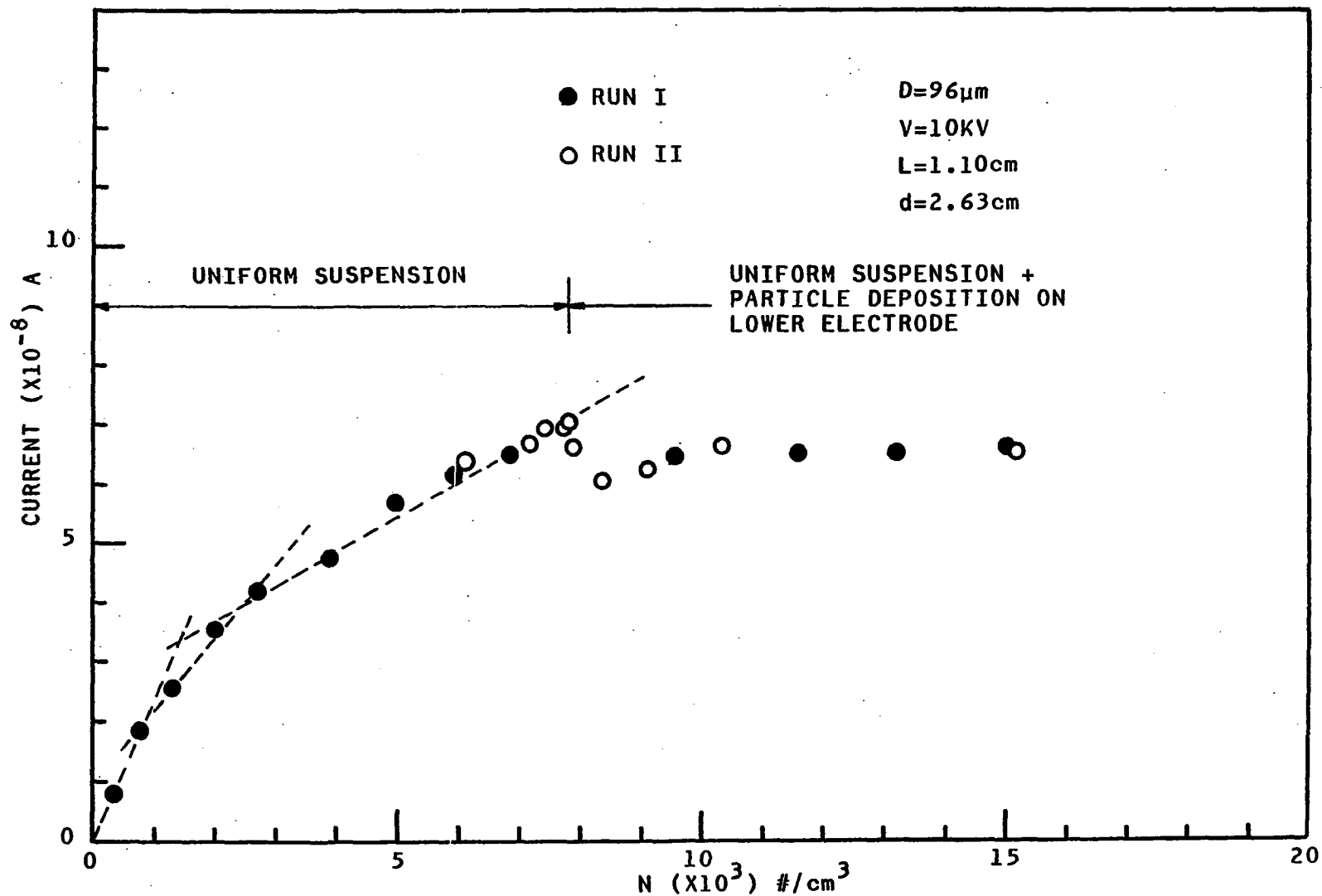


Figure 2.6a. Current vs. particle number density at fixed electric field strength, $D = 96 \mu\text{m}$

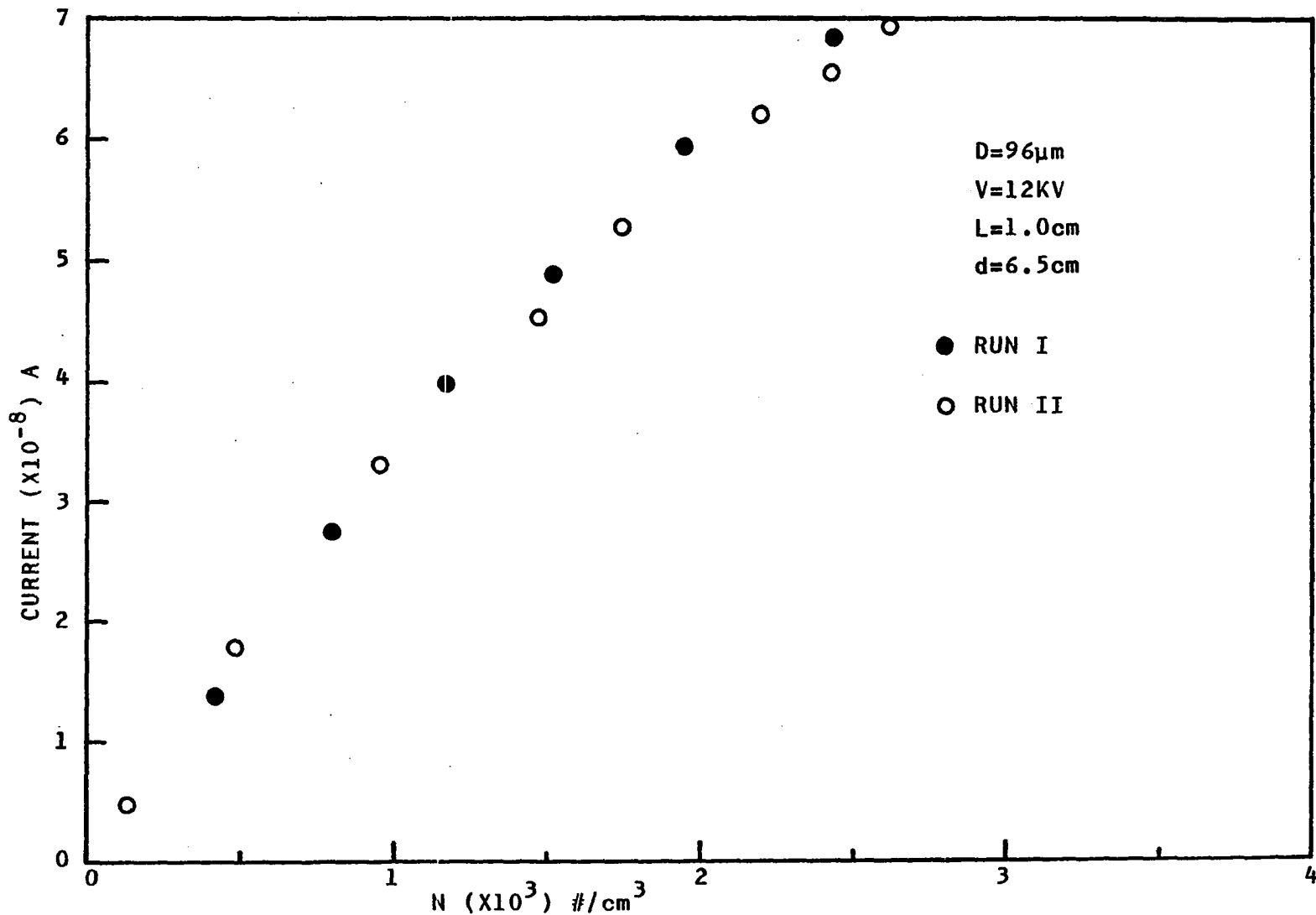


Figure 2.6b. Current vs. particle number density at fixed electric field strength, $D = 96 \mu\text{m}$

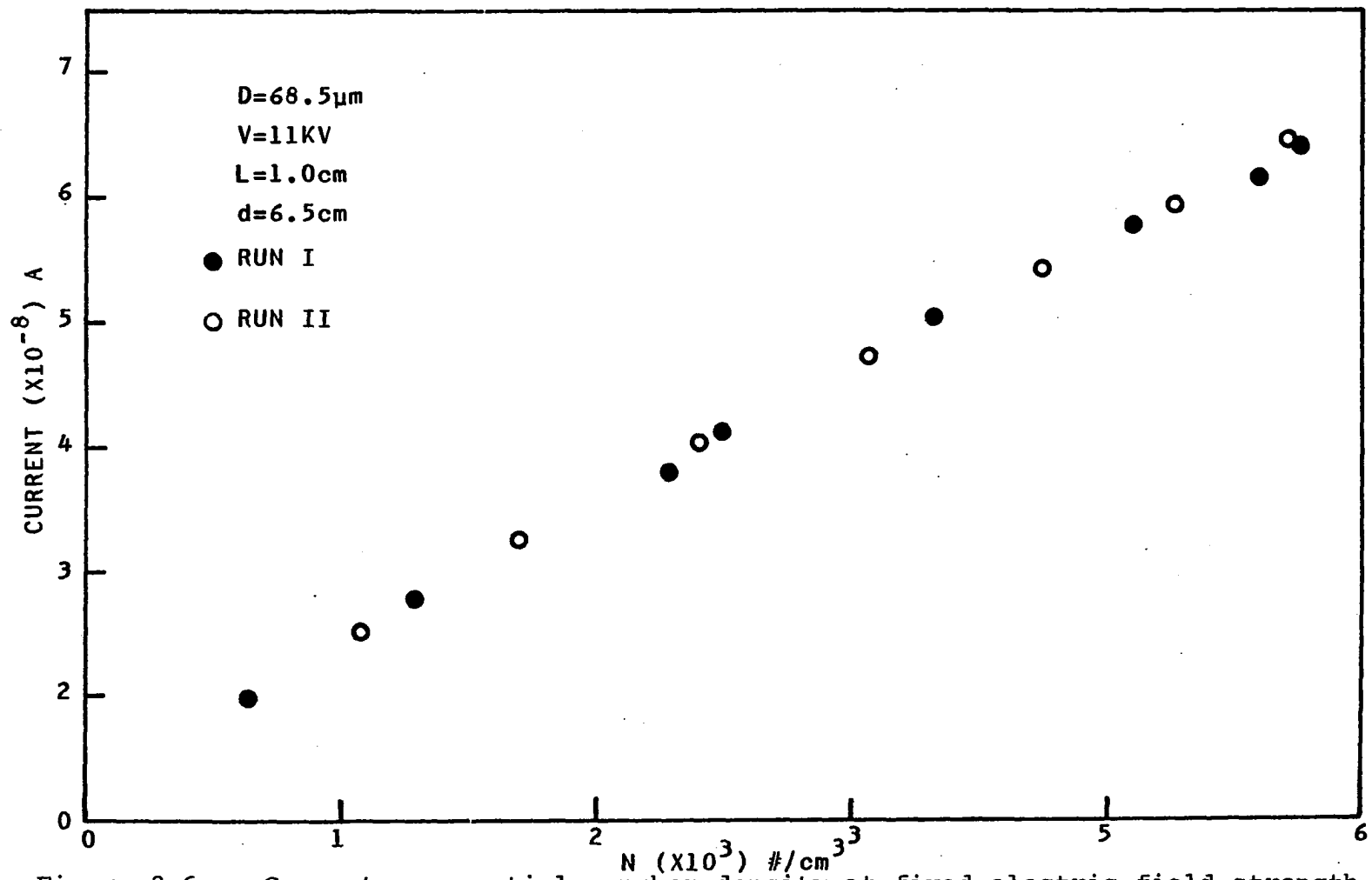


Figure 2.6c. Current vs. particle number density at fixed electric field strength, D = 68 μ m

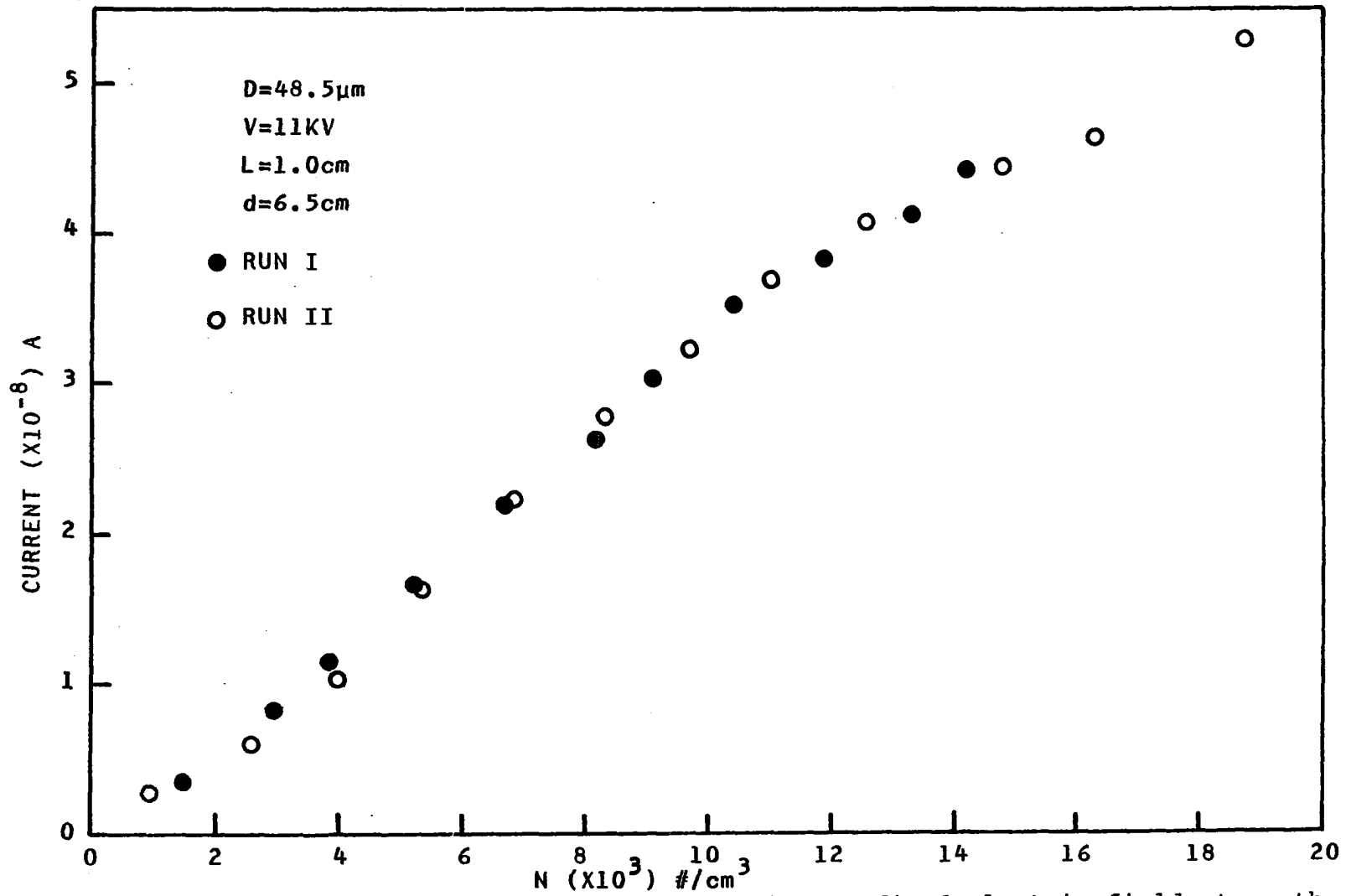


Figure 2.6d. Current vs. particle number density at fixed electric field strength, $D = 48 \mu\text{m}$

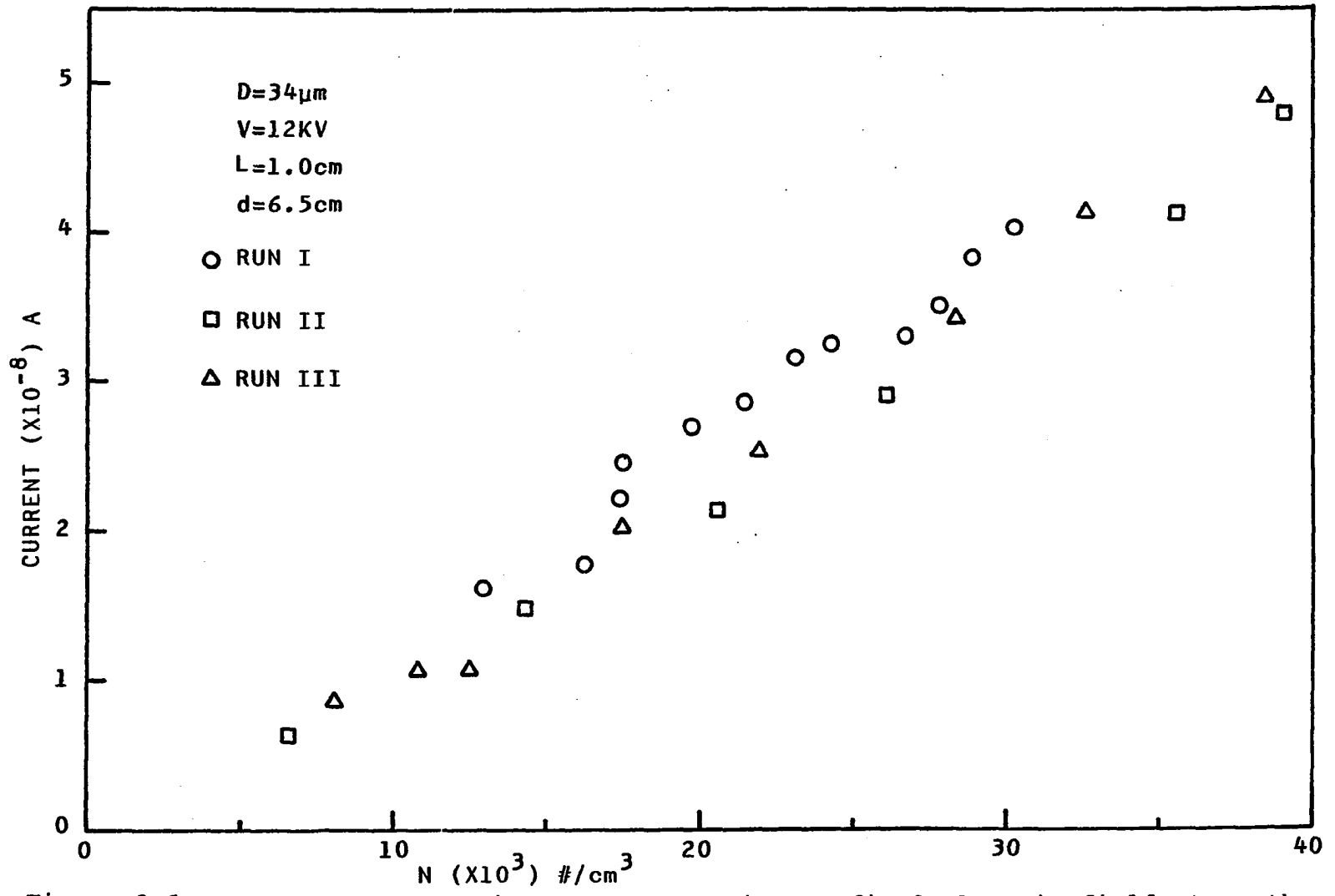


Figure 2.6e. Current vs. particle number density at fixed electric field strength, $D = 34 \mu\text{m}$

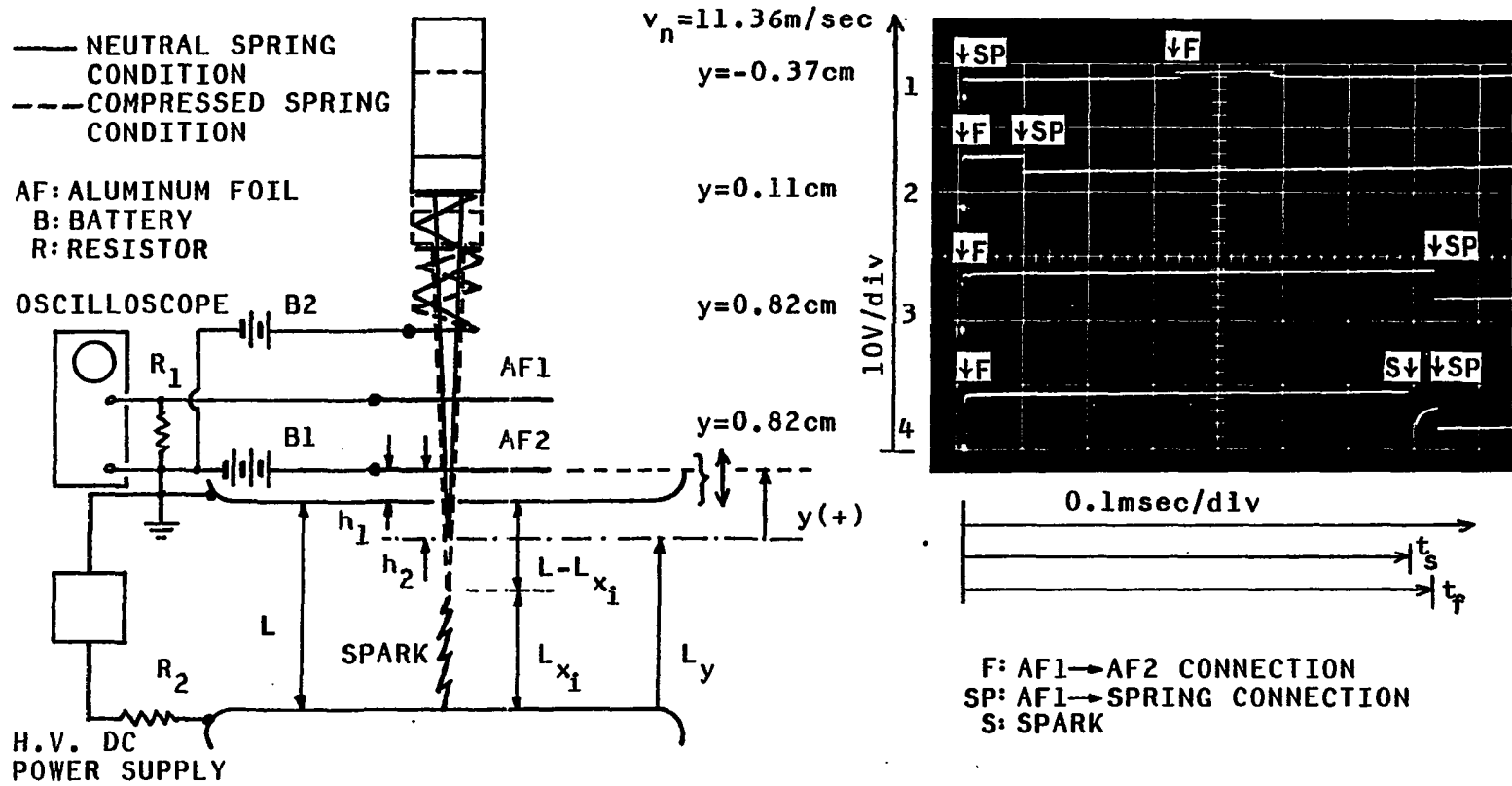


Figure 2.7. On-off circuit, two-step signals and sketch of electrode gap showing various relevant distances

signal. This signal lasts until the voltage drops to B2 completing a pulse when the needle makes contact between AF1 and the spring which is also connected to another lower voltage source, the battery B2 (see traces 2 and 3 in Figure 2.7). The trace 1 in Figure 2.7 is the signal triggered first by the AF1-spring connection and then by the AF1-AF2 connection.

For calibration, y is defined as the distance from AF2 to the needle tip for the condition that the needle just touches the spring. Negative y refers to the compression distance of the spring. Therefore, these two steps in Figure 2.7 correspond to the time interval required for the needle tip to move from AF2 to the reference needle tip position. The time intervals stored on the scope were taken by lowering the upper electrode (i.e., AF2) until the needle failed to puncture the foil (AF2), and are plotted against the position y in Figures 2.8a-b for various pressures of the compressed air. This procedure allowed exploration of the needle response before and during deceleration. The position of the upper electrode was directly measured with a dial gauge having a ± 0.0005 in resolution. Figure 2.8a shows good linearity for all curves based on the time and the position y . Thus, it is evident that the needle velocity (depending on pressure) is constant until the needle hits the spring.

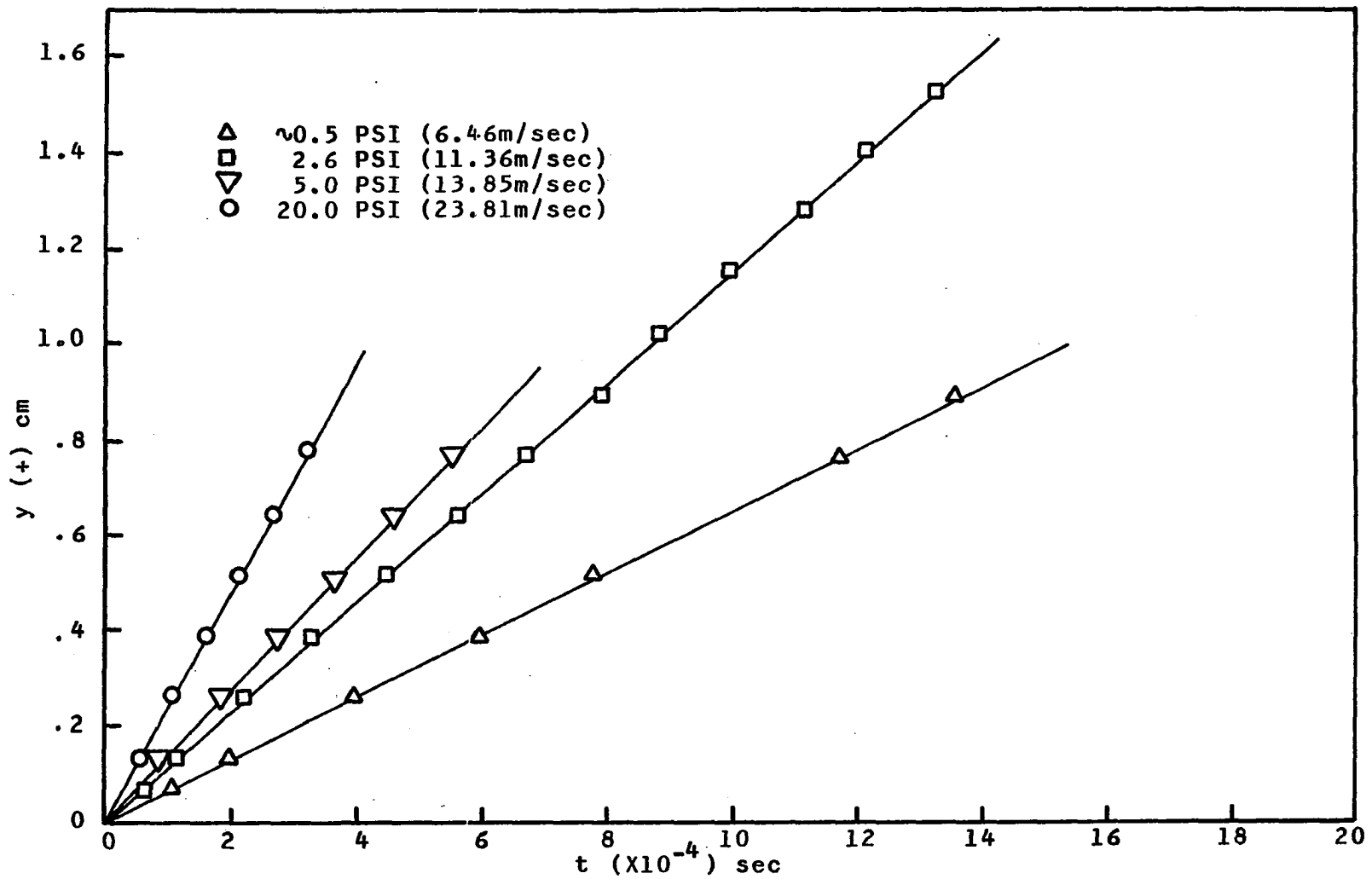


Figure 2.8a. Needle position vs. time, $y \geq 0$

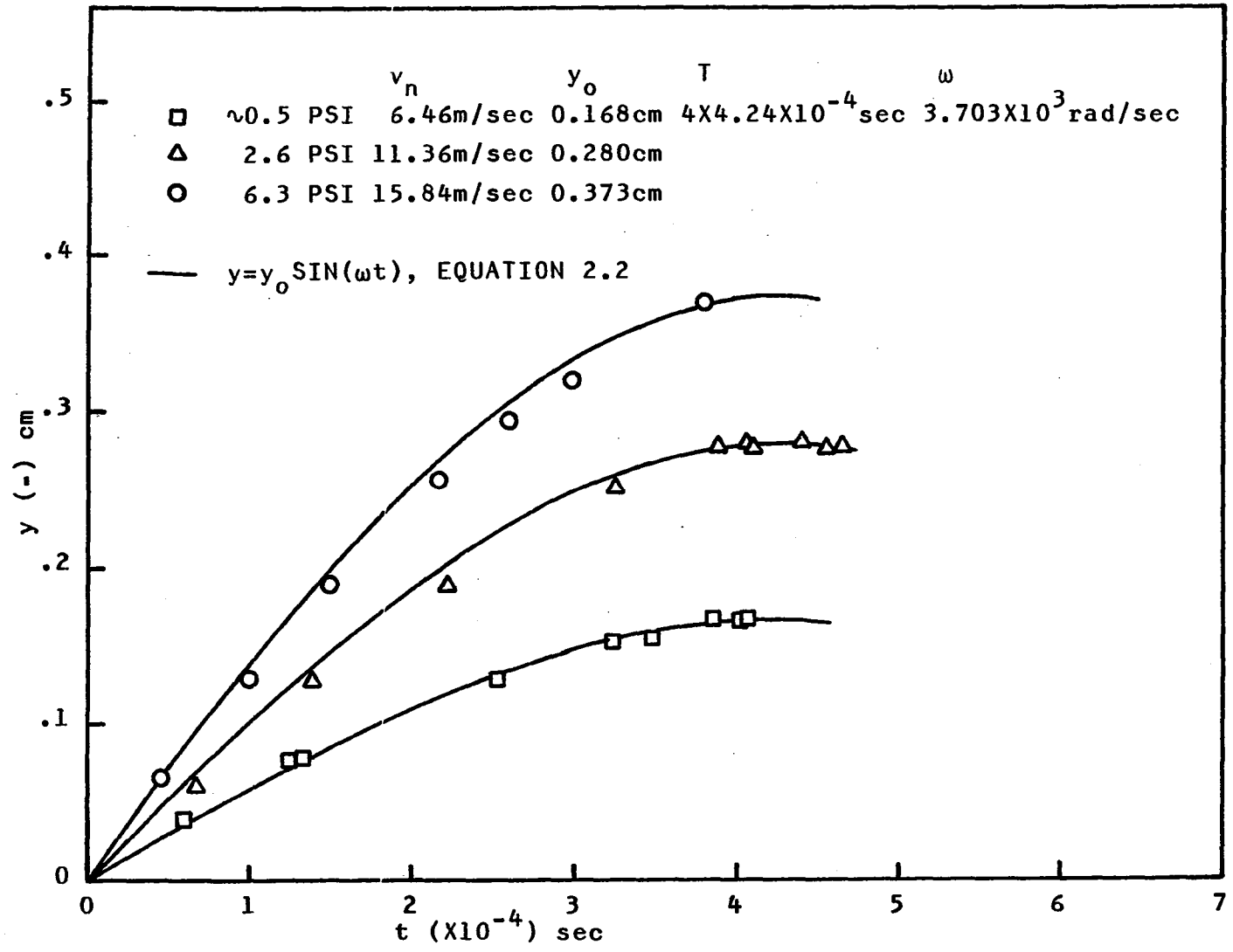


Figure 2.8b. Needle position vs. time, $y \leq 0$

However, when the needle was undergoing deceleration, the curves could be represented as one-fourth of a cycle (Figure 2.8b). Thus, spring motion could be expressed as

$$y = y_0 \sin \omega t \quad (2.2)$$

where the natural angular frequency ω is $\sqrt{\frac{K_s}{m_n}} = \frac{2\pi}{T}$. The maximum compression distance y_0 and period T were measured and are shown in Figure 2.8b. The period was nearly constant, $4 \times 4.24 \times 10^{-4}$ sec, regardless of the needle initial velocity (or pressure). The needle motion could be predicted with Equation 2.2 within 10% error. The natural angular frequency measured from Figure 2.8b, 3.70×10^3 rad/sec, was compared with the calculated value, 4.03×10^3 rad/sec, based on measurements of the spring constant $K_s = 1.5 \times 10^8$ g/sec² and the needle mass 9.23 g. The slightly larger value could be expected because of the effect of the spring mass. When the effect of the spring mass was included in the calculation, the natural angular frequency was 3.56×10^3 rad/sec.

III. ELECTRICAL BREAKDOWN OF UNIFORM PARTICULATE CLOUDS

A. Experimental Procedure

The experimental system bed was adjusted vertically to prevent the needle tip from touching the flat electrode placed on the lower electrode during compression of the spring. At least a 3 mm gap was allowed between the reference needle tip position and the flat electrode (i.e., L_y shown in Figure 2.7) based on a needle velocity of 11.36 m/sec as used in this study. Also, the bed was adjusted horizontally so that the needle passed precisely through the center line of the upper electrode hole.

Three Pyrex glass cylinders were used to adjust the separation distance of the two parallel electrodes. These cylinders were 0.75, 1.02 and 2.00 cm in height and 2.63 cm in inside diameter. This design resulted in a closed system giving a uniform particulate suspension. The applicable voltage range was restricted by the maximum voltage without sparking over the glass cylinders and by the minimum voltage for lifting the particles against gravitational forces. Painting the lips of the glass cylinders with a corona dope (manufactured by GC Electronics Co.) helped to reduce corona and spark over. For a 1.02 cm electrode gap, the allowable voltage range for testing was from 20 KV to

5 KV.

During the penetration of the moving needle, a spark was initiated at a needle position that depended on the applied voltage. The sparking process was monitored visually and stored on the Tektronix Model 434 oscilloscope as a pulse trace similar to the trace 4 shown in Figure 2.7. Only sparks which appeared before the needle touched the spring were included in the analysis so as to isolate the needle velocity effect. For every run, the particles were replaced since some particles could escape through the small hole in the upper electrode. The two foil strips were also shifted to provide fresh surfaces.

The time intervals t_s and t_f indicated in Figure 2.7 were measured, and the nondimensional needle penetration distance at the time of sparking was calculated by

$$(1-x_i) = \frac{L-L_{x_i}}{L} = \frac{h_2}{L} \left(\frac{t_s}{t_f} - \frac{h_1}{h_2} \right) \quad (3.1)$$

Figure 2.7 illustrates h_1 and h_2 . This equation was possible since a constant needle velocity was observed.

When an electrical breakdown triggered by a stationary needle in a particle free gap was studied, the needle was moved down manually very slowly until a breakdown was observed at a fixed applied voltage.

B. Results and Discussion

1. Breakdown voltage and needle position

The electrical breakdown process is a random event, therefore, the same test was performed at a fixed condition more than 10 times, sometimes up to 50 times, depending on the probability of the needle position at breakdown (L_{x_i}). For the purpose of analysis or correlation, the arithmetically averaged breakdown needle position (L_x), i.e., the value with 50 percent probability, was used as the most probable value. However, not only the range of the results was shown on figures but also their probability distribution was also studied. Figure 3.1 shows a typical photograph of a spark initiated by a moving needle in a uniform particulate suspension.

a. Effect of polarity The effect of needle polarity was investigated for the stationary and moving needle in the present electrode system. The experimental results of the applied voltage V plotted against the average non-dimensional breakdown needle penetration distance $(1-x)$ are shown in Figure 3.2 for various experimental conditions (positive and negative needle, moving and stationary needle, and with and without particles).

Corona discharge pulses were only observed with the

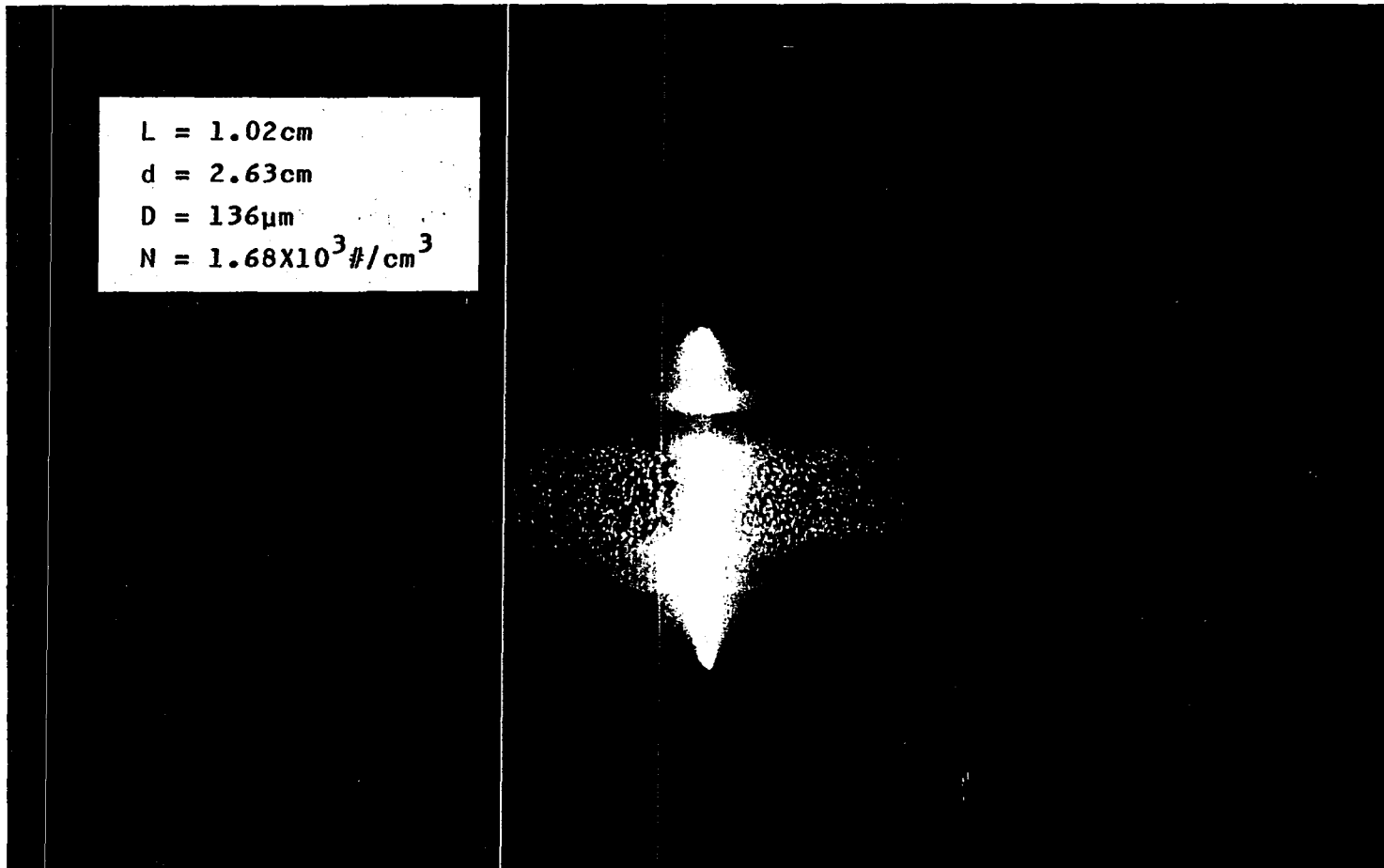


Figure 3.1. Photograph of a spark triggered by a positive moving needle in a uniform particulate cloud

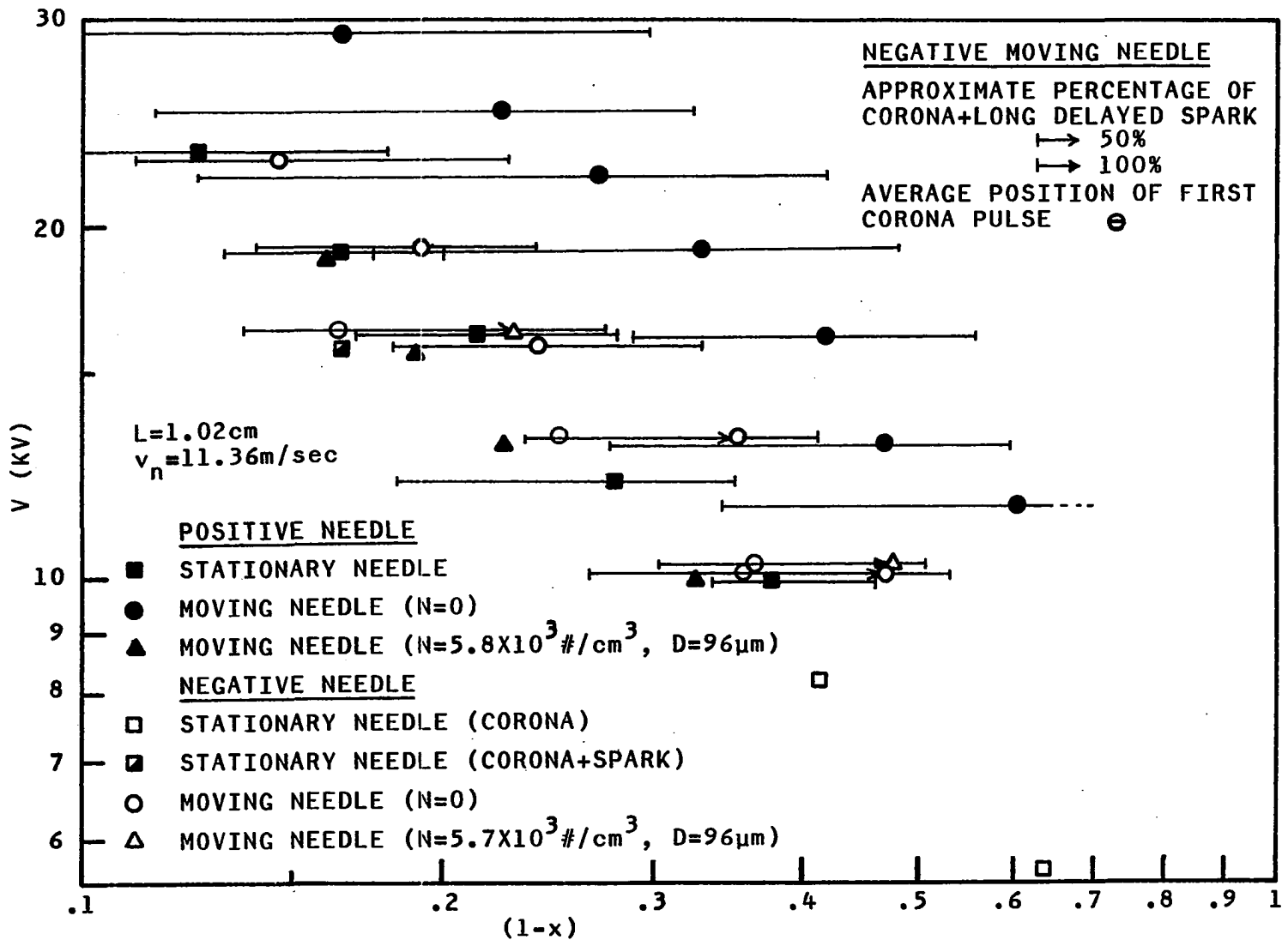


Figure 3.2. Breakdown voltage vs. average nondimensional needle penetration distance, effect of needle polarity

negative stationary needle until $(1-x)$ decreased to a value smaller than 0.16 in which case the pulses and sparks appeared simultaneously. The continuous pulses were identified, using current measurement, as the well-known Trichel pulses (with 10 mA peak and 15 μ sec period, see Figure 4.3). Since these continuous pulses completely discharged the system capacitor, resulting in a voltage drop, it was difficult with the stationary needle to increase the voltage high enough so as to initiate a spark. The spark is well-known to have a much higher breakdown voltage than the corona initiation voltage for the negative needle-to-plane gap as discussed by Nasser [13]. By comparison, the negative moving needle could trigger a spark followed by several continuous pulses. One explanation is that the field strength of the moving needle tip was exceeding the spark breakdown field strength before these initiatory pulses could reduce the applied voltage. When the applied voltage was increased above 10 KV, the number of runs involving discharges of the negative moving needle which showed initiatory continuous pulses was decreased.

In contrast to the negative needle, the positive stationary or positive moving needle readily triggered spark breakdown. Actually, for the stationary needle, the spark

followed a corona pulse with a very short time delay at a condition which depended on the breakdown needle position and voltage. The detail of the temporal development of the current pulses is discussed in the next chapter.

It was found that the positive moving needle required a higher applied voltage than that for the positive stationary needle so as to have the same needle position at breakdown. For the negative needle, it was difficult to find a voltage difference as a result of the needle motion because the spark breakdown position of the negative stationary needle was unknown, although, the spark breakdown voltage can be expected to be larger than that for a corona discharge (Nasser [13]).

With the negative moving needle, the presence of the particulate clouds did not produce any special effect on the average breakdown needle penetration distance $L(1-x)$, but the probability for the appearance of continuous pulses before a main spark was increased. However, with a positive moving needle, it was observed that the presence of a particulate cloud lowered $L(1-x)$ at a constant applied voltage.

It was also visually observed that a single spherical copper particle of about 1 mm diameter when oscillating between two parallel electrodes of 1.0 cm gap width initiated

a spark (at ~ 14 KV) mostly when the particle was near to ($\sim 0.5-2.0$ mm) a positive electrode, regardless of whether it was the upper or the lower one. A possible explanation is that a micro-discharge between the particle and the positive electrode bridges them electrically and behaves as a protrusion. This bridge reduces the breakdown voltage more so for a positive than for a negative electrode.

Abde-Salam and Abul-Shohoud [103] observed that a protrusion 2 mm high and 1 mm in radius at the negative plane electrode of a point-to-plane gap appeared to have little influence on the spark breakdown voltage, while the protrusion over the positive plane electrode resulted in a significant reduction in the spark breakdown voltage. The present result also seems to indicate that the conditions of and near to an electrode, such as the presence of a particle (or particles) or the presence or motion of a needle, are more important in influencing the breakdown characteristics of a positive electrode than of a negative electrode.

The remainder of this study was thus restricted to the case of the positive needle electrode.

b. Effect of needle velocity The average non-dimensional breakdown needle penetration distances ($l-x$) for five different needle velocities including a stationary

case are compared in Figure 3.3 without particles. The comparison reveals almost no difference in the breakdown position for the needle velocity range of 11.64 to 2.63 m/sec. Compared to a stationary needle, the breakdown was delayed about 2.5 mm at 11 KV or 1 mm at 25 KV as a result of the needle motion. Typical time delays were calculated to be 10^{-3} to 10^{-4} sec, which is of the order of the statistical time lag of breakdown [10]. Thus, the velocity effect might be explained as a time delay related to the occurrence of simultaneous events; that is, the existence of an adequate field strength with a spontaneous initiating electron in the vicinity of the needle tip. It is noteworthy that as the needle penetrates parallel electrodes, the field strength at its tip increases monotonically. The likelihood of this chance meeting is increased with residence time of the needle electrode. (See review discussion on statistical time lags.)

c. Effect of uniform particulate clouds Extensive experiments were performed using a moving positive needle at 11.36 m/sec to obtain the average nondimensional breakdown needle penetration distance $(1-x)$ of uniform particulate clouds suspended in the closed system of a 1.02 cm parallel electrode gap in terms of the particle number density N , average particle diameter D , and the applied voltage V .

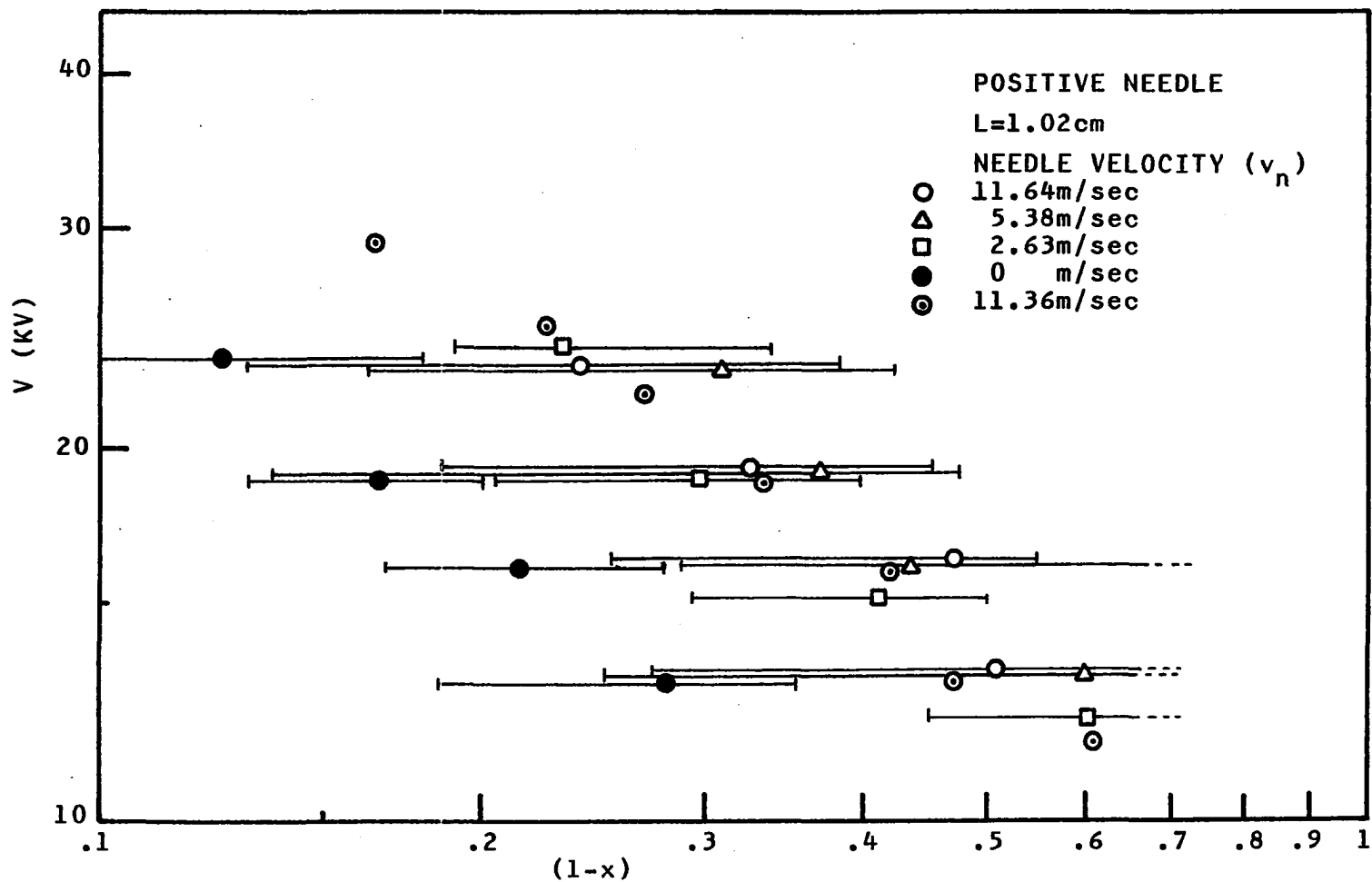


Figure 3.3. Breakdown voltage vs. average nondimensional needle penetration distance, effect of needle velocity

The nondimensional breakdown position $(1-x)$ was plotted in Figures 3.4a-c against the particle number density N for different average diameters of 40, 96, 136 and 356 μm and applied voltages of 10.0, 13.0, 16.0 and 19.0 KV on semi-logarithmic scales (found to be the most adequate scales for correlation purposes). The figures show that the relationship of $(1-x)$ and N is similar for each applied voltage and particle diameter, and thus, a curve could be shifted in $(1-x)$ and N directions and placed on another curve of different applied voltage and particle diameter.

In Figure 3.4a, $(1-x)$ for 136 μm particles at 19.0 KV is decreased to about 0.16 as N approaches to 10^3 ($\#/\text{cm}^3$), and then remains almost constant with a further increase in N . This critical value 0.16 is nearly the same for the various particle diameters, so that it appears that there is a minimum possible (critical) distance $(1-x)_c$ for which the breakdown needle position becomes independent of the particle number density. The transitional particle number density N_* at which $(1-x)$ becomes a critical value appears to be a function of the particle diameter. When $(1-x)$ is larger than its critical value, smaller particles in size require more particles per unit volume to trigger a spark at the same needle position and applied voltage.

The same experiment was repeated with two additional

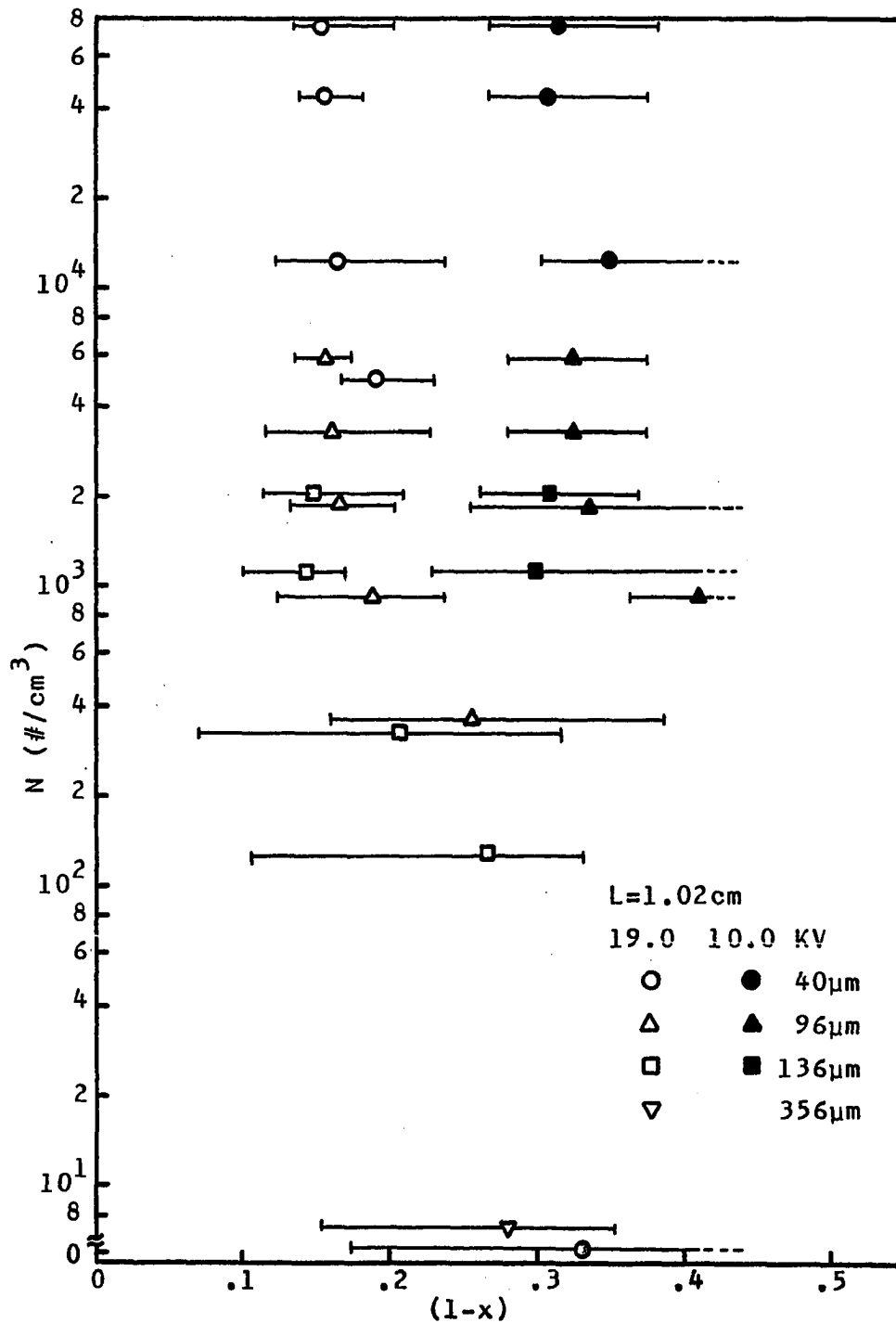


Figure 3.4a. Particle number density vs. average non-dimensional needle penetration distance at breakdown, $L=1.02\text{ cm}$, and $V=10.0, 19.0\text{ KV}$

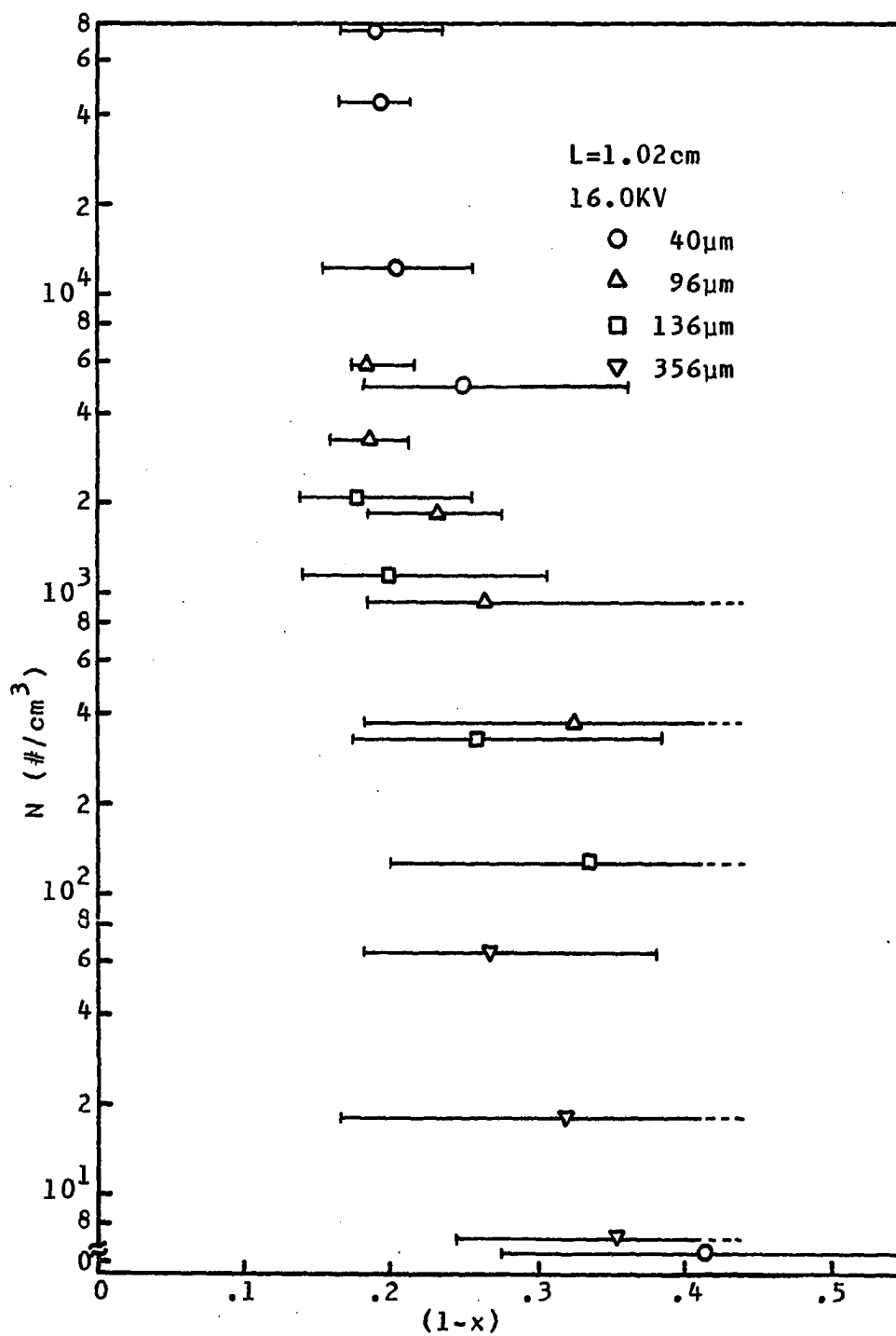


Figure 3.4b. Particle number density vs. average non-dimensional needle penetration distance at breakdown, $L=1.02\text{ cm}$, and $V=16.0\text{ KV}$

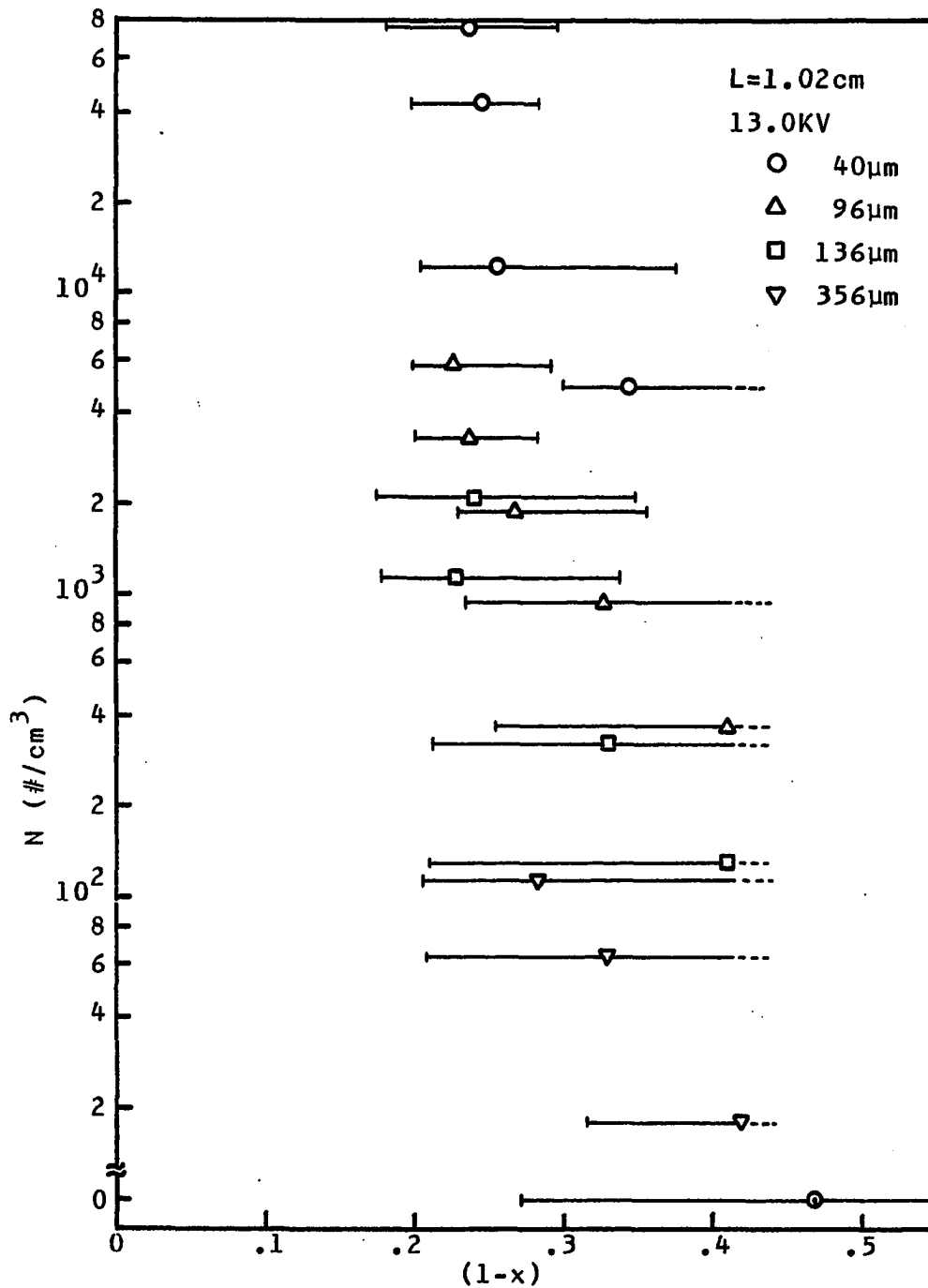


Figure 3.4c. Particle number density vs. average non-dimensional needle penetration distance at breakdown, $L=1.02\text{ cm}$, and $V=13.0\text{ KV}$

containers of 2.00 and 0.75 cm height and with a voltage range from 9.5 to 31.3 KV. Figures 3.5a-b and 3.6 show that the results are similar to the previous case, while the transitional N was observed to depend also on the gap width of the parallel electrodes.

2. Correlation

The variables influencing the spark breakdown in the particulate suspensions of this experimental system are summarized in Table 3.1.

From the literature review, dimensional analysis is not seen to have evolved as a useful analytical tool for characterizing sparks. This follows since sparkings are transient phenomena, comprised of several more or less independent stages. Thus, it would be difficult here to generalize electrical breakdown associated with particulate suspensions in terms of nondimensional groups obtainable from dimensional analysis of Table 3.1 variables without first understanding the mechanisms involved. Furthermore, the breakdown also depends on such additional variables as the electrode geometry, surface condition and material, and the humidity. Therefore, 5 variables, V , L_x , L , N , and D , were selected from Table 3.1, based on their relevance in engineering, for the present experimental study and correlation.

The two variables, N and D , when correlated on

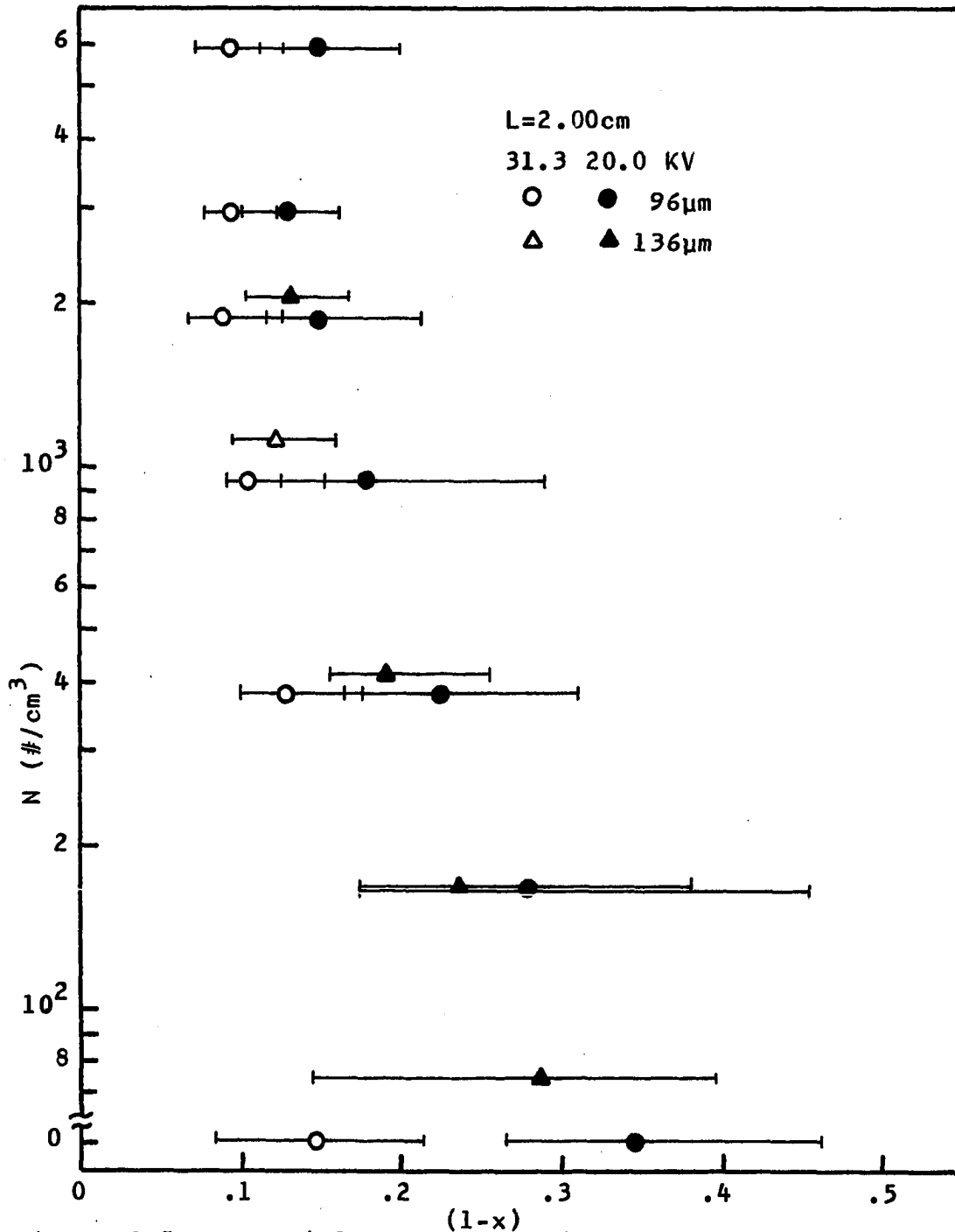


Figure 3.5a. Particle number density vs. average non-dimensional needle penetration distance at breakdown, $L=2.00\text{ cm}$, and $V=20.0, 31.3\text{ KV}$

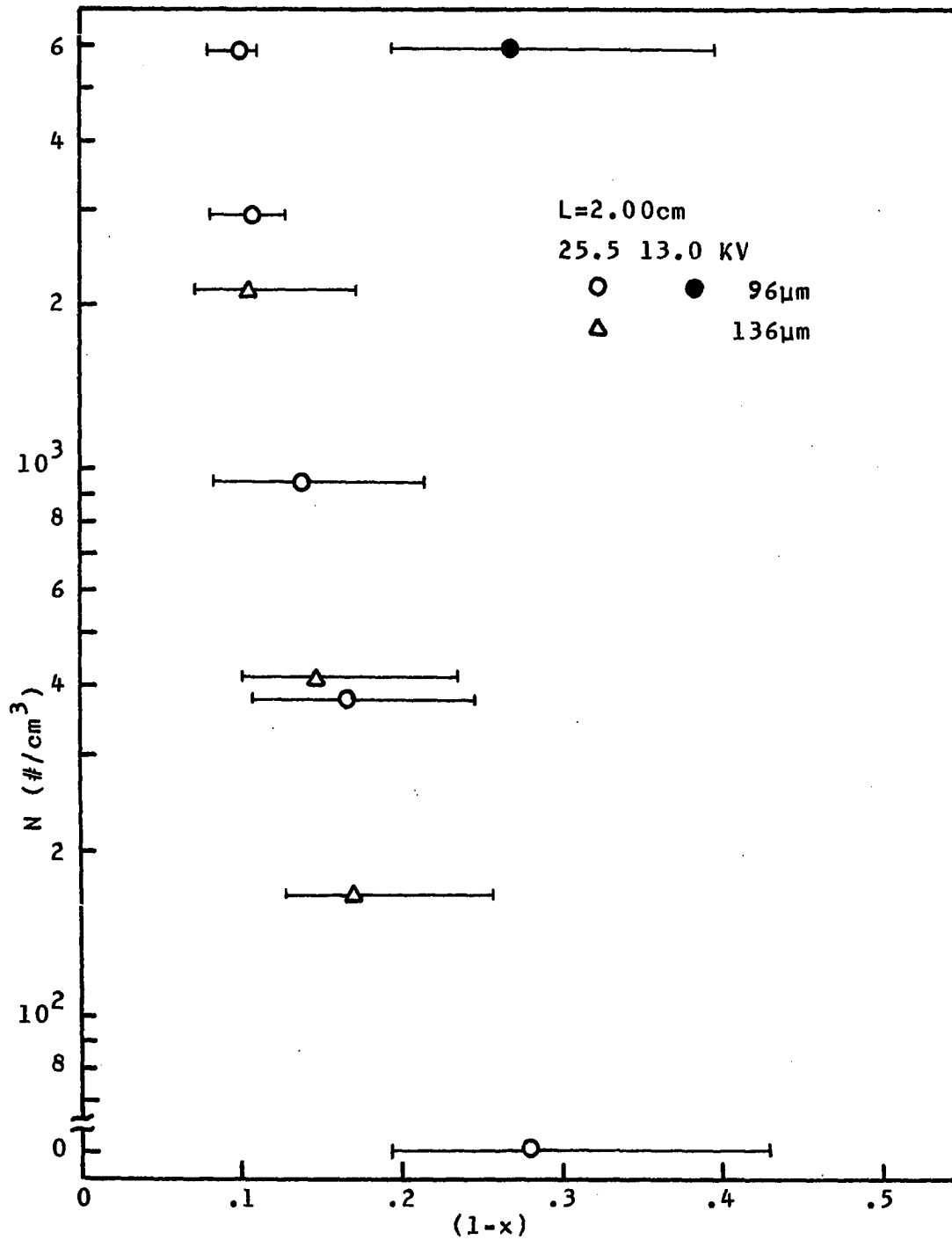


Figure 3.5b. Particle number density vs. average non-dimensional needle penetration distance at breakdown, $L=2.00\text{ cm}$, and $V=13.0, 25.5\ \text{KV}$

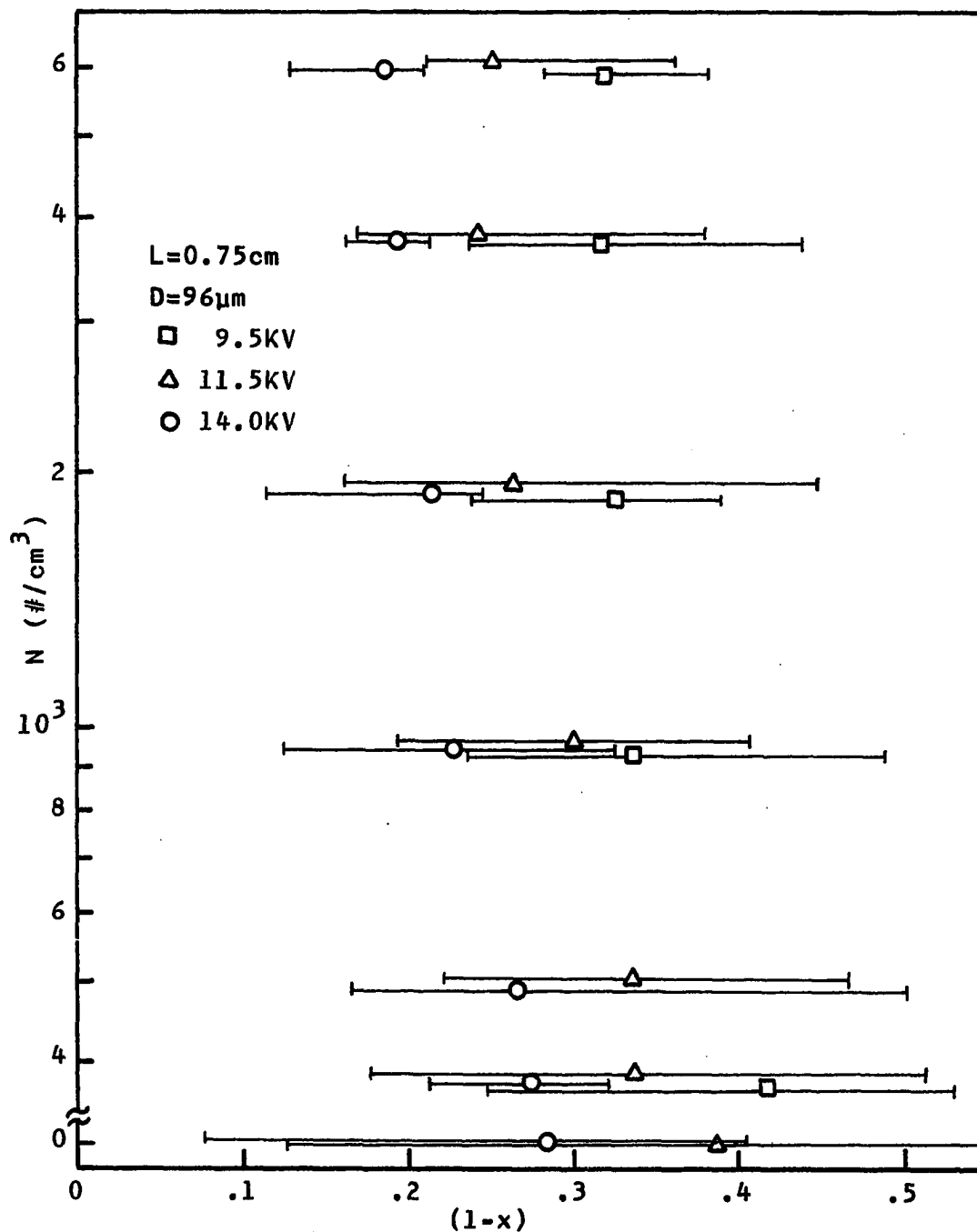


Figure 3.6. Particle number density vs. average non-dimensional needle penetration distance at breakdown, $L=0.75\text{ cm}$, and $V=9.5, 11.5, 14\text{ KV}$

Table 3.1. Variables influencing spark breakdown in particulate suspensions

Variable	Dimension
Applied voltage, V	$ML^2 I^{-1} t^{-3}$
Electric field strength, E_f	$MLI^{-1} t^{-3}$
Parallel electrode gap width, L	L
Needle position at breakdown, L_x	L
Needle velocity, v_n	Lt^{-1}
Gas pressure, P	$ML^{-1} t^{-2}$
Gas dielectric permittivity, ϵ	$M^{-1} L^{-3} I^2 t^4$
Electron (ion) density, n	L^{-3}
Townsend first coefficient, α	L^{-1}
Overall Townsend second coefficient, γ	-
Electron attachment coefficient, η	L^{-1}
Particle number density, N	L^{-3}
Particle diameter, D	L
Particle permittivity, ϵ_p	$M^{-1} L^{-3} I^2 t^4$
Particle charge, Q_p	It
Particle velocity, v_p	Lt^{-1}
Particle mean free path, λ	L
Particle electrical conductivity, σ	$M^{-1} L^{-3} I^2 t^3$
Mass, M	
Length, L	
Current, I	
Time, t	

logarithmic scales, were found to have a linear relationship for various sets of given V , $(1-x)$ and L . Figure 3.7 shows the linear family of lines obtained by a linear regression method. These lines have an average slope of $-1/2.0$. The first correlated parameter was, therefore, taken as

$$ND^2 = A\{V, (1-x), L\} \quad (3.2)$$

When $(1-x) > (1-x)_c$

However, when $(1-x)$ becomes its critical value $(1-x)_c$, $(1-x)$ does not depend on ND^2 (N or D) but on V and L . Using the new parameter ND^2 all data were replotted on Figures 3.8, 3.9, and 3.10, which show that the influence of particle size on the particle number density in breakdown can be reflected in the new parameter ND^2 forming a single characteristic line for each applied voltage and parallel electrode gap width. It is again evident that a transitional ND^2 i.e., $(ND^2)_*$ (like a transitional particle number density N_*), exists where $(1-x)$ becomes constant with increasing ND^2 , N or D . ND_*^2 was estimated from each figure and is shown in Table 3.2.

The critical values of $(1-x)$ were replotted in Figure 3.11 against the applied breakdown voltage from all data when ND^2 was greater than the estimated transitional value. These data lie on one straight line on log-log scales, except

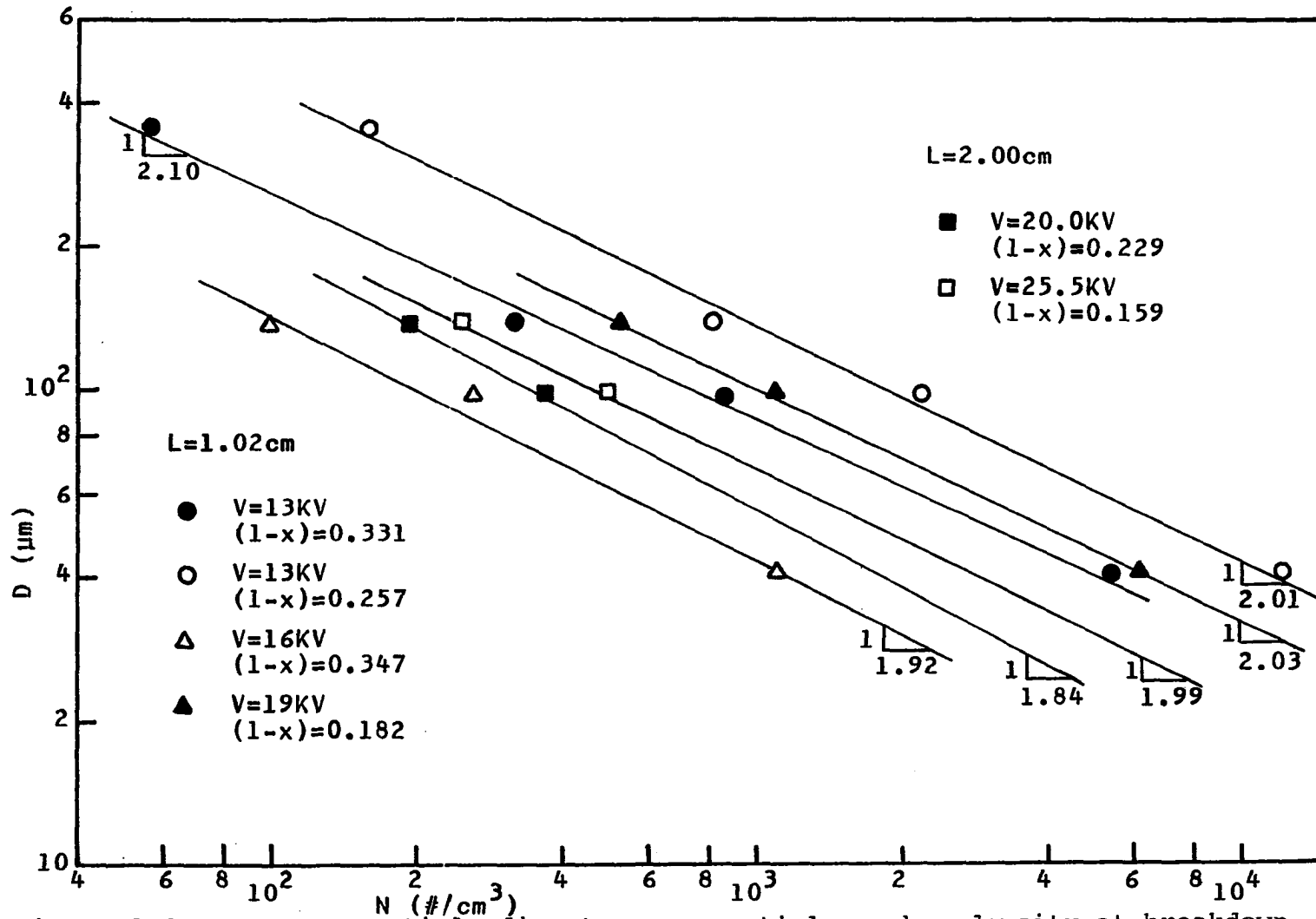


Figure 3.7. Average particle diameter vs. particle number density at breakdown, $(1-x) > (1-x)_c$

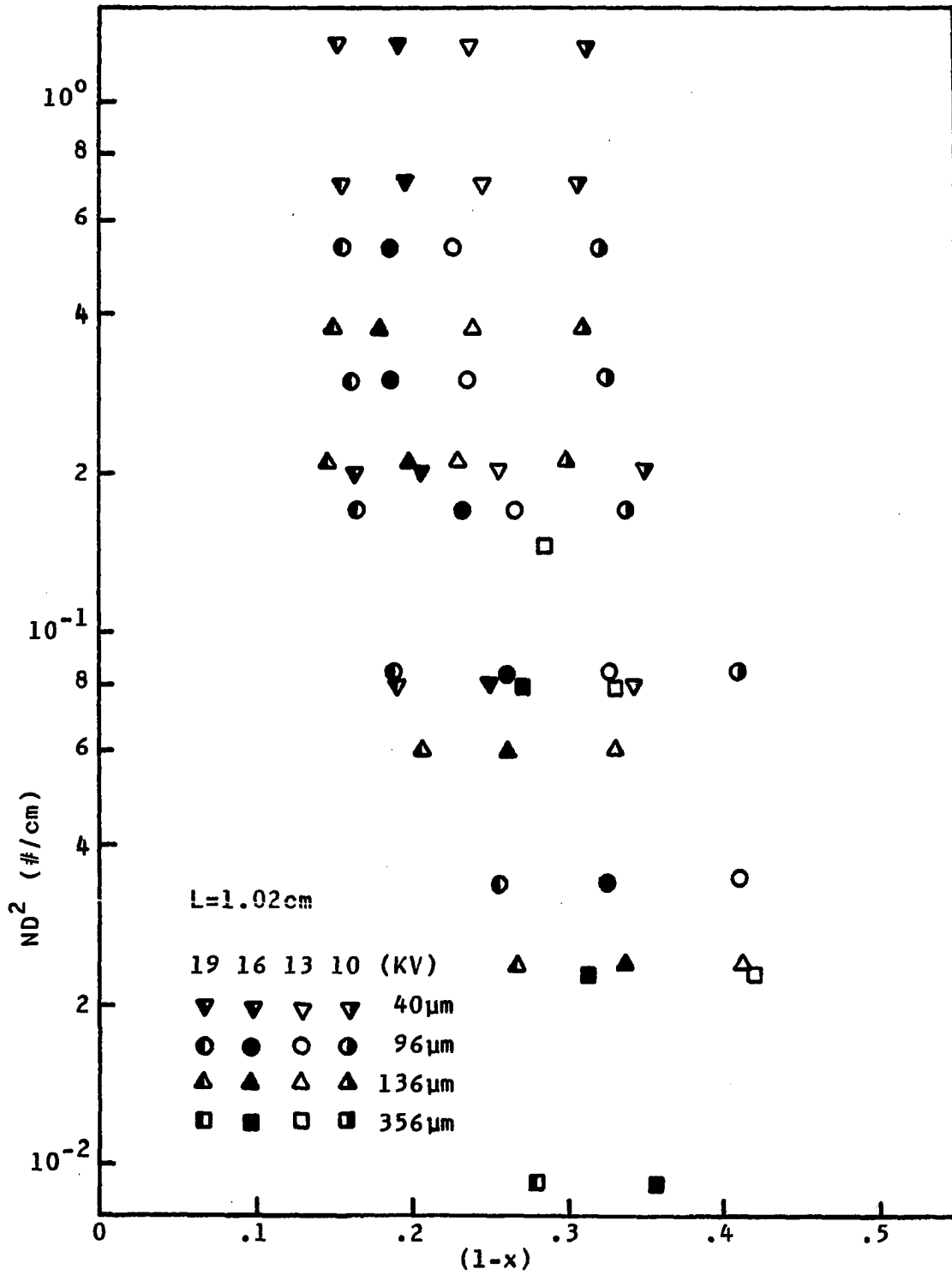


Figure 3.8. Particle mean free path parameter vs. average nondimensional needle penetration distance at breakdown, $L=1.02\text{ cm}$

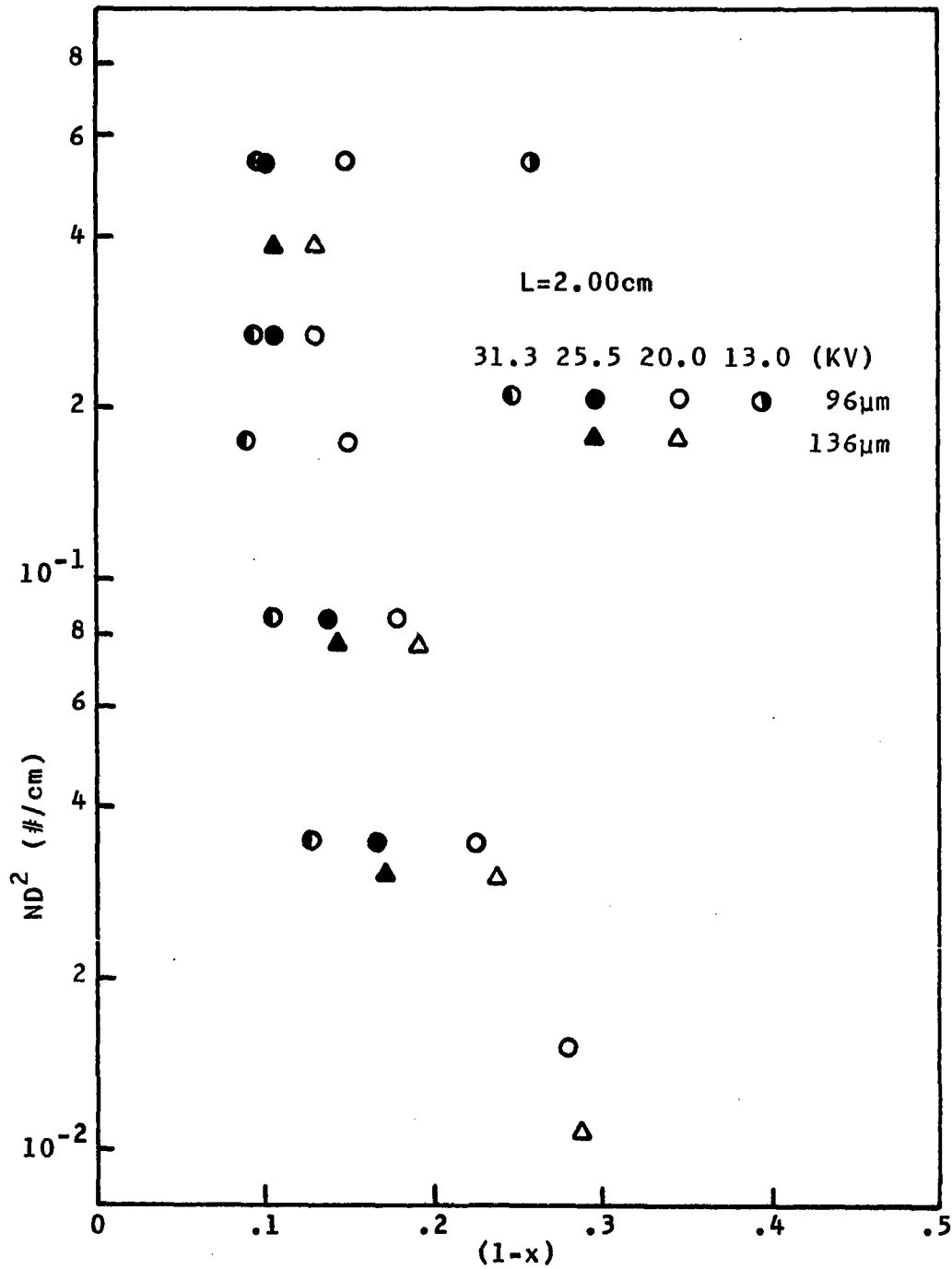


Figure 3.9. Particle mean free path parameter vs. average nondimensional needle penetration distance at breakdown, L=2.00 cm

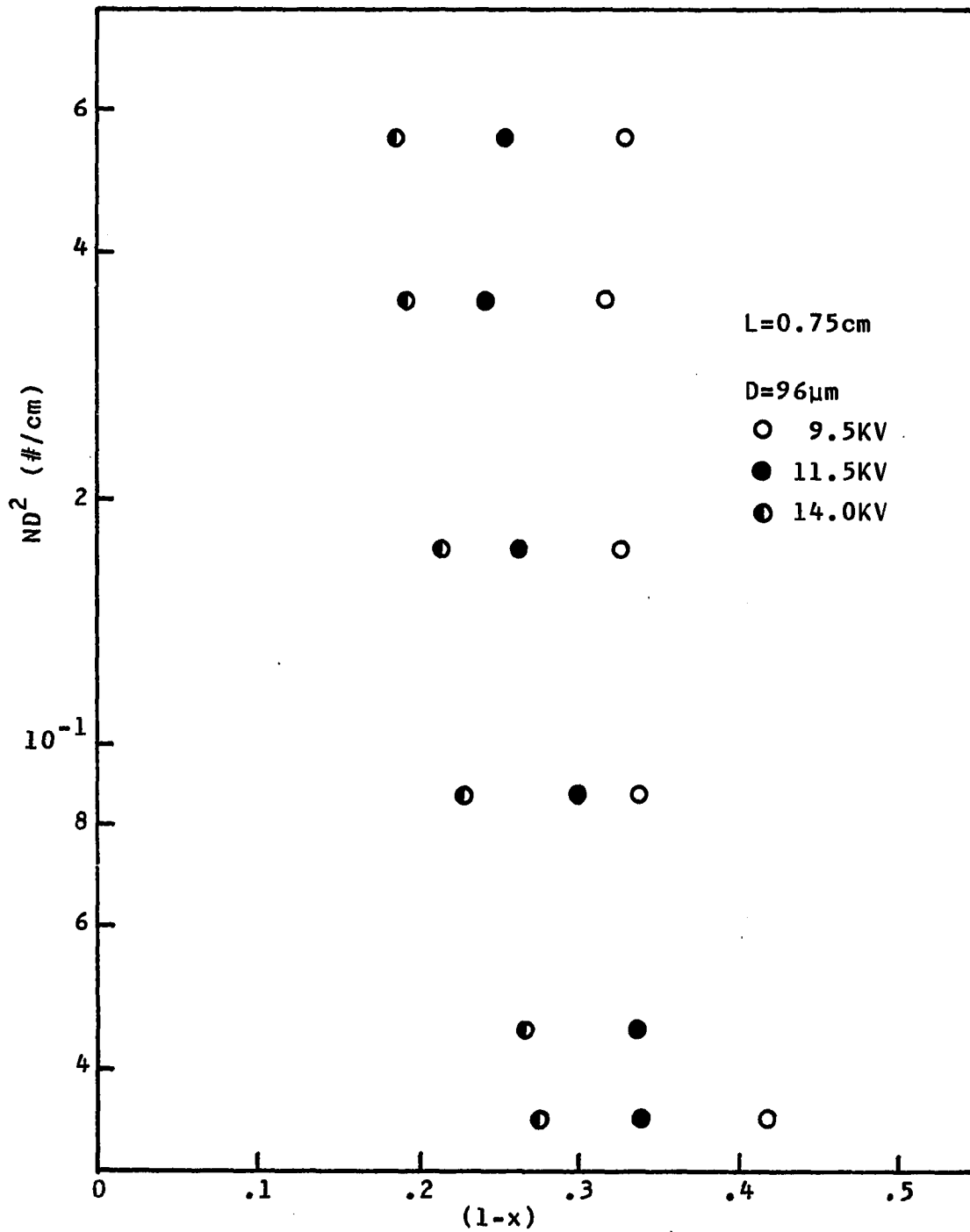


Figure 3.10. Particle mean free path parameter vs. average nondimensional needle penetration distance at breakdown, $L=0.75\text{ cm}$

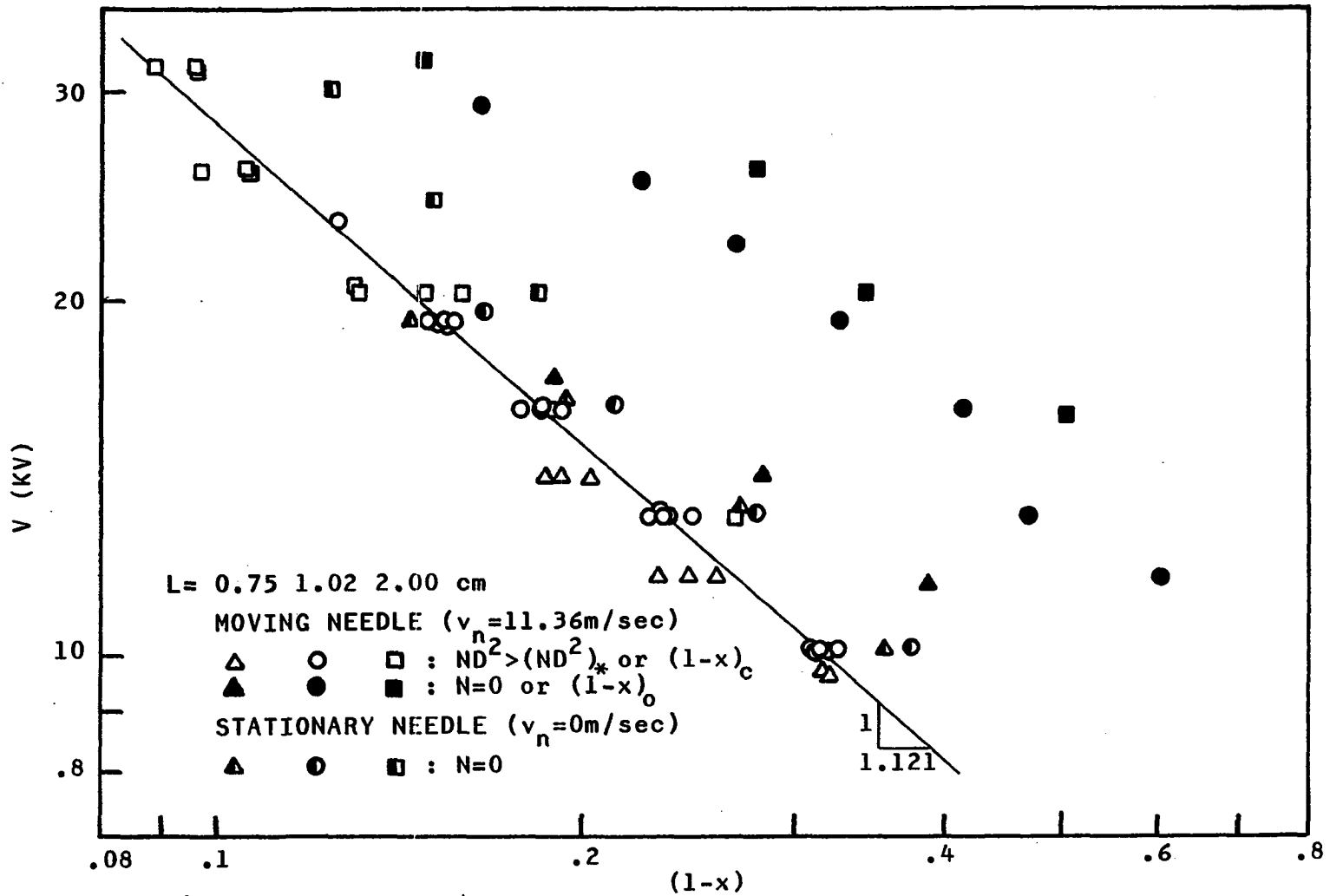


Figure 3.11. Breakdown voltage vs. average nondimensional needle penetration distance ($(1-x)_o$ and $(1-x)_c$)

Table 3.2. Correlation constants

L (cm)	$(ND^2)_*$ (cm ⁻¹) Estimation	λ_* (cm) Calculation	B_o [(KV) ^{1.121}]	B_* [(KV) ^{1.121}]	$\frac{B_*}{B_o} [= (\frac{V_*}{V_o})^{1.121}]$
2.00	0.13	1.731	10.29	4.19	0.407
1.02	0.22	1.023	8.86	4.19	0.473
0.75	0.30	0.750	5.80	3.81	0.657

for 0.75 cm which falls slightly below the line. Similar breakdown data were taken with a moving and stationary positive needle at zero particle number density and are also shown in Figure 3.11 for 3 parallel electrode separation distances. These data again give straight lines parallel with each other as well as being parallel with the line of critical $(1-x)$ (which has a slope of $-1/1.121$). It was then assumed that the effect of adding particles is to move the line of constant ND^2 toward the critical $(1-x)$ line. The equation describing this behavior can be written as

$$(1-x)V^{1.121} = B\{ND^2, L\} \quad (3.3)$$

when $(1-x) > (1-x)_c$ or $ND^2 \leq (ND^2)_*$

When ND^2 is larger than $(ND^2)_*$, since $(1-x)$ becomes only a function of V and L , Equation 3.3 becomes

$$(1-x)V^{1.121} = B_*\{L\} \quad (3.4)$$

The constant B_* obtained from Figure 3.11 is shown in Table 3.2. It should be noted that the slope of $-1/1.121$ is not a valid magnitude when the needle is near the upper or lower electrode.

One additional correlation with L was required in Equation 3.3 to generalize the experimental results. Several attempts were made to correlate the electrode geometric

effect caused by L , but these were not successful. However, the variable B was put into a normalized form according to $(B_0 - B)/(B_0 - B_*)$, where B_0 is for no particles in Equation 3.3. The values of B_0 extrapolated from Figure 3.11 are shown also in Table 3.2. Based on the two variables, $(B_0 - B)/(B_0 - B_*)$ and ND^2 , Figure 3.8, 3.9 and 3.10 could then be transformed into Figure 3.12. However, the breakdown characteristics denoted by ND^2 still showed a dependence on the electrode separation distance L in Figure 3.12.

It is helpful to add some physical interpretation to the meaning of $(ND^2)_*$ through the particle mean free path λ . For random particle motion, this is (Kennard [104])

$$\lambda = \frac{1}{\sqrt{2}\pi ND^2} \quad (3.5)$$

The calculated λ_* (using $(ND^2)_*$) is compared with L in Table 3.2 and the agreement is striking. An alternative interpretation to $(ND^2)_*$ is through the average particle separation distance given as

$$s = N^{-1/3} \quad (3.6)$$

A characteristic length of the suspension is then

$$L_s = s^3/D^2 = 1/ND^2 \quad (3.7)$$

If it is assumed that the breakdown is initiated from or to the needle tip, the collision condition of the

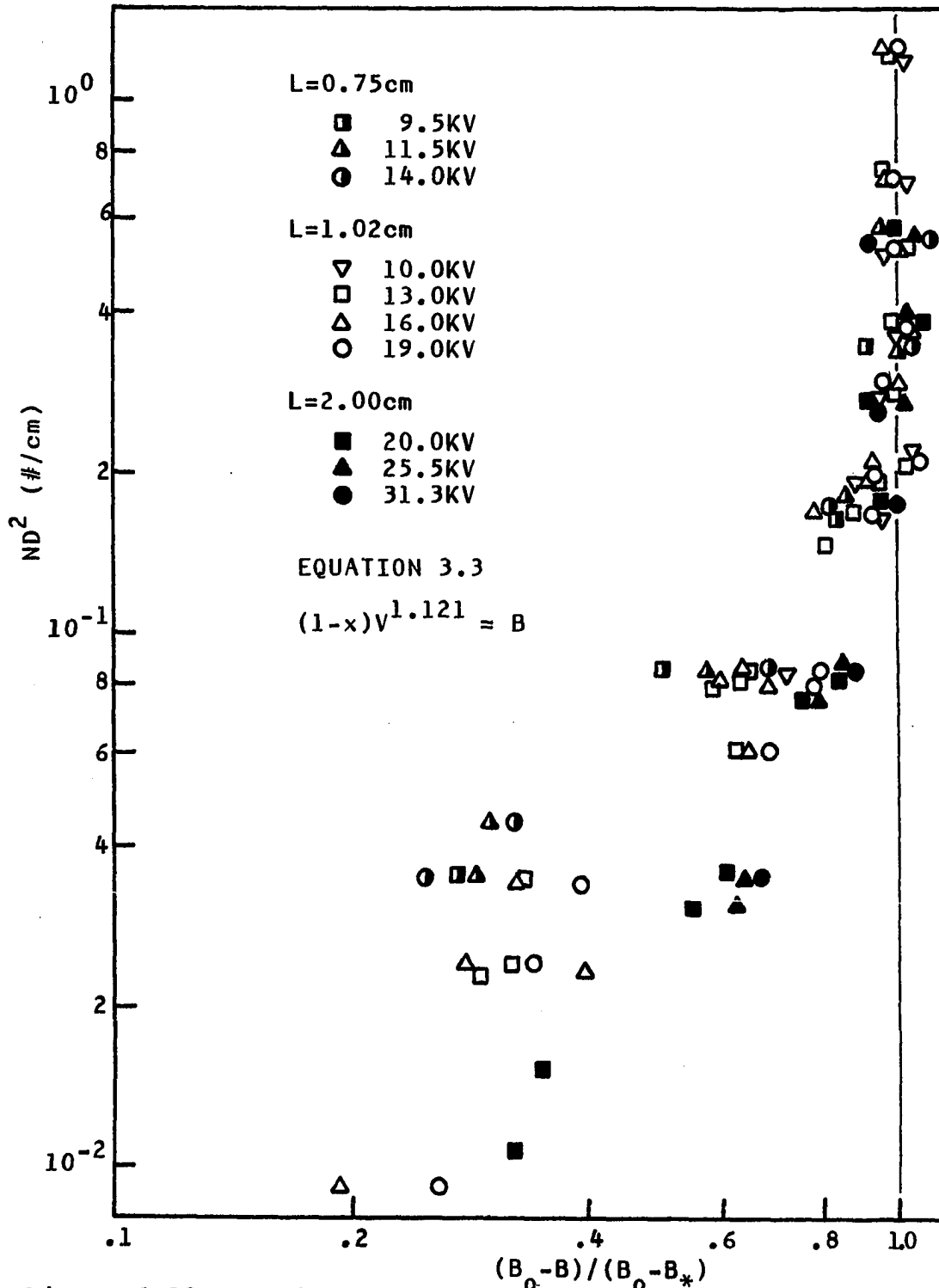


Figure 3.12. Particle mean free path parameter vs. normalized breakdown voltage with needle position

particulate cloud near the tip, which is determined by L_x/L_p , is believed to be an important parameter of the breakdown triggering mechanism. Here, L_p is the average effective particle collision distance of the present system. This distance can be calculated as the volume of a hemisphere of λ radius divided by its bottom area. This gives $\frac{2}{3}\lambda$, which has been rigorously derived by integration over all angles as given by Kennard [104]. Therefore, the average distance L_p becomes

$$L_p = \frac{2}{3}\lambda = \frac{2}{3\sqrt{2}\pi ND^2} \quad (3.8)$$

Using the ratio of the breakdown needle position and the average effective collision distance L_x/L_p and the normalized variable $(B_o - B)/(B_o - B_*)$, Figure 3.12 was again replotted as Figure 3.13 using logarithmic scales. A reduction in the data scatter is the result of Figure 3.13 with two trends for all of the averaged data now emerging $L_x/L_p \lesseqgtr 1.0$. According to this correlation, Equation 3.3 can be rewritten as a function of L_x/L_p , that is

$$\frac{B_o - B}{B_o - B_*} = C\left\{\frac{L_x}{L_p}\right\} \quad (3.9)$$

where $B = (1-x)V^{1.121}$ (Equation 3.3). Therefore, the line of slope $-1/1.121$ considered in Figure 3.11 can be interpreted

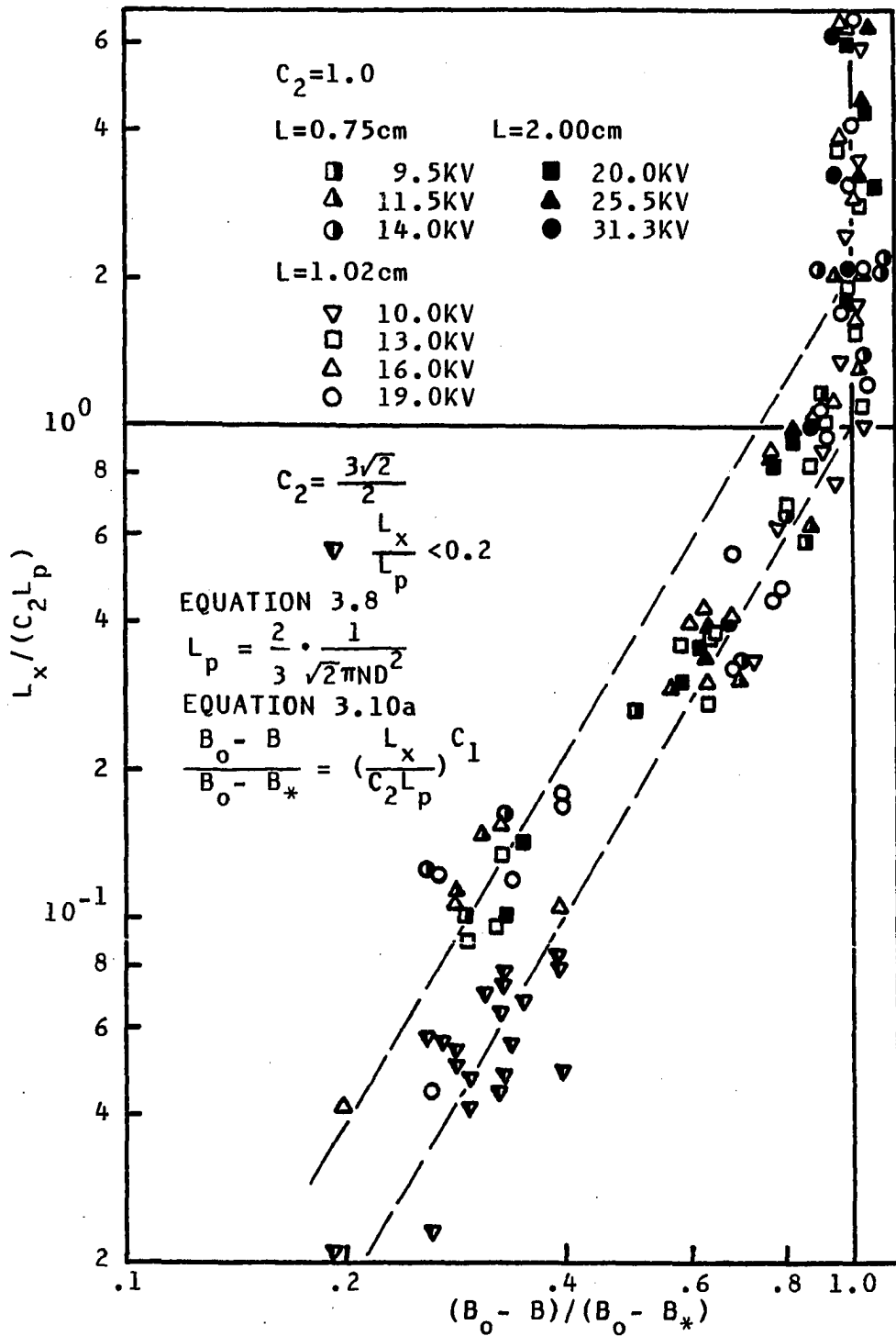


Figure 3.13. Particle collision parameter at breakdown needle position vs. normalized breakdown voltage with needle position

to represent constant L_x/L_p instead of ND^2 at a given L . If a straight line starting from $L_x/L_p = 1.0$ is visually adjusted to the data in Figure 3.13 for $0.2 \leq L_x/L_p \leq 1.0$, the resulting equation can be written as

$$\frac{B_o - B}{B_o - B_*} = \left(\frac{L_x}{C_2 L_p} \right)^{C_1} \quad (3.10a)$$

with the constant $C_1 = 0.4$ and $C_2 = 1.0$. Using linear regression for the same data¹ gives $C_1 = 0.44$, $C_2 = 1.02$, and $r = 0.86$ for the correlation coefficient. When $\frac{L_x}{L_p} < 0.2$, if a shifted line starting at $\frac{L_x}{L_p} = \frac{3\sqrt{2}}{2}$ is assumed for correlation purposes, Equation 3.10a can be used with the constants $C_1 = 0.4$ and $C_2 = \frac{3\sqrt{2}}{2}$. With the constant $C_1 = 0$, Equation 3.10a can be extended to include the region where $L_x/L_p > 1.0$ (linear regression also shows that $C_1 = 0.000$, $C_2 = 1.000$ and $r = 0.997$).

Therefore, all experimental results can be correlated reasonably well by Equation 3.10a or the following equation:

$$V = (1-x)^{-0.892} [B_o - (B_o - B_*) \left(\frac{L_x}{C_2 L_p} \right)^{C_1}]^{0.892} \quad (3.10b)$$

where

$$\frac{L_x}{C_2 L_p} = \frac{3\sqrt{2}}{2C_2} \pi ND^2 L_x$$

¹For the combined data, $L_x/L_p \leq 1.0$, $C_1 = 0.39$, $C_2 = 1.08$ and $r = 0.972$.

with

$$\begin{aligned}
 c_1 = 0 \quad \text{and} \quad c_2 = 1.0, & \quad \frac{L_x}{L_p} > 1.0 \\
 c_1 = 0.4 \quad \text{and} \quad c_2 = 1.0, & \quad 0.2 \leq \frac{L_x}{L_p} \leq 1.0 \\
 c_1 = 0.4 \quad \text{and} \quad c_2 = \frac{3\sqrt{2}}{2}, & \quad \frac{L_x}{L_p} < 0.2
 \end{aligned}$$

When $\frac{L_x}{L_p} = 1.0$, the transitional $(ND^2)_*$ can be expressed by

$$(ND^2)_* = \frac{2}{3} \frac{1}{\sqrt{2}\pi L_{xc}} \quad (3.11)$$

This result, Equation 3.10, is recommended in the present study for numerical calculations because of its improved accuracy in the region of low ND^2 ($L_x/L_p < 0.2$). An alternative correlation will be considered which emphasizes the particle collision probability effect.

Equation 3.10 shows that the breakdown characteristics of particulate clouds such as the breakdown voltage V and the average breakdown needle penetration distance $L(1-x)$ can be related to the particle collision dynamics as determined by the ratio L_x/L_p (when the constants B_0 and B_* are given). An alternative interpretation for breakdown involving the particle spacing can also be given using Equation 3.7.

Cotroneo and Colver [99] discussed the mode of particle charge loss due to particle collisions and proposed approximately the dependence of charge loss on the particle

mean free path and the particle moving distance from the bottom electrode, i.e., $\pi ND^2 L_x$ (see Appendix A). However, their numerical result was based on one dimensional collisions in the direction of the applied field at a low particle number density (about $1 \sim 10 \text{ \#/cm}^3$), so that the random factor $\frac{1}{\sqrt{2}}$ for the mean free path and $\frac{2}{3}$ for the average effective collision distance did not appear in their expression. Colver and Howell [100] and Colver [101] point out that in fact, this random factor varies from 1 to $1/\sqrt{2}$, depending on the particle number density.

Therefore, if the coefficient $\frac{3\sqrt{2}}{2C_2}$ in the final correlation is considered as the degree of randomness, when $L_x/L_p < 0.2$, the coefficient becomes 1.0 so that average particles seem to interact in a one-dimensional manner perpendicular to the parallel electrodes. But, when $0.2 \leq L_x/L_p \leq 1.0$, since $C_2 = 1.0$, it is probable that particles are moving randomly. These three separate regions in Figure 3.13 (or of Equation 3.10) seem to correspond with the three regions in the calibration curves of current-particle number density in Figures 2.6a and 2.6b ($N = 0 \rightarrow 0.6 \sim 0.7 \rightarrow 1.95 \sim 2.40 \rightarrow \sim 7.5 \times 10^3 \text{ \#/cm}^3$ or $L/L_p = 0 \rightarrow 0.37 \sim 0.47 \rightarrow 1.2 \sim 1.6 \rightarrow 5.1$, for 96 \mu m particles).

If the above point of view of explaining the discontinuities is correct, the transitions around $L_x/L_p \approx 0.2$

and 1.0 seem to arise, at least in part, from the characteristics of the present system in which particles are charged and are moving so as to undergo collision.

Another way of handling the experimental data for ND^2 is to assume a correlation in the form $1 - \exp(-\frac{L_x}{C_2 L_p})$ and $\frac{B_o - B}{B_o - B_*}$. This is shown in Figure 3.14 and compared with Equation 3.10. Assuming three straight lines from the figure, the correlation can be expressed by

$$\frac{B_o - B}{B_o - B_*} = C_3 [1 - \exp(-\frac{L_x}{C_2 L_p})] + C_4 \quad (3.12)$$

where $B = (1-x)v^{1.121}$ and

$$\frac{L_x}{C_2 L_p} = \frac{3\sqrt{2}}{2C_2} \pi ND^2 L_x$$

with

$$C_3=0, \quad C_4=1.0 \text{ and } C_2=1.0, \quad \frac{L_x}{L_p} > 1.0$$

$$C_3=1.0, \quad C_4=0.37 \text{ (or } e^{-1}) \text{ and } C_2=1.0, \quad 0.2 \leq \frac{L_x}{L_p} \leq 1.0$$

$$C_3=5.32, \quad C_4=0 \text{ and } C_2=\frac{3\sqrt{2}}{2}, \quad \frac{L_x}{L_p} < 0.2$$

Although, in this correlation, there is at present no way to confirm the value of C_2 when $L_x/L_p < 0.2$, $C_2 = \frac{3\sqrt{2}}{2}$ was chosen, since the particle motion could be expected to be one-dimensional near $L_x/L_p \sim 0$ as discussed in references [99], [100], and [101].

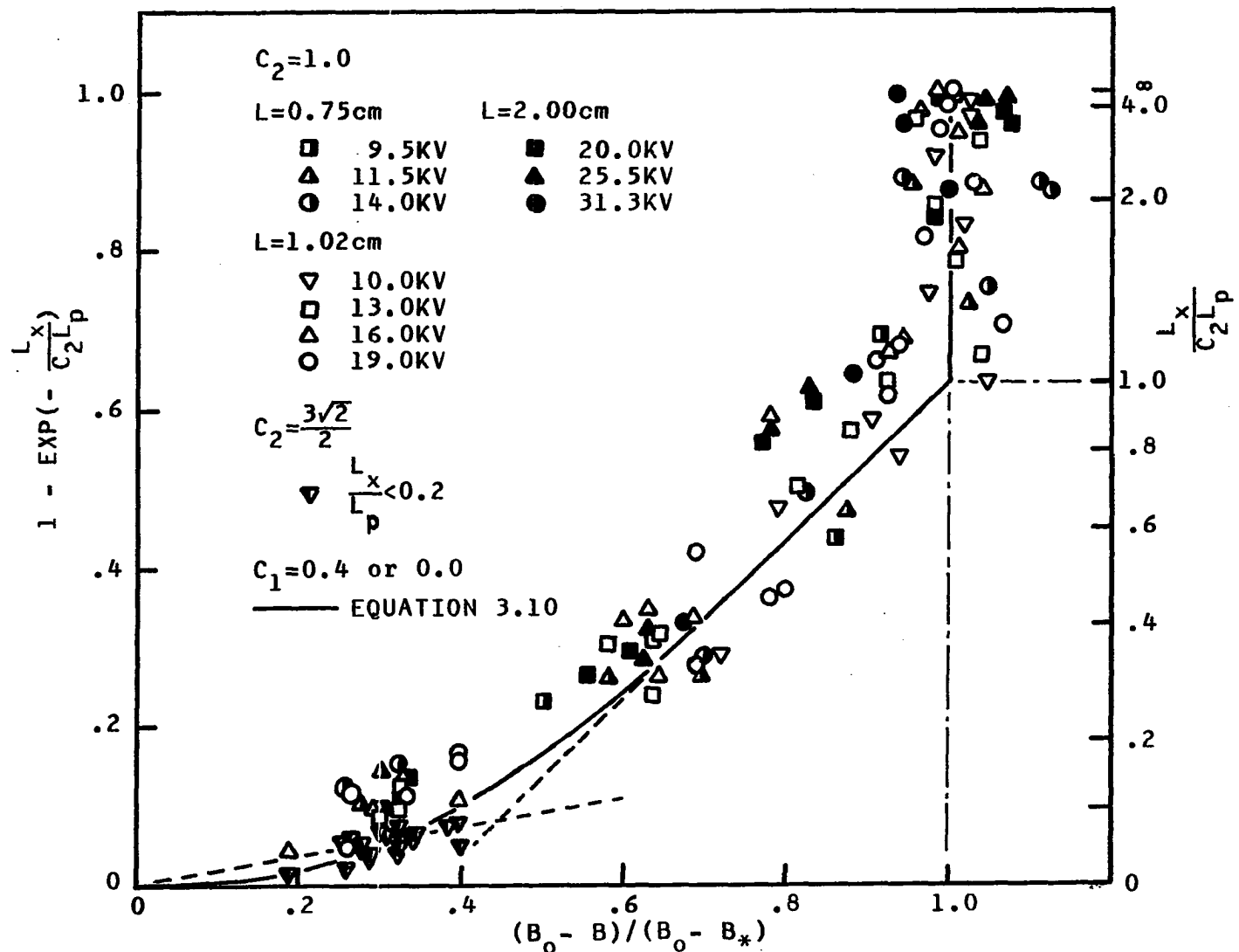


Figure 3.14. Particle collision probability vs. normalized breakdown voltage with needle position

This final correlation is interesting since $1 - \exp(-\frac{L_x}{C_2 L_p})$ is the probability that a particle will undergo a collision with another particle in traveling a distance L_x normal to the electrode (Soo [105]). As noted previously, Equation 3.10 is recommended over Equation 3.11 for purposes of numerical calculations because of improved accuracy at low ND^2 .

From the above analysis, it follows that the observed electrical breakdown behavior of a particulate cloud can be explained in terms of two parameters, $B (= (1-x)V^{1.121})$ and $L_x/C_2 L_p (= \frac{3\sqrt{2}}{2C_2} ND^2 L_x)$, which represent the breakdown characteristics of the present electrode system and the particle collision characteristics, respectively.

Also, it appears that the breakdown behavior is not influenced directly by the particle or the needle motion since the breakdown occurs over times that are much smaller than any characteristic event times associated with their motions. Rather, breakdown is determined by the simultaneous event probabilities of a negative particle-positive particle discharge in the region of the needle tip or a negative particle-positive needle discharge. The possibility of such a micro-discharge followed by a main discharge may depend on the particle charge magnitude (i.e., in average, the particle charge density per unit volume of clouds) near

the needle electrode tip which is determined by the particle collision process.

The effect of particle charge on the breakdown voltage was discussed by Anis and Srivastava [36], who computed its effect using their theoretical model for a spherical aluminum particle of 1 mm radius between coaxial electrodes at 1 atm in SF₆. They observed that an increase in the amount of charge from 1.57×10^{-10} C to $5 \times 1.57 \times 10^{-10}$ C led to a decrease in the breakdown voltage from 300 KV to 260 KV.

From the final correlation of Equation 3.12, it appears that when $L_x/L_p \leq 1.0$, the breakdown voltage V or the breakdown needle penetration distance $(1-x)$ increases with a decrease in the collision probability, such that the decreasing breakdown effect of the particles is compensated for an increasing field strength (V/L_x) effect at the tip. When $L_x/L_p > 1.0$, an increase of L_x/L_p is not affecting either V or $(1-x)$. Thus, $(1-x)$ remains constant at its critical value and becomes only a function of V or L (the electrode system). One possible explanation is that in this region the effect of increasing particle number density (and collision probability) may be counterbalanced by the decreasing influence of the particles themselves (because of charge loss).

Furthermore, for a fixed $(1-x)$, Equation 3.12 can be rewritten as

$$\frac{1 - \left(\frac{V}{V_0}\right)^{1.121}}{1 - \left(\frac{V_*}{V_0}\right)^{1.121}} = C_3 \left[1 - \exp\left(-\frac{Lx}{C_2 L_p}\right)\right] + C_4 \quad (3.13)$$

where V_0 is the breakdown voltage in a particle-free gap and V_* is the minimum possible breakdown voltage in a particulate cloud gap for the specified $(1-x)$. The constant $(V_*/V_0)^{1.121}$ is given in Table 3.2. It has not been tested experimentally that either V_0 , V_* , C_3 , or C_4 depends on electrode geometry, voltage history or needle velocity. However, this equation may be applied for stationary cases. For example, if a uniform particulate cloud identical to the present parallel electrode suspension is assumed with a stationary needle, the normalized breakdown voltage (left side of Equation 3.13) should be determined by the particle collision probability alone (right side of Equation 3.13) and this is in turn independent of the needle velocity. For a uniform electric field, the collision probability $\left[1 - \exp\left(-\frac{L}{C_2 L_p}\right)\right]$ is also expected to play an important role in the breakdown process.

It should be noted that the breakdown with a moving needle without particles is delayed about 10^{-3} to 10^{-4} seconds, probably as a result of a statistical time lag¹,

¹The statistical time lag in the present study differs from that more generally used with a time independent field strength [10] in that the electric field at the needle tip is monotonically increasing with time.

after the needle passes the breakdown position of a stationary needle. It then follows that the decrease of $(1-x)$ with an increase of the particle number density at the same applied voltage corresponds to a decrease in the breakdown delay time.

Wootton et al. [30] conclude, based on their experiment of measurements, that particle initiated breakdown results when the simultaneous requirements of breakdown are met such as, the critical distance between a particle and electrode, the presence of initiatory electrons and the particle orientation. They further conclude that the presence of any other particles has no effect on the minimum breakdown voltage but acts to increase the probability factor effect and to shorten the statistical time lag.

The average decrease in the breakdown time due to the presence of the particles, as measured from the time of breakdown in a particle free gap by the moving needle, can be calculated according to

$$\tau = \frac{L}{v_n} [(1-x) - (1-x)_0] \quad (3.14)$$

with the needle velocity v_n being about 11.36 m/sec and with $(1-x)_0 = B_0 V^{-1.121}$. This decrease in τ will be assigned a minus sign. By applying Equation 3.12 into the above equation, the decrease time τ is then

$$\tau = - \frac{L}{v_n} [(1-x)_o - (1-x)_c] \{ C_3 [1 - \exp(-\frac{Lx}{C_2 L_p})] + C_4 \} \quad (3.15)$$

It is interesting to see that τ is the maximum decreased delay time multiplied by the term related with the particle collision probability, as in Equation 3.12.

3. Probability

The cumulative positional breakdown distribution (cumulative fraction of breakdowns versus $(1-x_i)/(1-x)$), given by the normalized total number of experimentally determined breakdowns (at constant voltage and electrode gap distance) for a nondimensional breakdown needle penetration position smaller than $(1-x_i)$, are shown in Figures 3.1 through 3.17, where the arithmetic average is $(1-x)$.

Figure 3.15a shows the data points of 4 different voltages with the particle-free gap of 1.02 cm. There is not a significant deviation for the different voltages. In fact, a single trend line is apparent between $(1-x_i)/(1-x) = 0.6$ and 1.4 passing through 1.0 at a 0.5 cumulative fraction of breakdowns (i.e., 50% needle position probability of breakdown occurrence). Similar curves for $L = 2.00$ and 0.75 cm are shown and compared with the curve for $L = 1.02$ cm in Figure 3.15b. The slope of $(1-x_i)/(1-x)$ becomes steeper as the gap width decreases.

Breakdown data taken with particulate clouds at

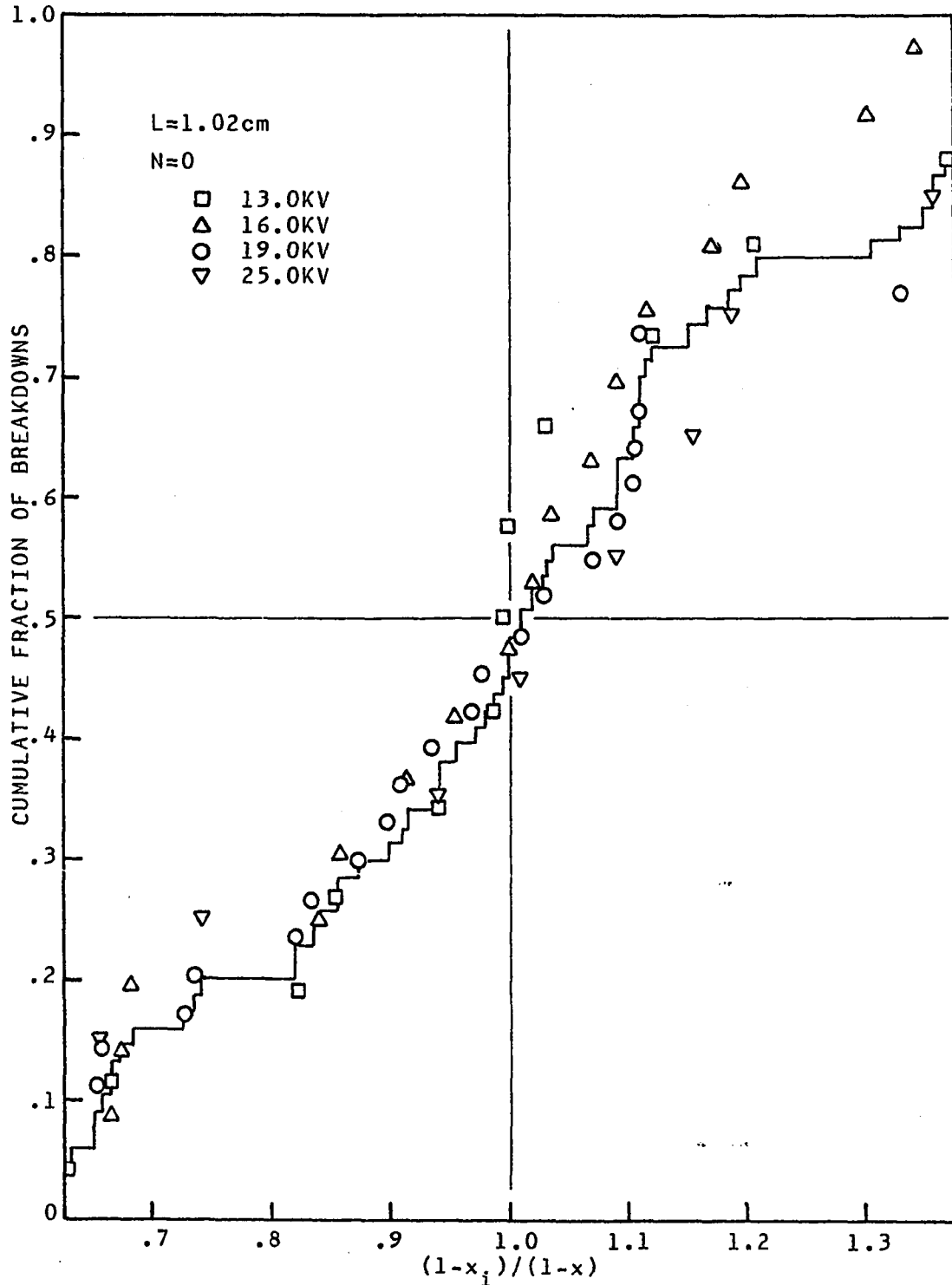


Figure 3.15a. Cumulative positional breakdown distribution, $L=1.02\text{ cm}$ when $N=0$

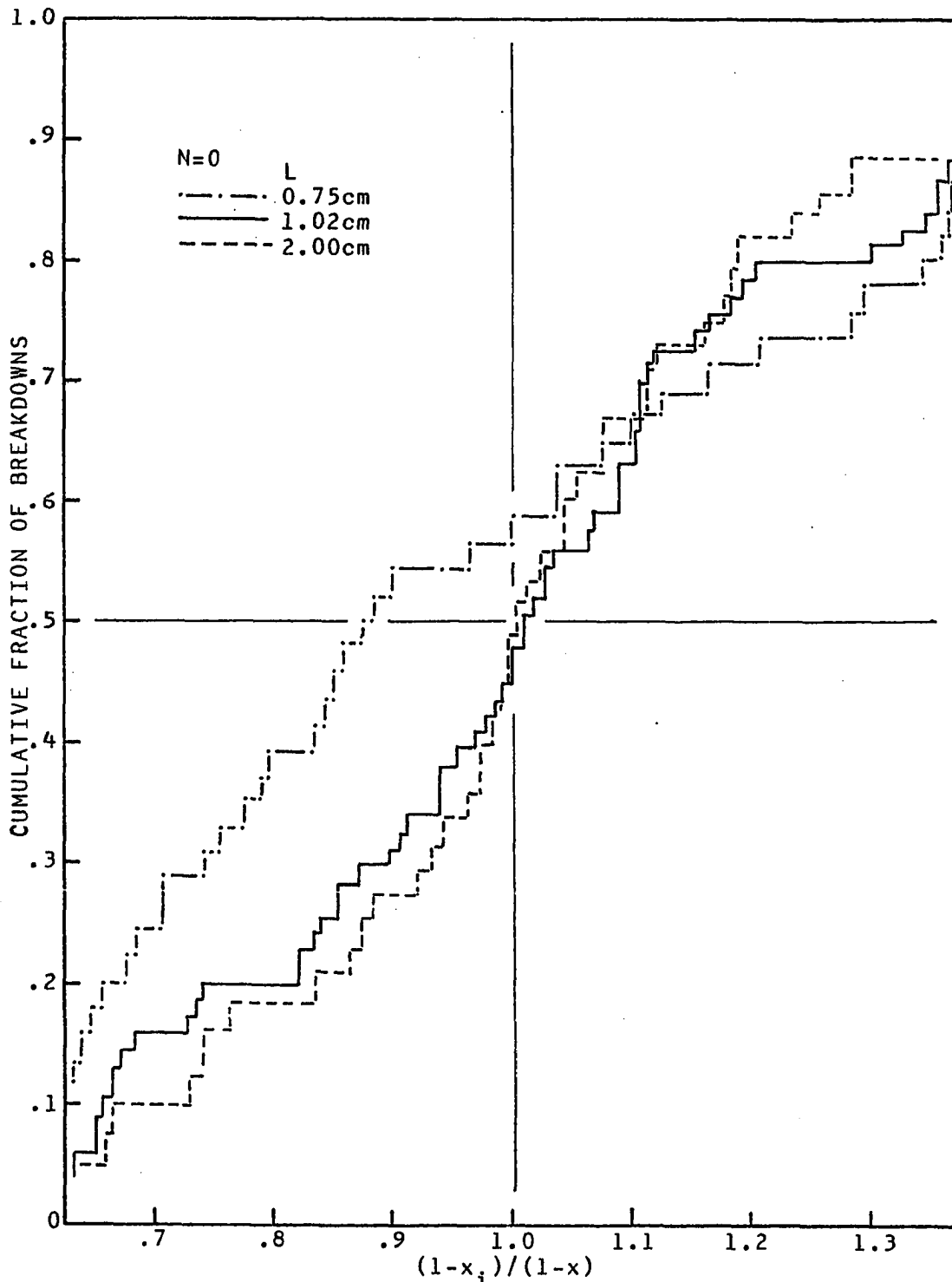


Figure 3.15b. Cumulative positional breakdown distribution,
 $L=0.75, 1.02, 2.00$ cm when $N=0$

$L = 1.02$ cm, $D = 40$ μm and $ND^2 > (ND^2)_*$ show also a single trend line in Figure 3.16a, which does not depend on either the voltage or the particle number density and has its average near 0.5. Similar results were also found for the larger sizes of particles (96 and 136 μm diameter). These results are compared with those of a particle free gap at the same separation distance in Figure 3.16b. The comparison indicates a negligible broadening of the distribution when the particle size is increased and a significant broadening of the distribution when particles are removed. Thus, it is quite certain that the presence of a particulate cloud makes the experimental distribution range of $(1-x_i)$ narrow, in addition, it causes the average $(1-x)$ itself to decrease.

When ND^2 is smaller than $(ND^2)_*$, it is expected that the distribution should lie between the above two extremes. This is shown in Figures 3.17a-c.

When $(1-x_i)$ is related with the time lag, the exponential relationship (Equation 1.12) found by Tilles [25] and Zuber [23] between the cumulative fraction of breakdowns and the statistical time lag is not observed. This may be a result of different experimental conditions such as the presence of particulate clouds, a time increasing field strength, or the affect of field nonuniformity.

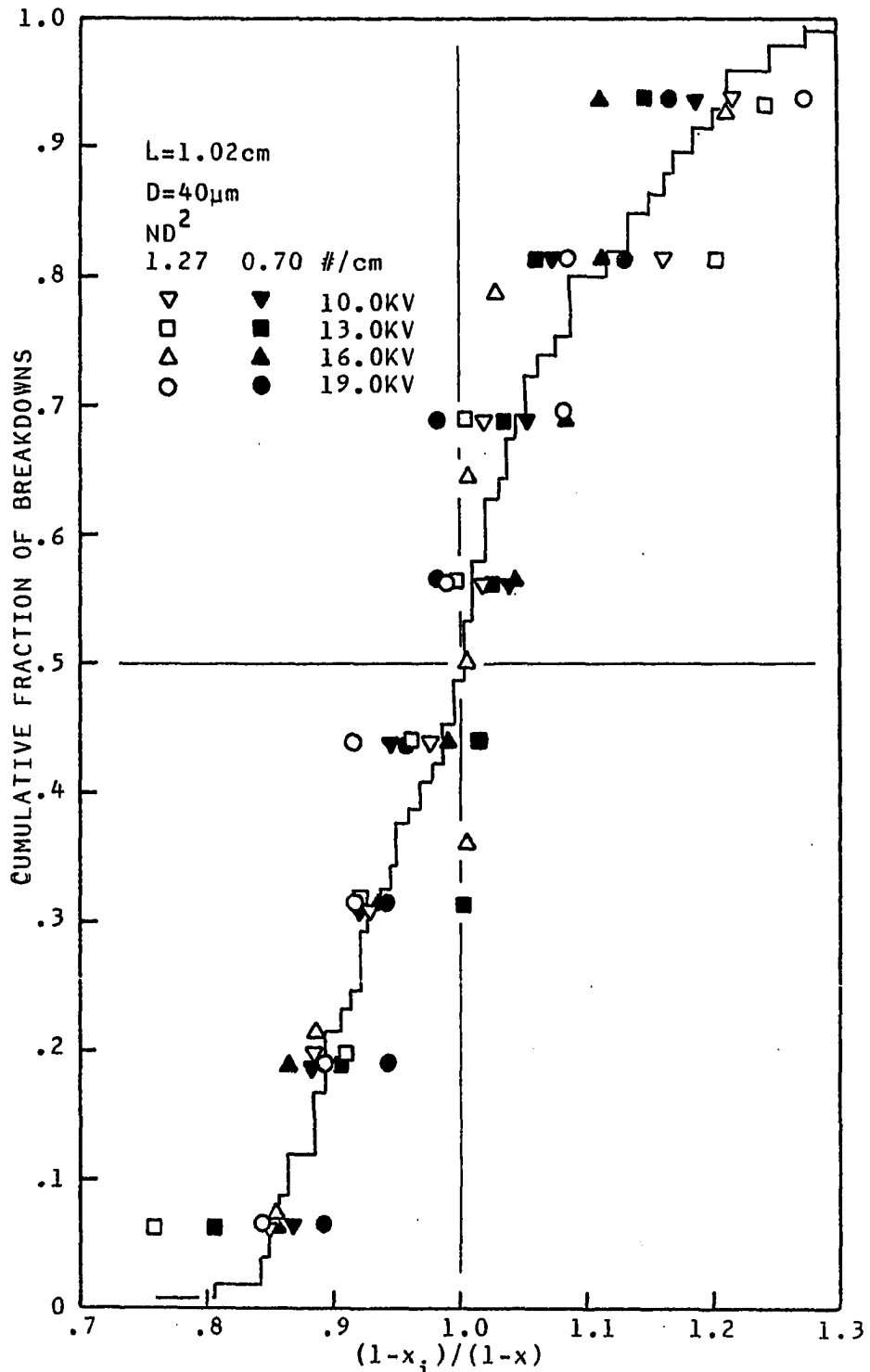


Figure 3.16a. Cumulative positional breakdown distribution, $L=1.02\text{ cm}$ when $ND^2 > (ND^2)_*$

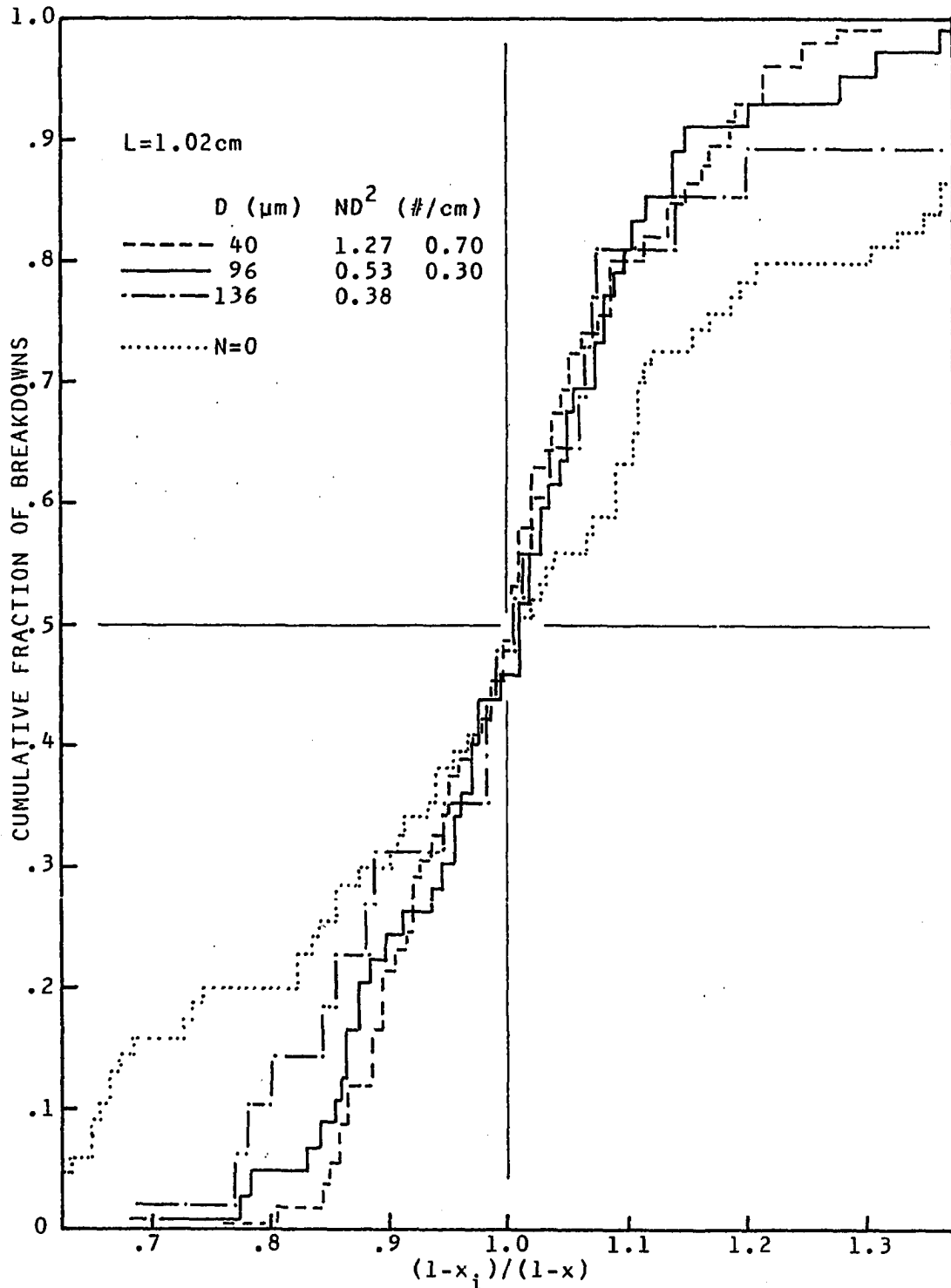


Figure 3.16b. Cumulative positional breakdown distribution, $L=1.02$ cm when $ND^2 > (ND^2)_*$

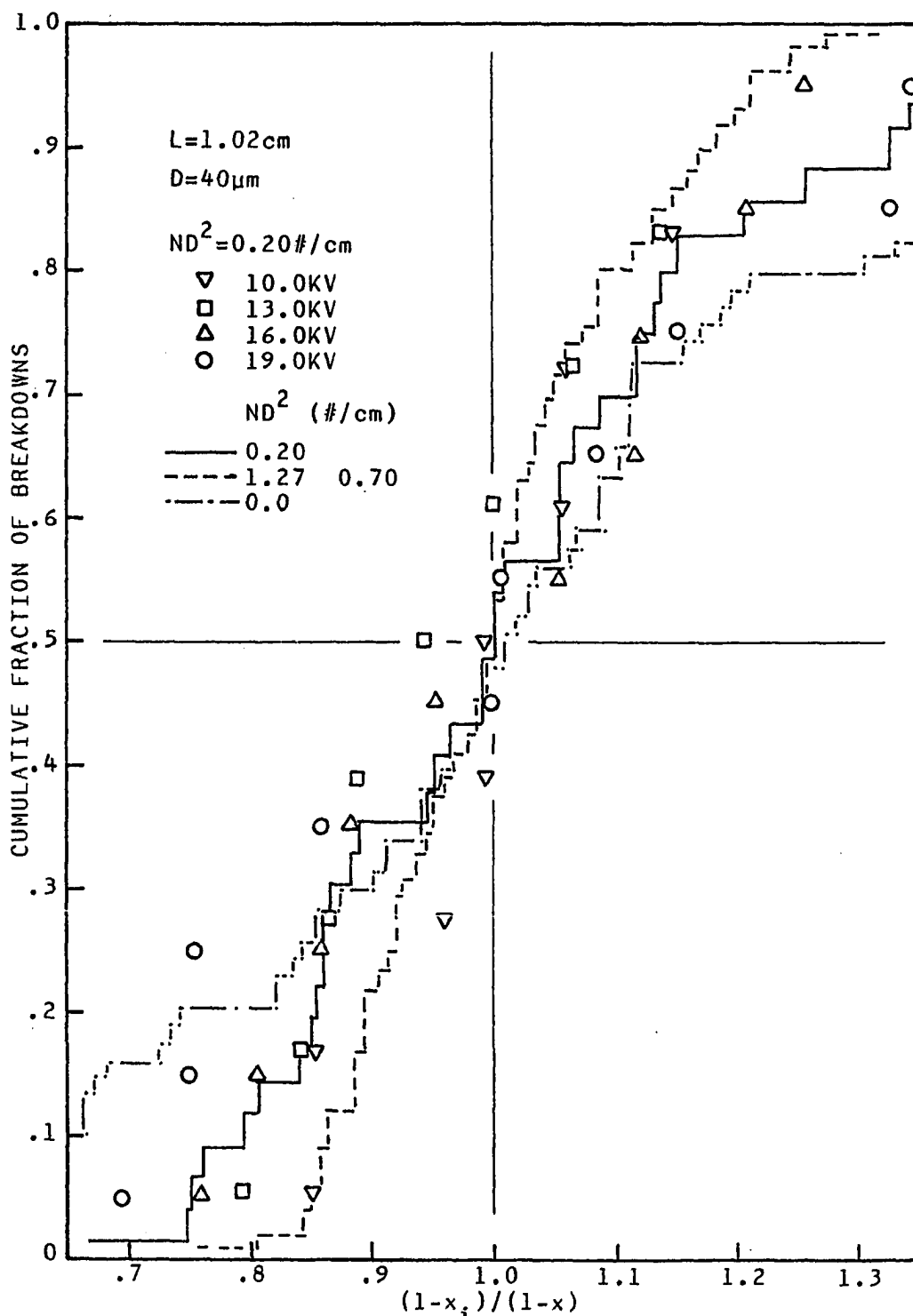


Figure 3.17a. Cumulative positional breakdown distribution, $L=1.02$ cm when $ND^2 < (ND^2)_*$

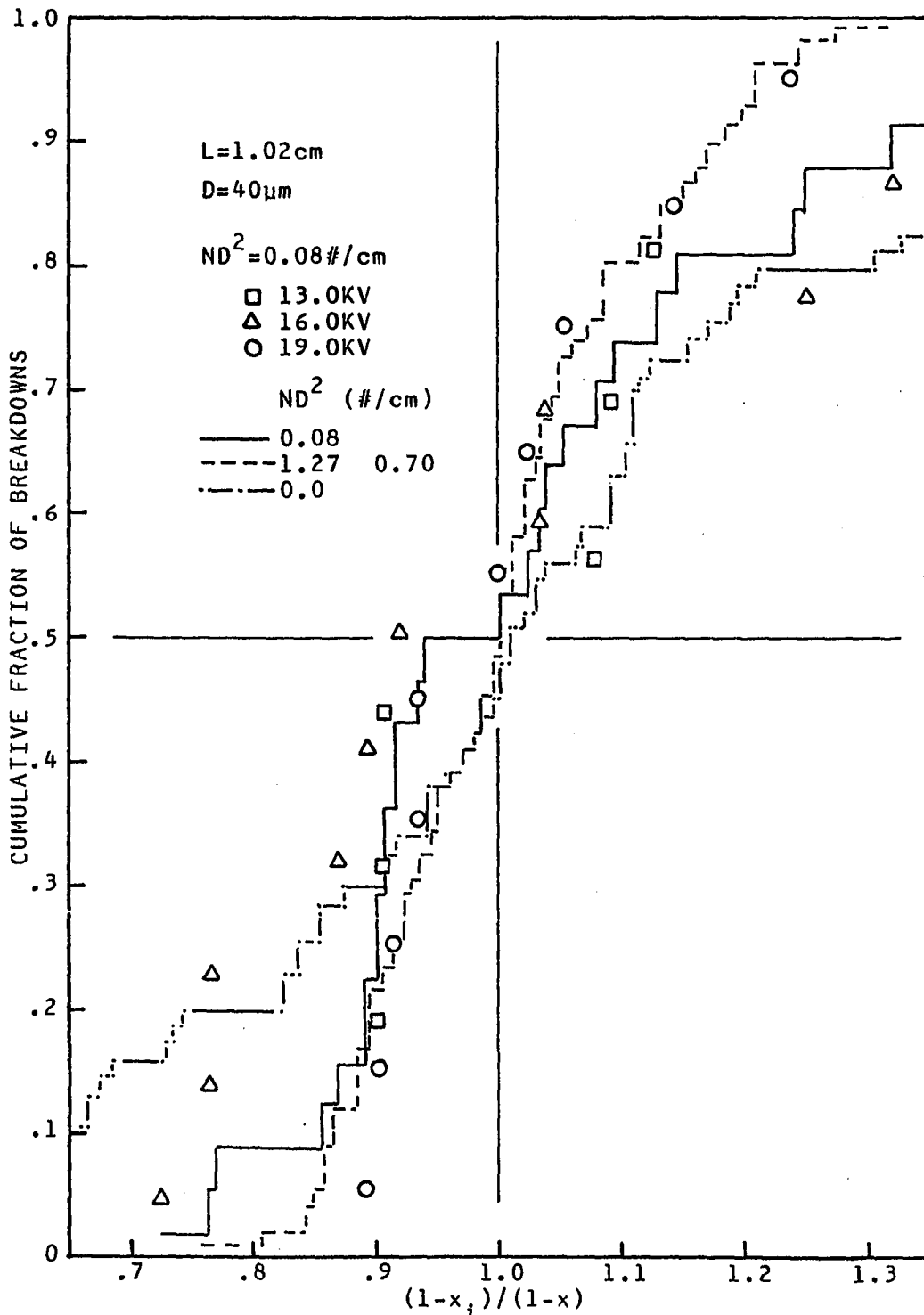


Figure 3.17b. Cumulative positional breakdown distribution, $L=1.02\text{ cm}$ when $ND^2 < (ND^2)_*$

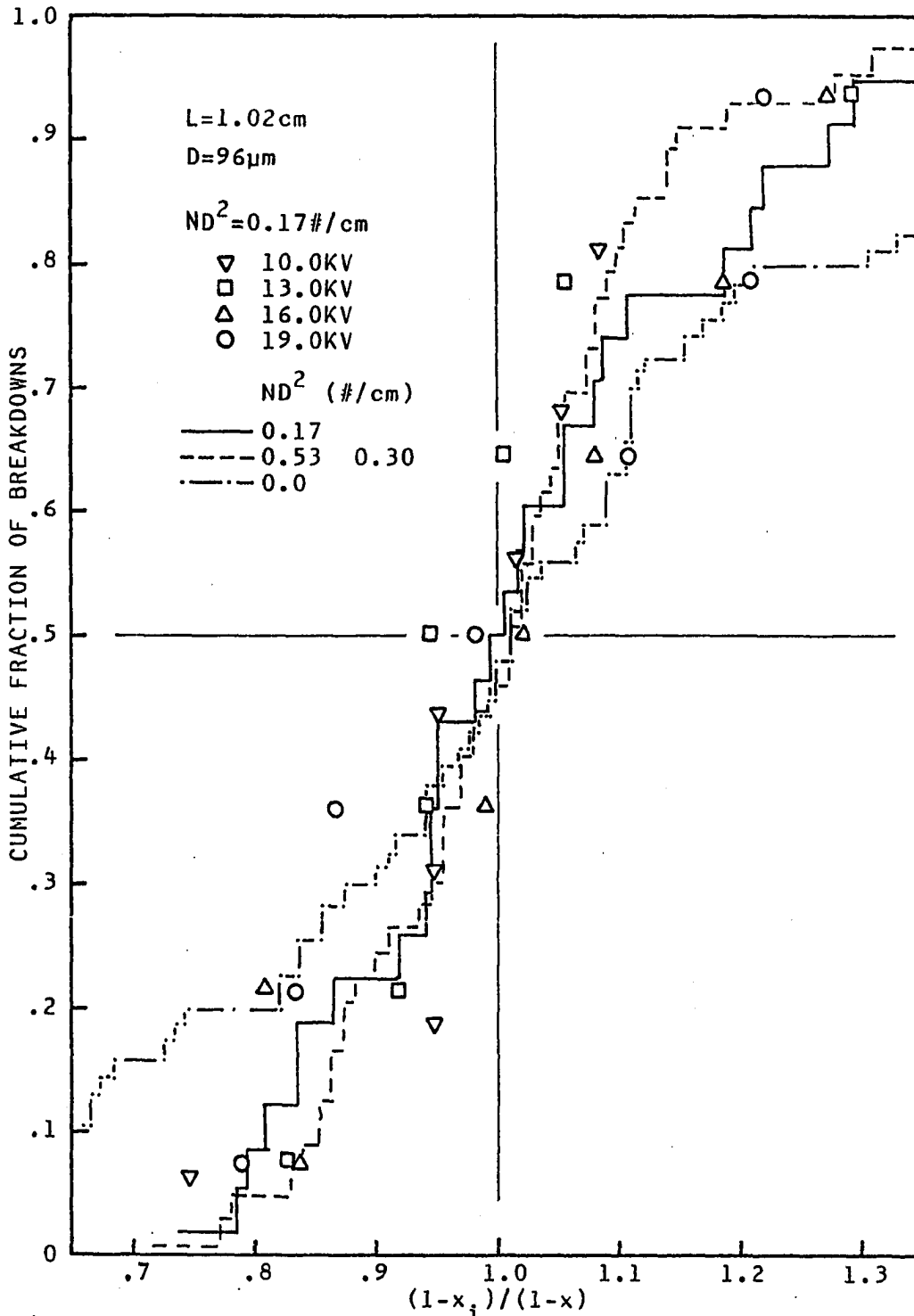


Figure 3.17c. Cumulative positional breakdown distribution, $L=1.02\text{ cm}$ when $ND^2 < (ND^2)_*$

The present trends suggest integral curves of a sort of Gaussian distribution, specially when particles are suspended, similar to those found by Wilson [27] for his experimental results on formative time lags. However, the symmetry of the present curves suggests the presence of random effects due to the particles on breakdown initiation.

C. Conclusion

The electrical breakdown of the present experimental system, consisting of two parallel plane electrodes and a moving needle used for triggering the discharge, appears to depend both on the particle conditions near the positive needle tip, such as the presence of a particle (or particles), and on the needle motion. For a negative needle electrode, corona discharge has a significant effect on the breakdown.

The positive moving needle requires higher breakdown voltage than that of a stationary needle at the same needle position. This appears to be the result of a statistical time lag.

It is observed that a particle of 1 mm diameter initiates a breakdown at a lower voltage than that of a particle-free parallel electrode gap and that this breakdown occurs when the oscillating particle was near the positive electrode.

The presence of a particulate cloud suspension between the two parallel electrodes always lowers the voltage of breakdown when triggered at the same position of a moving needle.

Experimental results of the average nondimensional breakdown needle penetration distance $(1-x)$, applied voltage V , electrode gap width L , particle number density N and particle average diameter D are correlated with the two parameters, $(1-x)V^{1.121}$ and $1-\exp(-\frac{3\sqrt{2}}{2C_2} \pi ND^2 L_x)$. The former represents the breakdown characteristics of a needle-parallel plane gap and the latter is the collision probability of a particulate cloud near the needle tip with the coefficient $3\sqrt{2}/2C_2$ related to the randomness of particle motion. When $\frac{L_x}{L_p}$ ($= \frac{3\sqrt{2}}{2} \pi ND^2 L_x$) is smaller than one, i.e., the breakdown needle gap distance is smaller than the particulate cloud characteristic distance, the breakdown voltage increases with a decrease of the particle mean free path parameter ND^2 at a given L_x . However, when the distance ratio is larger than unity, the breakdown needle gap distance L_x reaches its critical value and remains a constant which depends on the breakdown voltage and the parallel electrode gap width.

When correlations are considered as a function of $(1-x)$ at a fixed applied voltage, the decrease of $(1-x)$ with an increase of the particle number density N (or L_x/L_p)

can be explained as due to a decrease in the statistical time lag, i.e., a statistical breakdown time reduction relative to the no particle breakdown time.

Finally, the cumulative positional breakdown distribution as a function of nondimensional needle penetration distance $(1-x_i)$ at breakdown results in a distribution curve which is narrowed in the presence of particles. For $ND^2 > (ND^2)_*$, no such narrowing is observed.

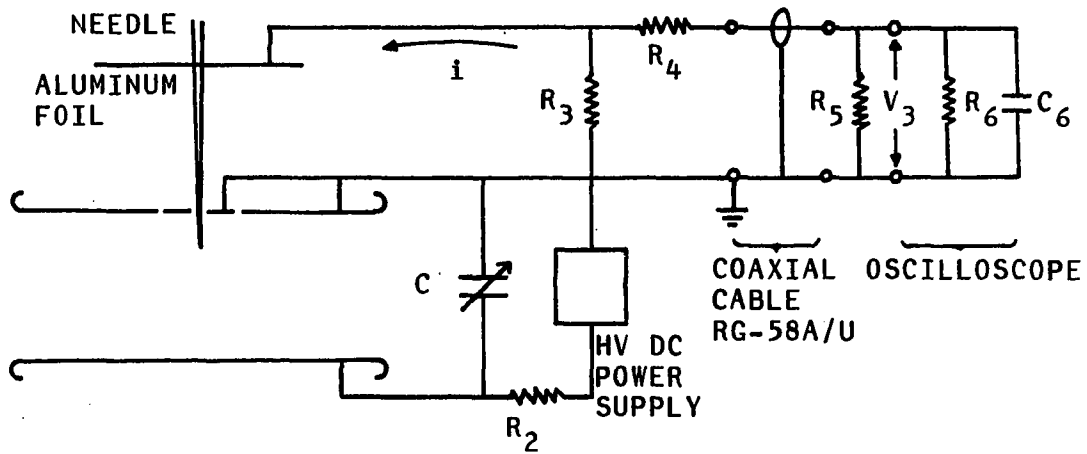
IV. TEMPORAL DEVELOPMENT OF A SPARK BREAKDOWN IN UNIFORM PARTICULATE CLOUDS

In this study, measurements are reported for the current associated with a spark discharge with and without the presence of particles. Also studied is the total released charge and energy of the spark, again considering the effects of particulate clouds.

A. Experimental Technique

The same electrode system used for the previous study was used again. An external capacitor was added to store additional charge, and a special circuit was designed to pick up the discharge current having a 1×10^{-10} nsec event time response. The experimental setup is shown in Figure 4.1. The external variable capacitor was consisting of the particle reservoir and an outer sliding copper cylinder. The capacitance of the total circuit could be varied, by sliding the outer cylinder, giving 13 to 310 pF. This includes the capacitance of two main electrodes, external capacitor, wires and support of the system. The lower electrode was connected through a large resistor of about 980×10^6 ohms.

The capacitor had a charging RC time longer than 12 msec so that the main electrode system and the circuit



$R_3 = 3.0\Omega$	$R_m = 1.496\Omega$ ($R_4 = 48.28\Omega$)
$R_4 = 48.26$ or 995.0Ω	0.1434Ω ($R_4 = 995.0\Omega$)
$R_5 = 50.0\Omega$	
$R_6 = 1.0M\Omega$	$C_6 = 20.0pF$
$R_2 = 980M\Omega$	$C = 13.0 \sim 310.0pF$

Figure 4.1. External circuit for spark current measurement

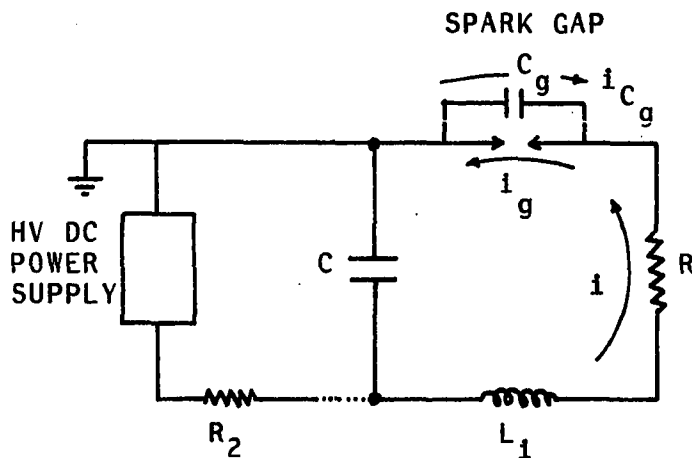


Figure 4.2. Equivalent circuit

including the external capacitor could be isolated from the power supply during the short time of a spark discharge. The needle was grounded through a 3 ohm carbon resistor to generate voltage difference by spark current.

The voltage trace was displayed on a high speed oscilloscope (Teck. 475) through a voltage dividing resistor R_4 and a coaxial cable (type RG-58A/U) of no more than 1 m length (Figure 4.1). The cable was matched with a 50 ohms resistor (R_5) at the end to avoid undesirable "ringing" caused by high frequency signals propagating along the transmission line. The fast signals on the oscilloscope screen were taken with a Polaroid still camera (Tektronix C40) using Polaroid high speed film (type 617, ASA 10,000). However, because the signal was too fast to sensitize the film, further signal intensification was necessary by reducing the picture size.

The requirement of a small resistor 3 ohms implies a low sensitivity to current change, a small RC time constant of the measuring circuit, and a negligibly small energy loss by the resistor compared to that released in the electrode gap. The RC time was then varied from 0.03 to 0.9 nsec, depending on the external capacitance, which were reasonably small times relative to observed event times of the spark breakdown. The stray inductance of the system,

such as due to circuit cables, was about $4.0 \times 10^{-7} \text{H}$. The total circuit was then basically an RLC series circuit. The equivalent circuit is shown in Figure 4.2.

Difficulties were noted by Rose and Pride [46] and Johnsson et al. [106] in inserting the necessary measuring equipment, such as a resistor, into the spark circuit without significantly altering the discharge process. However, nano-second oscillation-free current pulses were obtained (Barreto et al. [44] and Marode [41, 107]), by minimizing the stray inductance and the capacitance between the needle and the upper-innermost electrode.

The needle discharge current i was calculated from the voltage V_3 displayed on the oscilloscope based on the relationship given by

$$i = \frac{V_3}{R_m} \quad (4.1)$$

R_m was derived with simple circuit theories, such as Ohm's law and Kirchhoff's law. That is

$$R_m = \frac{R_3 R_5}{(R_3 + R_4) \left(\frac{R_5}{R_6} + 1 \right) + R_5} \approx \frac{R_3 R_5}{R_3 + R_4 + R_5} \quad (4.2)$$

since

$$\frac{R_5}{R_6} = \frac{50 \Omega}{1 \text{ M}\Omega} \approx 0$$

Two resistors, 48.26Ω and 995Ω , were used for R_4 giving $R_m = 1.496\Omega$ and 0.1434Ω . For high current pulses, the larger R_4 was utilized since the maximum measurable voltage was limited to 40V by the oscilloscope.

The total spark current i in the external circuit shown in Figure 4.2 should be both the conduction current i_g from the needle to the lower electrode produced by the motion of charged ions and electrons during discharge and the displacement current i_{C_g} of the capacitor C_g composed of the needle to the lower electrode. That is,

$$i = i_g + i_{C_g} \quad (4.3)$$

or

$$i = -C \frac{dV_C}{dt} = i_g + C_g \frac{dV_{C_g}}{dt} \quad (4.4)$$

However, since C_g was designed to be negligibly small (~ 0.1 pF), i_g could be measured from the voltage difference across R caused by i successfully. As a numerical example, from Figure 4.3a at 26 KV taking $\Delta V_{C_g} \sim 26$ KV and $\Delta t \sim 20$ μ s gives $i_g \sim 10.15$ A and $i_{C_g} \sim 1 \times 10^{-3}$ A.

For a stationary needle, the spark was triggered by illuminating the gap at a slightly lower voltage than the breakdown voltage with a neon lamp of a stroboscope or by connecting the high voltage lead of the power supply to the electrode at a slightly higher voltage. In the case of the

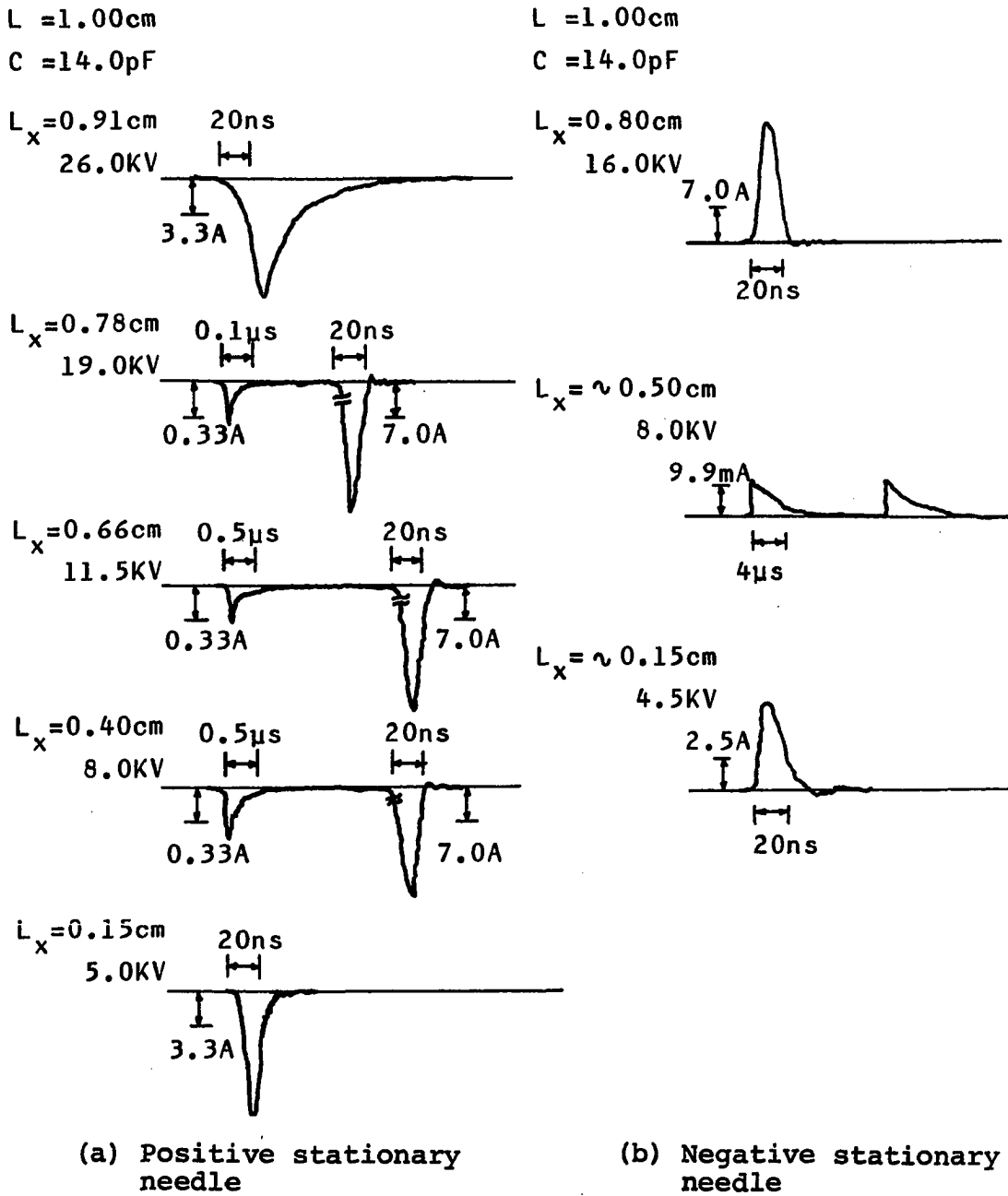


Figure 4.3. Temporal development of spark breakdown

latter method, the incremental voltage was chosen to give enough time to charge the circuit capacitor before breakdown.

As in the previous study, the experimental features of this study includes the generation of uniform particulate clouds, the measurement of particle number density and applied voltage, and the use of a moving needle as a triggering device for spark breakdown.

B. Results and Discussion

1. Spark discharge and energy

As previously discussed in the review, spark breakdown involves very complicated phenomena which depend on electrode geometry and experimental conditions such as ambient pressure, percent overvoltage, etc. A part of this study was directed toward understanding how the present experimental system was different from others in the temporal development of breakdown discharge and its energy transfer to gases.

Previous studies on breakdown have usually been made on uniform electric field systems of two parallel electrodes or a nonuniform system of a point (or hemisphere)-to-plate electrode gap. Since the present system involved a combination of these, the temporal development of the spark breakdown was expected to show both characteristics, depending on the needle position. The dependence of breakdown discharge

on the needle position is sketched in Figure 4.3a based on current measurements for a positive stationary needle between two parallel electrodes. When $L_x \approx 0.91$ cm, that is, the needle penetration distance is very small, a single strong pulse is obtained similar to that observed under a uniform electric field by Barreto [42] and Barreto et al. [43, 44]. But, as the needle penetration is increased, the primary (or first) pulse, i.e., the avalanche and streamer stages (referred to Barreto [42]) or the corona discharge stage (referred to Marode [41]), is always observed to precede the main pulse (spark). Again, only a single pulse is observed as L_x becomes very small.

It is important to note that the time interval between the two pulses and the discharge mode itself were strongly influenced by the applied voltage relative to the breakdown voltage of 50% probability. For example, at $L_x = 0.66$ cm, a partial weak discharge (corona), as observed by Marode [41], appears without the main spark (second pulse) at about 10 KV with times longer than 1 sec between successive weak pulses. But, as the applied voltage was increased, the time interval of the two pulses decreased with an increase of the first pulse height. When the applied voltage became 17 KV (i.e., overvoltage), the two signals merged into one, with an appearance similar to that of the first pulse. This

transition was observed to correspond to a change of the spark shape and color in the gap from a white narrow line-like channel to an intense red channel.

By comparison, the positive moving needle always produced a single spark with a damped oscillation, looking somewhat similar to the first pulse for the stationary needle (see Figure 4.4). Because the spark breakdown of the moving needle was produced under over field-strength conditions relative to the stationary needle case, the single pulse is not unexpected based on results obtained with the overvolted stationary needle.

The mode of breakdown was quite different under a reversed polarity. With a negative needle, only corona pulses (so-called Tirschel pulses) were observed, except when the needle tip was placed very close to the top or bottom electrode where a single pulse appeared. Figure 4.3b shows the typical currents.

For the rest of this study, a positive polarity was adopted. It was difficult to include two-pulse traces on a single oscilloscope photograph with reasonable resolution since the duration time of each pulse was shorter than the time interval between the two signals. Also, the magnitude of the second pulse was much larger than the first one. Therefore, the two pulses were separately displayed on the

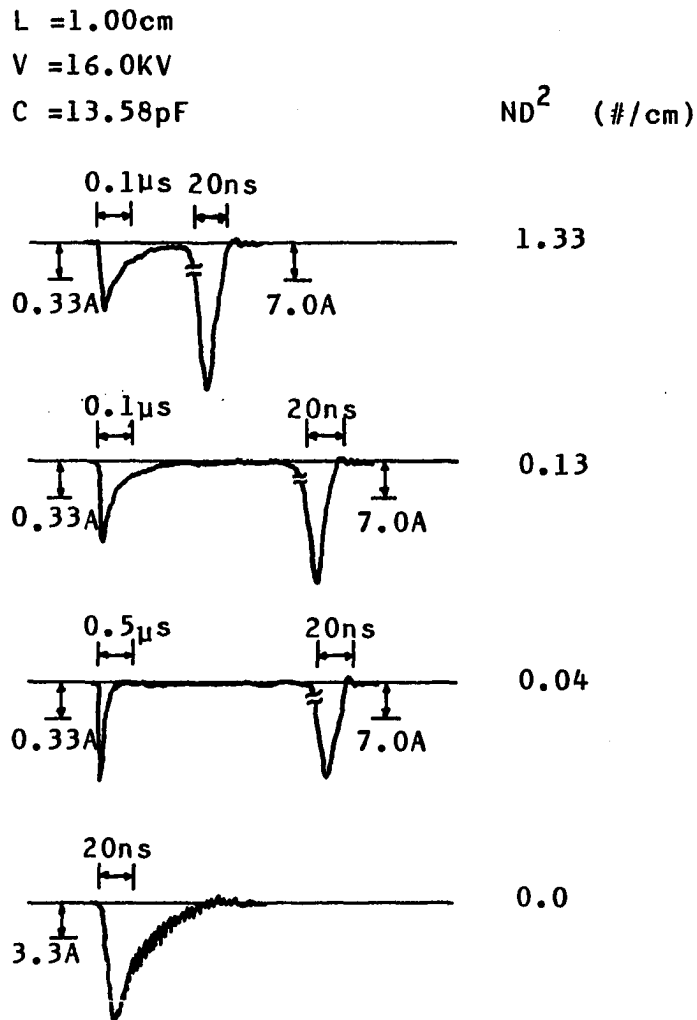


Figure 4.4. Temporal development of spark breakdown associated with a particulate cloud and a positive moving needle

oscilloscope by controlling the trigger level.

A Keuffel & Esser Co. planimeter (type 4236) was used to integrate the oscilloscope recorded current-time traces. The released charge of a spark was found from the equation

$$Q_s = \int_0^t i dt \quad (4.5)$$

For a two-pulse spark, the integrated values were averaged over three different runs for the first and second pulses and each average was added to give the total released charge of a spark. Measured spark charges using various capacitors and applied voltages are shown in Figure 4.5. The results show that the percentage of the released charge averaged in this way is within 90 to 110% of the stored charge ($Q_0 = CV_{g_0}$), whether the needle is stationary or moving. From the measurements of the discharge with the stationary needle at $L_x = 0.40$ cm, it was found that the charge magnitude of the first pulse (streamer) at a fixed voltage of 6.8 KV remained constant, about 12×10^{-9} C, with increasing capacitance. Therefore, it follows that the value of capacitance does not influence the streamer discharge so that the increased stored charge with capacitance has to be released through the main spark. Similar conclusions were made by Barreto et al. [44] from their sphere to water surface discharges. At a fixed capacitance, it was also observed that the amount of charge released in the first pulse

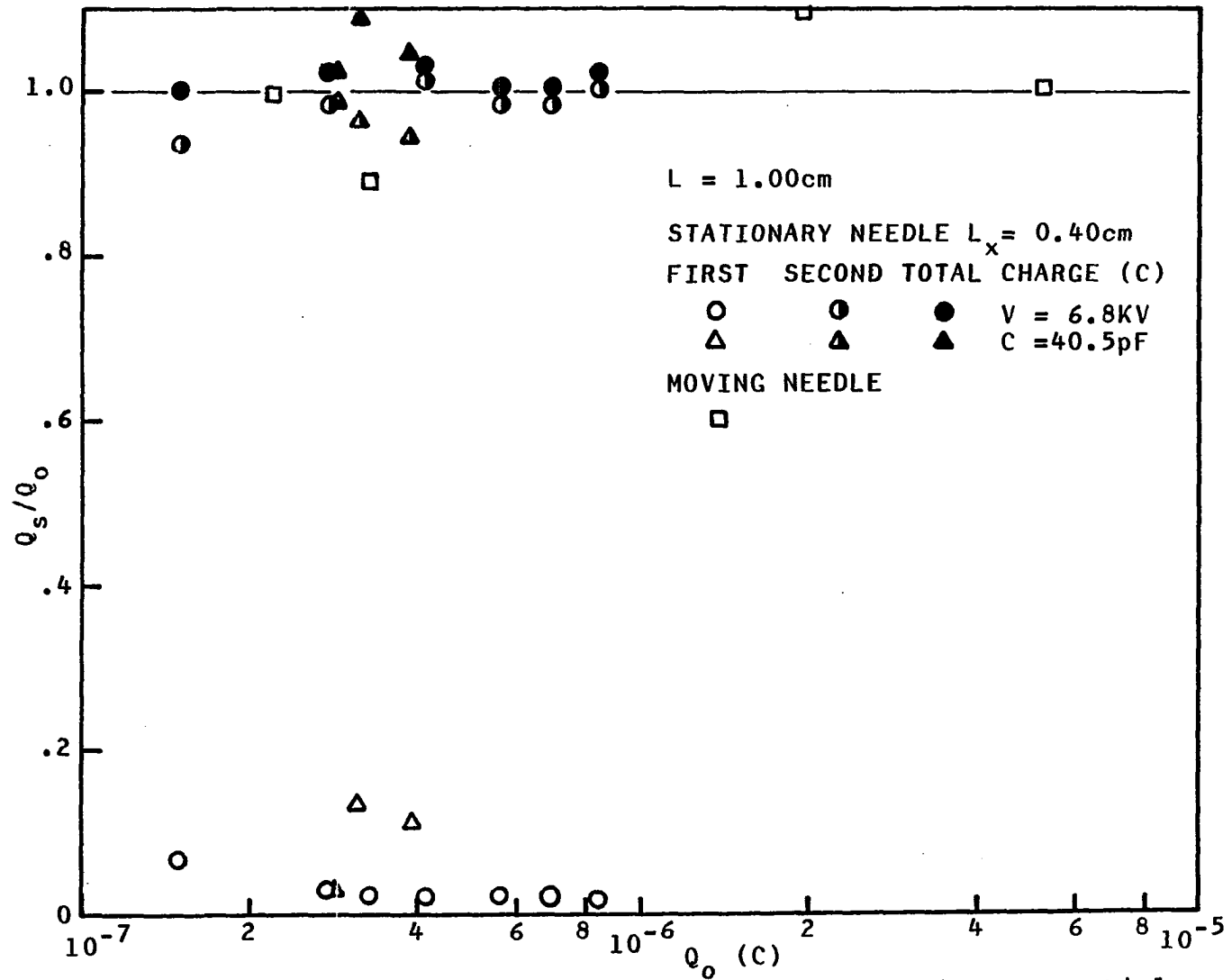


Figure 4.5. Ratio of spark charge to stored charge, without particles

increased as the applied voltage increased.

Using the measured charge, the total and first pulse energy of the spark could be calculated from

$$E_s = \frac{1}{2C} [Q_o^2 - Q_t^2] \quad (4.6a)$$

or

$$E_s = \frac{1}{2C} [Q_o^2 - (Q_o - Q_s)^2] \quad (4.6b)$$

Where Q_o is the initial stored charge, Q_t is the residual charge left on the capacitor, and Q_s is the released spark charge. These equations were derived based on Equation 1.16 where the gap voltage was assumed to be exactly the same as the capacitor voltage. Since the values of the resistor R and stray inductance L_i are very small, the voltage drops across them should be negligible compared to the applied voltage.

From Equation 4.6b, the ratio of the spark energy and stored energy becomes

$$\frac{E_s}{E_o} = \left(\frac{Q_s}{Q_o}\right) \left[2 - \left(\frac{Q_s}{Q_o}\right)\right] \quad (4.7)$$

When the total spark charge from integration was greater than the initial stored charge (due to the method of averaging), the "minus" in Equation 4.6a was replaced with "plus" to distinguish the excess charge from the charge left after a spark. The energy ratio of the second pulse

E_{s2} was calculated from

$$\frac{E_{s2}}{E_o} = \frac{E_s - E_{s1}}{E_o} \quad (4.8)$$

where E_{s1} is the energy released in the first pulse.

Calculated values of energy are plotted in Figure 4.6.

The figure also confirms that all of the stored energy was released within $\pm 2\%$. It is interesting to see from the calculations (or Equation 4.7) that about 10% of the total stored charge left on capacitor is equivalent only to 1% of the total stored energy.

2. Effects of uniform particulate clouds

The same tests as those above were performed with a moving needle to trigger a spark at various particle number densities and particle diameters at a fixed applied voltage of 16 KV and capacitance of 13.58 pF. The temporal developments of current pulses of electrical breakdowns associated with the particulate suspensions are sketched in Figure 4.4.

The fraction of the stored charge released in each pulse is plotted in Figure 4.7 against ND^2 , since ND^2 was found not only to be related to the breakdown needle position L_x for the fixed applied voltage from the previous study but also to give reasonable correlation for these experimental results. The percentage of the first pulse charge seemed to

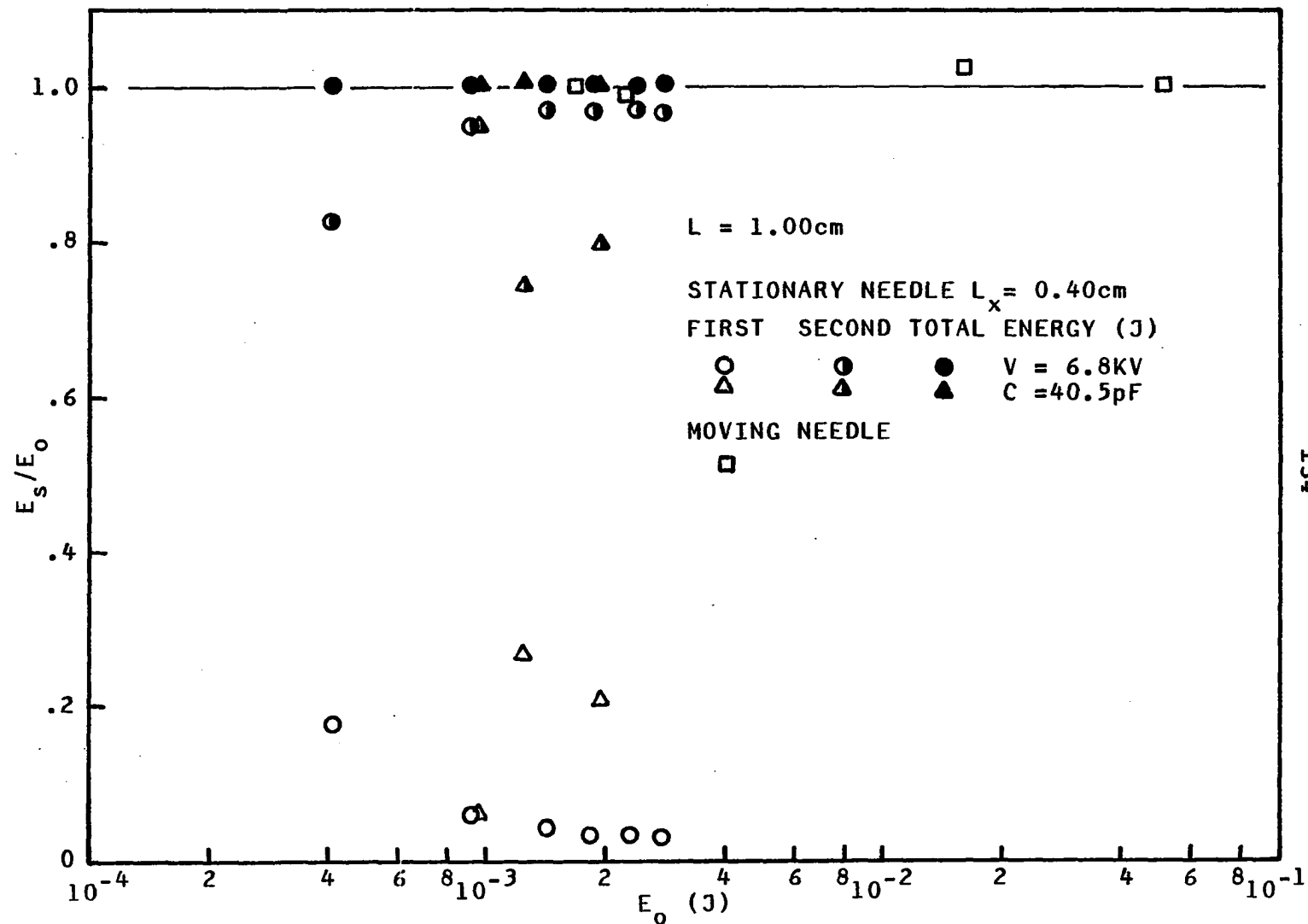


Figure 4.6. Ratio of spark energy to stored energy, without particles

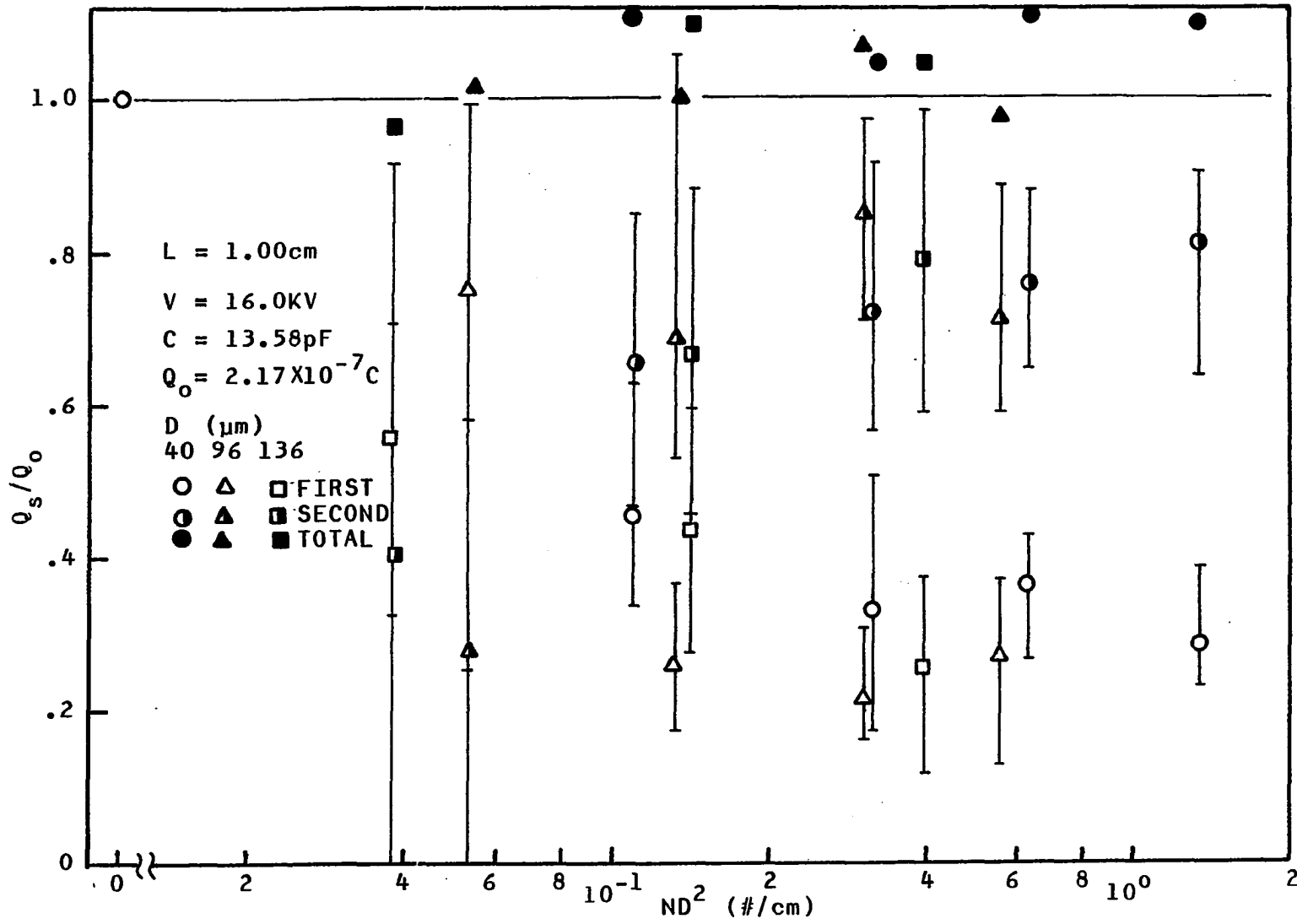


Figure 4.7. Ratio of spark charge to stored charge, with particles

decrease from its maximum (100 percent) when no particles were present to about constant (30 percent) when ND^2 was larger than about 0.19 #/cm (i.e., $(ND^2)_*$), while the total spark charge remained around 90 ~ 110% of the stored charge. When $ND^2 < (ND^2)_*$ (or $\frac{L_x}{L_p} < 1.0$), the relative increase of charge in the first pulse (streamer) is not unexpected since the breakdown is triggered under overvolted conditions compared to that of a stationary needle (see Figure 3.11).

The total spark energy was also calculated and is shown in Figure 4.8 showing less than +2% difference from the stored energy. Similar curve trends are observed when the first and second pulses of energy are compared with the corresponding pulses of charge in Figure 4.7. It is again evident that the charge and energy magnitudes of the first pulse discharge depends on ND^2 which is related to the breakdown needle position L_x at a fixed applied voltage.

Colver [1] proposed two possible particle related effects, particle precharge and increased system capacitance, on the spark charge and energy, but calculated that maximum contributions of these additional effects would probably be negligibly small for electric suspensions. The present results were not accurate enough to check his results, but generally, no such particle effects were observed.

The time interval between two pulses was observed to

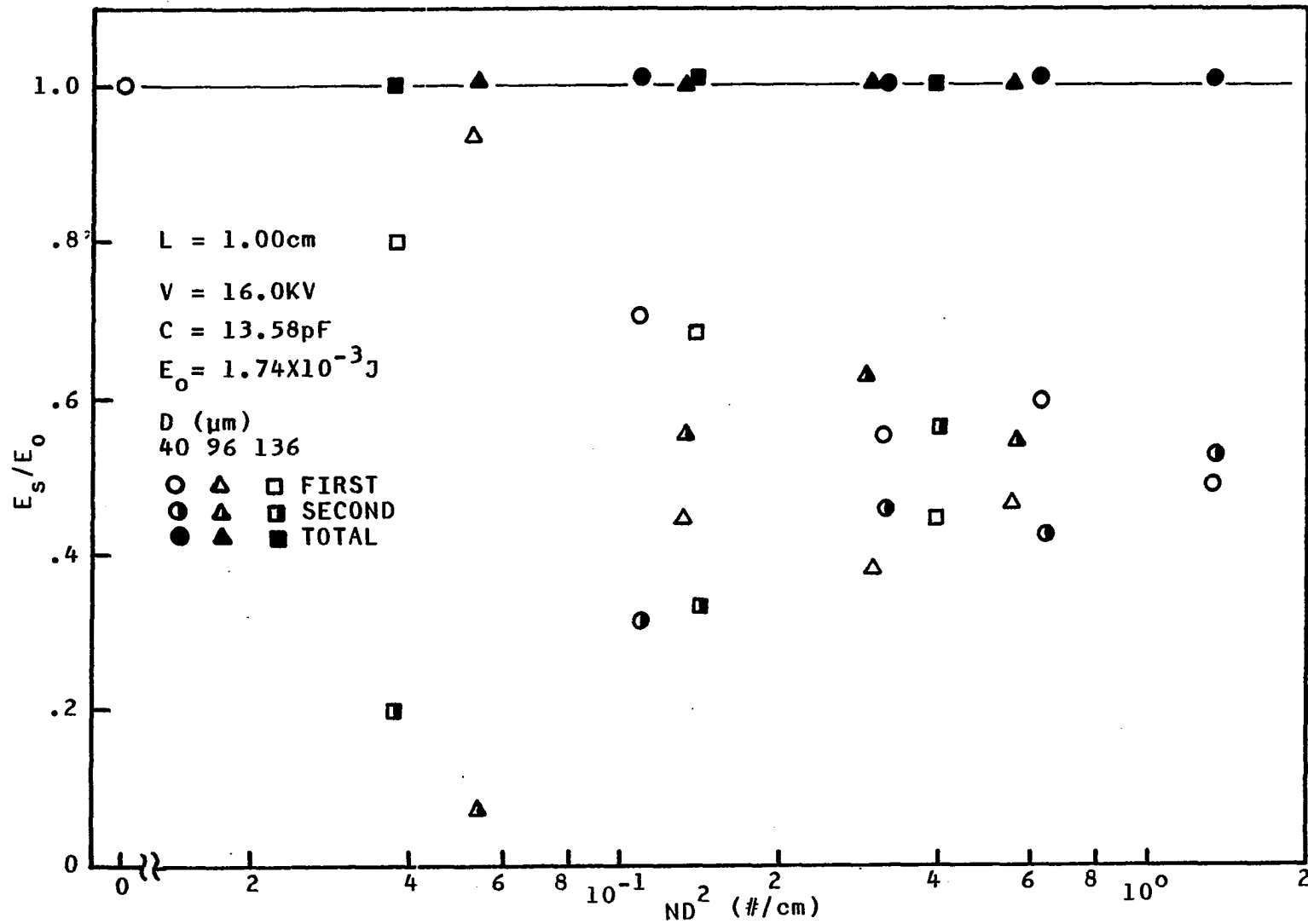


Figure 4.8. Ratio of spark energy to stored energy, with particles

increase with decreasing ND^2 from a constant interval of about 0.2 μsec (when $ND^2 > (ND^2)_*$, see Figure 4.9). However, contrary to the stationary needle results obtained by Marode [41] in the absence of particles, the time interval shown in Figure 4.10 seems to increase slightly with an increase in the magnitude of the first streamer discharge (decrease in ND^2).

It was difficult to isolate the effect of particles on the temporal development of a discharge because of the near impossibility of obtaining the same breakdown position L_x with varying ND^2 as that for a stationary needle in a particle-free gap at a given applied voltage. The previous study shows that when ND^2 is greater than about 0.19 $\#/cm$ at 15 KV (L_x/L_p is greater than one), the breakdown needle position becomes the critical value (about 0.82 cm), and also the breakdown voltage (15 KV) is slightly lower than that voltage (17 KV) for a stationary needle at the same needle position. Therefore, except for the effect of the particles in lowering the breakdown voltage of the moving needle to 15 KV from 26 KV (for a particle-free gap), the breakdown mode associated with high number density particulate clouds ($ND^2 > (ND^2)_*$) at 15 KV seems (from a comparison of photographs in Figures 4.3a and 4.4) to be similar to that triggered by the stationary needle in a particle-free gap at 17 KV and 0.82 cm needle position L_x (see Figure 3.11).

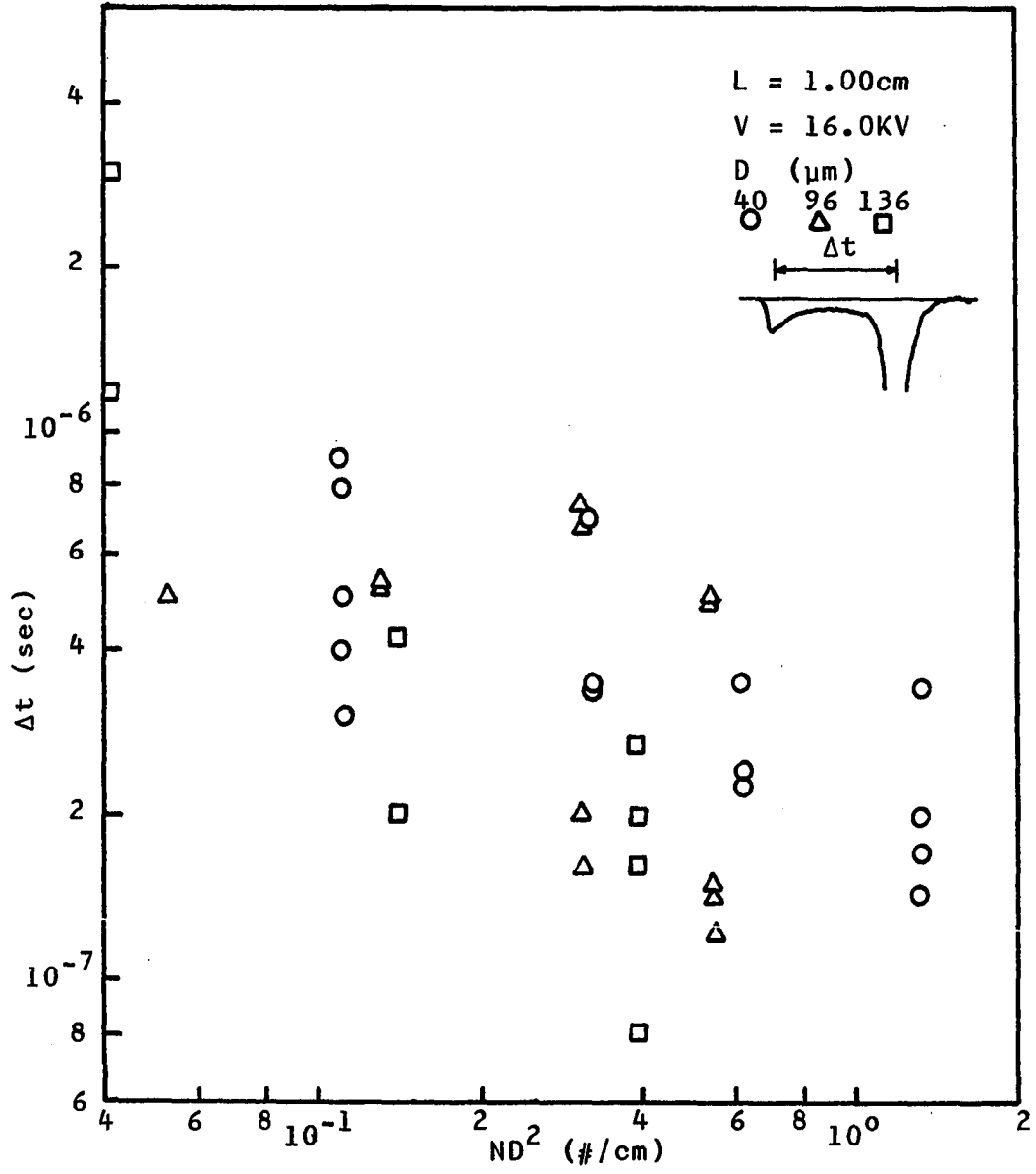


Figure 4.9. Time interval between two pulses, with particles

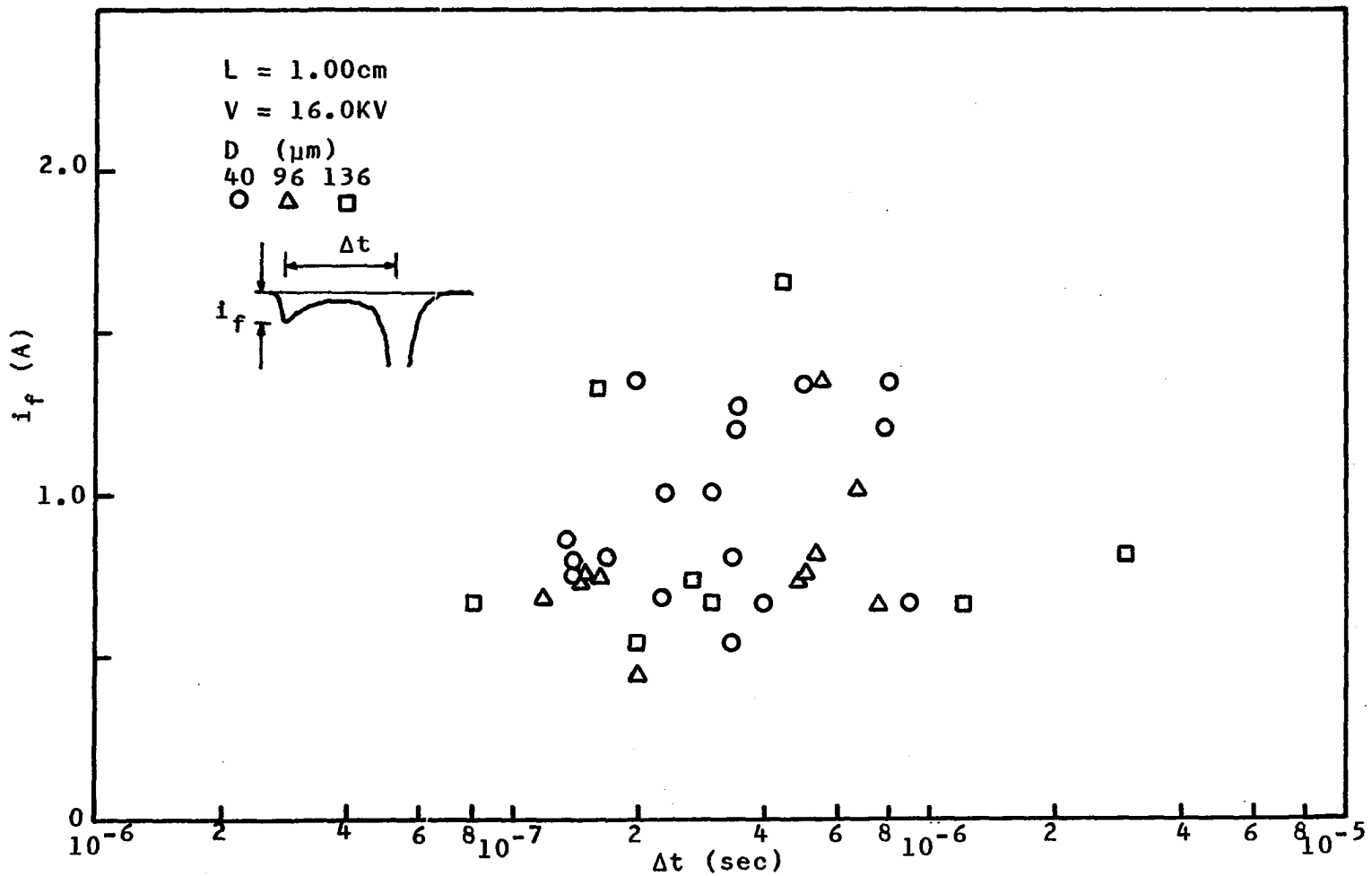


Figure 4.10. Peak current magnitude of the first pulse vs. time interval between two pulses, with particles

C. Conclusion

It has been confirmed that the stored charge or energy of the present moving needle electrode system in the range of $0.15 \sim 5.0 \times 10^{-6} \text{C}$ and $0.4 \sim 50 \text{ mJ}$, respectively, is released entirely in a spark discharge.

The electric field nonuniformity or electrode polarity seems to have a significant influence on the mode of the spark breakdown. If the field is nonuniform, the streamer discharge precedes the main spark. The magnitude of the released streamer charge or energy remains nearly the same with the increase of capacitance.

It is observed that high number density charged particles with a positive moving needle initiate sparks with time delays between the initial streamer discharge and the main spark and with current-time profiles similar to those initiated by free electrons with a stationary needle, at least, when the breakdown voltage and the breakdown needle position of the two cases have similar values (at $ND^2 > (ND^2)_*$).

No pre-charged particulate cloud effect is observed on the total amount of spark charge or energy.

V. SPARK IGNITION OF UNIFORM PARTICLE-GAS MIXTURES

The spark ignition characteristics of a spherical copper (inert) particulate cloud dispersed uniformly with a combustible gas were investigated by varying the particle number density, particle diameter, spark energy and the fuel-air ratio. The open suspension system was employed for this study, where make-up flows for the particles and the combustible gas mixtures were supplied as mass was leaked from the system.

A. Experimental Technique

1. Experimental setup

Figure 2.1b shows schematically the open suspension system. The two parallel electrodes were bounded outside by two Plexiglas plates and between by a Plexiglas cylinder of 11 cm diameter. The cylinder was divided into two halves so that it could be freely expanded in case of ignition. The bottom Plexiglas had several holes near its edge to allow particles to fall out, without piling inside (see Figure 2.1b). The Plexiglas cylinder also had several holes around its upper and lower edges to allow the combustible gas mixtures to escape. Forming the cylindrical enclosure was necessary to make the area exposed to air small so as

to minimize the dilution effect of ambient air diffusing into the test region.

The propane gas (99% purity) and low relative humidity (<5%) air from commercial compressed tanks were mixed without further purification and used as a combustible gas. Figure 5.1 shows how these gases are mixed and regulated. Two Gilmont flow meters, No. A-2855 (max. 260 mL/min air flow) and No. B-5284 (max. 1800 mL/min air flow), were used to measure propane and air flow rates, respectively. These flow meters were calibrated in this laboratory. Gas line pressures before and after the flow meters were monitored for possible flow rate corrections using manometers filled with indicator fluid. Check valves were used to protect against inverse flow. A flashback arrestor (for a flame in the gas delivery system) was constructed from a tube packed with small glass beads and placed at the end of the mixing system.

The particle feeding system and the pneumatic gun are shown in Figure 2.2 and were not altered from the previous studies.

2. Flowmeter calibration

A standard device utilizing soap bubble rise time in a glass tube between two lines of known volume, 10 ml or 106 ml, was used to calibrate the two ball flow meters. The calibrations are shown in Figures 5.2a and 5.2b. These

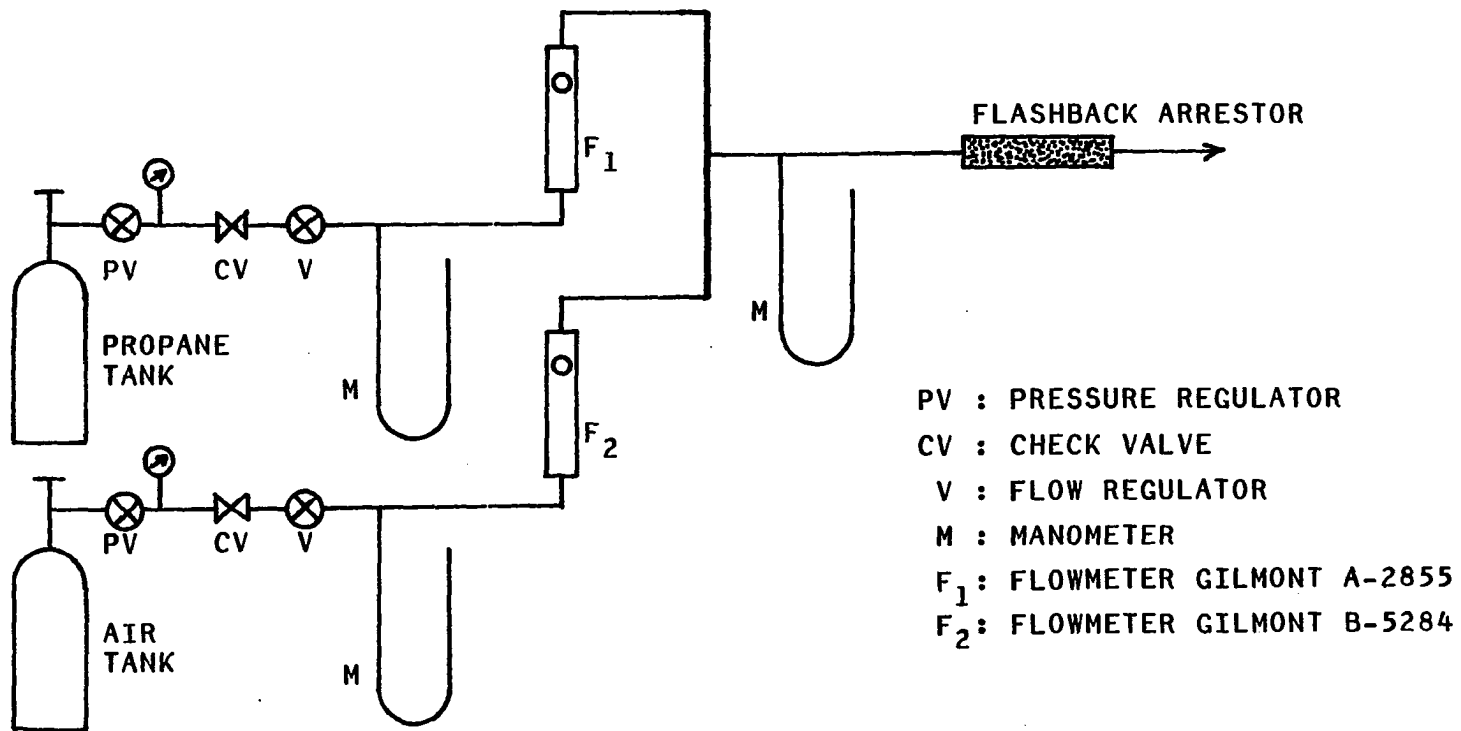


Figure 5.1. Layout for combustible gas mixing

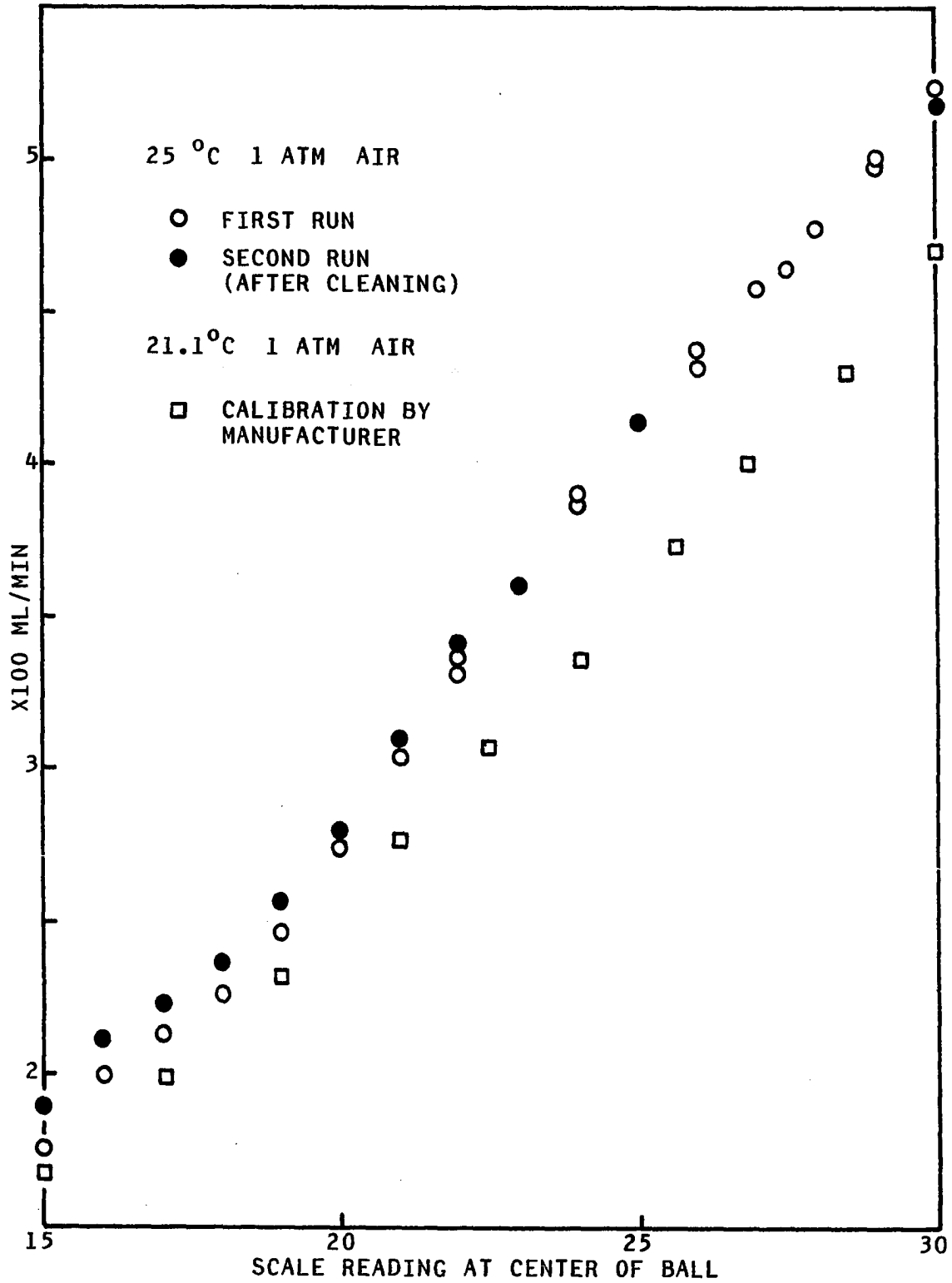


Figure 5.2a. Flowmeter calibration, Gilmont B-5284

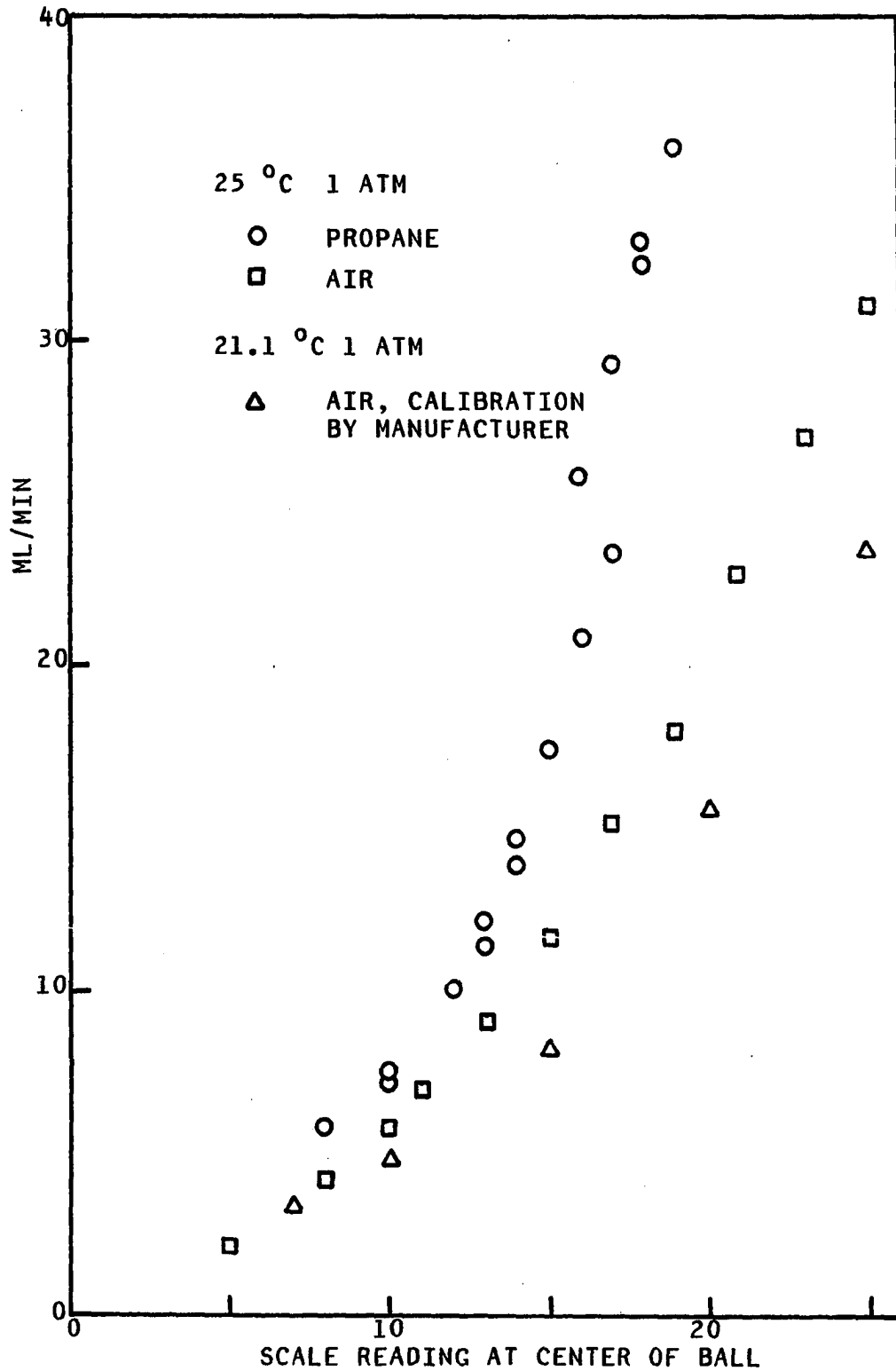


Figure 5.2b. Flowmeter calibration, Gilmont A-2855

calibrated results were noticeably different from those provided by the manufacturer for air.

Propane was also used to calibrate the small flow meter (Gilmont A-2855). The propane flow rate shown in Figure 5.2b is higher than the air flow rate at the same reading, which was expected because of different gas viscosity and molecular weight. Factors affecting the flow rate of these variable-area flow meters are discussed in Appendix C.

3. Experimental procedure

For the small flow meter (A-2855), some difficulty was found in adjusting the propane gas flow rate accurately in order to control the fuel-air ratio of the gas mixture. For example, for fuel-air ratios from 0.03 to 0.065 which represent the flammability limits of propane in air, the small flow meter provides only four marked 1 mm scales when a constant air flow rate is assumed. To solve this problem, two fixed propane flow rates were chosen, 14.6 mL/min and 10.6 mL/min, and the air flow rate was controlled from 349 to 211 mL/min. The total flow rate produced less than 2 cm/sec gas velocity right above the screen of the lower electrode (see Figure 2.2), and thus, it was concluded that the gas flow would not disturb the cloud uniformity.

In order to ignite a particle-free combustible gas

using a stationary needle, a spark was triggered by illuminating the gap with an external light source or by applying a slightly overvolted input to the system in the same way as was done for the discharge current measurement. When a breakdown voltage smaller than the minimum at a given needle-to-plane gap distance (L_x) was required (to test for a minimum ignition energy of the particle-free combustible gas), very few particles were added to induce the breakdown voltage and therefore the minimum ignition energy.

By comparison, in order to ignite a uniform particle-combustible gas mixture, a spark was triggered by the moving needle. The needle-electrode system was adjusted to allow the needle to move into the parallel electrode gap of 1.0 cm width only when it was compressing a spring and then to a maximum compression distance of about 0.28 cm (for 11.36 m/sec needle approach velocity). This was necessary to prevent multiple breakdowns which would result for a larger needle penetration. The needle gap distance at sparking (L_x) for a 1.0 cm parallel plate gap was found to be in the range of 0.72 ~ 0.85 cm when the applied voltage was controlled (to about 16.0 KV without particles) depending on the particle number density. The range of the applied voltage was 12.5 ~ 16.0 KV.

The needle position at the time of sparking was measured only for the purpose of investigating the effect of needle

motion on ignition (without particles). The reference needle gap distance (L_y , see Figure 2.7) and the applied voltage were adjusted so as to control the spark gap distance ($L_x \approx 0.1 \sim 0.6$ cm) and also to produce a single spark only during the period of spring compression. However, for this case, the spark (and needle) position signal as shown in Figure 2.7 did not appear since the spring was already grounded. Because of this problem, the time of sparking was monitored through a coil wound inside the spring holder. This signal (electromagnetic signal caused by the spark) was fed to the storage oscilloscope, which was operating in a chopped mode, in addition to the two-step signal formed with two foils (AF1 and AF2) and the spring. Time intervals measured on the oscilloscope as based on the distance from foil 2 (AF2) to the spring and foil 2 to the spark were used to calculate the spark needle position from Equation 2.2. Alternatively, it could be found from the calibrated figure (Figure 2.8b) by measuring the time to spark. The maximum compression distance was measured to be about 0.280 cm at the needle velocity of 11.36 m/sec.

When particles were supplied continuously, first the high voltage was increased to a voltage suitable for use with the calibration of the particle number density vs. current shown in Figure 2.6 so as to measure the current

induced by particle suspension (i.e., to find the particle number density). With the particle feed rate constant, the voltage was again increased to a value required for the ignition study.

The appearance of a flame between the gap after a spark was regarded as ignition. The spark energy was changed by varying either C or V until a discernible transition from ignition to nonignition was observed at a fixed particle number density and fuel-air ratio. The ignition energy was found to be independent of an overvoltage condition by Blanc et al. [108] and this result was confirmed in the present study.

B. Results and Discussion

1. Ignition of combustible gases

The reaction of propane with oxygen can be written



When the oxygen is supplied in air, the stoichiometric fuel-air ratio by volume (or mole) is

$$f_{\text{st}} = \frac{1}{5 \left(1 + \frac{78+1}{21}\right)} = 0.042$$

since the composition of air on a mole basis is approximately 21 percent oxygen, 78 percent nitrogen and 1 percent

argon (Van Wylen and Sonntag [109]).

Two values of energy, the smallest energy for ignition and the largest energy for nonignition taken over more than 10 tests, were plotted versus the propane-air ratio in Figure 5.3 for three different point-to-plane distances (0.20, 0.70, and 0.80 or 0.90 cm) using a stationary needle. The stored energy of the total capacitance (including parallel electrodes, sliding capacitor, and leads) was taken as the spark energy, since it was confirmed in the last study that they were nearly identical. The average nonignition energy was usually slightly larger than the average ignition energy resulting in a sharp transitional value as observed by Moorhouse et al. [56]. The transitional energy increased toward either lean or rich mixtures having a minimum at about a fuel-air ratio of 0.050 which is somewhat richer than for stoichiometry (0.042).

The present ignition energies are comparable in magnitude with the results of Moorhouse et al. [56] (used a two-point gap of 0.22 cm), but are larger than the values given by Lewis and von Elbe [54] and Calcote et al. [55] (see Figure 5.3). It should be noted that the reported ignition energies (in the latter two references) were based on the minimum ignition energy measured at the quenching distance which is also a function of the fuel-air ratio. The ignition energy will be lowered if the gap is adjusted for every

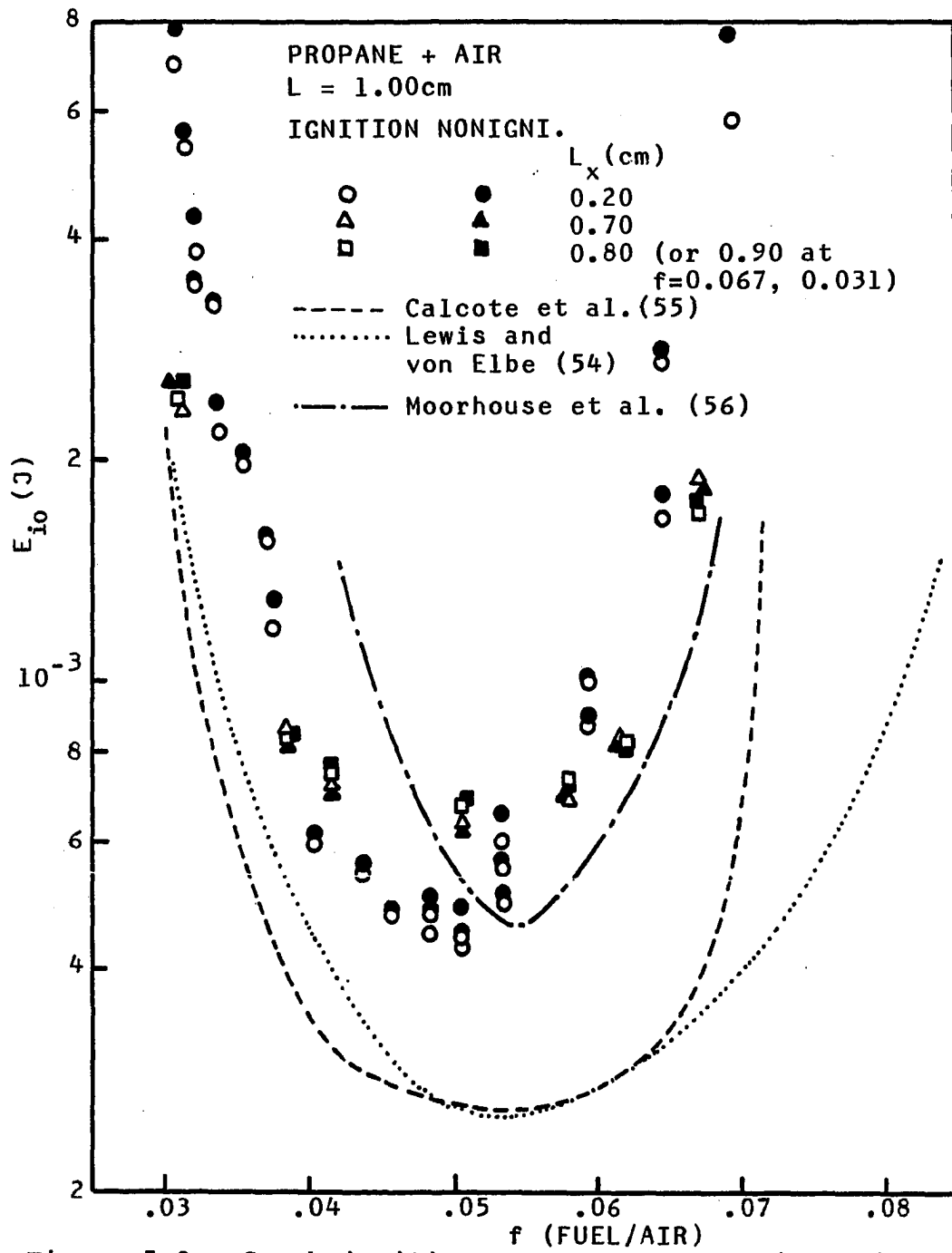


Figure 5.3. Spark ignition energy vs. fuel-air ratio, without particles

fuel-air ratio to the quenching distance. The present experiments were carried out at the fixed electrode gap distances of 0.20, 0.70 and 0.80 (or 0.90) cm which correspond to three quenching distances. But, none of the observed ignition energies were as small as those referenced above. Moorhouse et al. [56] argued that the results of Lewis and von Elbe, and Calcote et al. relate to the case when one ignition occurs in hundred tests, i.e., an ignition probability of 0.01 (these minimum values of ignition energy are frequently taken as standards in relation to safety).

However, all of the above results are in agreement in showing a minimum at a fuel-air ratio of $0.050 \sim 0.055$. Lewis and von Elbe [54] and Moorhouse et al. [56] said that the deviation of the minimum from stoichiometry is attributed to the difference in diffusivity between the fuel and the oxygen at atmospheric temperature (about 22°C).

The effect of the top plate electrode on ignition was carefully checked by varying its position at the same energy; however, no effect was found as long as the needle-to-plate distance was fixed and was smaller than the parallel electrode separation distance. These results apply outside of the parallel plate quenching distance.

2. Effect of a moving needle

Since the main purpose of this study was to investigate the particulate cloud quenching effect during ignition, the use of the moving needle was again necessary to trigger a spark. In Figure 5.4, the ignition and nonignition energies are plotted against the needle gap distance for both the moving and stationary needle cases. The gap distance of the moving needle is based on its position at the time of sparking. By controlling the applied voltage and reference needle gap position (L_y), the spark was triggered with the moving needle only when the needle compressed the spring. Therefore, the needle velocity at sparking was always smaller than the approach velocity, 11.36 m/sec, and the maximum needle penetration depth after a spark was always smaller than the 0.280 cm compression distance of the spring corresponding to a time smaller than 424 μ sec (see Figure 2.8b).

Ignition energies in Figure 5.4 appear close to those for the stationary needle, even though the needle moves into the quenching region following the spark. This result indicates that during spark kernel development, the motion of the needle into the spark kernel or directly into the quenching region by a small distance does not seriously interfere with the ignition process. For comparison, Gordon et al. [110] showed that the quenching effect of wire bits could be reduced if they were rapidly removed from the kernel of the

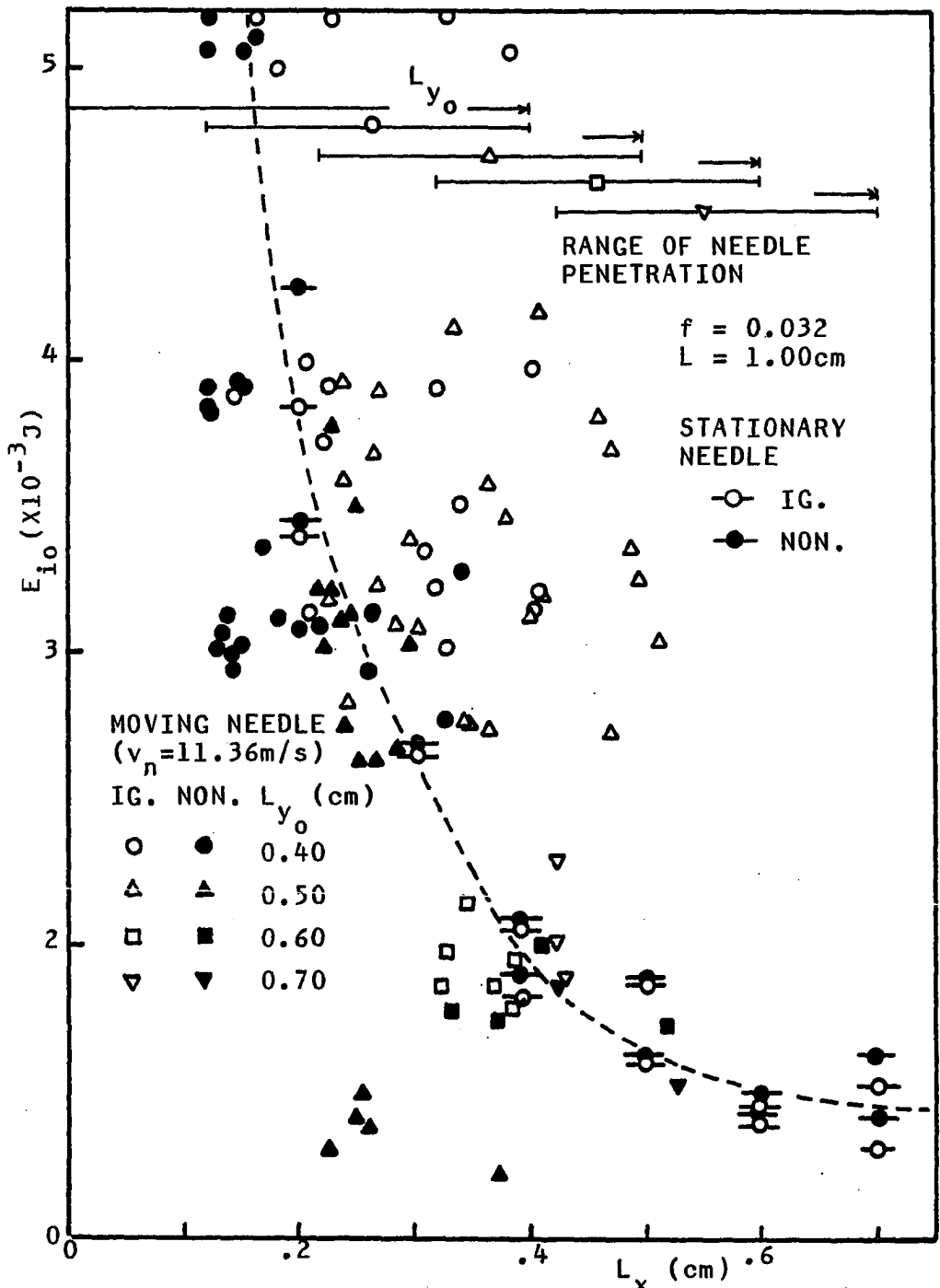


Figure 5.4. Spark ignition energy vs. needle-to-plane gas distance, moving needle effect

growing flame. Moorhouse et al. [56] showed that a flame of n-pentane with air at 0.75 atm appeared about 100 μ sec after a spark when the continuously decreasing expansion velocity of a spark kernel reached about 10 m/sec. Thus, it is concluded that the allowable maximum velocity of a needle penetrating into the quenching region (or the minimum velocity of wires retracting from the quenching region) so as not to disturb the ignition process seems to be related to the kernel expansion velocity.

3. Effect of uniform particulate suspensions

Figure 5.5 is a photograph of the spark ignition of a uniform inert particle-combustible gas mixture. Because of using the moving needle, the spark needle gap distance (L_x , see Figure 2.7) was observed to be varying randomly from 0.72 to 0.85 cm. The effect of this variation on ignition energy was checked to be as small as 0.1 mJ, based on the previous ignition study which showed that the variation of spark position of the stationary needle from 0.70 to 0.80 cm resulted in an ignition energy change of less than 0.1 mJ. Therefore, it was expected that any influence of the presence of particles on ignition could be isolated, independent of the presence of the needle.

Spherical copper particles were again used for this study. The ignitability of the multiphase mixtures was

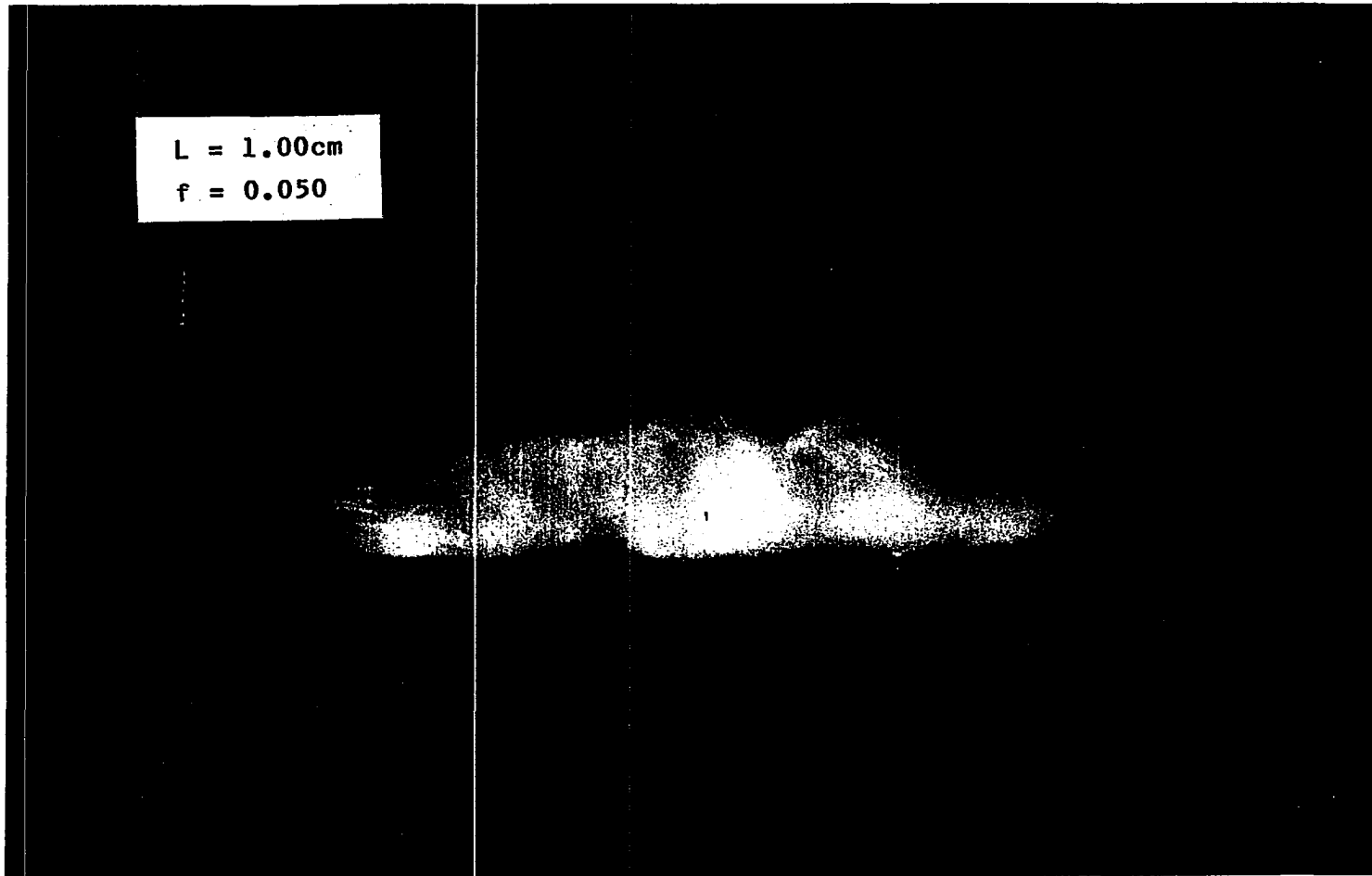


Figure 5.5. Photograph of the spark ignition of a uniform inert particle-gas mixture

tested by changing the spark energy, the particle number density, and the propane-air ratio using 96 μm diameter particles with the needle-parallel electrode system ($L = 1.0$ cm and $L_x = 0.72 \sim 0.85$ cm). Figures 5.6a to 5.6c show the spark energies of ignition and nonignition against the particle number density at various fuel-air ratios. In these experiments, the range of spark energies was from 1.4 to 40 mJ, where the lower energy was limited by the minimum breakdown voltage of the moving needle. The average values of ignition and nonignition energies taken from Figure 5.3 for the gap distances of 0.70 and 0.80 (or 0.90) cm are marked in the figures for $N=0$.

It is quite evident that these results show reasonable boundaries between ignition and nonignition, where the higher particle number density corresponds to the higher spark energy for ignition. Therefore, it would appear that the additional energy required was used to compensate energy losses to particles during ignition.

The variation of the limiting particle number density for ignition taken from Figures 5.6a-c, for three different spark energies, is plotted against fuel-air ratios in Figure 5.7. The results indicate that the limiting particle number density increases with the decrease of the ignition energy of the particle-free mixtures which, in turn, is a

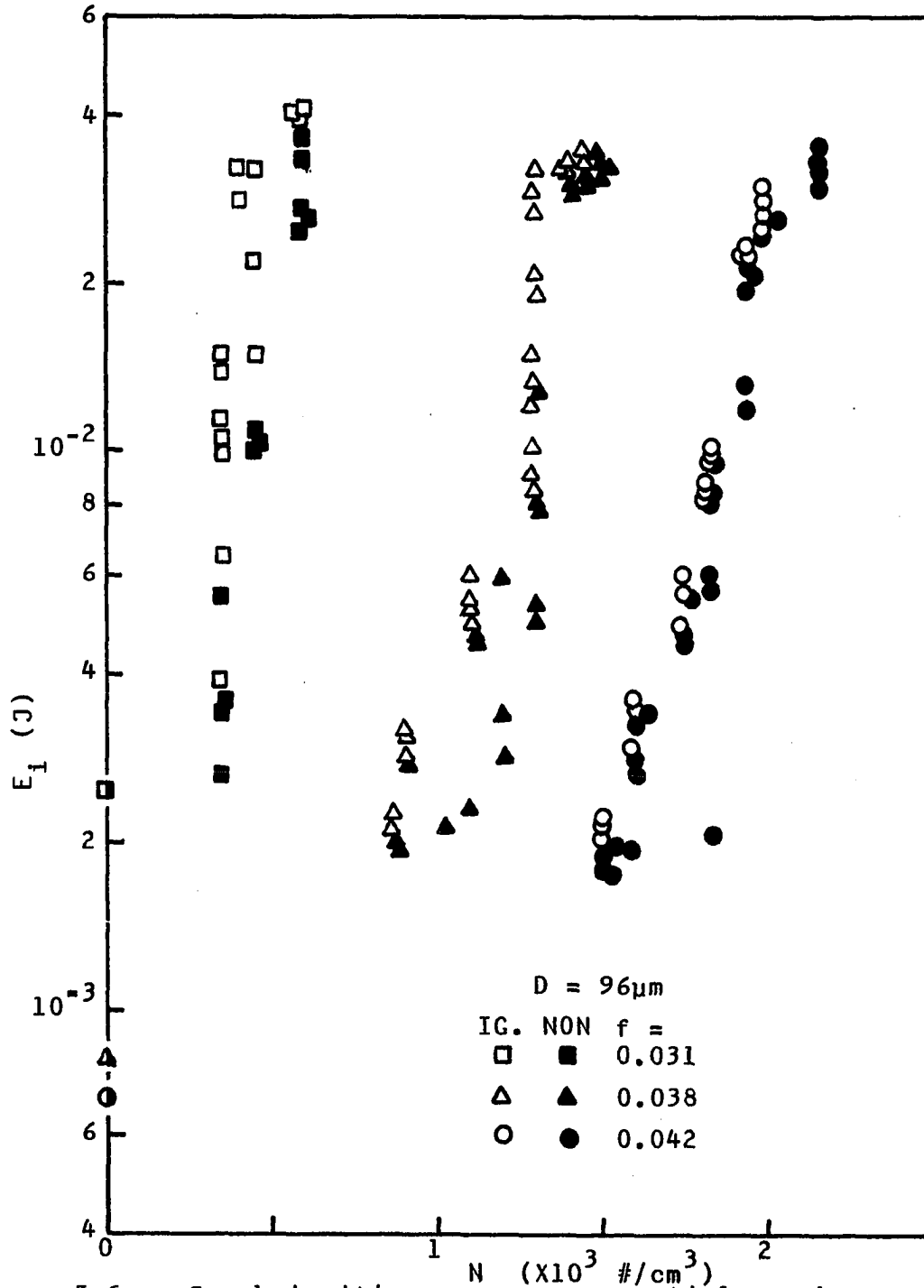
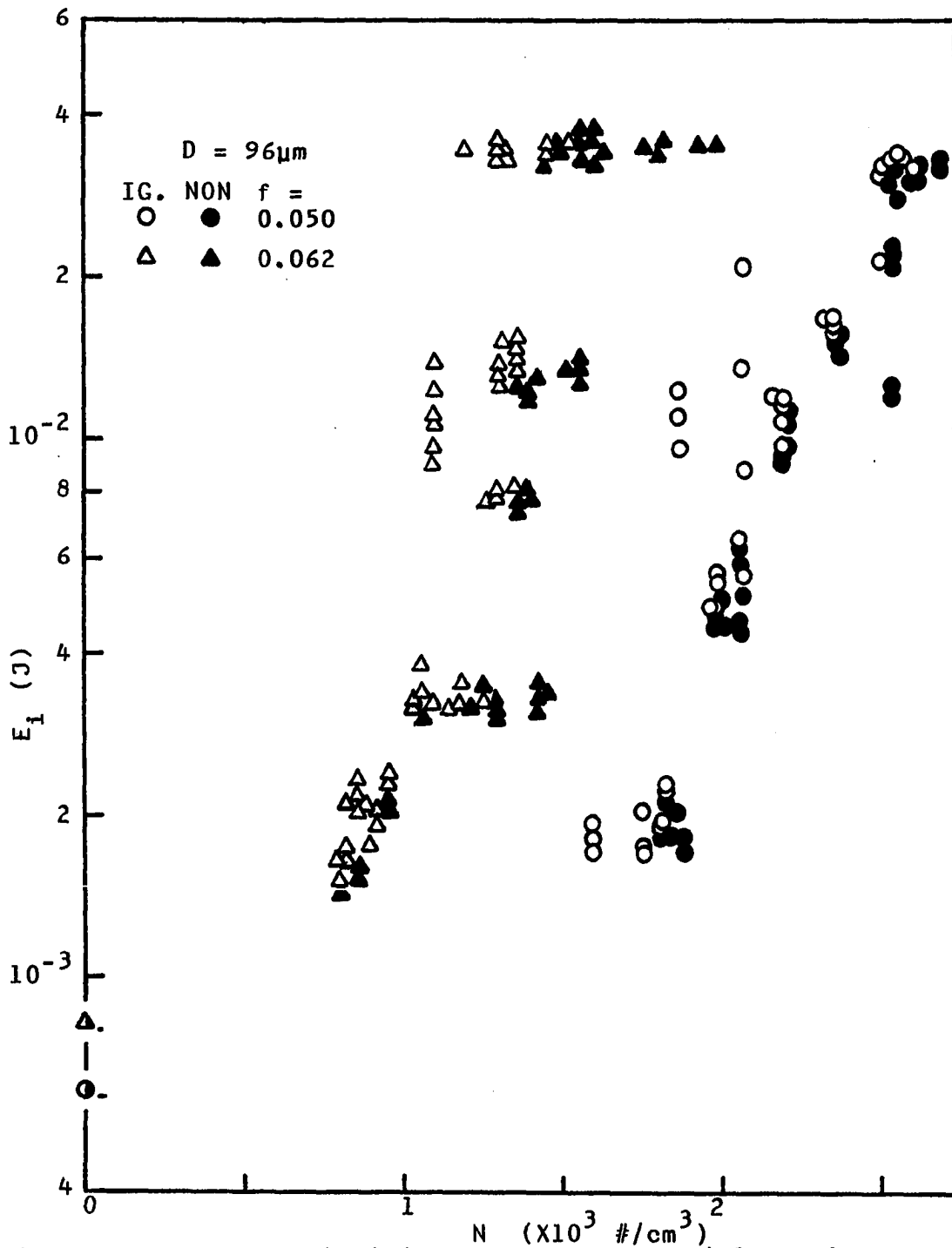


Figure 5.6a. Spark ignition energy vs. particle number density, $D = 96 \mu\text{m}$



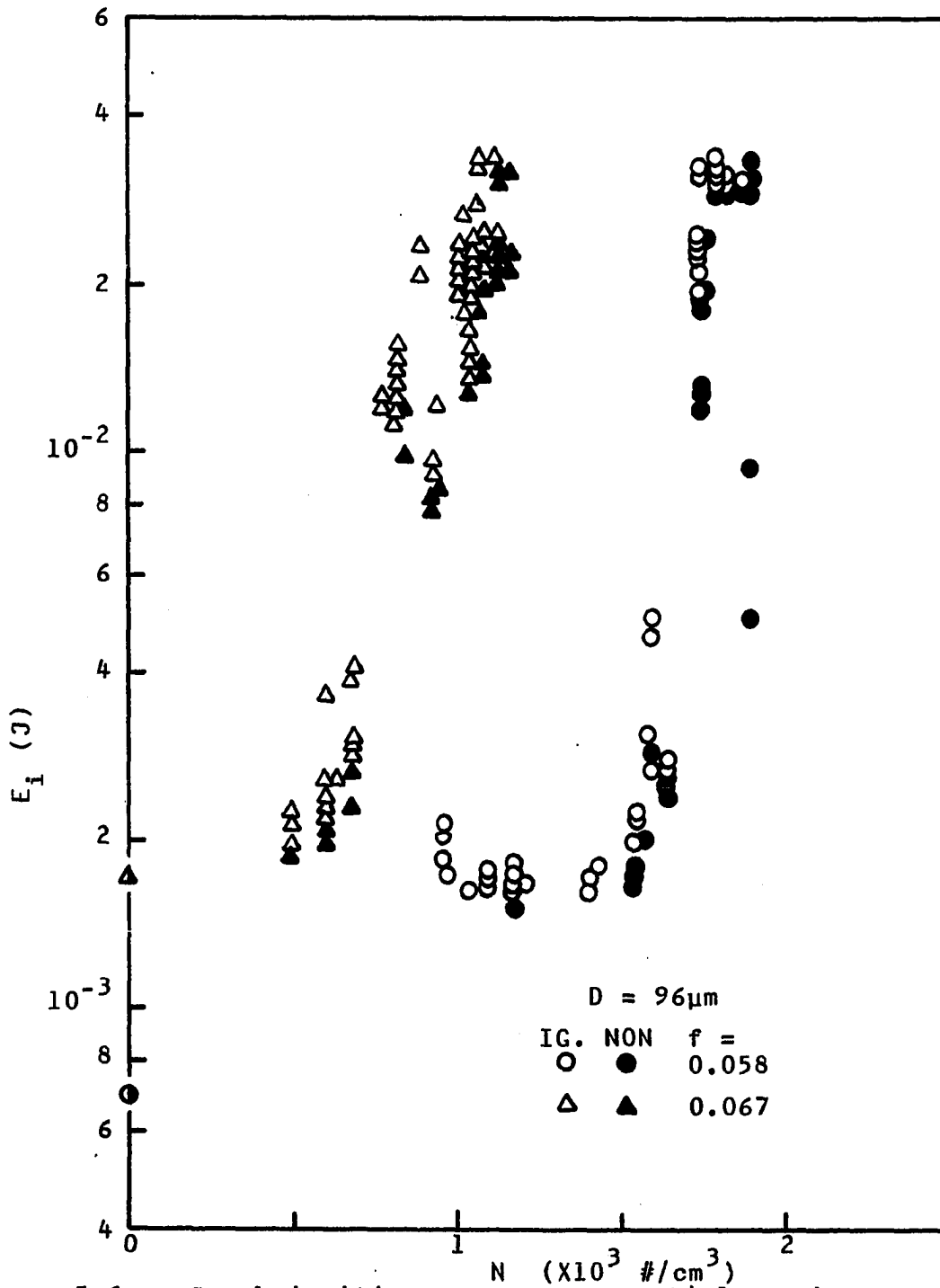


Figure 5.6c. Spark ignition energy vs. particle number density, $D = 96 \mu\text{m}$

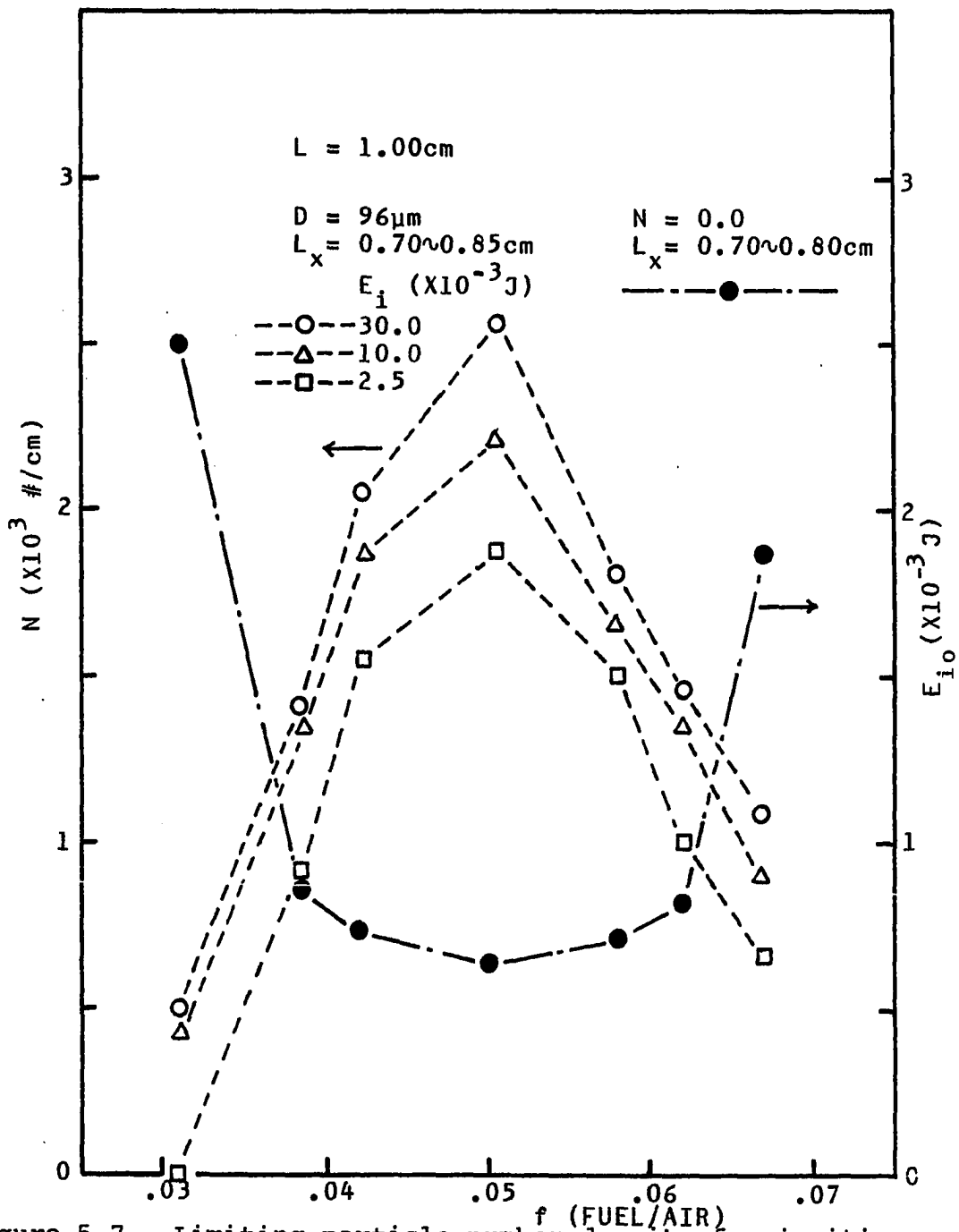


Figure 5.7. Limiting particle number density for ignition vs. fuel-air ratio

function of the heat of combustion (or the adiabatic flame velocity). Therefore, the rate of heat generation must be also an important factor governing the thermal equilibrium of the multiphase mixture during ignition. The figure also predicts that the ignition range of fuel-air ratio (minimum to maximum) is decreased and goes to zero for a given spark energy when the particle number density increases.

Likewise, further experiments were carried out for different average particle diameters of 68, 48 and 34 μm and are shown in Figures 5.8 through 5.10. Similar trends but different ranges in the particle number density for the various particle sizes are observed. For 34 μm particles, the experiment was carried out for a particle number density always above $20 \times 10^3 \text{ \#/cm}^3$, since the clouds tend to become unsteady when the particle feed rate is decreased so as to generate a smaller particle number density.

4. Correlation

The limiting particle number densities for ignition are shown against the average particle diameter, at the same ignition energy and fuel-air ratio, in Figure 5.11. These appear to be linear on logarithmic scales with the average slope of about -2.0, except for the case of 34 μm particles. Therefore, a new parameter relating to the ignition phenomena can be taken as ND^2 . The critical spark energy for

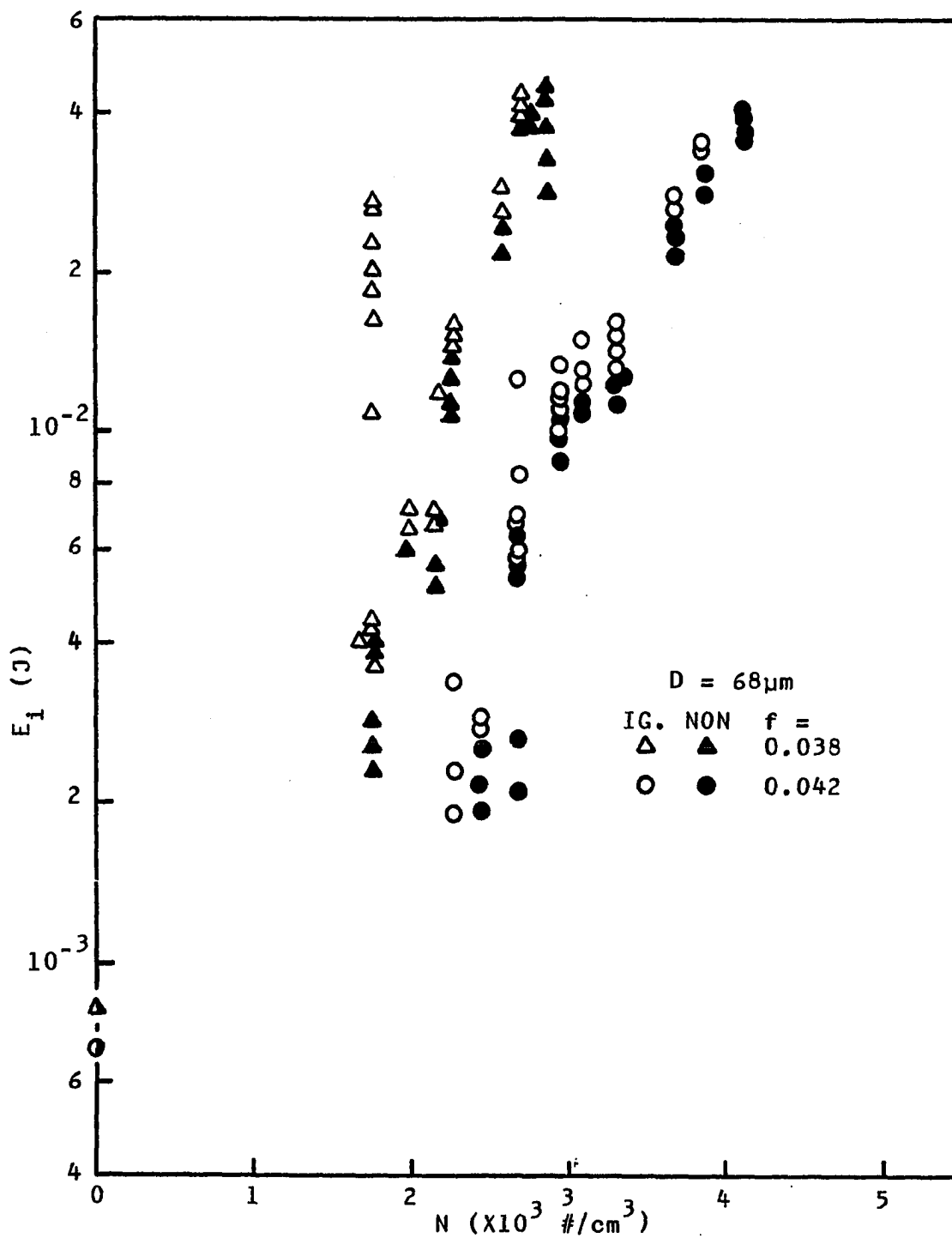


Figure 5.8a. Spark ignition energy vs. particle number density, $D = 68 \mu\text{m}$

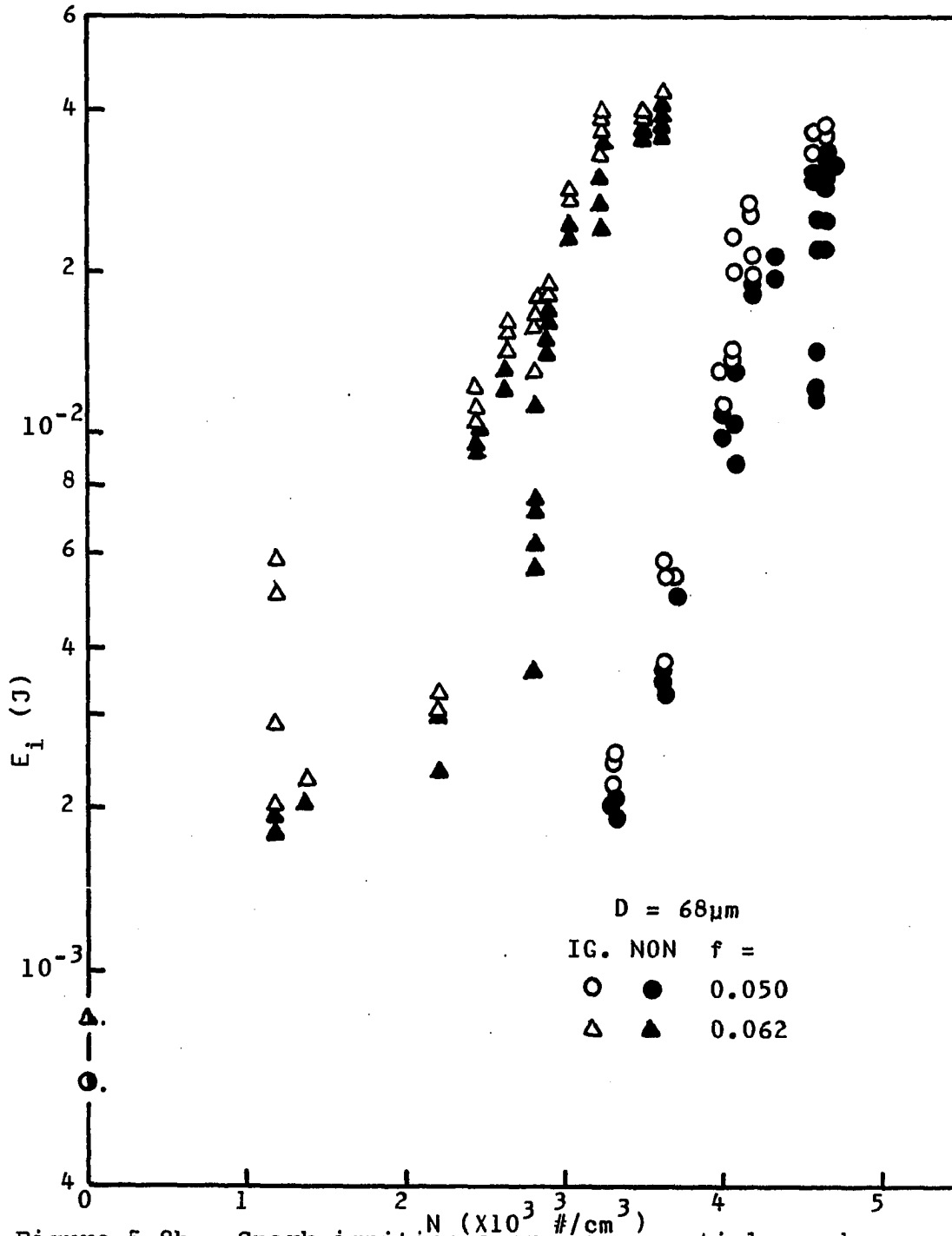


Figure 5.8b. Spark ignition energy vs. particle number density, $D = 68 \mu\text{m}$

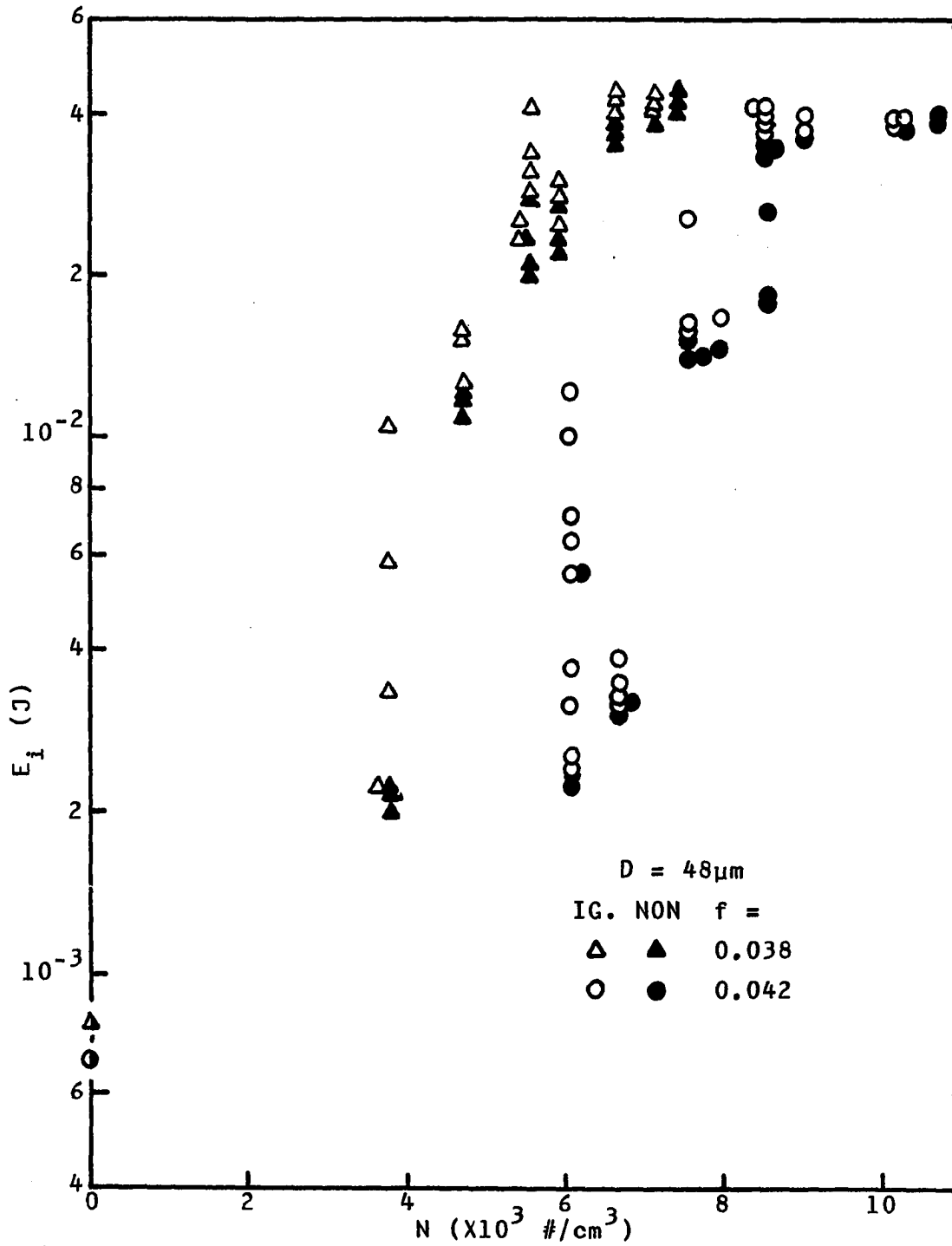


Figure 5.9a. Spark ignition energy vs. particle number density, $D = 48 \mu\text{m}$

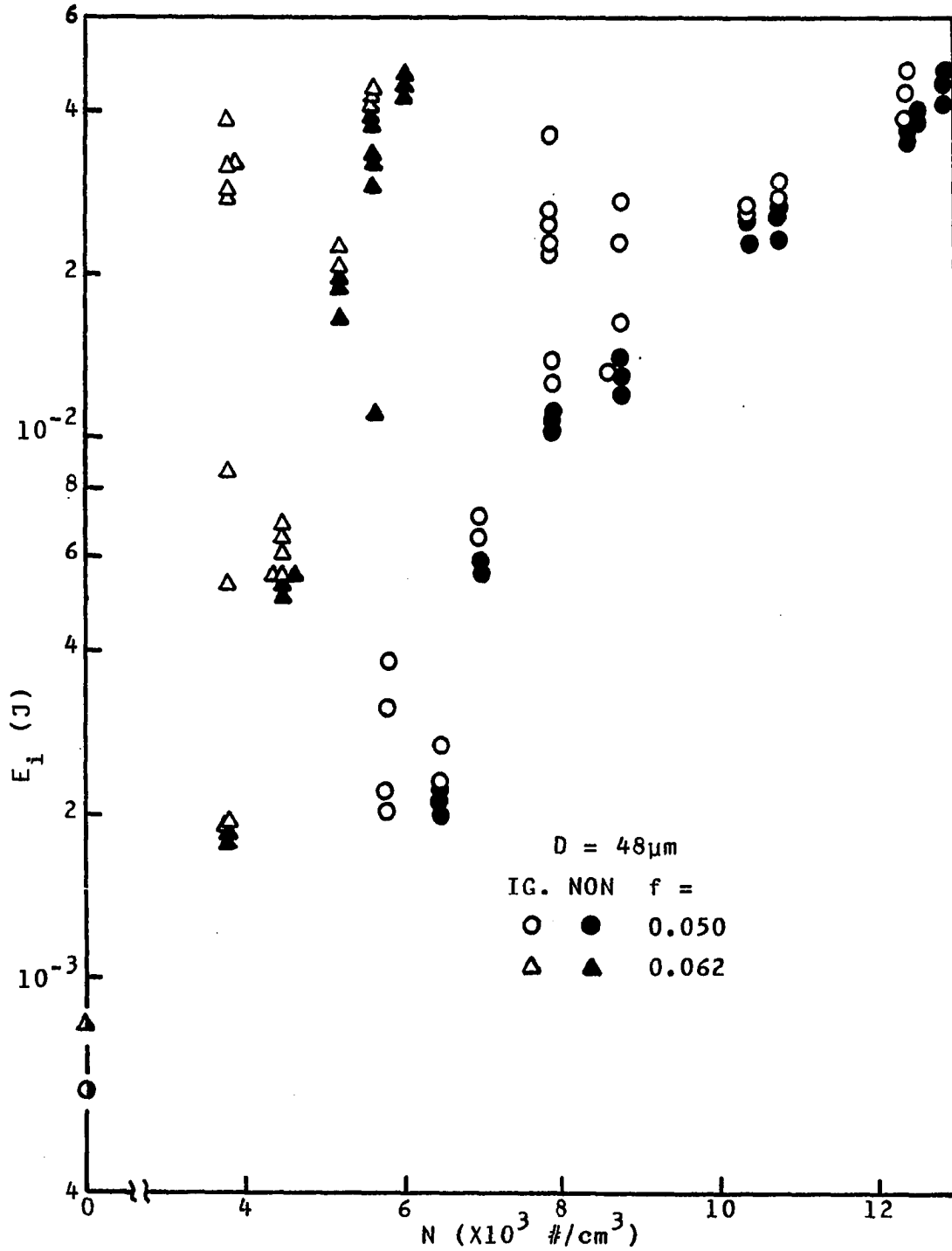


Figure 5.9b. Spark ignition energy vs. particle number density, $D = 48 \mu\text{m}$

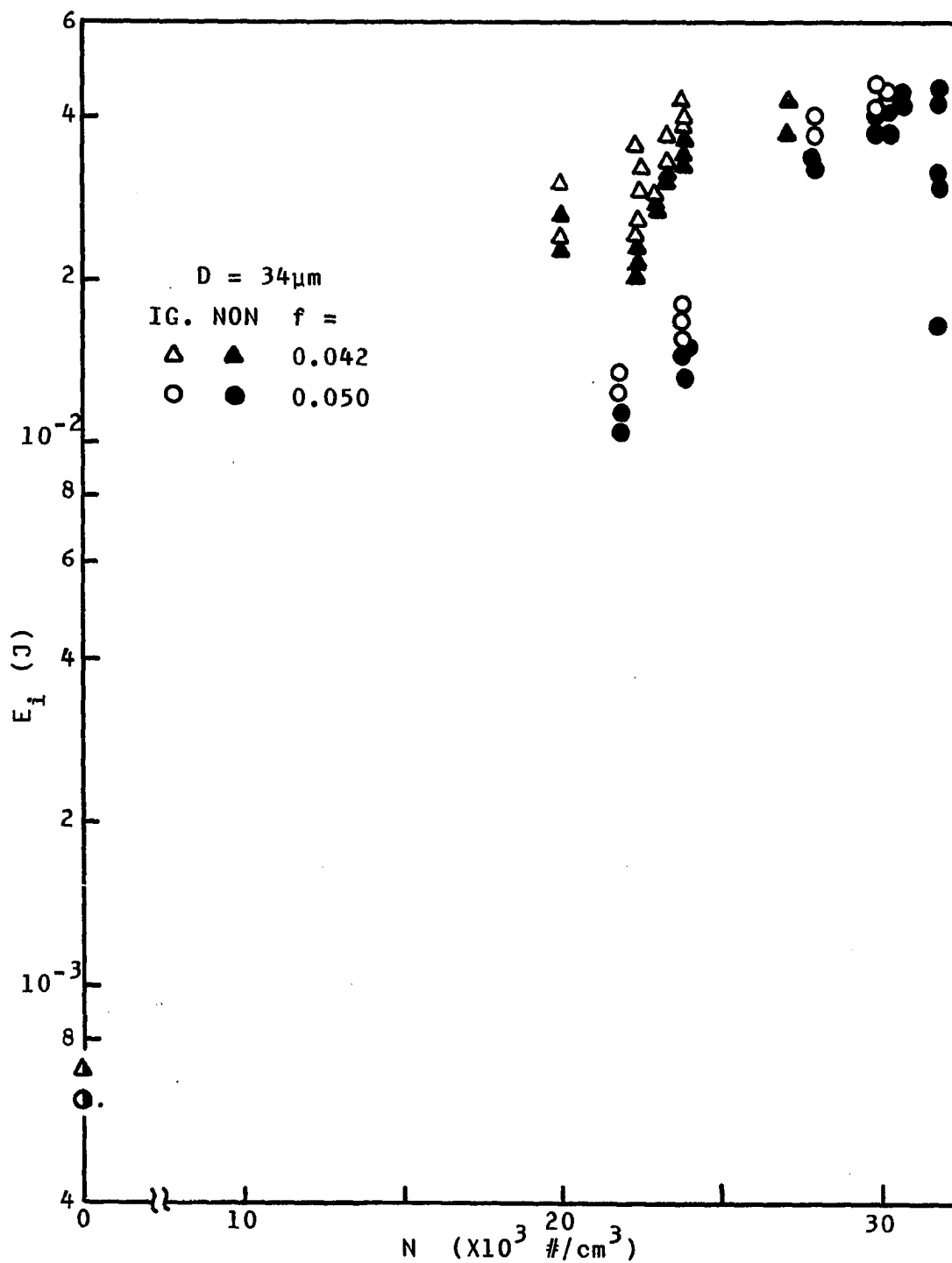


Figure 5.10. Spark ignition energy vs. particle number density, $D = 34 \mu\text{m}$

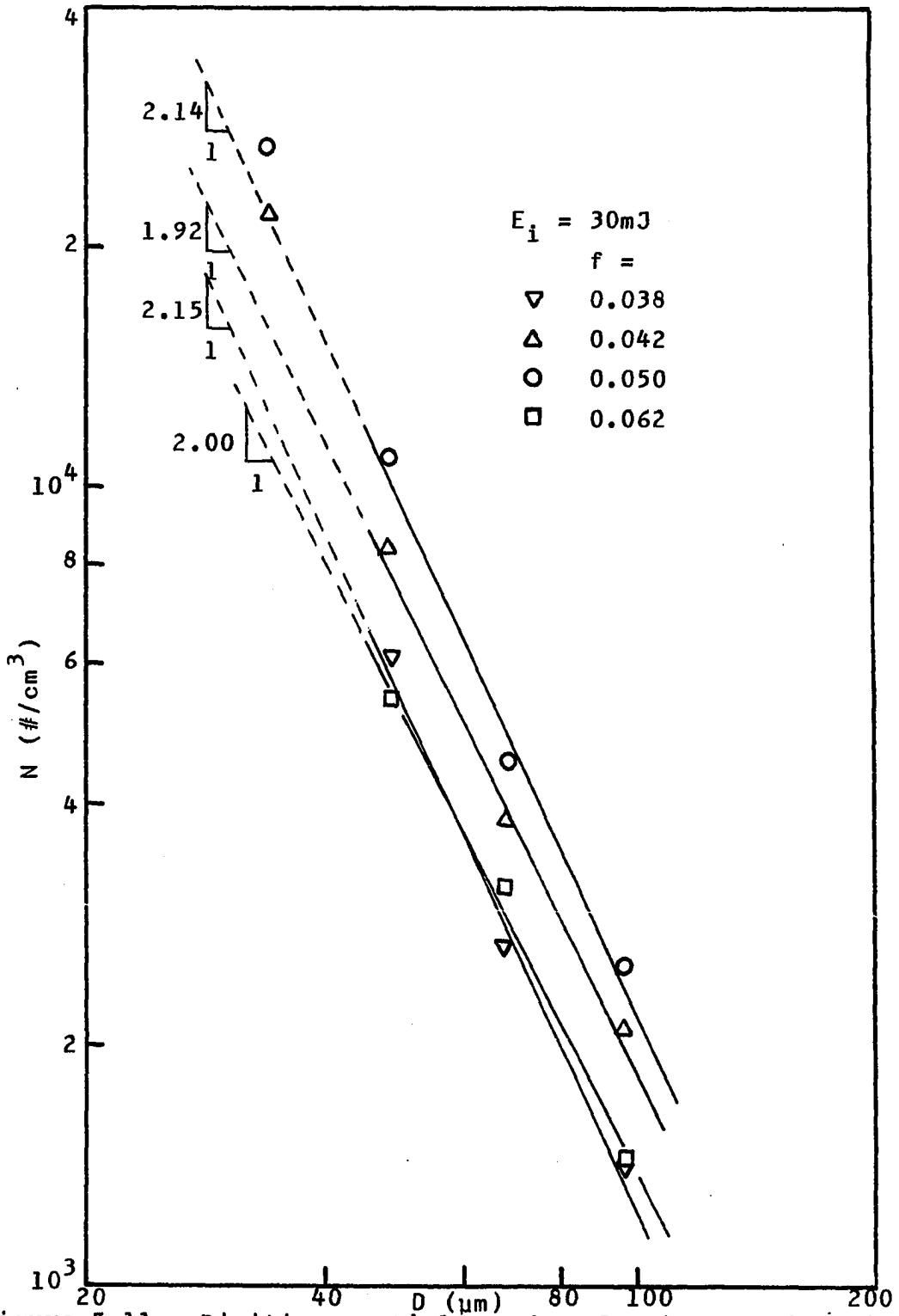


Figure 5.11. Limiting particle number density for ignition vs. average particle diameter

ignition (E_i) was then replotted in Figures 5.12a-d versus ND^2 showing correlated single trends.

For 34 μm particles, these points are shifted somewhat toward a higher ND^2 . One possible explanation for the shift is that a high energy of a spark may disturb the uniformity of the cloud during its channel expansion, thus, more particles per volume were required to quench the ignition process at that spark energy. Creagh et al. [111] and Somerville and Williams [112] reported three stages of spark channel expansion in air, these are, the initial rapid compressed air expansion following the shock wave, the thermal expansion of the high temperature channel, and finally, the cooling down stage of the channel. Line et al. [113] noted that the short duration spark could disturb lycopodium dust of 30 μm diameter significantly and thus required more energy to ignite the clouds than that of the long duration spark. But, such effects of the particle size have not been clarified in terms of a disturbance caused by the spark channel expansion with or without ignition. Results from Figures 5.12b and 5.12c seem to show that the disturbance becomes noticeable when the spark energy increases and the particle size decreases; for example, with 48.5 μm particles at larger than 30 mJ and with 34 μm particles at larger than 25 mJ.

However, such a deviation of results for small particles

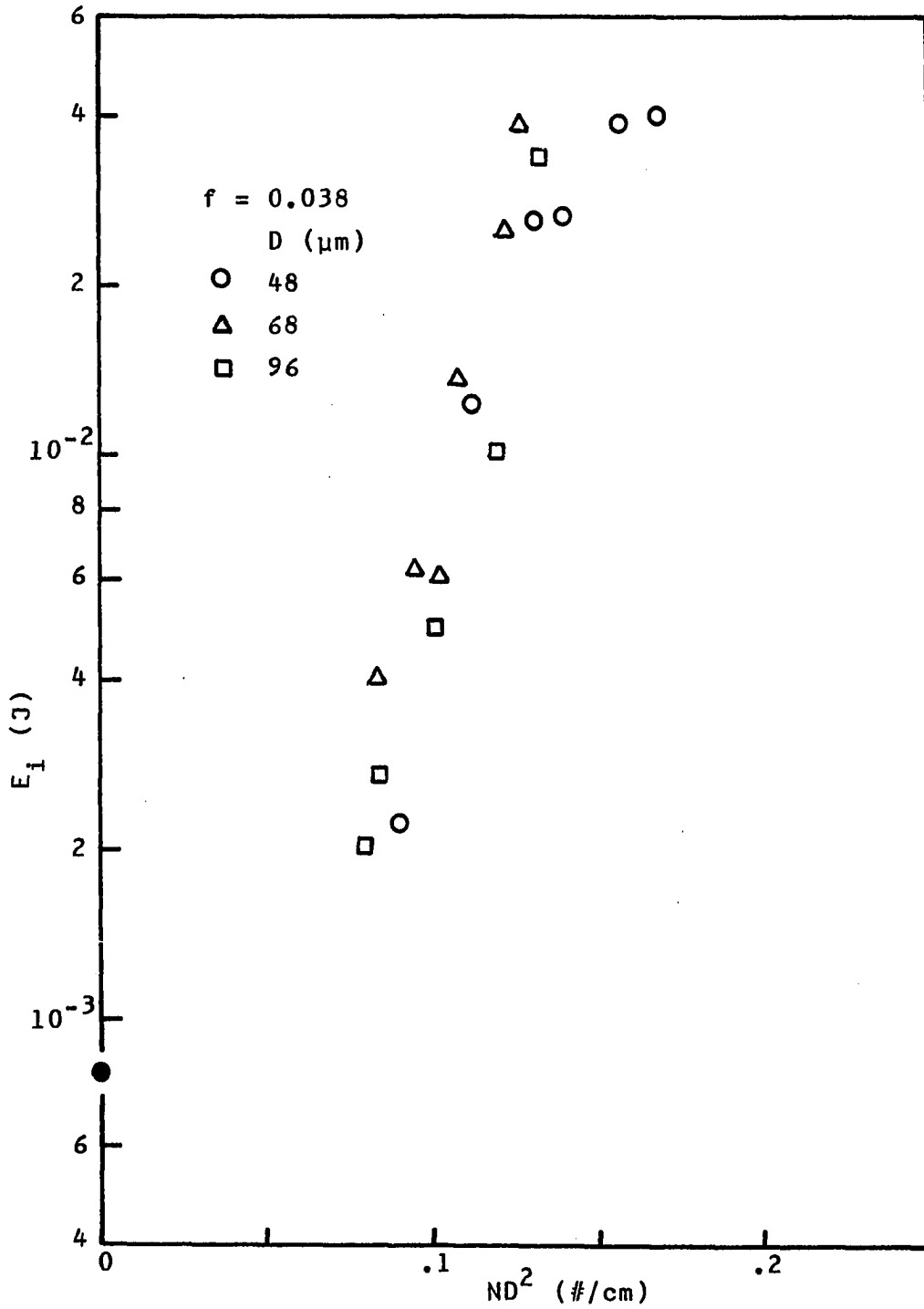


Figure 5.12a. Spark ignition energy vs. particle surface area per mixture volume, $f = 0.038$

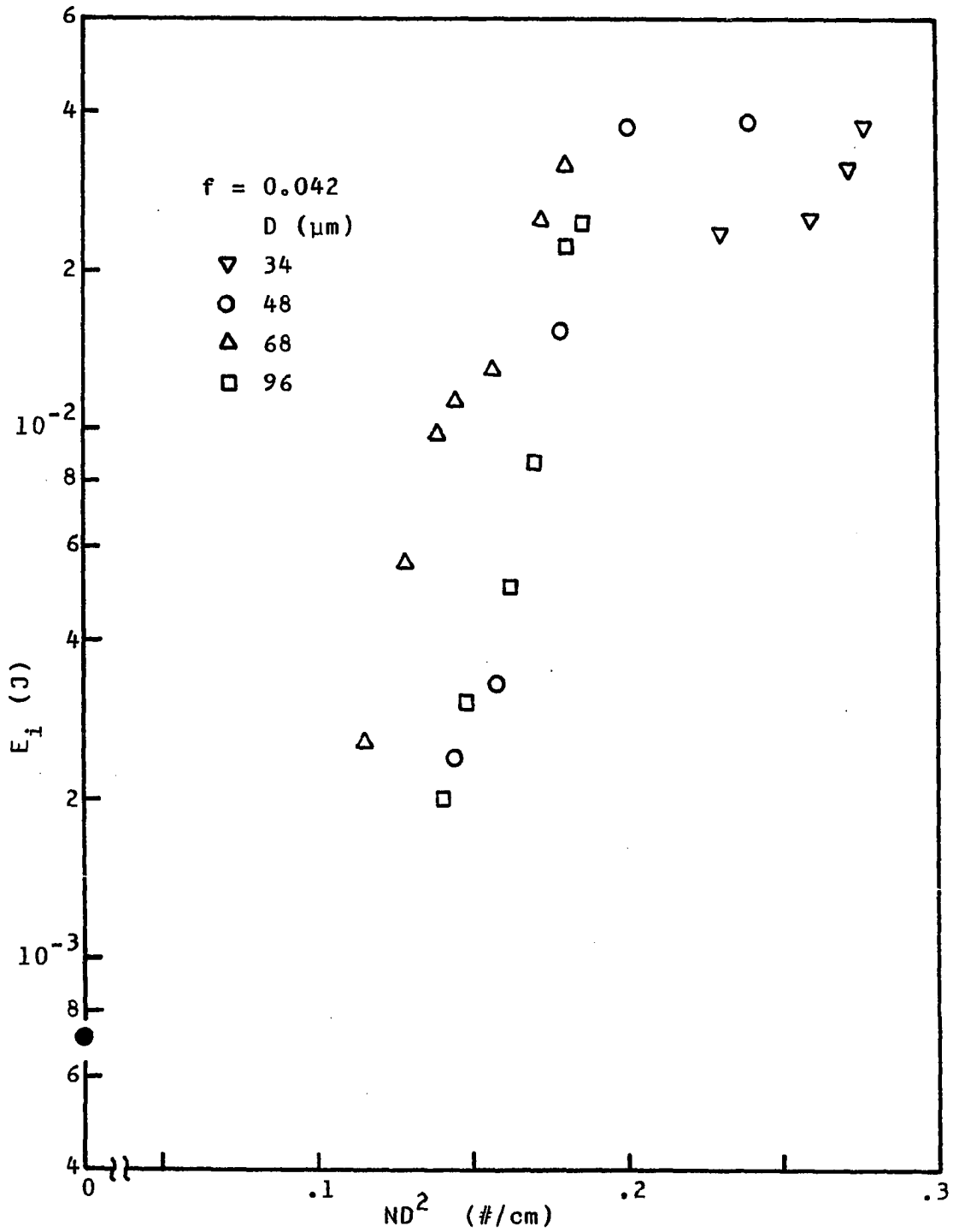


Figure 5.12b. Spark ignition energy vs. particle surface area per mixture volume, $f = 0.042$

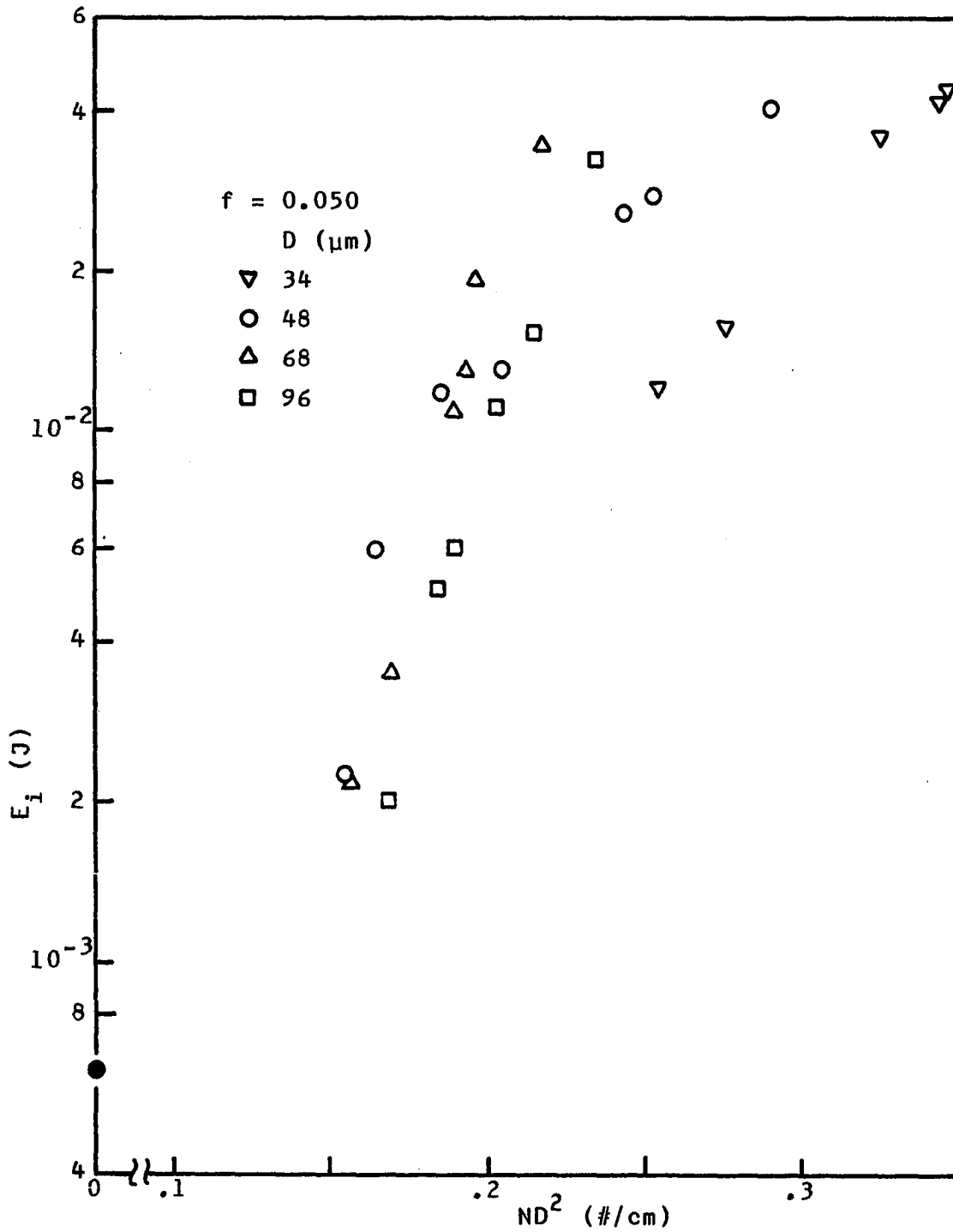


Figure 5.12c. Spark ignition energy vs. particle surface area per mixture volume, $f = 0.050$

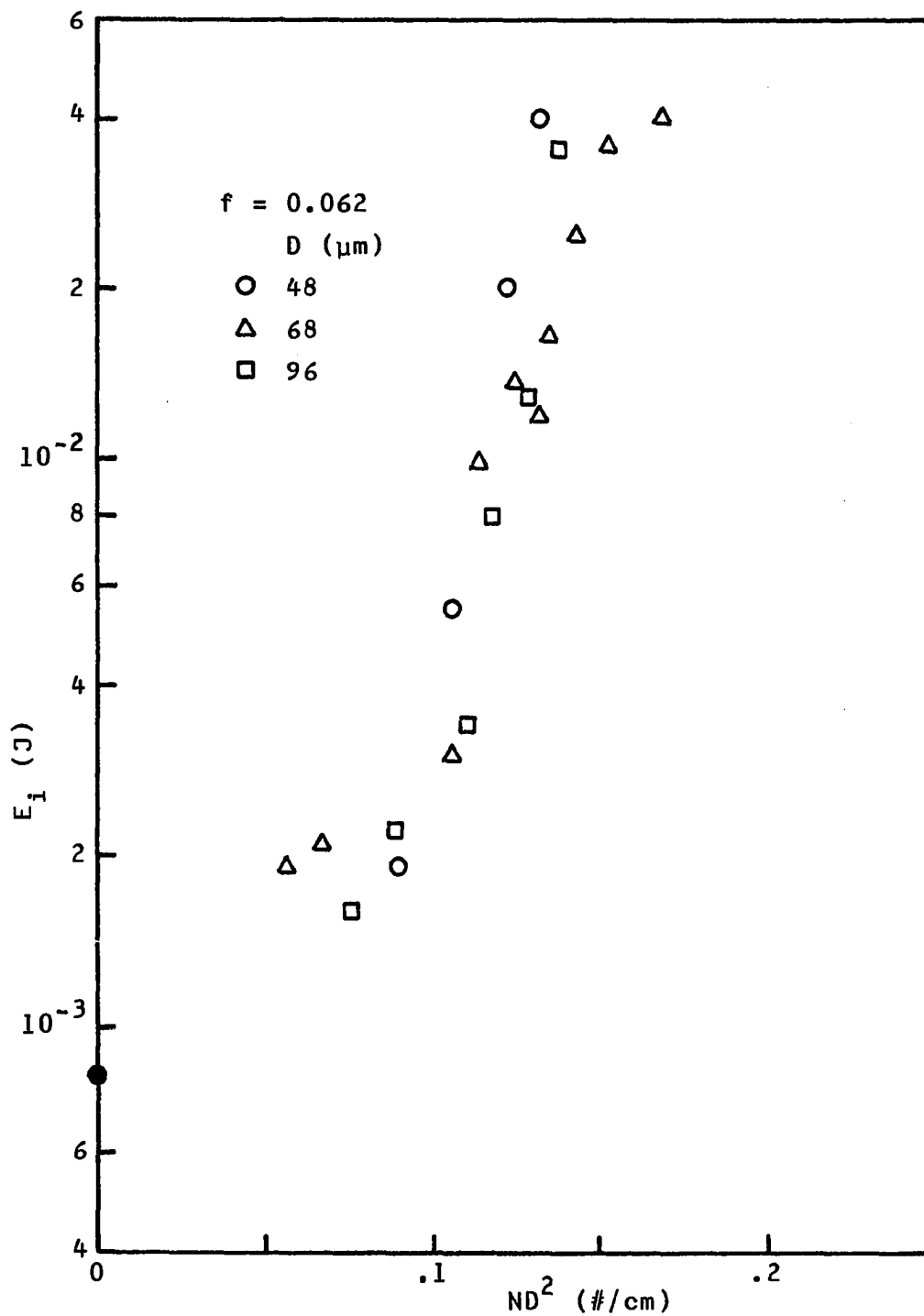


Figure 5.12d. Spark ignition energy vs. particle surface area per mixture volume, $f = 0.062$

from the normal trend of E_i vs. ND^2 can be removed, if the average particle diameter of the cloud is assumed to be $39\sim 40\ \mu\text{m}$, since the particle number density determined by the current-particle number density calibration curve can be smaller at the same current. This follows since the particle number density recalculated from Equation 2.1 becomes smaller at the same W and larger D . However, such an assumption is not expected since the most probable size of the particles shown in Appendix B seems to be just smaller than $34\ \mu\text{m}$.

The correlation parameter ND^2 can be interpreted as the total surface area of particles per volume of particle-gas mixtures. The theory developed by Dewitte et al. [92] for the flame inhibition by solid inert particles based on the kinetic theory of gases predicted the actual kinetic temperature of the nonadiabatic flame as a function of ND^2 . They calculated the limiting mean kinetic temperature, from the critical particle number density of $4.9 \times 10^5\ \text{\#/cm}^3$ for alumina (Al_2O_3) particles of $20\ \mu\text{m}$ diameter in $10.9\% \text{CH}_4$ - $21.6\% \text{O}_2$ - $67.5\% \text{N}_2$ gases, below which no flame can be self-sustaining. Although their theory was of a steady state nature, the parameter as a total heat transfer area between particles and gases seems to play an important role in the unsteady process of ignition.

Evidently, the reciprocal $1/(N \frac{\pi}{4} D^2)$ has the dimension

of length. This is either the mean distance over which a radical of reacting gases has to diffuse before reaching a solid particle or the particle-to-particle distance in the cloud based on the particle projected area. Therefore, it can be said that the particle-gas mixture can not be ignited when its characteristic length is shorter than the some allowable minimum length for ignition at a given spark energy. This concept is similar to the quenching distance. For example, when $E_i = 30 \times 10^{-3} \text{ J}$ and $f = 0.050$, the critical length is

$$\frac{1}{\frac{\pi}{4} ND^2} = \frac{1}{\frac{\pi}{4} \times 23} = 0.0554 \text{ m} = 5.54 \text{ cm}$$

It is noteworthy that the characteristic length $1/(\frac{\pi}{4} ND^2)$ for flame quenching can be calculated to be 0.65 cm from the critical particle number density $4.9 \times 10^5 \text{ \#/cm}^3$ reported by Dewitte et al. [92], where the quenching distance of the gas mixture is about 0.22 cm (Lewis and von Elbe [54]). Therefore, it appears that the range of particle number density in the present study is much below the critical particle number density for flame inhibition (propagation limit).

An attempt was made to correlate the ignition energy E_i and ND^2 . This was done by plotting experimental results based on $\text{Log}(E_i/E_{i0})$ and ND^2 in Figure 5.13 using log-log

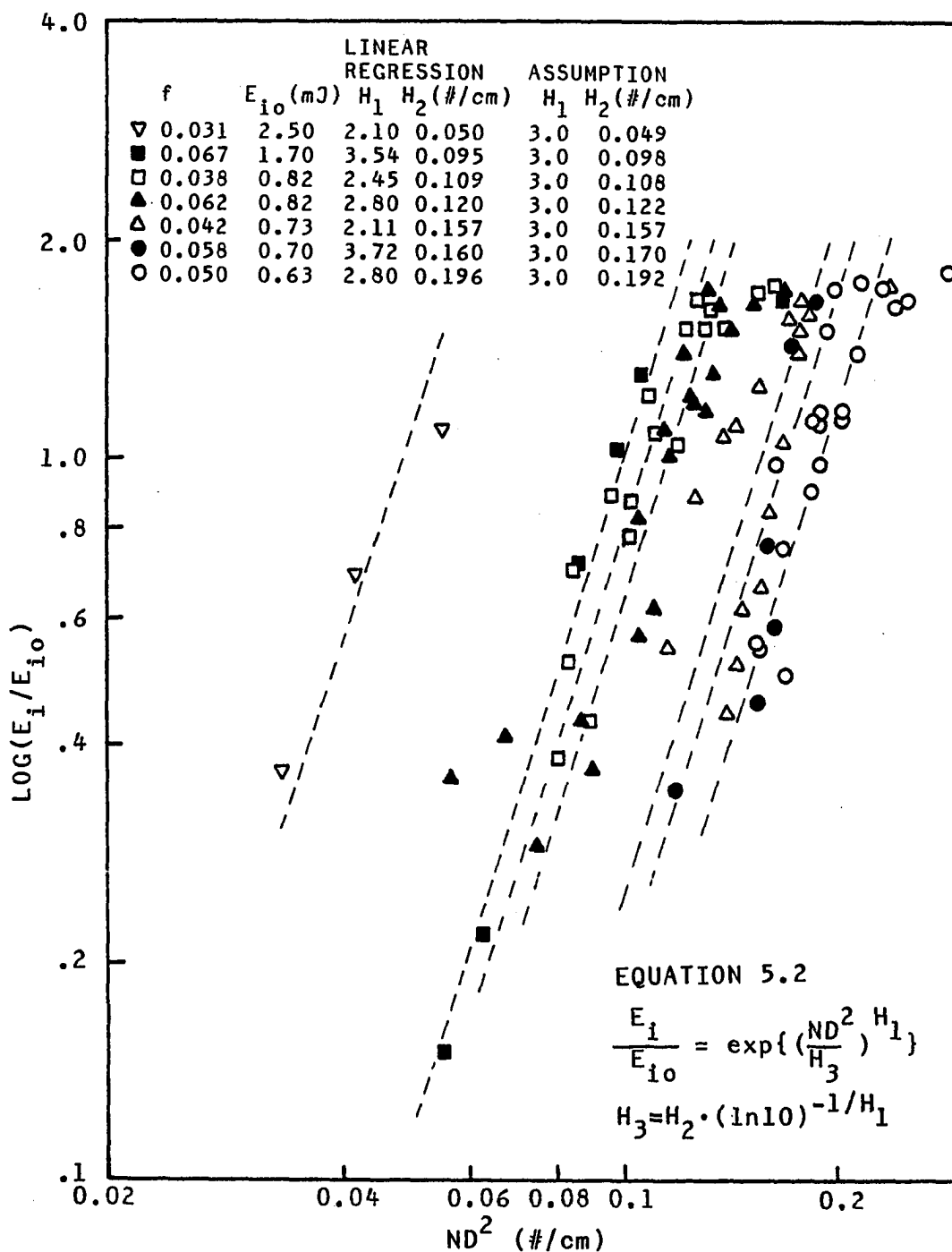


Figure 5.13. Logarithm of nondimensional spark ignition energy vs. particle surface area per mixture volume

scales for various fuel-air ratios, where E_{i0} is the ignition energy of a particle-free combustible gas. When linear lines are assumed, the ignition energy can be written

$$E_i = E_{i0} \exp\left[\left(\frac{ND^2}{H_3}\right)^{H_1}\right] \quad \text{and} \quad H_3 = H_2 [\ln 10]^{-1/H_2} \quad (5.2)$$

where H_1 and H_2 are only a function of the fuel-air ratio. The values of H_1 and H_2 obtained using the linear regression method are given in Figure 5.13. The lines shown in the figure represent Equation 5.2 with $H_1 = 3.0$ and assumed values of H_2 (which are compared with calculated values in the figure). The experimental data are replotted in Figure 5.14 using semi-logarithmic scales and compared with Equation 5.2 again for $H_1 = 3.0$ and the assumed H_2 .

Finally, values of ND^2 calculated from Equation 5.2 for $H_1 = 3.0$ and the assumed H_2 are plotted in Figure 5.15 against fuel-air ratios for four ignition energies. Trends in this figure are similar in form to those in Figure 5.7.

C. Conclusion

The moving needle of this system into the quenching region is observed not to be significantly influencing the ignition process, at least, when its velocity is probably smaller than the ignition kernel expansion velocity. Also, it is found that additional spark energy is always required

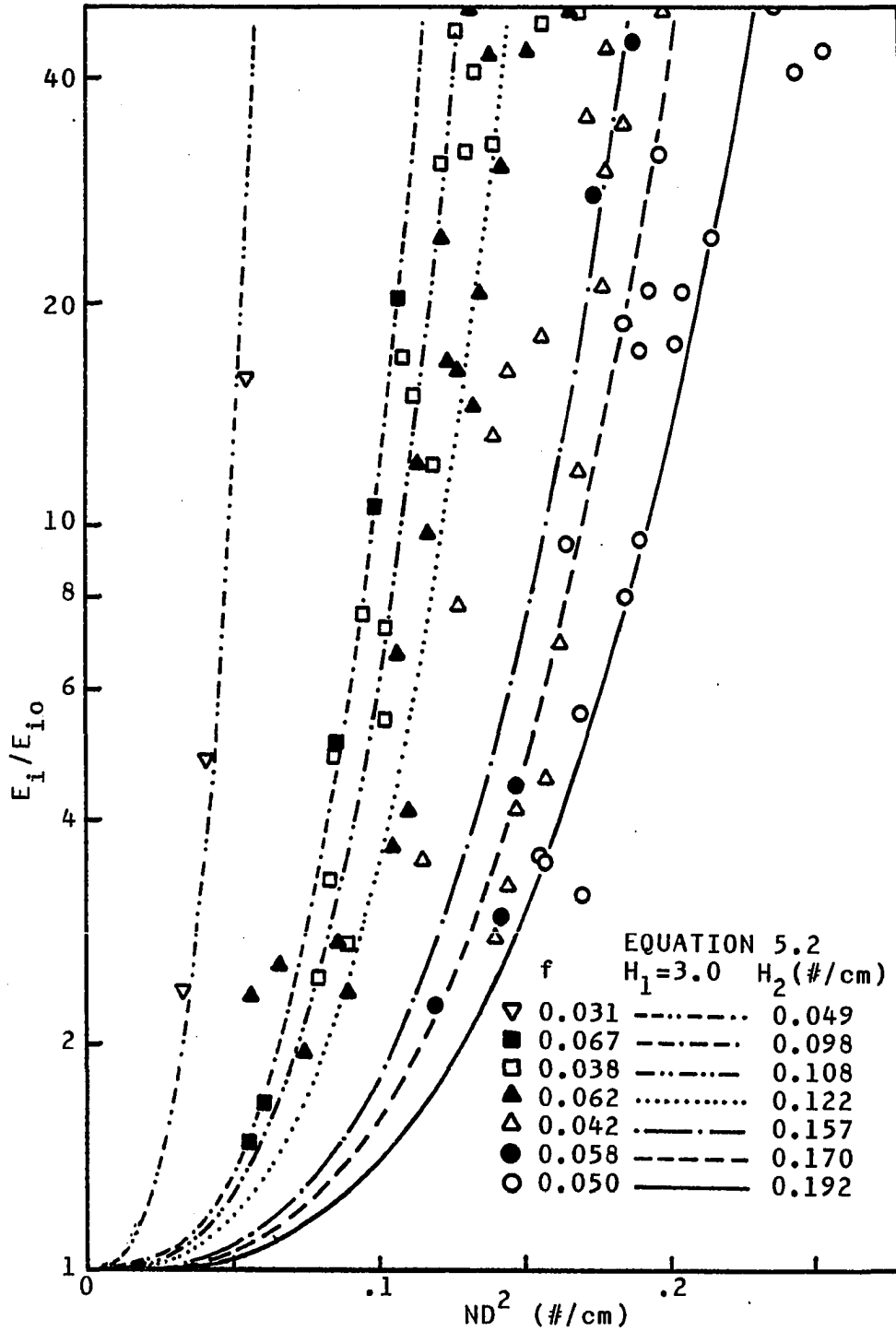


Figure 5.14. Nondimensional spark ignition energy vs. particle surface area per mixture volume

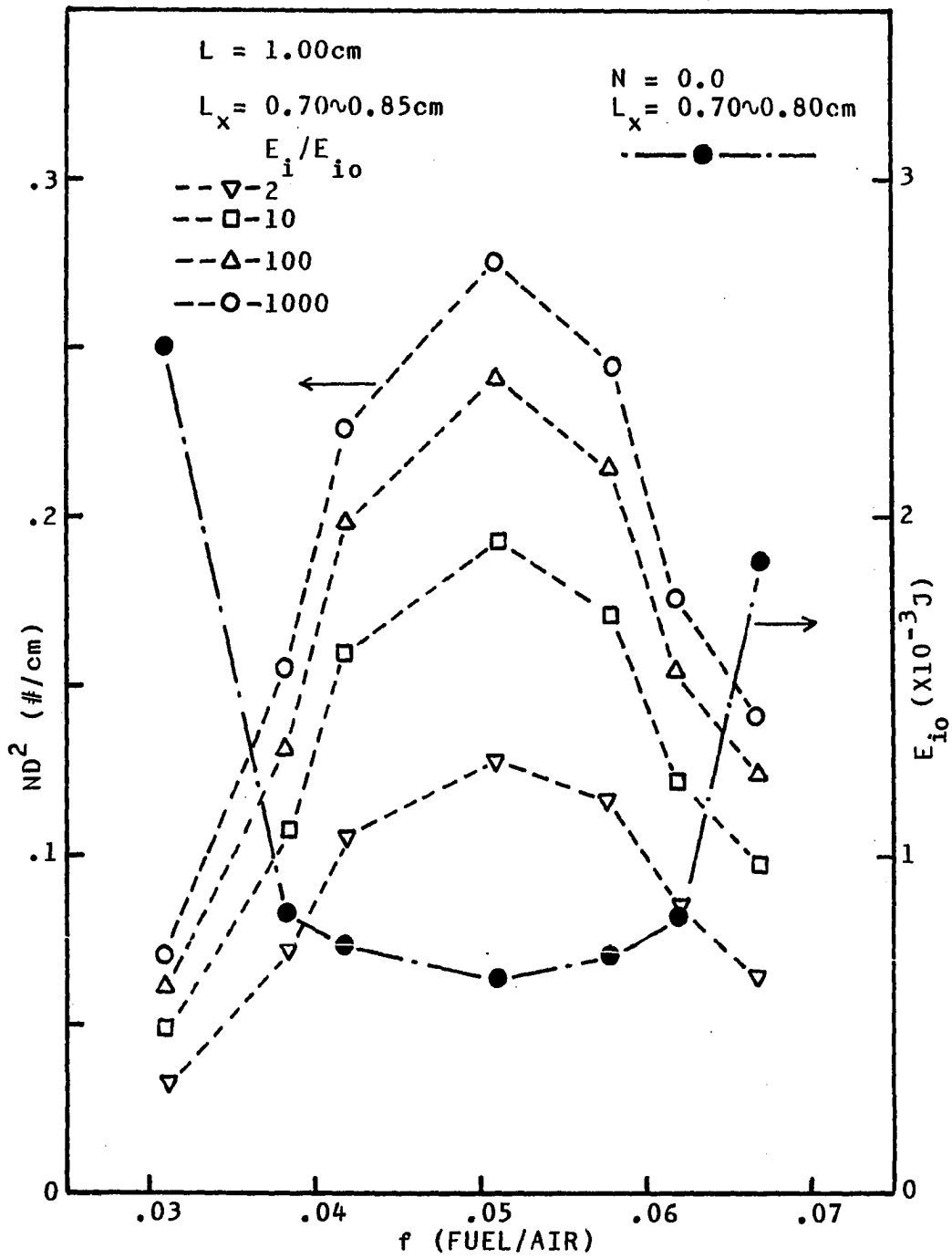


Figure 5.15. Particle surface area per mixture volume vs. fuel-air ratio

in order to ignite the uniform inert particle-combustible gas mixture as the particle number density increases.

The average particle diameter and the limiting particle number density for ignition at a fixed spark energy and fuel-air ratio are correlated to give a new parameter πND^2 (the total surface area of particles per volume of the mixture) or $(\frac{\pi}{4} ND^2)^{-1}$ (the mean particle characteristic length). The latter can be considered as either the mean diffusion distance of a radical before touching a particle or the average particle-to-particle distance based on its projected area. Therefore, it can be said that in order to initiate a self-sustaining flame by a spark through the multiphase mixture for a given spark energy and fuel-air ratio, the total particle surface area per mixture volume should be smaller than its limiting value or the mean characteristic length should be longer than its limiting value. Furthermore, the spark energy for ignition is observed to increase exponentially with $(ND^2)^3$.

When the particle number density increases, the ignition range of the fuel-air ratio for the multiphase mixture is decreased for a given spark energy until the particle number density reaches a maximum allowable value for ignition at a propane-air ratio of 0.050.

VI. CONCLUSIONS AND RECOMMENDATIONS

An experimental study has been conducted to determine the effects of particles, which are uniformly suspended between parallel electrodes, on electrical breakdown, electrical discharge, and ignition in the presence of a combustible gas. The spark was triggered by a needle injected into the system at high speed so as not to disturb the uniformity of the suspension.

The primary variables investigated were the particle number density, particle diameter, breakdown voltage, breakdown needle position, electrode separation distance, stored charge, stored energy, and the fuel-air ratio. Because of randomness associated with electrical breakdown, electrical discharge and ignition, tests were repeated so as to get an average effect. The following conclusions can be drawn from the investigation:

1. For the same breakdown needle position, the breakdown voltage of a positive moving needle is about 50 percent higher than that of a positive stationary needle, while the breakdown voltage of a negative moving needle is not significantly different from that of a negative stationary needle. For a fixed applied voltage, the breakdown is delayed about $10^{-3} \sim 10^{-4}$ sec after the positive

needle passes the position of breakdown of a positive stationary needle (this time is the same order of magnitude as a statistical breakdown time lag).

2. A particle of about 1 mm diameter oscillating between parallel electrodes initiates breakdown at a lower voltage than a particle-free breakdown voltage and usually when it is near the positive electrode.
3. Pre-charged particulate clouds show little influence on the breakdown voltage of a negative moving needle, but have a strong influence on the breakdown voltage of a positive moving needle by lowering the voltage as much as one-third to one-half of its value in the absence of particles. For a positive needle and a fixed applied voltage, the presence of particles shortens the breakdown delay time compared to that of a particle-free gap by increasing the probability of breakdown triggering. With particles, the spread in the randomness of the needle position at breakdown is reduced.
4. The breakdown characteristics of a positive moving needle can be described by two parameters. One is related to the geometry of the two electrode-needle

system. The other is related to the particle suspension dynamics; more specifically, it is the characteristic value of a breakdown needle gap distance compared to a particle effective mean free path. This characteristic value represents the probability that a particle will undergo a collision in traveling the distance from the negative electrode to a needle tip at the breakdown position. As such, it should determine the charge interchange and/or charge loss during these collisions. An equation is given which satisfactorily correlates the data based on the two aforementioned parameters.

5. The two-pulse discharge triggered by a positive moving needle through a charged particulate cloud is similar to that observed for a particle-free gap triggered by a positive stationary needle via free electrons. This comparison is possible as long as the breakdown voltage and the needle position at breakdown are nearly the same and the systems are not overvolted.
6. The total amount of spark charge or energy released from a capacitor for either a one or a two-pulse discharge (~ 10 nsec) is nearly the same as the

stored charge or energy whether a particulate cloud is present or the electrodes are overvolted.

7. For the ignition of uniform mixtures of inert particle-combustible gases, an average particle surface area per unit volume of the mixture should be smaller than a critical value (or an inter-particle distance based on the particle projected area should be longer than its critical value), and the spark energy should be larger than its critical value. This critical spark energy increases exponentially with the third power of the particle surface area per unit volume.
8. The range of fuel-air ratio for ignition, at a given spark energy, decreases with an increase in the particle surface area per unit mixture volume until it reaches its maximum value at the propane-air ratio of 0.05 (somewhat richer than stoichiometric).

Overall, the present study shows that the presence of uniform particulate clouds influence the electrical breakdown, electrical discharge, and the ignition behavior of gas-solid mixtures.

To further clarify the phenomena and to extend the investigation, the following recommendations are made:

1. Further analysis and investigation are required which lead to modeling of the most probable mechanisms of electrical breakdown triggered by charged uniform particles and also which clarify the validity of the present correlations for application to different electrode geometries, needle velocities, voltage history applications, particle shapes, and particle materials.
2. Based on the proposed interpretation of the present correlation for ignition, both the detailed and the overall quenching mechanisms as a result of the presence of uniform inert particulate clouds during spark ignition should be investigated.
3. As a result of anomalous data collected on small particles ($\sim 34 \mu\text{m}$), further studies are suggested which clarify how thermal or shock waves (for example, generated by a strong spark) interact with uniform particulate clouds.

VII. BIBLIOGRAPHY

1. Colver, G. M. "Spark Breakdown of Particulate Clouds, a Review." Paper presented at the 13th Annual Conference, Fine Particle Society, Chicago, 1982.
2. Tryon, G. H., and McKinnon, G. P. Fire Protection Handbook. Boston: National Fire Protection Association, 1969.
3. Palmer, K. N. Dust Explosions and Fires. London: Chapman and Hall, 1973.
4. Bartknecht, W. Explosions. Berlin: Springer-Verlag, 1981.
5. Gugan, K. Unconfined Vapor Cloud Explosions. Rugby, Warks, England: The Institution of Chemical Engineers, 1978.
6. Townsend, J. S. "The Conductivity Produced in Gases by the Motion of Negatively-Charged Ions." Nature 62 (1900): 340-341.
7. Townsend, J. S. The Theory of Ionization of Gases by Collision. London: Constable & Co. Ltd., 1910.
8. Townsend, J. S. Electrons in Gases. London: Hutchinson's Scientific and Technical Publications, 1947.
9. Loeb, L. B., and Meek, J. M. The Mechanism of the Electric Spark. Stanford, California: Stanford University Press, 1941.
10. Loeb, L. B. Fundamental Processes of Electrical Discharge in Gases. New York: John Wiley & Sons, Inc., 1947.
11. Loeb, L. B. Basic Processes of Gaseous Electronics. Berkeley: University of California Press, 1955.
12. Cobine, J. D. Gaseous Conductors. New York: McGraw-Hill Book Company, Inc., 1941.
13. Nasser, E. Fundamentals of Gaseous Ionization and Plasma Electronics. New York: John Wiley and Sons, Inc., 1971.

14. Raether, H. Electron Avalanches and Breakdown in Gases. Washington: Butterworths, 1964.
15. Haydon, S. C. Discharge and Plasma Physics. Armidale, Australia: The University of New England, 1964.
16. Loeb, L. B. Electrical Coronas. Berkeley: University of California Press, 1965.
17. Gallo, C. F. "Corona-A Brief Status Report." IEEE Transactions on Industry Applications IA-13 (1977): 550-557.
18. Pedersen, A. "Criteria for Spark Breakdown in Sulfur Hexafluoride." IEEE Transactions on Power Apparatus and Systems PAS-89 (1970):2043-2048.
19. Karlsson, P. W., and Pedersen, A. "Inherent Limitations in Uniform Field Discharge Data for SF₆." IEEE Transactions on Power Apparatus and Systems PAS-91 (1972): 1597-1601.
20. Cookson, A. H. "Electrical Breakdown for Uniform Fields in Compressed Gases." Proceedings of IEE 117 (1970): 268-280.
21. Cookson, A. H. "Review of High-voltage Gas Breakdown and Insulators in Compressed Gases." Proceedings of IEE 128 (1981):303-312.
22. Farrall, G. A. "Conduction and Breakdown in Vacuum." GE Report No. 78CRD149, 1978.
23. Zuber, K. "Über die Verzögerungszeit bei der Funkenentladung." Annalen der Physik 76 (1925):231-260.
24. Laue, M. V. "Bemerkung zu K. Zubers Messung der Verzögerungszeiten bei der Funkenentladung." Annalen der Physik 76 (1925):261-265.
25. Tilles, A. "A Survey of Time Lag of Sparkover in a Uniform Field." Physical Review 46 (1934):1015-1022.
26. White, H. J. "Effect of Intense Illumination on Time Lag in Static Spark Breakdown." Physical Review 49 (1936):507-512.

27. Wilson, R. R. "Very Short Time Lag of Sparking." Physical Review 50 (1936):1082-1088.
28. Colver, G. H. "Dynamic and Stationary Charging of Heavy Metallic and Dielectric Particles against a Conducting Wall in the Presence of a DC Applied Electric Field." Journal of Applied Physics 47 (1976):4839-4849.
29. Berger, S. K. "Reduction of Breakdown Voltage in Uniform and Coaxial Fields in Atmospheric Air through Moving Conducting Spheres." Third International Conference on Gas Discharges (Conference Publication No. 118), pp. 380-384. London: IEE, 1974.
30. Wootton, R. E., Cookson, A. H., Emery, F. T., and Farish, O. "Investigation of High-Voltage Particle-Initiated Breakdown in Gas-Insulated Systems." EL-1007, Electric Power Research Institute Research Project 7835, DOE E(49-18)-2125, 1979.
31. Cookson, A. H., Bolin, P. C., Doepken, H. C., Jr., Wootton, R. E., Cooke, C. M., and Trump, J. G. "Recent Research in the United States on the Effect of Particle Contamination Reducing the Breakdown Voltage in Compressed Gas-Insulated Systems." Paper No. 15-9. International Conference on Large High Voltage Electric Systems, Paris, 1976.
32. Cooke, C. M., Wootton, R. E., and Cookson, A. H. "Influence of Particles on AC and DC Electrical Performance of Gas Insulated Systems at Extra-High-Voltage." IEEE Transactions on Power Apparatus and System PAS-96 (1977):768-777.
33. Anis, H., and Srivastava, K. D. "Movement of Charged Conducting Particles Under Impulse Voltages in Compressed Gases." Conference Record-IAS Annual Meeting, pp. 1048-1055. New York: IEEE, 1980.
34. Anis, H., and Srivastava, K. D. "Free Conducting Particles in Compressed Gas Insulation." IEEE Transactions on Electrical Insulation EI-16 (1981):327-338.

35. Anis, H., and Srivastava, K. D. "Generalized Break-down Criteria for Particle-Contaminated Sulphur Hexafluoride under DC, AC and Impulse Voltages." Sixth International Conference on Gas Discharges and their Applications (Conference Publication No. 189), pp. 220-223, London: IEE, 1980.
36. Anis, H., and Srivastava, K. D. "Particle-Initiated Breakdowns in Compressed Gas Insulation under Time-Varying Voltages." IEEE Transactions on Power Apparatus and Systems PAS-100 (1981):3694-3699.
37. Hara, M., and Akazaki, M. "A Method for Prediction of Gaseous Discharge Threshold Voltage in the Presence of a Conducting Particle." Journal of Electrostatics 2 (1976/1977):223-239.
38. Schulz, W. "The Influence of Dust on the A.C. Break-down Voltage of a Rod Gap in Air." Sixth International Conference on Gas Discharges and their Applications (Conference Publication No. 189), pp. 155-158. London: IEE, 1980.
39. Laghari, J. R., and Qureshi, A. H. "A Review of Particle-Contaminated Gas Breakdown." IEEE Transactions on Electrical Insulation EI-16 (1981):388-398.
40. Mulcahy, M. J. "Effect of Particles and Fibers on DC Breakdown Voltages in Air at Atmospheric Pressure." Second International Conference on Gas Discharges (Conference Publication No. 90), pp. 382-384. London: IEE, 1972.
41. Marode, E. "The Mechanism of Spark Breakdown in Air at Atmospheric Pressure between a Positive Point and a Plane. I. Experimental: Nature of the Streamer Track." Journal of Applied Physics 46 (1975):2005-2015.
42. Barreto, E. "The Formation of Sparks of Minimum Ignition Energy." IEEE Transactions on Industry Applications IA-14 (1978):530-536.
43. Barreto, E., Jurenka, H., and Reynolds, S. I. "The Formation of Small Sparks." Journal of Applied Physics 48 (1977):4510-4520.

44. Barreto, E., Reynolds, S. I., and Jurenka, H. "Ignition of Hydrocarbons and the Thermalization of Electrical Discharges." Journal of Applied Physics 45 (1974): 3317-3327.
45. Parnell, T. H. "The Spark and the External Circuit." Discharge and Plasma Physics, pp. 409-418. Edited by Haydon, S. C. Armidale, Australia: The University of New England, 1964.
46. Rose, H. E., and Pride, T. "An Investigation of the Characteristics of Spark Discharges as Employed in Ignition Experiments." Seventh Symposium (International) on Combustion 7 (1959):65-74.
47. Lee, J. H., Knystautas, R., and Guirao, C. M. "Critical Power Density for Direct Initiation of Unconfined Gaseous Detonations." Fifteenth Symposium (International) on Combustion 15 (1975):53-67.
48. Kono, M., Iinuma, K., Kumagai, S., and Sakai, T. "Spark Discharge Characteristics and Igniting Ability of Capacitor Discharge Ignition Systems." Combustion Science and Technology 19 (1978):13-18.
49. Maly, R., and Vogel, M. "Initiation and Propagation of Flame Fronts in Lean CH₄-Air Mixtures by the Three Modes of the Ignition Spark." Seventeenth Symposium (International) on Combustion 17 (1978):821-831.
50. Ballal, D. R., and Lefebvre, A. H. "The Influence of Spark Discharge Characteristics on Minimum Ignition Energy in Flowing Gases." Combustion and Flame 24 (1975):99-108.
51. Eckhoff, R. K. "Towards Absolute Minimum Ignition Energies for Dust Clouds?" Combustion and Flame 24 (1975):53-64.
52. Eckhoff, R. K. A Study of Selected Problems related to the Assessment of Ignitability and Explosibility of Dust Clouds. Bergen: A. S. John Geiegs Boktrykkeri, 1976.
53. Kono, M., Kumagai, S., and Sakai, T. "The Optimum Condition for Ignition of Gases by Composite Sparks." Sixteenth Symposium (International) on Combustion 16 (1976):757-766.

54. Lewis, B., and von Elbe, G. Combustion, Flames and Explosions of Gases. New York: Academic Press Inc., Publishers, 1951.
55. Calcote, H. F., Gregory, C. A., Jr., Barnett, C. M., and Gilmer, R. B. "Spark Ignition, Effect of Molecular Structure." Industrial and Engineering Chemistry 44 (1952):2656-2662.
56. Moorhouse, J., Williams, A., and Maddison, T. E. "An Investigation of the Minimum Ignition Energies of Some C₁ to C₇ Hydrocarbons." Combustion and Flame 23 (1974):203-213.
57. Kono, M., Kumagai, S., and Sakai, T. "Ignition of Gases by Two Successive Sparks with Reference to Frequency Effect of Capacitance Sparks." Combustion and Flame 27 (1976):85-98.
58. Knystautas, R., and Lee, J. H. "On the Effective Energy for Direct Initiation of Gaseous Detonations." Combustion and Flame 27 (1976):221-228.
59. Lee, J. H., and Matsui, H. "A Comparison of the Critical Energies for Direct Initiation of Spherical Detonations in Acetylene-Oxygen Mixtures." Combustion and Flame 28 (1977):61-66.
60. Rompe, Von R., and Weizel, W. "Über das Toeplersche Funkengesetz." Zeitschrift für Physik 122 (1944): 636-639.
61. Vlastós, A. E. "The Channel Resistance of Sparks." International Conference on Gas Discharges (Conference Publication No. 70), pp. 31-35. London: IEEE, 1970.
62. Hill, R. D. "Thermalization of a Spark Discharge." Journal of Applied Physics 46 (1975):2910-2914.
63. Andreev, S. I., and Vanyukov, M. P. "Application of Spark Discharge to Obtain Intense Light Flashes of Length 10⁻⁷-10⁻⁸ sec." Soviet Physics - Technical Physics 6 (1962):700-708.
64. Jones, G. W. "Inflammation Limits and Their Practical Application in Hazardous Industrial Operations." Chemical Review 22 (1938):1-26.

65. Mullins, B. P., and Penner, S. S. Explosions, Detonations, Flammability and Ignition. New York: Pergamon Press, 1959.
66. Potter, A. E., Jr. "Flame Quenching." Progress in Combustion Science and Technology, pp. 145-181. Edited by Ducarme, J., Gerstein, M., and Lefebvre, A. H. New York: Pergamon Press, 1960.
67. Putnam, A. A., and Jensen, R. A. "Application of Dimensionless Numbers to Flash-Back and Other Combustion Phenomena." Third Symposium on Combustion and Flame and Explosion Phenomena 3 (1949):89-98.
68. Cullen, R. E. "A Nondimensional Correlation of Flame Propagation at Subatmospheric Pressures." Transactions of the American Society of Mechanical Engineers 75 (1953):43-49.
69. Daniell, P. J. "The Theory of Flame Motion." Proceedings of Royal Society of London A126 (1930):393-405.
70. Spalding, D. B. "A Theory of Inflammability Limits and Flame-Quenching." Proceedings of Royal Society of London A240 (1956):83-100.
71. Mayer, E. "A Theory of Flame Propagation Limits Due to Heat Loss." Combustion and Flame 1 (1957):438-452.
72. Berlad, A. L., and Yang, C. H. "A Theory of Flame Extinction Limits." Combustion and Flame 4 (1960): 325-333.
73. Gerstein, M., and Stine, W. B. "Analytical Criteria for Flammability Limits." Fourteenth Symposium (International) on Combustion 14 (1972):1109-1118.
74. Friedman, R. "The Quenching of Laminar Oxyhydrogen Flames by Solid Surfaces." Third Symposium on Combustion and Flame and Explosion Phenomena 3 (1949):110-120.
75. Simon, D. M., Belles, F. E., and Spakewski, A. E. "Investigation and Interpretation of the Flammability Region for Some Lean Hydrocarbon-Air Mixtures." Fifth Symposium (International) on Combustion 5 (1952): 126-138.

76. Berlad, A. L., and Potter, A. E., Jr. "Prediction of the Quenching Effect of Various Surface Geometries." Fifth Symposium (International) on Combustion 5 (1952): 728-735.
77. Potter, A. E., Jr., and Berlad, A. L. "A Thermal Equation for Flame Quenching." NACA Technical Report 1264 (1956).
78. Aly, S. L., and Hermance, C. E. "A Two-Dimensional Theory of Laminar Flame Quenching." Combustion and Flame 40 (1981):173-185.
79. Rosen, G. "Ignition of Combustive Gases." Journal of Chemical Physics 30 (1959):298-303.
80. Ballal, D. R., and Lefebvre, A. H. "Flame Quenching at Turbulent Flowing Gaseous Mixtures." Sixteenth Symposium (International) on Combustion 16 (1976):1689-1698.
81. Ballal, D. R., and Lefebvre, A. H. "Ignition and Flame Quenching in Flowing Gaseous Mixtures." Proceedings of Royal Society of London A357 (1977):163-181.
82. Ballal, D. R., and Lefebvre, A. H. "A General Model of Spark Ignition for Gaseous and Liquid Fuel-Air Mixtures." Eighteenth Symposium (International) on Combustion 18 (1981):1737-1746.
83. Maly, R. "Ignition Model for Spark Discharges and the Early Phase of Flame Front Growth." Eighteenth Symposium (International) on Combustion 18 (1981): 1747-1755.
84. Litchfield, E. L. "Chronology and Topography of Sparks at Minimum Energy for Ignition." Combustion and Flame 5 (1961):235-240.
85. Hill, R. D. "Ignition of Hydrocarbons by Small Sparks." Journal of Applied Physics 50 (1979):127-131.
86. Adelman, H. G. "A Time Dependent Theory of Spark Ignition." Eighteenth Symposium (International) on Combustion 18 (1981):1333-1342.

87. Akindede, O. O., Bradley, D., Mak, P. W., and McMahon, M. "Spark Ignition of Turbulent Gases." Combustion and Flame 47 (1982):129-155.
88. Yang, C. H. "Theory of Ignition and Auto-ignition." Combustion and Flame 6 (1962):215-225.
89. Dixon-Lewis, G., and Shepherd, I. G. "Some Aspects of Ignition by Localized Sources, and of Cylindrical and Spherical Flames." Fifteenth Symposium (International) on Combustion 15 (1974):1483-1491.
90. Overley, J. R., Overholser, K. A., and Reddien, G. W. "Calculation of Minimum Ignition Energy and Time Dependent Laminar Flame Profiles." Combustion and Flame 31 (1978):69-83.
91. Burgoyne, J. H., and Thomas, N. "Effects of Very Fine Solid Particles on Flame Propagation." Nature 163 (1949):765-766.
92. Dewitte, M., Vrebosch, J., and von Tiggelen, A. "Inhibition and Extinction of Premixed Flames by Dust Particles." Combustion and Flame 18 (1964):257-266.
93. McCamy, C. S., Shoub, H., and Lee, T. G. "Fire Extinguishment by Means of Dry Powder." Sixth Symposium (International) on Combustion 6 (1957):795-801.
94. Joulin, G. "Asymptotic Analysis of Non-Adiabatic Flames." Eighteenth Symposium (International) on Combustion 18 (1981):1395-1404.
95. Mitani, T. "A Flame Inhibition Theory by Inert Dust and Spray." Combustion and Flame 43 (1981):243-253.
96. Hartman, I., Nagy, J., and Brown, H. R. "Inflammability and Explosibility of Metal Powders." Report of Investigations No. 3722, USDI-Bureau of Mines, 1943.
97. Ishihama, W., and Enomoto, H. "New Experimental Method for Studies of Dust Explosions." Combustion and Flame 21 (1973):177-186.
98. Ballal, D. R. "Ignition and Flame Quenching of Quiescent Dust Clouds of Solid Fuels." Proceedings of Royal Society of London A369 (1980):479-500.

99. Cotroneo, J. A., and Colver, G. M. "Electrically Augmented Pneumatic Transport of Copper Spheres at Low Particle and Duct Reynolds Numbers." Journal of Electrostatics 5 (1978):205-223.
100. Colver, G. M., and Howell, D. L. "Particle Diffusion in an Electric Suspension." Conference Record - IAS Annual Meeting, pp. 1056-1062. New York: IEEE, 1980.
101. Colver, G. M. "Dynamics of an Electric (Particulate) Suspension," In Advances in the Mechanics and the Flow of Granular Materials. Edited by Wöhlbier, R., and Shahinpoor, M. New York: McGraw Hill, 1982. (In progress)
102. Bierkamp, J., and Colver, G. M. "Charge Transfer Characteristics and Kinematic Behavior of Electrodynamic Suspensions." Department of Mechanical Engineering, Iowa State University, 1978. (Unpublished)
103. Abde-Salam, M., and Abul-Shohoud, W. "Effect of Polarity on the Breakdown Voltage of Gas Gaps." Gaseous Dielectrics II (Proceedings of the Second International Symposium), pp. 108-113. New York: Pergamon Press, 1980.
104. Kennard, E. H. Kinetic Theory of Gases. New York: McGraw-Hill Book Company, 1938.
105. Soo, S. L. Analytical Thermodynamics. Englewood Cliffs, N.J.: Prentice-Hall Inc., 1962.
106. Johnsson, L., Strid, K. G. and Johansson, S. R. "Measurement of the Energy Released in Nanosecond Electric Sparks." Combustion Science and Technology 5 (1972):1-6.
107. Marode, E. "Nature of the Primary-Secondary Streamer Sequence in a Positive Point to Plane Discharge." International Conference on Gas Discharges (Conference Publication No. 70), pp. 525-529. London: IEE, 1970.
108. Blanc, M. V., Guest, P. G., von Elbe, G., and Lewis, B. "Ignition of Explosive Gas Mixtures by Electric Sparks. I. Minimum Ignition Energies and Quenching Distances of Mixtures of Methane, Oxygen, and Inert Gases." Journal of Chemical Physics 15 (1947):798-802.

109. Van Wylen, G. J., and Sonntag, R. E. Fundamentals of Classical Thermodynamics. New York: John Wiley & Sons, Inc., 1965.
110. Gordon, R. L., Lord, H., and Widginton, D. W. "Ignition of Gas by Sparks produced by breaking Wires at High Speed." Nature 191 (1961):1085-1086.
111. Creagh, D. C., Fletcher, N. H., and Somerville, J. M. "The Decay of a Spark Channel which has Ceased to Carry Current." Proceedings of Physics Society 81 (1963):480-489.
112. Somerville, J. M., and Williams, J. F. "The Early Stages of Spark Channel Expansion." Proceedings of Physics Society 74 (1959):309-315.
113. Line, L. E., Rhodes, H. A., and Gilmer, T. E., Jr. "The Spark Ignition of Dust Clouds." Journal of Physical Chemistry 63 (1959):290-294.
114. Eckert, E. R. G., and Drake, R. M., Jr. Analysis of Heat and Mass Transfer. New York: McGraw-Hill Book Company, 1972.
115. Thermophysical Properties of Refrigerants. New York: American Society of Heating, Refrigerating and Air-Conditioning Engineers, Inc., 1973.
116. Beckwith, T. G., Buck, N. L., and Marangoni, R. D. Mechanical Measurements. Reading, Massachusetts: Addison-Wesley, 1982.
117. Kennedy, J. B., and Neville, A. M., Basic Statistical Methods for Engineers and Scientists. New York: Harper & Row Publishers, 1976.
118. Pugh, E. M., and Winslow, G. H. The Analysis of Physical Measurements. Reading, Massachusetts: Addison-Wesley, 1966.
119. Beers, Y. Introduction to the Theory of Error. Reading, Massachusetts: Addison-Wesley, 1962.

VIII. ACKNOWLEDGMENTS

The author wishes to express his heartfelt gratitude to Prof. Gerald M. Colver, his thesis advisor, for all of his patient guidance, continuous encouragement and invaluable instruction.

The author is also indebted to his doctoral committee, Prof. Arthur E. Bergles, Prof. William J. Cook, Prof. Bruce R. Munson, Prof. Lennox N. Wilson and Prof. Robert C. Fellinginger, for their interest, suggestions and encouragement throughout the course of his doctoral study.

Thanks are extended to Mr. Hap Steed and Mr. Gay Scandrett of the Mechanical Engineering Department, who helped in the design and construction of the experimental apparatus.

The author would like to give special thanks to Mr. Harold D. Skank and Mr. George E. Holland (Instrument Services, Ames Laboratory) for their courtesy and patience in loaning out the high speed oscilloscope (Tek. 475) for use in this study, and to Prof. Robert E. Post (EE) for helpful suggestions in interpreting data relating to the temporal development of a spark.

The author is thankful to the Department of Mechanical Engineering, the Engineering Research Institute and the Graduate College for the financial support, direct and indirect, given to him during the course of this research.

Portions of this work were also sponsored by the ALCOA Foundation and the National Science Foundation under contract No. Eng 78-09880.

The author wants to give thanks to his wife for her patience and understanding during these recent trying years.

Finally, the author wants to dedicate this work to his mother, whose constant love, sacrifice and encouragement sustained him throughout his life.

IX. APPENDIX A: ELECTROSTATIC SUSPENSION

The motion of a particle oscillating between parallel electrodes responding to the influence of an electric field of strength E_f may be described by

$$\frac{d^2 x_p}{dt^2} = \frac{Q_p E_f}{m} \pm g \quad (9.1)$$

neglecting drag, lift, pressure gradient, apparent fluid mass and particle history (Basset) effects. Colver [28] showed that the latter magnitudes were small compared to the electrostatic and gravitational forces; thus, from Equation 9.1 he derived the average particle velocity v_p to be

$$v_p = (1+e) \left(\frac{L}{8}\right)^{\frac{1}{2}} \left\{ \left[\frac{Q_p E_f}{m(1-e^2)} + \frac{g}{1+e^2} \right]^{\frac{1}{2}} + \left[\frac{Q_p E_f}{m(1-e^2)} - \frac{g}{1+e^2} \right]^{\frac{1}{2}} \right\} \quad (9.2)$$

He also found the electrically induced particle charge to be equal to

$$Q_p = \pi \epsilon D^2 E_f \quad (1.64) \quad (9.3)$$

for a conducting spherical particle placed on an electrode.

Multiparticles are expected to be suspended similarly but with interparticle collisions considered. Cotroneo

and Colver [99] proposed the current flux

$$J = NQ_p v_p [e^{-\pi ND^2 L} + \gamma_c (1 - e^{-\pi ND^2 L})] \quad (9.4)$$

caused by charge transport of particles with the modification in square brackets to account for the reduced particle charge and velocity due to particle collisions. The first exponential term is the probability of a particle traversing the electrode gap without a collision based on one-dimensional motion of the particles.

As an example, taking a spherical copper particle with the following conditions:

$$V = 10 \times 10^3 \text{ V}$$

$$L = 1.1 \text{ cm}$$

$$D = 96 \times 10^{-4} \text{ cm}$$

$$\epsilon = \frac{1}{36\pi} \times 10^{-11} \left[\frac{\text{F}}{\text{cm}} \text{ or } \frac{\text{C}}{\text{V cm}} \right]$$

$$m = \frac{4}{3} \pi \left(\frac{D}{2}\right)^2 \rho_p$$

$$\rho_p = 8.954 \text{ g/cm}^3$$

$$g = 980 \text{ cm/sec}^2$$

$$e = 0.68$$

The particle charge from Equation 9.3 is

$$Q_p = 3.817 \times 10^{-13} \text{ C}$$

the average particle velocity from Equation 9.2 is

$$v_p = 155.4 \text{ cm/sec}$$

and neglecting γ_c and choosing a small value for the particle number density ($N = 1 \times 10^3 \text{ \#/cm}^3$) from Figure 2.6a gives the current flux in Equation 9.4 as

$$J = 4.314 \times 10^{-8} \text{ A/cm}^2$$

X. APPENDIX B: PARTICLE SIZE AND SHAPE
DISTRIBUTION

The size and shape range of particles first classified by a mechanical and sonic siever were analyzed by a Lemont Scientific Image Analyzer (B10 system) with a JEOL-U₃ scanning electromicroscope. Table 10.1 shows the statistical data for 88~104, 44~53 and 30~38 μm sieved particles. The width measurement is based on the shortest distance across any particle (including an attached particle) and the length on the longest distance. Visually, it was observed with a microscope that most particles are spherical, while some very small particles are observed to be stuck on other larger particles. The attached particles may be responsible for a decreased width/length ratio in Table 10.1. The diameter was calculated based on the average projected area of a sphere.

The histogram of 88~104 μm particles and distribution of width/length ratio are shown in Figures 10.1 and 10.2, respectively.

Table 10.1. Statistical particle size and shape data obtained by a Lemont Scientific Image Analyzer

	Area μm^2	Width (μm)	Length (μm)	W/L	Diameter (μm)
Sieve range: 88-104 μm					
Average sieve size: 96 μm					
Magnification: 100					
<u>Counted particle number: 152</u>					
Average	5140	77.621	93.157	0.841	80.92
Median	6400	79.809	93.034	0.865	90.29
Most probable	7300	79.500	93.500	0.875	96.41
Standard deviation	878	10.50	10.40	0.113	-
Sieve range: 44-53 μm					
Average sieve size: 48.5 μm					
Magnification: 200					
<u>Counted particle number: 151</u>					
Average	1280	37.726	47.103	0.809	40.37
Median	1440	38.187	44.786	0.848	42.82
Most probable	1600	35.501	44.500	0.875	45.14
Standard deviation	378	7.55	8.19	0.144	-
Sieve range: 30-38 μm					
Average sieve size: 34 μm					
Magnification: 200					
<u>Counted particle number: 253</u>					
Average	548	23.6	32.8	0.720	26.42
Median	525	24.1	33.0	0.750	25.83
Most probable	450	19.5	33.5	0.780	23.84
Standard deviation	198	5.57	6.15	0.132	-

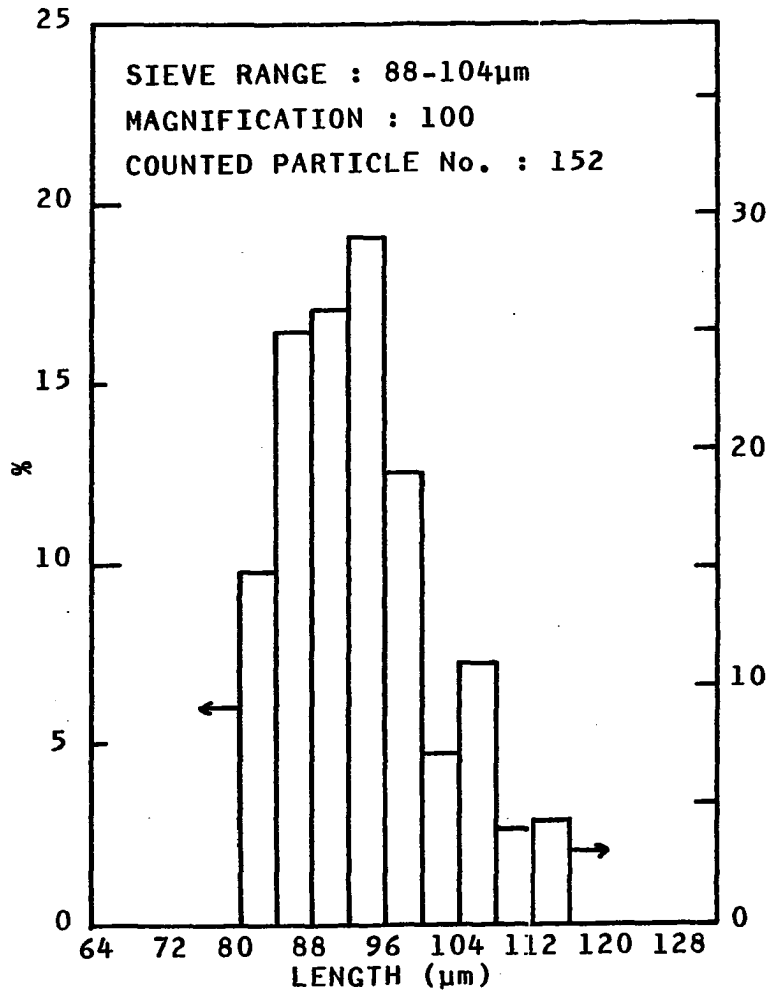


Figure 10.1. Histogram of 88-104 μ m particles

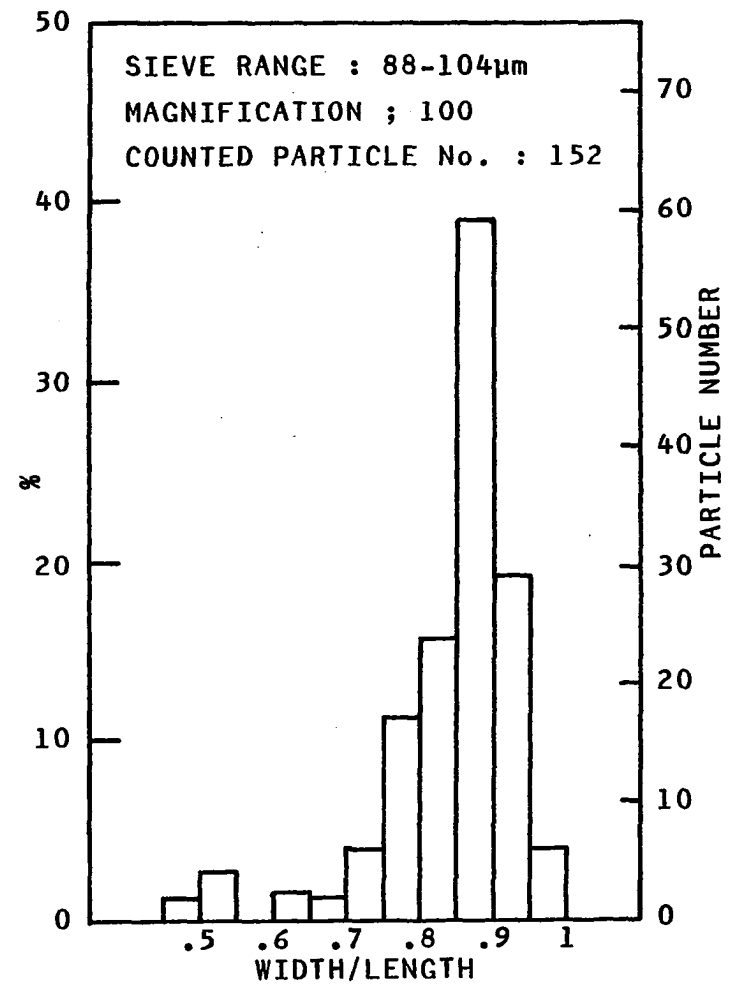


Figure 10.2. Width-length ratio of 88-104 μ m particles

XI. APPENDIX C: FLOWMETER

The volumetric flow rate of a variable-area flow meter like the Gilmont flowmeters used here can be calculated by

$$q = A_w C_d \left[\frac{W_f (\rho_f - \rho)}{\rho_f \rho} \right]^{\frac{1}{2}} \quad (11.1)$$

$$q \approx A_w C_d \left[\frac{W_f}{\rho} \right]^{\frac{1}{2}} \quad (11.2)$$

since the float density ρ_f is much larger than the gas density ρ , i.e., $\rho/\rho_f \sim 10^{-3}$. A flow rate which has the same reading under different conditions of temperature, pressure and molecular weight will be different from the calibrated flow rate. When the flow rate at the condition 1 is compared to the calibrated condition 0 at the same reading, the flow rate ratio becomes

$$\frac{q_1}{q_0} = \left(\frac{C_{d1}}{C_{d0}} \right) \left(\frac{\rho_0}{\rho_1} \right)^{\frac{1}{2}} = \left(\frac{C_{d1}}{C_{d0}} \right) \left[\left(\frac{T_1}{T_0} \right) \left(\frac{M_{w0}}{M_{w1}} \right) \left(\frac{P_0}{P_1} \right) \right]^{\frac{1}{2}} \quad (11.3)$$

since the float weight W_f and the flowmeter geometric dimension A_w are constant and $\rho = (M_w P) / (\bar{R}T)$ from ideal gas conditions. The discharge coefficient C_d must be determined from the correlation chart provided by Gilmont Company as the function of the Stokes number being

$$S_t = 1.042 \times 10^{-4} \frac{W_f (\rho_f - \rho) \rho}{\mu^2 \rho_f} R^3 \quad (11.4)$$

$$\approx 1.042 \times 10^{-4} \frac{W_f \rho}{\mu^2} R^3$$

where R is a function of the scale reading, or from the relation

$$C_d = \frac{[(3.83 - 1.17 \log R)^2 + 4(3.08 \log R - 1.25) \cdot (\log S_t - 0.111 \log R)]^{1/2}}{2(3.08 \log R - 1.25)} \quad (11.5)$$

However, when $S_t < 5$, the coefficient can be calculated from

$$C_d = 0.0852 \sqrt{S_t}$$

and thus Equation 11.3 becomes

$$\frac{q_1}{q_0} = \frac{\mu_0}{\mu_1}$$

For example, for the Gilmont flow meter A-2855, the following are given:

$$A_w = 59.8 \times 0.0625 R \left[\frac{R}{100} + 2 \right] \left(\text{cm} \frac{\text{sec}}{\text{min}} \right)$$

$$W_f = 0.0053 \text{ (g cm/sec}^2\text{)}$$

$$\rho_f = 2.53 \times 10^{-3} \text{ (g/cm}^3\text{)}$$

When R is chosen to be 5 and the air density and viscosity are given, from Eckert and Drake [114] at 28°C and 1 atm,

$$\rho = 1.177 \times 10^{-3} \text{ g/cm}^3$$

$$\mu = 1.98 \times 10^{-4} \text{ g/cm sec}$$

the above formulas give

$$S_t = 2.067$$

$$C_d = 0.0852 [2.0670]^2 = 0.123$$

and thus $q = 9.95 \text{ (cm}^3\text{/min or mL/min)}$

If the propane density and viscosity are given, from the table [114] at 28°C and 1 atm,

$$\rho = 1.800 \times 10^{-3} \text{ g/cm}^3$$

$$\mu = 8.15 \times 10^{-5} \text{ g/cm sec}$$

the Stoke's number and coefficient become (for R=5)

$$S_t = 18.707$$

$$C_d = 0.300$$

Therefore, the ratio of propane to air flow rate at the same scale reading and flow conditions (temperature and pressure) becomes

$$\frac{q_{\text{propane}}}{q_{\text{air}}} = \left(\frac{0.300}{0.123}\right) \left(\frac{1.177}{1.800}\right)^{\frac{1}{2}} = 1.9811$$

which shows that the propane flow rate is about two times higher than the air flow rate.

The expected error caused by different measuring conditions of pressure and temperature from the calibrated conditions can be evaluated. If the propane flow meter is used at 20°C and 1 atm, the propane density and viscosity are

$$\rho = 1.8 \times 10^{-3} \frac{(273+28)}{(273+20)} = 1.843 \times 10^{-3} \text{ g/cm}^3$$

$$\mu = 7.97 \times 10^{-3} \text{ g/cm sec}$$

therefore,

$$S_t = 20.030$$

$$C_d = 0.307$$

and the flow rate ratio is

$$\frac{q_{20^\circ\text{C}}}{q_{28^\circ\text{C}}} = \left(\frac{0.307}{0.300}\right) \left(\frac{1.80}{1.843}\right)^{\frac{1}{2}} = 1.011$$

which shows that about 1% variation can be expected. If the propane flows at a different pressure of 1.01 atm but at the same temperature 28°C,

$$\rho = 1.8 \times 10^{-3} \frac{1.01}{1.0} = 1.818 \times 10^{-3} \text{ g/cm}^3$$

$$\mu = 8.15 \times 10^{-5} \text{ g/cm sec}$$

and

$$S_t = 18.894$$

$$C_d = 0.300$$

thus, the flow rate ratio becomes

$$\frac{q_{1.01 \text{ atm}}}{q_{1.0 \text{ atm}}} = \left(\frac{0.3}{0.3}\right) \left(\frac{1.80}{1.818}\right)^{\frac{1}{2}} = 0.9950$$

which is still smaller than 1% variation.

XII. APPENDIX D: ERROR ANALYSIS

Whenever measurements are made, uncertainties in the raw data occur usually because of three types of errors: illegitimate, systematic and random. Illegitimate errors are caused by mistakes in reading instruments and performing calculations or variations in experimental conditions. Such errors may be reduced by using care and repetition of the experiments and calculations. Systematic errors are of consistent form and result from inaccurate calibration of the instruments, improper conditions or incorrect procedures. These errors can be reduced through calibration. However, the third type of error, random, deals with irregularity and originates from a variety of causes such as fluctuating experimental conditions or disturbances. Random error cannot usually be avoided since these errors are inherently present in any measuring system. However, the random uncertainties can be minimized through experimental design. Hence, to estimate the accuracy of the experimental data it is necessary to determine the total uncertainty through the use of statistics in a propagation-of-error analysis.

The expression to be used to calculate the uncertainty U in any quantity Z is (Beckwith et al. [116], and Kennedy and Neville [117])

$$U_z = \left[\sum_{i=1}^n \left(\frac{\partial Z}{\partial Y_i} U_{Y_i} \right)^2 \right]^{\frac{1}{2}} \quad (12.1)$$

where Y_i is any of n parameters of which the quantity Z is a function. When the uncertainty of a measured quantity, U_{Y_i} , is chosen to be the absolute value of the maximum expected deviation from a measured result Y_i , the uncertainty of calculated quantity, U_z , indicates the maximum expected deviation from the reported experimental result.

The uncertainty U_N of the particle number density defined as

$$N = \frac{W}{\frac{4}{3}\pi \left(\frac{D}{2}\right)^3 \rho_p \pi \left(\frac{d}{2}\right)^2 L} \quad (2.1)$$

can be expressed as

$$U_N = \left\{ \left(\frac{W}{\frac{4}{3}\pi \left(\frac{D}{2}\right)^3 \rho_p \pi \left(\frac{d}{2}\right)^2 L} \right)^2 \left[\left(\frac{U_W}{W} \right)^2 + \left(-\frac{3U_D}{D} \right)^2 + \left(-\frac{U_{\rho_p}}{\rho_p} \right)^2 + \left(-\frac{2U_d}{d} \right)^2 + \left(-\frac{U_L}{L} \right)^2 \right] \right\}^{\frac{1}{2}} \quad (12.2)$$

The fractional uncertainty of the particle number density can be defined as

$$\frac{U_N}{N} = \frac{U_N}{\left[\frac{4}{3} \pi \left(\frac{D}{2}\right)^3 \rho_p \left(\frac{d}{2}\right)^2 L \right]} = \left[\left(\frac{U_W}{W}\right)^2 + \left(-\frac{3U_D}{D}\right)^2 + \left(-\frac{U_{\rho_p}}{\rho_p}\right)^2 + \left(-\frac{2U_d}{d}\right)^2 + \left(-\frac{U_L}{L}\right)^2 \right]^{\frac{1}{2}} \quad (12.3)$$

Also, the fractional uncertainty of the parameter ND^2 is given as

$$\frac{U_{ND^2}}{ND^2} = \left[\left(\frac{U_W}{W}\right)^2 + \left(-\frac{U_D}{D}\right)^2 + \left(-\frac{U_{\rho_p}}{\rho_p}\right)^2 + \left(-\frac{2U_d}{d}\right)^2 + \left(-\frac{U_L}{L}\right)^2 \right]^{\frac{1}{2}} \quad (12.4)$$

$$= \left[\left(\frac{U_N}{N}\right)^2 - 8\left(\frac{U_D}{D}\right)^2 \right]^{\frac{1}{2}}$$

The following data are given with their maximum expected uncertainties:

$$L = 1.02 \pm 0.01 \text{ cm}$$

$$d = 2.63 \pm 0.005 \text{ cm}$$

$$W = 0.1315 \text{ g} \pm 1.0\%$$

$$\rho_p = 8.954 \pm 0.001 \text{ g/cm}^3$$

But, difficulties are present in choosing the most representative particle diameter of sieved particles, since they are not of the same size and shape.

By assuming spherical particles, an arithmetic average

of the particle diameter is

$$D = \frac{\sum_{i=1}^n D_i}{n} \quad (12.5)$$

However, $\frac{4}{3}\pi\left(\frac{D}{2}\right)^3$ of Equation 2.1 represents the average volume per particle; therefore, the average particle diameter D should be the average diameter weighted by particle volume, which is dependent on the size distribution of particles. When the rectangular distribution of the particle size between D_1 and D_2 is assumed, the weighted average particle diameter can be given as (Pugh and Winslow [118])

$$D_V = \left[\int_{D_1}^{D_2} D_i^3 \frac{1}{(D_2 - D_1)} dD_i \right]^{\frac{1}{3}} = \left[\frac{1}{4}(D_1 + D_2)(D_1^2 + D_2^2) \right]^{\frac{1}{3}} \quad (12.6)$$

Alternatively, if a normal (Gaussian) distribution of particle size is assumed, the weighted average particle diameter is

$$D_V = \left\{ \int_0^{\infty} D_i^3 \frac{1}{\sigma\sqrt{2\pi}} \exp\left[-\frac{(D_i - D)^2}{2\sigma^2}\right] dD_i \right\}^{\frac{1}{3}} \quad (12.7)$$

$$= \left[2\sqrt{\frac{2}{\pi}} \sigma^3 + 3\sigma^2 D + 3\sqrt{\frac{2}{\pi}} \sigma D^2 + D^3 \right]^{\frac{1}{3}}$$

where σ is the standard deviation. For example, for the particles sieved between 88~104 μm size, the average sieve size, 96 μm , was used in Equation 2.1. But, when the

uniform particle diameter distribution is assumed from 80 to 106 μm (since an actual distribution analysis shows a somewhat wider range than the sieve range), the average particle diameters are, from Equations 12.5 and 12.6,

$$D = 93.0 \mu\text{m}$$

$$D_v = 93.6 \mu\text{m}$$

The histogram of Figure 10.1 appears similar to a normal distribution. Thus, assuming first of all that the particle length reported in Table 10.1 is the average particle diameter $D = 93.157 \mu\text{m}$ and also taking $\sigma = 10.4 \mu\text{m}$ leads in Equation 12.7 to

$$D_v = 101.9 \mu\text{m}$$

Since the equivalent hypothetical diameter of a nonspherical particle is expected to be slightly smaller than its maximum reported length, the most representative particle diameter to be used in Equation 2.1 may be smaller than 101.9 μm . Therefore, it can be reasonably assumed that the uncertainty in D is less than ± 6 ($=102-96$) μm , choosing $\pm 4 \mu\text{m}$. With these uncertainties, Equations 12.2 and 12.3 give

$$\frac{U_N}{N} = 0.126 \quad \text{or} \quad 12.6\%$$

$$\text{and } U_N = 5.721 \times 10^3 \times 0.126 \text{ \#/cm}^3 = 7.209 \times 10^2 \text{ \#/cm}^3$$

In the same way, the uncertainties in ND^2 are, from Equation 12.4,

$$\frac{U_{ND^2}}{ND^2} = 0.044 \text{ or } 4.4\%$$

$$U_{ND^2} = 0.527 \times 0.044 \text{ \#/cm} = 0.0232 \text{ \#/cm}$$

For $D = (34 \pm 4) \mu\text{m}$ particles, the uncertainties

are

$$\frac{U_N}{N} = 0.353 \text{ or } 35.3\%$$

$$U_N = 1.288 \times 10^5 \times 0.353 \text{ \#/cm}^3 = 4.547 \times 10^4 \text{ \#/cm}^3$$

and

$$\frac{U_{ND^2}}{ND^2} = 0.199 \text{ or } 11.9\%$$

$$U_{ND^2} = 1.489 \times 0.119 \text{ \#/cm} = 0.177 \text{ \#/cm}$$

It is interesting to see that by using the correlated parameter ND^2 , the effect of the uncertainty in N on the overall analysis can be made smaller.

Since the nondimensional breakdown needle position is calculated from

$$x_i = 1 + \left[\frac{h_2}{L} \left(\frac{h_1}{h_2} - \frac{t_s}{t_f} \right) \right] \quad (12.8)$$

its uncertainty is

$$\begin{aligned}
 U_{x_i} = & \left\{ \left(-\frac{t_s}{L t_f} U_{h_2} \right)^2 + \left[-\frac{h_2}{L^2} \left(\frac{h_1}{h_2} - \frac{t_s}{t_f} \right) U_L \right]^2 + \left(\frac{1}{L} U_L \right)^2 \right. \\
 & \left. + \left(\frac{h_2}{L t_f} U_{t_s} \right)^2 + \left[\frac{h_2}{L} \left(\frac{t_s}{t_f^2} \right) U_{t_f} \right]^2 \right\}^{\frac{1}{2}} \quad (12.9)
 \end{aligned}$$

When the experimental data are given,

$$h_1 = 0.3683 \pm 0.01 \text{ cm}$$

$$h_2 = 0.7833 \pm 0.05 \text{ cm}$$

$$t_s = (5.0 \pm 0.1) \times 10^{-4} \text{ sec}$$

$$t_f = (7.0 \pm 0.1) \times 10^{-4} \text{ sec}$$

$$L = 1.02 \pm 0.01 \text{ cm}$$

the uncertainties are

$$\frac{U_{x_i}}{x_i} = 0.0480 \text{ or } 4.80\%$$

$$U_{x_i} = 0.8090 \times 0.0480 = 0.0389$$

Since the same experiment was performed more than 7 times, the uncertainties in the averaged nondimensional breakdown needle position are (Beers [119])

$$\frac{U_x}{X} = \frac{1}{\sqrt{7}} \frac{U_{x_i}}{x_i} = 0.0180 = 1.80\%$$

$$U_x = \frac{U_{x_i}}{\sqrt{7}} = 0.0147$$

The breakdown voltage is a strong function of environmental pressure (see Equation 1.5). It was observed during the course of experiments that $p = 760 \pm 30$ mm Hg. There is at present no clear way to estimate how much the pressure

change affects the breakdown voltage of the needle-to-plane particulate cloud system as used in this study. However, it can be observed from Figure 7.8 of Cobine [12] that a ± 30 mm Hg pressure deviation causes ± 100 V difference in the breakdown voltage of a uniform field system of 1.02 cm parallel gap width.

The stored charge and energy are

$$Q_o = CV$$

$$E_o = \frac{1}{2}CV^2$$

Therefore,

$$U_{Q_o} = CV \left[\left(\frac{U_C}{C} \right)^2 + \left(\frac{U_V}{V} \right)^2 \right]^{\frac{1}{2}} \quad (12.10)$$

$$U_{E_o} = \frac{1}{2}CV^2 \left[\left(\frac{U_C}{C} \right)^2 + \left(\frac{2U_V}{V} \right)^2 \right]^{\frac{1}{2}} \quad (12.11)$$

For example, if the following experimental data are given

$$C = 300 \pm 3 \text{ pF}$$

$$V = 15.0 \pm 0.2 \text{ KV}$$

the above equations give

$$\frac{U_{Q_o}}{Q_o} = 0.0167 \text{ or } 1.67\%$$

$$U_{Q_o} = 4.5 \times 10^{-6} \times 0.0167 \text{ C} = 7.515 \times 10^{-8} \text{ C}$$

and

$$\frac{U_{E_o}}{E_o} = 0.0285 \text{ or } 2.85\%$$

$$U_{E_o} = 33.75 \times 0.0285 \text{ mJ} = 0.962 \text{ mJ}$$

The fuel air ratio is

$$f = \frac{\dot{Q}_F}{\dot{Q}_A}$$

and the uncertainty is

$$U_f = \frac{\dot{Q}_F}{\dot{Q}_A} \left[\left(\frac{U_{\dot{Q}_F}}{\dot{Q}_F} \right)^2 + \left(- \frac{U_{\dot{Q}_A}}{\dot{Q}_A} \right)^2 \right]^{\frac{1}{2}} \quad (12.12)$$

If the most typical experimental data are given,

$$\dot{Q}_F = 14 \pm 1 \text{ mL/min}$$

$$\dot{Q}_A = 230 \pm 5 \text{ mL/min}$$

the uncertainties are

$$\frac{U_f}{f} = 0.0747 \text{ or } 7.47\%$$

$$U_f = 0.0609 \times 0.0747 = 0.00455$$

Uncertainties in the parameters, L_x/L_p and $(B_o - B)/$
 $(B_o - B_*)$ used in the final correlation of Equation 3.10a,
 can be estimated from the following equations:

$$\frac{U_{L_x}}{L_p} = \frac{L_x}{L_p} \left[\left(\frac{U_{L_x}}{L_x} \right)^2 + \left(- \frac{U_{L_p}}{L_p} \right)^2 \right]^{\frac{1}{2}} \quad (12.13)$$

where

$$U_{L_x} = L_x \left[\left(\frac{U_L}{L} \right)^2 + \left(\frac{U_x}{x} \right)^2 \right]^{\frac{1}{2}}$$

and

$$U_{L_p} = L_p \frac{U_{ND}^2}{ND^2}$$

$$\frac{U_{B_o-B}}{B_o-B_*} = \left\{ \left[\frac{B_*-B}{(B_o-B_*)^2} U_{B_o} \right]^2 + \left[\frac{1}{B_o-B_*} U_B \right]^2 + \left[\frac{B_o-B}{(B_o-B_*)} U_{B_*} \right]^2 \right\}^{\frac{1}{2}} \quad (12.14)$$

where $U_B = (1-x)V^{1.121} \left[\left(\frac{U_{1-x}}{1-x} \right)^2 + \left(\frac{1.121 U_V}{V} \right)^2 \right]^{\frac{1}{2}}$

and

$$U_{1-x} = U_x$$

For example, based on experimental measurements and the previous calculations,

$$L = 1.02 \pm 0.01 \text{ cm}$$

$$V = 20 \pm 0.3 \text{ KV}$$

$$x = 0.8090 \pm 0.0147$$

$$ND^2 = 0.090 \pm 0.010 \text{ \#/cm}$$

$$B_o = 8.86 \text{ (KV)}^{1.121}$$

$$B_* = 4.19 \text{ (KV)}^{1.121}$$

Equation 12.13 gives the following numerical results:

$$\frac{U_{L_x}}{L_x} = 0.0206 \text{ or } 2.06\%$$

$$\frac{U_{Lp}}{L_p} = 0.1111 \text{ or } 11.11\%$$

$$\frac{U_{Lx}}{L_p} = 0.1129 \text{ or } 11.29\%$$

and

$$\frac{U_{Lx}}{L_p} = \frac{1.02 \times 0.8090}{2} \times 0.1129 = \frac{0.8252}{1.6681} \times 0.1129 = 0.0558$$

$$3\sqrt{2}\pi \ 0.090$$

Similarly, Equation 12.14 gives

$$\frac{U_B}{B} = 0.0787$$

and

$$U_B = 5.49 \times 0.0787 = 0.432 \text{ (KV)}^{1.121}$$

Furthermore, since B_o and B_* are based on 8 and 31 data points, respectively, (compared to B which is based on one point)

$$\frac{U_{B_o}}{B_o} = \frac{0.0503}{\sqrt{8}} = 0.0178$$

resulting in

$$U_{B_o} = 8.86 \times 0.0178 = 0.1576 \text{ (KV)}^{1.121}$$

and

$$\frac{U_{B_*}}{B_*} = \frac{0.1021}{\sqrt{31}} = 0.0183$$

resulting in

$$U_{B_*} = 4.19 \times 0.0183 = 0.0768 \text{ (KV)}^{1.121}$$

Therefore, the uncertainty in $(B_o - B)/(B_o - B_*)$ is

$$\frac{U_{B_o - B}}{\frac{B_o - B}{B_o - B_*}} = 0.1299 \text{ or } 12.99\%$$

$$\frac{U_{B_o - B}}{B_o - B_8} = 0.7216 \times 0.1299 = 0.0937$$

It should be noted that all uncertainties in the above calculations are a result of random errors associated with measurements, and do not include the additional random effect of the spark breakdown process itself. This latter random effect will be considered in what follows.

If the values of N , D , L , and $(1-x)$ are known, the breakdown voltage V can be readily predicted from Equation 3.10b, i.e.,

$$V = (1-x)^{-0.892} [B_o - (B_o - B_*) \left(\frac{Lx}{C_2 L_p}\right)^{C_1}]^{0.892} \quad (3.10b)$$

The fractional uncertainty of the breakdown voltage is

$$\frac{U_V}{V} = \left\{ \left(\frac{-0.892 U_{1-x}}{1-x} \right)^2 + \left[\frac{0.892}{B_o - (B_o - B_*) \left(\frac{Lx}{C_2 L_p}\right)^{C_1}} \right]^2 \right\} x$$

$$\left\{ \left[\left(1 - \frac{L_x}{C_2 L_p} \right) U_{B_0} \right]^2 + \left[\left(\frac{L_x}{C_2 L_p} \right) U_{B_*} \right]^2 + \left[- \frac{\frac{U_{L_x}}{L_p}}{\frac{L_x}{L_p}} (B_0 - B_*) C_1 \left(\frac{L_x}{C_2 L_p} \right) \right]^2 \right\}^{\frac{1}{2}} \quad (12.15)$$

In order to estimate this uncertainty, the following data will be used;

$$L = 1.02 \pm 0.01 \text{ cm}$$

$$x = 0.8090 \pm 0.0147$$

$$ND^2 = 0.090 \pm 0.010 \text{ \#/cm}$$

along with the results obtained previously, that is,

$$\frac{U_{1-x}}{1-x} = \frac{0.0147}{0.1910} = 0.0770$$

$$\frac{L_x}{L_p} = \frac{0.8252}{1.6681} = 0.4948$$

and

$$\frac{\frac{U_{L_x}}{L_p}}{\frac{L_x}{L_p}} = 0.1129$$

If the total uncertainties in B_0 and B_* are given as the values of maximum deviation about the mean values so as to include all uncertainties caused by data measurements

and random breakdown phenomena, then,

$$B_o = 8.86 \pm 0.53 \text{ (KV)}^{1.121}$$

and

$$B_* = 4.19 \pm 0.41 \text{ (KV)}^{1.121}$$

Calculations show, from Equation 12.15, that

$$\frac{U_V}{V} = 0.0932 \text{ or } 9.32\%$$

and

$$U_V = 19.5 \times 0.0932 = 1.817 \text{ KV}$$

If $\frac{L_x}{L_p} > 1.0$, Equation 12.15 becomes

$$\frac{U_V}{V} = \left[\left(-0.892 \frac{U_{1-x}}{1-x} \right)^2 + \left(0.892 \frac{U_{B_*}}{B_*} \right)^2 \right]^{\frac{1}{2}} \quad (12.16)$$

Therefore, the uncertainty is

$$\frac{U_V}{V} = 0.0900 \text{ or } 9.00\%.$$

Repeating the above and considering the various ranges of data for the maximum propagated uncertainty, when $L_x/L_p \leq 1.0$, it can be shown that Equation 12.15 becomes

$$\frac{U_V}{V} \leq \left\{ \left(\frac{-0.892 U_{1-x}}{1-x} \right)^2 + \left(\frac{0.892}{B_*} \right)^2 [U_{B_0}^2 + \right.$$

$$\left. \left[\frac{U_{L_x}}{\frac{L_p}{\frac{L_x}{L_p}} (B_0 - B_*) C_1} \right]^2 \right\}^{\frac{1}{2}}$$

By substituting Equation 12.13, $\frac{U_{L_p}}{L_p} = \frac{U_{ND}^2}{ND^2}$, and

$$\frac{U_x}{x} \approx \frac{U_{1-x}}{1-x}, \text{ finally,}$$

$$\frac{U_V}{V} \leq \left[0.9538 \left(\frac{U_{1-x}}{1-x} \right)^2 + 3.5577 \left(\frac{U_{B_0}}{B_0} \right)^2 + 0.1582 \left(\frac{U_L}{L} \right)^2 \right.$$

$$\left. + 0.1582 \left(\frac{U_{ND}^2}{ND^2} \right)^2 \right]^{\frac{1}{2}} \quad (12.17)$$

Inserting the above mentioned data, that is,

$$\frac{U_{1-x}}{1-x} = \frac{0.0147}{0.8090} = 0.0244$$

$$\frac{U_L}{L} = \frac{0.01}{1.02} = 0.0098$$

$$\frac{U_{ND}^2}{ND^2} = 0.1111$$

} uncertainty in measurement

and

$$\frac{U_{B_0}}{B_0} = \frac{0.53}{8.86} = 0.0598$$

} total uncertainty

leads in Equation 12.17 to

$$\frac{U_V}{V} \leq 0.1247 \quad \text{or} \quad 12.47\%$$

for the fractional uncertainty in breakdown voltage.

If U_{B_0}/B_0 alone is considered in Equation 12.17,

$$\frac{U_V}{V} \leq 0.1128 \quad \text{or} \quad 11.28\%$$

In conclusion, the uncertainty in the breakdown voltage predicted from Equation 3.10b is apparently smaller than about 10% as long as the variables x , L , N , and D have smaller uncertainties than those values used here.

The breakdown voltages calculated from Equation 3.10b are compared with the experimental results in Figure 12.1. Of these points, 92% lie within $\pm 10\%$ deviation of the breakdown voltage. This is consistent with the estimated error range found previously.

The uncertainty in the breakdown time delay defined by Equation 3.15 is

$$\begin{aligned} \frac{U_\tau}{\tau} = & \left[\left(\frac{U_L}{L} \right)^2 + \left(\frac{U_{V_n}}{V_n} \right)^2 + \left(\frac{U_{B_0}}{B_0 - B_*} \right)^2 + \left(\frac{U_{B_*}}{B_0 - B_*} \right)^2 \right. \\ & \left. + \left(C_1 \frac{U_L x}{L_p} \right)^2 \right]^{\frac{1}{2}} \end{aligned} \quad (12.18)$$

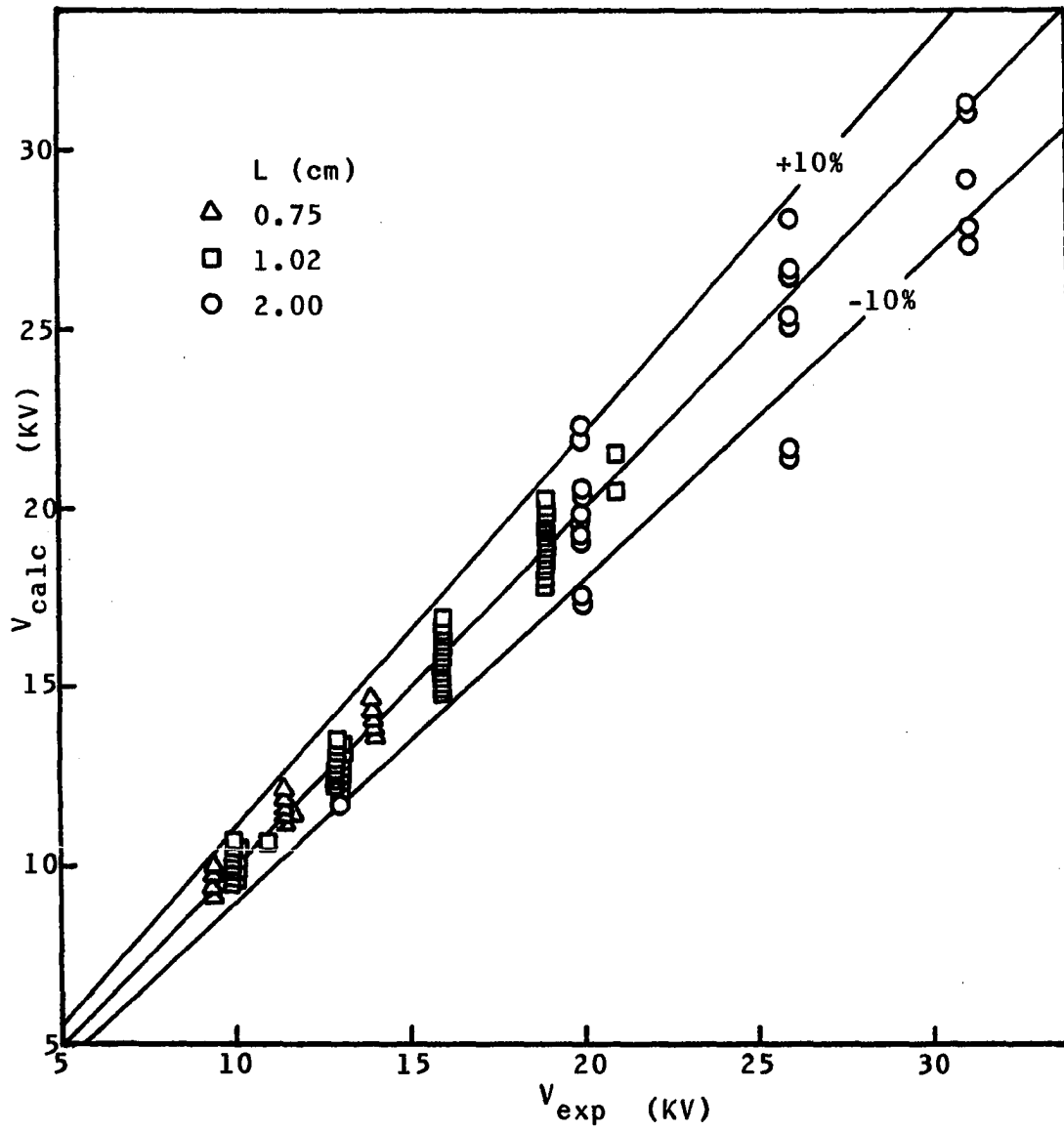


Figure 12.1. Comparison of experimental breakdown voltage data with Equation 3.10b

with $(1-x)_o = B_o V^{-1.121}$ and $(1-x)_c = B_* V^{-1.121}$

Using the previous numerical results for U_L , U_{B_o} , etc. leads to

$$\frac{U_{\tau}}{\tau} = 0.1588 \quad \text{or} \quad 15.88\% \quad \text{with} \quad \frac{U_{v_n}}{v_n} = 0.05$$

Finally, the uncertainty in the spark ignition energy of the multiphase mixture given by Equation 5.2 is

$$\begin{aligned} \frac{U_{E_i}}{E_i} = & \left\{ \left(\frac{U_{E_{io}}}{E_{io}} \right)^2 + \left[3 \left(\frac{ND^2}{H_3} \right) \frac{U_{ND^2}}{ND^2} \right]^2 \right. \\ & \left. + \left[3 \left(\frac{ND^2}{H_3} \right) \frac{U_{H_3}}{H_3} \right]^2 \right\}^{\frac{1}{2}} \end{aligned} \quad (12.19)$$

Using the uncertainties,

$$\frac{U_{E_{io}}}{E_{io}} = 0.0285, \quad \frac{U_{ND^2}}{ND^2} = 0.119, \quad \text{and} \quad \frac{U_{H_3}}{H_3} = 0.100,$$

in Equation 12.19 gives

$$\frac{U_{E_i}}{E_i} = 0.4672 \quad \text{or} \quad 46.72\%, \quad \text{when} \quad \frac{ND^2}{H_3} = 1.0$$

This large uncertainty is expected because of the exponential dependence of $(ND^2/H_3)^3$ on E_i .